
Heat transfer and evaporation during single drop impingement onto a superheated wall

Wärmeübergang und Verdampfung während des Einzeltropfenaufpralls auf eine überhitzte Wand

Vom Fachbereich Maschinenbau der Technischen Universität Darmstadt zur Erlangung des akademischen Grades Doktor-Ingenieur (Dr.-Ing.) genehmigte Dissertation von M.Sc. Stefan Batzdorf aus Fulda
Tag der Einreichung: 22. Januar 2015, Tag der Prüfung: 21. April 2015
Darmstadt 2015 – D 17

1. Gutachten: Prof. Dr.-Ing. Peter Stephan
2. Gutachten: Prof. Dr.-Ing. habil. Bernhard Weigand
3. Gutachten: Apl. Prof. Dr. Sc. Tatiana Gambaryan-Roisman



TECHNISCHE
UNIVERSITÄT
DARMSTADT

TTD

Technische Thermodynamik

Heat transfer and evaporation during single drop impingement onto a superheated wall
Wärmeübergang und Verdampfung während des Einzeltropfenaufpralls auf eine überhitzte Wand

Genehmigte Dissertation von M.Sc. Stefan Batzdorf aus Fulda

1. Gutachten: Prof. Dr.-Ing. Peter Stephan
2. Gutachten: Prof. Dr.-Ing. habil. Bernhard Weigand
3. Gutachten: Apl. Prof. Dr. Sc. Tatiana Gambaryan-Roisman

Tag der Einreichung: 22. Januar 2015

Tag der Prüfung: 21. April 2015

Darmstadt – D 17

This thesis is available online at:

URN: urn:nbn:de:tuda-tuprints-45424

URL: <http://tuprints.ulb.tu-darmstadt.de/4542>

Dieses Dokument wird bereitgestellt von tuprints,

E-Publishing-Service der TU Darmstadt

<http://tuprints.ulb.tu-darmstadt.de>

tuprints@ulb.tu-darmstadt.de



This publication is available at the following Creative Commons license:

Attribution – Non-commercial – No-derivatives – 3.0 de

<http://creativecommons.org/licenses/by-nc-nd/3.0/de/>

Erklärung zur Dissertation

Hiermit versichere ich, die vorliegende Dissertation ohne Hilfe Dritter nur mit den angegebenen Quellen und Hilfsmitteln angefertigt zu haben. Alle Stellen, die aus Quellen entnommen wurden, sind als solche kenntlich gemacht. Diese Arbeit hat in gleicher oder ähnlicher Form noch keiner Prüfungsbehörde vorgelegen.

Darmstadt, den 22. Januar 2015

Stefan Batzdorf



Vorwort

Die vorliegende Dissertationsschrift entstand während meiner Tätigkeit am Institut für Technische Thermodynamik der Technischen Universität Darmstadt. Ich bedanke mich herzlich bei Herrn Prof. Peter Stephan für die Möglichkeit, diese Arbeit an seinem Fachgebiet durchzuführen, sein stetes Vertrauen in mich und meine Arbeit sowie für die mir eingeräumte Freiheit. Des Weiteren bedanke ich mich bei Frau Dr. Tatiana Gambaryan-Roisman, die stets ein offenes Ohr für mich hatte und mir wichtige Impulse zum Gelingen dieser Arbeit gab.

Darüber hinaus gilt mein herzlicher Dank Herrn Prof. Weigand, zum einen für seine Bereitschaft zur Übernahme des Koreferates, insbesondere aber auch für die maßgebliche Initiierung des Sonderforschungsbereiches SFB-TRR 75, innerhalb dessen diese Arbeit angesiedelt war. Die Zusammenarbeit mit den im Rahmen des SFBs beteiligten Kollegen der Universitäten Darmstadt und Stuttgart empfand ich jederzeit als inspirierend und konstruktiv.

Ich möchte mich aber auch bei jenen Personen bedanken, die mich während meines Studiums und meiner parallelen HiWi-Tätigkeit am TTD betreut haben und mir dadurch den Weg hin zur Promotion geebnet haben, Herrn Tobias Schulze und insbesondere Herrn Dr. Christian Kunkelmann. Während dieser Zeit konnte ich von beiden fachlich wie überfachlich Vieles lernen, was deutlich über die normale Wissensvermittlung im Studium hinausgeht.

Darüber hinaus danke ich meinen Kollegen am TTD für die gute Arbeitsatmosphäre am Institut und den Willen, Probleme nicht zu beschönigen sondern gemeinsam zu diskutieren und zu lösen. Dies gilt in erster Linie meinen Bürokollegen Dr. Axel Sielaff und Felix Crößmann. Allen voran aber gilt mein Dank Herrn Jochen Dietl, nicht nur für die aufmerksame Durchsicht des Manuskripts, sondern vor allem auch für die zahlreichen intensiven wie auch inspirierenden Diskussionen über den Teufel im Detail der Physik und der Numerik.

Nicht zuletzt gilt mein besonderer Dank meiner Frau Carmen für die Unterstützung, die sie mir während der zurückliegenden Jahre fortwährend zukommen ließ. Insbesondere in Zeiten des Zweifels hat sie mich immer wieder zurück auf den richtigen Weg gebracht.

Darmstadt, den 22. Januar 2015

Stefan Batzdorf



Abstract

Abstract

This thesis is aiming for the numerical simulation of the impingement process of a single droplet onto a wall which is superheated against the fluid's saturation temperature corresponding to the bulk pressure. The heat transfer during drop impingement is of particular importance in spray cooling which is a promising technology for the removal of high heat fluxes at a small temperature difference.

While the hydrodynamics of an impinging droplet have been studied extensively in the past, the heat transfer to the droplet during the impingement process in the non-isothermal case is not yet fully understood, in particular if evaporation comes into play. Moreover, many studies on pool boiling heat transfer have demonstrated that the evaporation at the 3-phase contact line, where the solid, liquid, and gas phase meet, might contribute significantly to the overall heat transfer. Hence, it can be expected that a proper knowledge of the physical processes at the contact line might be crucial for the understanding of the entire process. However, up to now no attempt has been made to model the heat transfer of an impinging droplet just above the boiling point taking into account the microscale thermodynamic effects at the contact line.

Zusammenfassung

Die vorliegende Dissertation zielt auf die numerische Simulation des Tropfenaufpralls auf eine Wand ab, die gegenüber der Sättigungstemperatur des Fluids überhitzt ist. Der Wärmeübergang während des Tropfenaufpralls ist von besonderer Bedeutung im Rahmen der Sprühkühlung, die eine hervorragend geeignete Technologie zur Übertragung großer Wärmemengen bei kleinen Temperaturdifferenzen darstellt.

Während die Hydrodynamik eines aufprallenden Tropfens in der Vergangenheit intensiv untersucht wurde, ist der Wärmeübergang während des Aufpralls im nicht isothermen Fall noch nicht vollständig verstanden, insbesondere wenn Verdampfungsprozesse relevant sind. Außerdem haben zahlreiche Forschungsarbeiten zu Siedevorgängen in der Vergangenheit gezeigt, dass die Verdampfung nahe der 3-Phasen Kontaktlinie, an der die flüssige, feste und gasförmige Phase aufeinander treffen, einen signifikanten Teil zum globalen Wärmeübergang beitragen kann. Daher ist zu erwarten, dass für ein tieferes Verständnis der globalen Vorgänge die genaue Kenntnis der physikalischen Vorgänge an der Kontaktlinie unumgänglich ist. Bislang ist jedoch noch kein Versuch unternommen worden, den Wärmeübergang beim Tropfenaufprall unter Berücksichtigung der Mikrothermodynamik an der Kontaktlinie zu modellieren.

To shed light on the individual heat transfer processes involved in the overall process and to quantify their individual importance, a numerical simulation of the drop impingement is conducted within this thesis. Numerical simulations provide data on small length and time scales which cannot be resolved with available measurement techniques. The numerical model is based on the Volume of Fluid method to track the evolution of the droplet shape. Evaporation is accounted for at the surface of the droplet. Special attention is paid to the modeling of the evaporative heat transfer in the vicinity of the moving 3-phase contact line.

The developed numerical model is validated with the help of highly resolved experimental data on single drop impingement. A good agreement of the model predictions to the measurements is achieved. At the same time the detailed information provided by the simulation are employed to identify the dominant phenomena governing the heat transfer during the entire impingement process. Moreover, the model is utilized to quantify the impact of the governing influence parameters. Thereby it is made use of the great advantage of numerical simulations that any parameter can be controlled individually without any additional effort. Even though the focus of this thesis is on single droplets, also the interaction of individual droplets during their impingement is addressed briefly.

Zur Erlangung eines tieferen Verständnisses der grundlegenden Wärmetransportmechanismen während des Tropfenaufpralls und um die Bedeutung der individuellen Mechanismen zu quantifizieren, wird im Rahmen dieser Dissertation eine numerische Simulation des Tropfenaufpralls durchgeführt. Numerische Simulationen bieten einen Einblick in Vorgänge auf Längen- und Zeitskalen, die jenseits der Auflösung etablierter Messtechniken liegen. Das numerische Modell basiert auf der Volume of Fluid Methode zur Verfolgung der Tropfenform. Die Verdampfung an der Phasengrenze wird im Rahmen des Modells berücksichtigt. Besondere Aufmerksamkeit wird der Modellierung des Wärmeübergangs durch Verdampfung im Bereich der bewegten 3-Phasen Kontaktlinie gewidmet.

Das entwickelte numerische Modell wird anhand hochaufgelöster experimenteller Daten zum Einzeltropfenaufprall validiert. Die numerischen Vorhersagen geben die Messdaten dabei in guter Übereinstimmung wieder. Gleichzeitig geben die detaillierten Berechnungsergebnisse Aufschluss über die dominanten Wärmetransportvorgänge während des Aufpralls. Darüber hinaus wird das Modell eingesetzt, um den Einfluss der wichtigsten Einflussgrößen zu untersuchen. Dabei wird der große Vorteil numerischer Simulationen ausgenutzt, dass alle Prozessparameter unabhängig kontrollierbar sind. Auch wenn der Schwerpunkt der vorliegenden Arbeit auf der Untersuchung von Einzeltropfen liegt, wird auch die Wechselwirkung von zwei simultan aufprallenden Tropfen qualitativ bewertet.

Contents

Abstract	v
Nomenclature	ix
1. Introduction	1
1.1. Motivation and practical relevance	1
1.2. Single drop impingement phenomena	2
1.2.1. Classification of impingement scenarios	3
1.2.2. Possible impingement morphologies	5
1.3. Evaporation in the vicinity of the 3-phase contact line	7
1.4. State of the art of non-isothermal drop impact	7
1.4.1. Numerical investigations	7
1.4.2. Experimental investigations	9
1.5. Aims and outline of this thesis	10
2. Micro scale heat and fluid flow near contact lines	13
2.1. Thermodynamics of the near wall liquid-vapor interface	15
2.1.1. Adhesion and the disjoining pressure	16
2.1.2. Thermodynamic equilibrium at the liquid-vapor interface	19
2.1.3. Evaporation at the liquid-vapor interface	23
2.2. Modeling of the evaporating micro region	26
2.2.1. One-dimensional lubrication model	27
2.2.2. Direct numerical simulation	37
2.3. Results	41
2.3.1. Influence of contact line motion on the microscopic heat and mass transfer	41
2.3.2. Validation of the one-dimensional lubrication model	43
2.3.3. Validation of further modeling assumptions	46
2.3.4. Sensitivity analysis	53
2.3.5. Parameterization of the results	55

3. Macro scale heat and fluid flow	59
3.1. Governing equations	59
3.2. Interface tracking	60
3.3. Reconstruction of the interface	63
3.3.1. Correction of boundary values	64
3.3.2. Interpolation	65
3.3.3. Reconstruction	67
3.3.4. Distance field and curvature calculation	68
3.4. Modeling of phase change	69
3.4.1. Calculation of the temperature gradient	70
3.4.2. Implicit formulation of the gradient	72
3.4.3. Distribution of the mass sources	73
3.5. Coupling of micro and macro region heat transfer	75
3.6. Conjugate heat transfer between fluid and solid	79
3.7. Acceleration techniques	80
3.7.1. Adaptive time step	80
3.7.2. Dynamic mesh refinement	81
3.7.3. Parallelization and load balancing	82
3.8. Model overview	84
3.9. Validation studies	86
3.9.1. Evaporation model	86
3.9.2. Contact line evaporation	89
4. Results and discussion	93
4.1. Single drop impingement	93
4.1.1. Reference experiment	93
4.1.2. Numerical setup	96
4.1.3. Basic phenomena and validation	99
4.1.4. Influence of modeling details	106
4.2. Identification of the governing influencing parameters	110
4.2.1. Influence of droplet parameters	111
4.2.2. Influence of wall properties	125
4.3. Coalescence of two simultaneously impinging droplets	128
5. Summary and conclusions	135
Bibliography	138
A. Appendix	149
A.1. Material properties	149
A.2. Correlation coefficients for the contact line model	150
A.3. Parametric study	151

Nomenclature

Latin symbols

Symbol	Description	Unit
A	dispersion constant	J
\tilde{A}	Hamaker constant	J
c	specific heat capacity	J/(kg K)
D	diameter	m
d	distance	m
E	energy	J
e	spacing parameter	-
\mathbf{F}	force	N
f	condensation coefficient	-
\mathbf{f}	volumetric force	N/m ³
F	volume fraction	-
g	gravitational acceleration	m/s ²
H	thickness	m
$H(x)$	Heaviside function	-
h	heat transfer coefficient	W/(m ² K)
h_{lv}	enthalpy of vaporization	J/kg
K	curvature	1/m
k	thermal conductivity	W/(m K)
L	length scale	m
M	mass	kg
\dot{M}	mass flow	kg/s
m	mass flux	kg/(m ² s)
N	number	-
N_A	Avogadro number	1/mol
\mathbf{n}	unit normal vector	m
p	pressure	N/m ²
Q	heat	J
\dot{Q}	heat flow	W
\dot{Q}	integrated heat flux	W/m
q	heat flux	W/m ²
R	radius	m

R_{int}	interfacial heat resistance	$(\text{m}^2 \text{K})/\text{W}$
R_{ϵ}	effusivity ratio	-
\mathcal{R}	gas constant	$\text{J}/(\text{kg K})$
r	radial coordinate	m
S	spreading ratio	-
S	surface area	m^2
\bar{S}	molar entropy	$\text{J}/(\text{kmol K})$
\mathbf{S}	surface vector	m^2
T	Temperature	K
t	time	s
Δt	time step	s
\hat{t}	time scale	s
\mathbf{u}, u	velocity	m/s
V	volume	m^3
\bar{V}	molar volume	m^3/kmol
W	work	J
Δx	grid size	m
x, y, z	Cartesian coordinates	m

Greek symbols

Symbol	Description	Unit
α	angle	deg
α	thermal diffusivity	m^2/s
Γ	correction term	-
δ	film thickness	m
ϵ	perturbation factor	-
ϵ	thermal effusivity	$\text{J}/(\text{m}^2 \sqrt{\text{s}} \text{K})$
η	local coordinate perpendicular to wall	m
θ	contact angle	deg
μ	chemical potential	J/kmol
μ	dynamic viscosity	$\text{kg}/(\text{m s})$
ν	kinematic viscosity	m^2/s
ξ	local coordinate along wall	m
ρ	density	kg/m^3
$\bar{\rho}$	molar density	kmol/m^3
Σ	source term	various
σ	surface tension	N/m
τ	dimensionless time	-
Φ	energy potential	J
Ψ	sphericity	-

Subscripts

Subscript	Description
0	initial conditions
c	computational cell
cl	contact line
disp	dispersion
drop	droplet
evap	evaporation
f	fluid
f	face
int	interface
l	liquid
p	point
s	solid
sat	saturation conditions
th	thermal
v	vapor
w	wall
∞	far field value

Superscripts

Superscript	Description
*	dimensionless

Abbreviations

Abbreviation	Description
ALE	Arbitrary Lagrangian-Eulerian
AMR	adaptive mesh refinement
CFD	Computational Fluid Dynamics
CPU	central processing unit
ODE	ordinary differential equation
VOF	Volume of Fluid

Dimensionless groups

Symbol	Description	Definition
Bi	Biot number	hH/k
Bo	Bond number	$\rho g D_0^2 / (4\sigma)$
E^*	dimensionless heat	$6Q / (\pi \rho D_0^3 h_{lv})$
Fo	Fourier number	$\alpha t / H^2$
Ja	Jacobs number	$c\Delta T / h_{lv}$
Nu	Nusselt number	hL_0/k
Oh	Ohnesorge number	$We^{1/2} / Re$
Pr	Prandtl number	$c\mu/k$
\dot{Q}^*	dimensionless heat flow	$6\dot{Q} / (\pi \rho D_0^2 u_0 h_{lv})$
Ra	Rayleigh number	$\Delta T g L_0^3 Pr / (T_\infty \nu^2)$
Re	Reynolds number	$\rho D_0 u_0 / \mu$
We	Weber number	$\rho D_0 u_0^2 / \sigma$

CHAPTER 1

Introduction

1.1 Motivation and practical relevance

"The splash of a drop is a transaction which is accomplished in the twinkling of an eye, and it may seem to some that a man who proposes to discourse on the matter for an hour must have lost all sense of proportion." [120]

With these words A. M. Worthington started his essay on the splash of a single droplet hitting a solid wall at the very end of the 19th century. Even though Worthington just wanted to express his fascination for the complexity of fluid dynamics, his statement also illustrates that there appears to be a discrepancy between the subject of fundamental research and its significance to technical applications. However, processes on technical length- and timescales might be governed by elementary phenomena occurring on much smaller scales. Therefore, a more precise knowledge about these elementary phenomena might be crucial for a better understanding of the overall technical process.

More than a hundred years after the work of Worthington, the impact of a single drop onto a solid wall is still not fully understood, especially when heat transfer and evaporation during the impingement process are relevant. At the same time, sprays are widely used in numerous technical applications. In some of these applications an interaction of the spray with the surrounding walls is in general not desired, for instance during the fuel injection into internal combustion engines. On the contrary, for the spray cooling technique the fluid-wall interaction is the key phenomenon in terms of the heat transfer performance. Spray cooling is characterized by an extremely high heat transfer coefficient compared to single phase natural or forced convection. It performs even better than other two-phase cooling concepts like nucleate boiling while at the same time a reduced amount of fluid is required [46]. Spray cooling is therefore particularly favored in cases in which a huge amount of heat has to be removed from a comparably small surface or at a low surface superheat. Hence, it is a promising technique for cooling of electronic devices. In this field the heat produced per unit area is continuously increasing due to the ongoing trend of miniaturization. At the same time the maximal acceptable surface temperature is limited in order to prevent damage of the electronic device.

The lack of knowledge about the exact process parameters dominating the fluid dynamics and the heat transfer on the small scales also complicates the design of the technical process. Usually, the design process is based on purely empirical principles. These design methods, however, could be significantly improved by understanding the underlying physics of the basic phenomena.

In order to enhance the basic knowledge about the droplet wall interaction considering heat transfer and evaporative phase change, a detailed numerical description of the impact process is aimed for in this work. It can be considered to be only a small step towards a better understanding of the underlying physics but some of the phenomena discovered can be directly linked to tendencies also observed on a technical scale.

1.2 Single drop impingement phenomena

The phenomenology of the drop impingement process might substantially differ from case to case depending on the exact boundary and initial conditions. Therefore a classification of different possible scenarios will be given in the following and the conditions relevant for this thesis will be defined more precisely.

In order to categorize the different phenomena coming into play for various configurations, a description based on dimensionless quantities is helpful. A quantity widely used to describe the influence of surface tension effects on the hydrodynamic characteristics of the droplet is the Weber number

$$\text{We} = \frac{\rho_1 D_0 u_0^2}{\sigma} \quad (1.1)$$

reflecting the ratio of inertial to surface tension forces. In addition the Reynolds number

$$\text{Re} = \frac{\rho_1 D_0 u_0}{\mu_1} \quad (1.2)$$

is employed as a measure for the ratio of inertial and friction forces. A combination of both numbers is also widely used in literature, namely the Ohnesorge number

$$\text{Oh} = \frac{\sqrt{\text{We}}}{\text{Re}} = \frac{\mu_1}{\sqrt{\rho_1 D_0 \sigma}}.$$

The effect of gravitational forces can be described by using the Bond number

$$\text{Bo} = \frac{\rho_1 g D_0^2}{4\sigma} \quad (1.3)$$

which is defined as the squared ratio of the droplet radius to the capillary length scale. A complete dimensional analysis following the Buckingham Π -theorem would result in additional dimensionless

numbers including the properties of the gas phase. However, in all cases investigated in this thesis the density and the dynamic viscosity of the gas phase can be completely neglected against the corresponding properties of the liquid phase.

In order to compare the hydrodynamic behavior of individual drop impact events, the physical time is rescaled using the hydrodynamic time scale, resulting in the definition of the dimensionless impact time

$$\tau = \frac{tu_0}{D_0}. \quad (1.4)$$

A frequently used measure of the hydrodynamic behavior of the droplet is the spreading ratio

$$S = \frac{D_{cl}}{D_0}, \quad (1.5)$$

which is the ratio of the diameter of the maximal wetted region on the wall to the initial diameter of the droplet.

1.2.1 Classification of impingement scenarios

An overview of possible combinations of the hydrodynamic boundary conditions for single drop impingement is given by Rein [79] as presented in Fig. 1.1. A classification can be done with respect to the properties of the liquid droplet itself, the impingement configuration and the constitution of the target surface.

Within this thesis initially spherical droplets of a pure liquid will be considered. Of course, at the time instant of the actual impact, the droplet might show a slight deformation as well as a weak internal circulation both being established during the time of free falling. The fluid investigated is considered to be Newtonian and the influence of surfactants¹ is not taken into account.

Moreover, only a normal impact onto the target surface will be considered without any cross flow. The solid surface will not be pre-wetted by any liquid and only plane and smooth surfaces will be considered. Any deformation of the surface due to the interaction with the impacting droplet will be neglected.

Concerning the thermal boundary conditions the problem can be further specified. In Figure 1.2 the lifetime of a water droplet deposited on a hot solid surface is shown for different surface temperatures. For a wall temperature below the liquid saturation temperature T_{sat} , the droplet slowly evaporates into the surrounding air atmosphere. In this regime, which will be referred to as *subcooled deposition*, the evaporation is governed by the diffusion of the vapor within the gas atmosphere. Since the evaporation of the droplet occurs on a much larger timescale than the actual impact, most of the research in this area is limited to the evaporation of sessile droplets. An overview of the basic theory and experimental investigations in this regime is given by Erbil [20].

¹ **surface active agents**

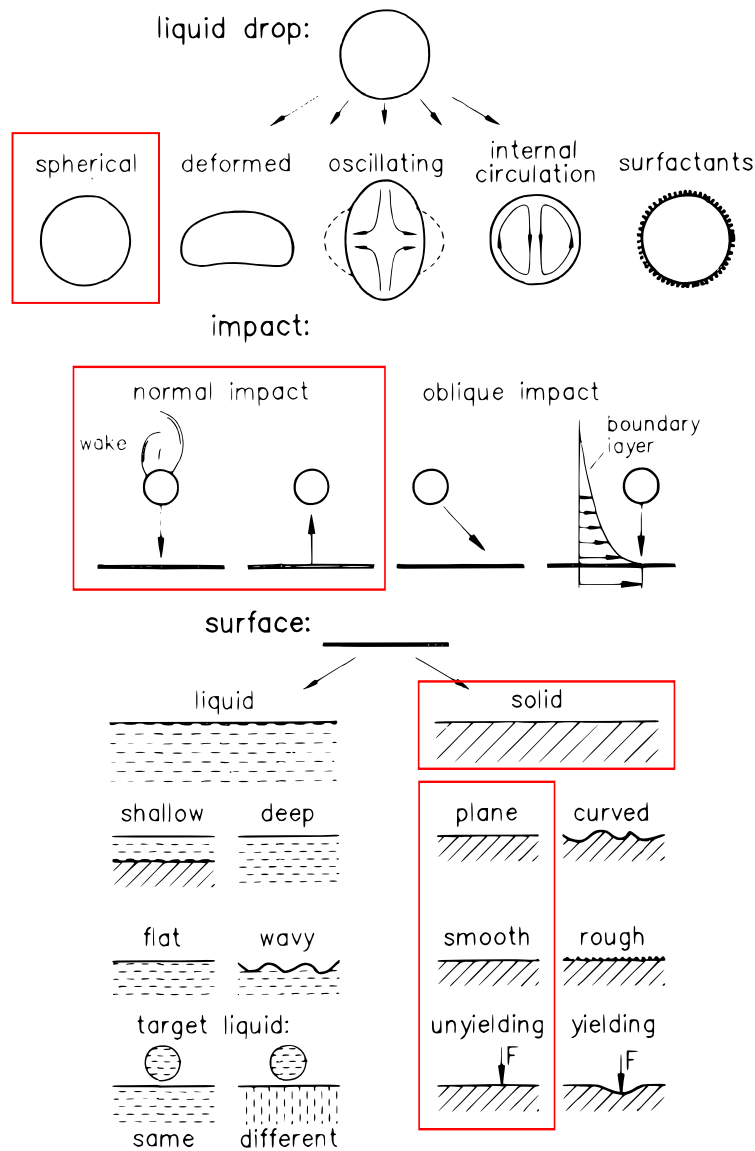


Figure 1.1.: Classification of possible drop impingement scenarios by Rein [79]. The conditions relevant for this thesis are indicated by the red boxes.

If the surface temperature is slightly above the saturation temperature, the droplet disappears much more rapidly after being placed on the surface due to an intense evaporation. In this case the evaporation is not longer limited by the diffusion process of the vapor but by the heat transfer from the surface towards the droplet. This regime will be referred to as *superheated deposition* within this thesis. If the surface temperature is further increased, nucleation of vapor bubbles starts at the solid-liquid interface. The number of created bubbles in this *nucleate boiling* regime increases with surface temperature. These bubbles might form larger vapor regions partially separating the liquid from the wall. Thereby the lifetime increases with the wall temperature within this transition regime.

As soon as the surface temperature exceeds the Leidenfrost temperature T_{Leid} , which is defined as the temperature at which the lifetime is maximal, the *Leidenfrost regime* is reached. In this regime there is no longer any direct contact between the droplet and the wall surface. Instead, the droplet levitates on a thin vapor cushion separating it from the wall completely. Due to its small thermal conductivity,

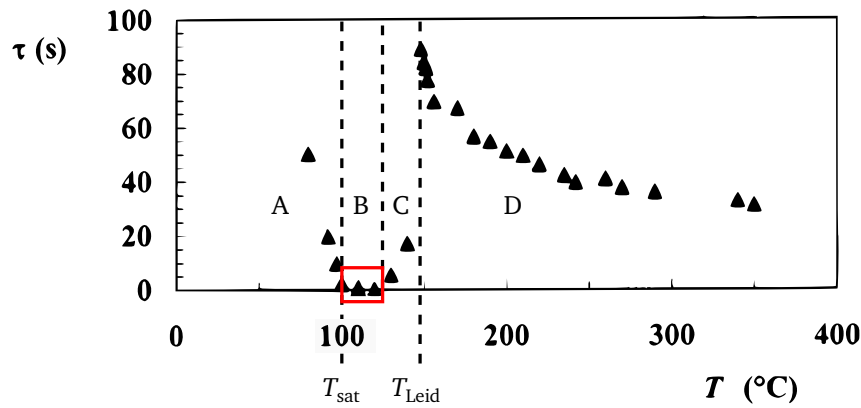


Figure 1.2.: Lifetime of a water droplet on a hot Duralumin plate, adapted from [8].
 A: subcooled deposition, B: superheated deposition, C: nucleate boiling and transition region, D: Leidenfrost regime.

this vapor film reduces the heat transfer towards the droplet. The Leidenfrost temperature is mostly given for a droplet being slowly deposited on the wall, but the transition temperature increases with the Weber number in case of an impacting droplet. In this case the transition temperature is referred to as the dynamic Leidenfrost temperature [104]. Moreover, the dynamic Leidenfrost temperature might also depend on the surface structure [105]. A review on drop impingement in the Leidenfrost state has recently been given by Quéré [77].

In this study the case of superheated deposition will be addressed, i.e. the surface temperature is above the liquid saturation temperature but well below the Leidenfrost point. Due to the intense evaporation in this regime, the droplet can be assumed to be surrounded by a pure vapor atmosphere. Any residual air will be pushed away from the liquid-vapor interface by the produced vapor and its transport has therefore not to be taken into account. Internal nucleation of vapor bubbles within the droplet occurring within the nucleate boiling impact regime at medium wall superheat as observed by Chandra and Avedisian [13] or Wang et al. [113] will not be taken into account. A modeling of this regime would require a detailed description of the stochastic process of heterogeneous nucleation at the wall which is in general not yet understood in detail [12, pp. 210–220] and subject to ongoing research.

1.2.2 Possible impingement morphologies

Depending on the impingement parameters and the surface properties of the wall the droplet will show a fairly different behavior during the impingement. A systematic classification of the scenarios which can be observed has been worked out by Rioboo et al. [83]. An excerpt of different characteristic phenomena is given in Figure 1.3.

If the inertia of the droplet is small compared to viscous effects corresponding to a small Reynolds number, the so-called droplet deposition will be observed (first row in Fig. 1.3). In this regime, no instabilities are observed and no secondary droplets will be created during the entire impingement process. During the spreading of the droplet on the surface the contact line expands radially outwards, and a characteris-

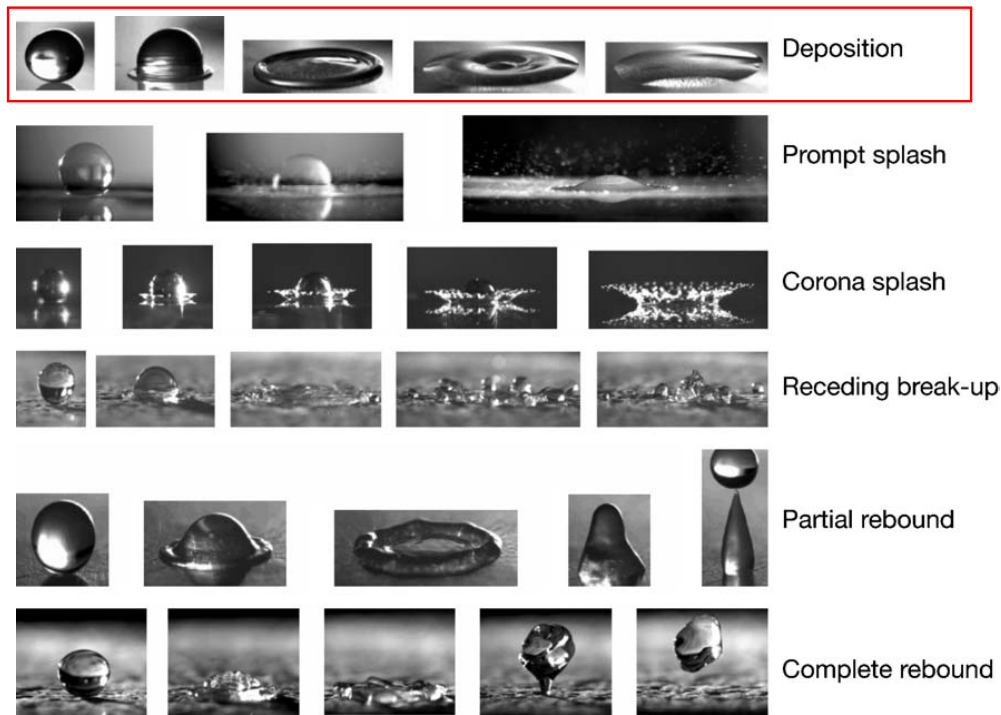


Figure 1.3.: Possible morphologies of drop impingement onto a dry wall [121] (originally published in [83]).

tic rim is created near the contact line surrounding a thin liquid film near the center of the drop, termed the lamella.

Depending on the wetting properties and the initial kinetic energy the droplet might contract after the wetted area has reached its maximal size. In this receding phase the contact line moves radially inwards driven by capillary forces. Finally, the droplet develops towards its equilibrium shape sitting on the surface. However, if the receding motion of the droplet is fast enough, a rebound might be observed. Thereby, in case of a partial rebound, a large secondary droplet might be generated while a certain amount of liquid is left on the surface. If the receding contact angle is very large, i.e. on superhydrophobic surfaces, the droplet might also completely leave the surface. From a macroscopic point of view this behavior is somewhat similar to the one of droplets in the Leidenfrost regime at a small Weber number.

Another phenomenon driven by the wetting properties is the receding break-up. If the receding contact angle tends to zero, the contracting contact line will leave several small secondary droplets on the surface during its motion.

If the inertia of the droplet becomes predominant over viscous and capillary forces, splashing occurs. In the splashing regime secondary droplets are generated during the spreading. For a prompt splash these droplets are generated directly at the advancing contact line. Whether this type of splashing can be observed or not strongly depends on the roughness properties of the wall. Another type of splashing is the corona splash. In this case a crown is formed which then breaks up into small droplets. The phenomenology of this splash type is similar to the splash of droplets impacting on shallow liquid films, which has also been extensively studied experimentally (e.g. by Cossali et al. [15]) and numerically (e.g.

by Rieber and Frohn [82]). The transition from the deposition to the splashing regime is influenced by numerous parameters but is mostly correlated with the characteristic K number

$$K = We Oh^{-0.4} = We^{0.8} Re^{0.4}. \quad (1.6)$$

The probability of splashing increases with the value of K . A typical value for the threshold value is $K_{\text{splash}} = 657$ [63]. For a millimetric droplet of FC-72 like used in this work, this corresponds to an impact velocity of $u_0 \approx 0.6$ m/s. However, large deviations from this value have been found depending on other parameters like the roughness, see for example [83].

Within this work only the droplet deposition regime will be addressed.

1.3 Evaporation in the vicinity of the 3-phase contact line

The apparent 3-phase contact line, where the liquid, gas and solid phase meet, is of special importance in boiling systems. In several experimental studies on single bubble pool boiling a minimum of the wall temperature close to the contact line could be observed [24, 90, 112] indicating a strong local heat transfer at this position. Similar observations have been made with generic experiments investigating the evaporation at a single meniscus with a capillary slot by Ibrahim et al. [37, 38].

The importance of the contact line region in boiling systems suggests that this region might also deserve special consideration when modeling the heat transfer during drop impingement onto a superheated wall. More details on the physical processes occurring near the contact line and reported modeling attempts will be given in Chapter 2.

1.4 State of the art of non-isothermal drop impact

A huge number of studies on single drop impingement is limited to isothermal conditions when heat transfer and evaporation are negligible. Several relevant contributions to this field of research have already been referred to in Section 1.2. A comprehensive review on numerical, experimental and theoretical work on the isothermal drop impact is given by Yarin [121]. In the following an overview of former studies will be given in which the focus is on the non-isothermal case.

1.4.1 Numerical investigations

An overview of studies on numerical simulation of drop impingement is given in Table 1.1. In spite of the focus on heat transfer, the pioneering work on the numerical description of isothermal single drop impingement by Fukai et al. [29] should not be left unmentioned. An Arbitrary Lagrangian-Eulerian description (ALE) was employed to track the deformable liquid-gas interface of the droplet. Thereby the Finite-Elements grid was deformed during the simulation such that the interface coincides with the mesh boundary. The gas atmosphere was not included into their consideration. Instead, the shear stress exhibited on the interface by the gas phase was neglected. The maximum spreading ratio was found

	interface representation	heat transfer	phase change included	contact line model	gas phase
Fukai et al. (1993) [29]	ALE	no	no	no	not included
Zhao et al. (1996) [122]	ALE	yes	no	no	not included
Bussmann et al. (1999) [11]	VOF	no	no	no	air
Pasandideh-Fard et al. (2002) [71]	VOF	yes	solidification	no	air
Francois & Shyy (2003) [25]	immersed boundary	yes	no	no	air
Nikolopoulos et al. (2007) [66]	VOF	yes	evaporation	no	air/vapor
Strotos et al. (2008) [101, 102]	VOF	yes	evaporation	no	air/vapor
Berberović et al. (2011) [6]	VOF	yes	no	no	air
present work	VOF	yes	evaporation	yes	pure vapor

Table 1.1.: Overview of numerical studies.

to increase with both, the Reynolds and the Weber number. Moreover, the dimensionless time at which the maximal spreading is reached was found to increase with the Weber number and slightly with the Reynolds number.

The computational framework of Fukai et al. was later extended to account for heat transfer by Zhao et al. [122]. They studied the impingement of a molten metal drop onto a cold wall in order to investigate the solidification during the impingement process. However, the solidification itself was not accounted for. A transient heat transfer behavior during the impingement process was found. The average heat transfer coefficient at the solid-liquid interface turned out to be maximal during the very initial stage of the impingement but considerably decreased during the spreading phase.

A further progress in the numerical description of the impingement processes was achieved through the development of interface tracking methods. In these methods the complex and computationally expensive step of re-meshing is no longer required. Especially the Volume of Fluid Method (VOF, see Hirt and Nichols [36]) has been widely used in the field of drop impingement. Using this numerical framework, Bussmann et al. [11] developed a three-dimensional model for isothermal drop impingement. This model has later been extended to account for heat transfer including solidification by Pasandideh-Fard et al. [71]. The numerical results were compared to experiments, but only with respect to the hydrodynamic behavior of the droplet. Francois and Shyy [25] observed a peak heat flux near the contact line for droplets impacting onto a hot surface at constant temperature. The characteristics of the wall heat flux profile was linked to the hydrodynamic behavior of the droplet. The average Nusselt number was found to decrease with increasing Reynolds and Weber number when compared at the same instant in terms of the dimensionless time. They also highlighted that the hydrodynamics in the later phase of the impact was significantly influenced by the usage of a dynamic contact angle model. This finding has also been supported by Šikalo et al. [93].

Drop impact onto superheated substrates within the transition region towards the Leidenfrost state has been simulated by Nikolopoulos et al. [66]. Although an evaporation model was included, no specific

treatment of the contact line has been employed. Moreover, nucleation was not modeled but evaporation was taking place within the droplet at a small vapor bubble entrapped during the initial stage of the impingement process. However, this entrapped bubble disappeared when the grid was refined.

Strotos et al. [101] computed the impact in the subcooled deposition regime. The evaporation was found to have a negligible influence on the cooling rate and the hydrodynamics during the spreading while it showed a considerable influence during the later stage of the impact. In addition the evaporation of the droplet was shown to slow down when the heat conduction within the solid substrate was accounted for [102]. Berberović et al. [6] accounted for the temperature dependency of the fluid properties and found an influence throughout all phases of the impact process.

Up to now, no attempt has been made to model the drop impingement process onto a wall just above the boiling point incorporating the effect of evaporation at the liquid-vapor interface as well as the microscale thermodynamic effects at the 3-phase contact line.

1.4.2 Experimental investigations

Besides the numerical studies, there are also a few experimental studies on heat transfer during drop impingement which are summarized in Table 1.2. A detailed overview on the hydrodynamics and regime transitions for the full range from subcooled deposition to the Leidenfrost state is given by Chandra and Avedisian [13]. The surface temperature was recorded only globally using thermocouples within the heater surface.

A method for measuring the local heat flux at the solid-fluid interface has been introduced by Lee et al. [53]. They employed an array of 96 feedback-controlled micro heaters. Thereby they were able to keep the temperature of the heater nearly constant and at the same time they could measure the amount of heat supplied by each individual heater. The overall heat transferred to the droplet was found to be larger during the phases when the droplet was spreading than during the stages of receding motion. However, the spatial resolution was not sufficient to draw conclusions about the local heat flux profile or the relevance of contact line evaporation. The local temperature field underneath a sessile droplet within a saturated vapor atmosphere has been measured by Sodtke et al. [94] using thermochromic liquid crystals. In contrast to local measurements performed in experiments on pool boiling (see e.g. [90]), no pronounced temperature minimum could be detected near the contact line, but the temperature showed a drastic change in the vicinity of the wetting front. Similar results were obtained by Weickgenannt et al. [117]. The impingement process could not be recorded by Sodtke et al. due to the quite low temporal resolution of 1 Hz. A measurement of the local wall temperature at the droplet center during the impingement has been performed by Bhardwaj et al. [7]. In the subcooled deposition regime the temperature has been found to be minimal when the droplet reached its maximal spreading radius and thereby the liquid film thickness at the center reaches its minimum.

A high spatial and temporal resolution of temperature measurements at the solid-fluid interface has been achieved by Chatzikyriakou et al. [14] and Fischer et al. [23, 34]. Both groups used an infrared transparent heater substrate on top of which a thin heating layer was added. Utilizing infrared thermography they were able to capture the temperature field of this heating layer. The local heat flux has afterwards

	temperature measurement	heat flux evaluation	heat transfer regime	gas atmosphere
Chandra & Avedisian (1992) [13]	global	no	subcooled deposition up to Leidenfrost	air/vapor
Lee et al. (2001) [53]	kept constant	global	superheated deposition to nucleate boiling	air/vapor
Bhardwaj & Attinger (2010) [7]	local at droplet center	no	subcooled deposition	air/vapor
Chatzikyriakou & Hewitt (2011) [14]	local	local	Leidenfrost regime	air/vapor
Fischer et al. (2013) [23, 34]	local	local	superheated deposition	pure vapor

Table 1.2.: Overview of experimental studies. The experiments of Fischer et al. will be used for validation of the numerical model.

been calculated numerically from the measured temperatures (for details on this procedure see [24]). While Chatzikyriakou et al. measured drop impingement in the Leidenfrost state, Fischer et al. present experiments in the superheated deposition regime. Since the experimental setup of Fischer et al. provides local temperature and heat flux data at the same time with data on the hydrodynamics, these experiments will be used for validation of the model developed within this thesis. More details on their methodology will be given in Section 4.1.1.

1.5 Aims and outline of this thesis

Considering the literature in the field of non-isothermal drop impact no complete description of the heat and mass transfer in the superheated deposition regime can be found. Experimental access to the entire physical process is difficult due to the wide range of time- and lengthscales involved. The effect of contact line evaporation on the overall heat transfer has not yet been quantified even though studies in different physical processes involving contact lines suggest that it might have a significant influence.

Therefore, in this thesis the development of a numerical model for the drop impingement in the superheated deposition regime is aimed for. Besides the numerical description of the complex two-phase flow, the evaporation at the liquid-vapor interface as well as at the contact line has to be considered. After its careful validation such a numerical tool can be used to shed light on the dominant physical processes during the impingement process and their relative importance for the overall heat transfer performance during the individual stages of the impact cycle.

The thesis will be structured as follows:

Chapter 1: The scope of this thesis is defined within the wide field of single drop impingement. A brief overview of existing models and experiments from the literature is presented and the aims of this thesis are derived.

Chapter 2: The thermodynamics of liquid-vapor interfaces and near wall films is reviewed and a model for the micro scale heat and fluid flow near moving contact lines is developed.

Chapter 3: The numerical model of the macro scale heat and fluid flow is presented. In particular, a model for evaporation at the free liquid-vapor interface is developed and the coupling of the

previously presented contact line model with the macroscopic model to an overall numerical model is presented. The validation for each novel model part is done individually.

Chapter 4: The results of the overall numerical model on single drop impingement onto a heated wall are presented. First, the hydrodynamics and heat transfer mechanisms are considered and compared with experimental results for a single impingement process. Afterwards the influences of relevant dimensionless parameters on the heat transfer performance are investigated. At the end of the chapter the impingement of two interacting droplets is discussed.

Chapter 5: The thesis is closed by some concluding remarks. An outlook and recommendations for future investigations are given.



Micro scale heat and fluid flow near contact lines

As already outlined in Section 1.3, various experimental studies of boiling systems have shown that the local heat transfer close to the 3-phase contact line is significantly higher than in the surrounding regions. As the thickness of the liquid layer separating the wall and the interface decreases towards the contact line, the thermal resistance through the liquid decreases, too. Since the temperature at the interface is fixed to the local saturation temperature in equilibrium, the small thermal resistance results in an extremely large heat flux if the wall is superheated.

However, according to the concept introduced by Potash and Wayner [76] on a microscopic scale there is no actual contact line. Instead, as indicated in Fig. 2.1, the apparently dry part of the wall adjacent to the vapor region is covered by a thin adsorbed film of fluid molecules. The thickness of this film is in the order of some nanometers. The fluid molecules within this layer are adsorbed to the wall due to the action of intermolecular dispersion forces as will be shown in detail in the next section. The dispersion forces influence the thermodynamic equilibrium, and the molecules of the adsorbed layer cannot enter the gas phase even if the wall temperature is above the bulk saturation temperature. The transition region between this adsorbed film and the macroscopic meniscus, referred to as the "interline region" by Potash and Wayner [76], is characterized by a sharp maximum in curvature of the liquid-vapor interface leading to the impression of a sharp contact line from a macroscopic point of view. In this work this transition region will be termed the "micro region" as introduced by Stephan and Busse [100] and Stephan [98] due to its very small characteristic length scale.

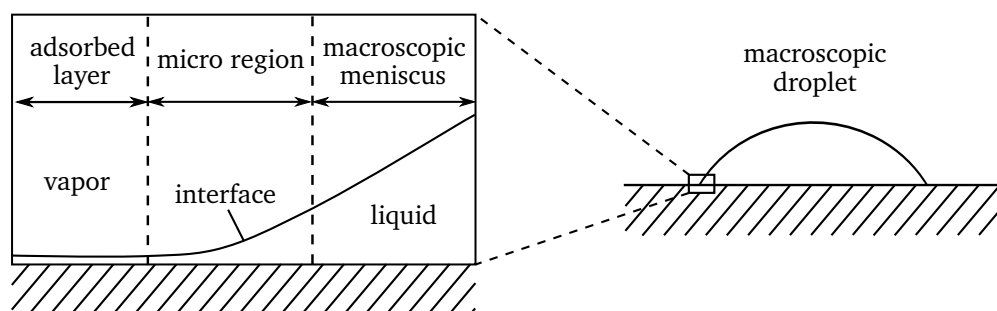


Figure 2.1.: Sketch of the droplet with the micro region.

The boundary separating the micro and the macro region is not sharp. However, within the micro region additional physical phenomena are relevant which are completely negligible on the macroscale. When the liquid-vapor interface comes very close to the solid wall, the thermodynamic equilibrium as well as the liquid flow are significantly influenced by intermolecular forces. Moreover, the thin liquid layer separating the wall from the interface has a low thermal resistance, making it necessary to consider the kinetics of evaporation at the interface as it might influence the rate of phase change in this situation. The liquid being evaporated at the liquid-vapor interface has to be delivered from the bulk area of the droplet resulting in a cross-flow of liquid towards the apparent contact line.

The first attempt to quantitatively model the fluid flow within the micro region has been done by Potash and Wayner [76]. As introduced above, they subdivided the full meniscus into two parts. According to their theory, in the macroscopic or intrinsic meniscus the driving force for the fluid flow is the capillary pressure, while in the micro region the flow is induced by a change of the "disjoining pressure", which originates from the intermolecular dispersion forces and will be described more closely below. Wayner et al. [115] used this approach to predict the average heat transfer coefficient in the micro region. Kamotani [43] came up with an approach accounting for the combined effect of capillarity and disjoining pressure within the micro region. This approach was further developed by Stephan [98] and Stephan and Busse [100] in order to calculate the heat transfer at heat pipe evaporator walls paying special attention to the micro region heat transfer. Like Wayner and Kamotani they utilized the lubrication theory to considerably simplify the governing equations by assuming the liquid film in the micro region to be comparably flat. Moreover, the fluid was assumed to perfectly wet the wall surface under isothermal conditions. Nevertheless, a non-zero contact angle is predicted by the models as soon as the wall is superheated against the fluid's saturation temperature.

During the last decades the models have been extended by various authors to account for the effect of binary mixtures [45], contact line motion [1, 62], thermal characteristics of the wall [62], Navier slip of the liquid [74] and fluids with partially wetting characteristics [1, 65]. In addition to the original application of this modeling approach of the micro region heat transfer to heat pipe evaporators, it has been successfully used in various studies on boiling heat transfer (e.g. in the groups of Dhir [3, 52, 96] and Stephan [27, 51, 99]) and in a theoretical investigation of the heat transfer performance of falling films on structured surfaces [30].

Measurements of physical quantities within the micro region are difficult due to the very small length and time scales involved. Hence it has not yet been possible to directly validate the micro region models by a comparison of local quantities. However, various studies have shown that macroscopic characteristics of evaporating contact lines could be captured at least qualitatively correct if a micro region model was employed. In terms of the influence of the wall superheat on the apparent contact angle, Raj et al. [78] as well as Fuhrmann and Dreyer [28] found a reasonable agreement between measurements and angles predicted by the model.

Despite the intensive research during the last decades, there are still open questions regarding the modeling of the micro region. First, in all micro region models the lubrication approximation is used to simplify the conservation equations. This approximation is however questionable if the apparent contact angle is large. This is in particular expected if the wall is strongly superheated or if the contact line is

advancing at a high speed as it will be the case during drop impingement. A two-dimensional description of the conductive and convective heat transfer within the micro region has been employed by Mathieu et al. [62]. They calculated the heat transfer at a moving contact line with the aid of a Finite Elements simulation while the shape of the liquid-vapor interface was calculated by a classical lubrication model. Even though they stated that convective heat transfer becomes important when the contact line is moving, their results can hardly be compared to other models since their computational domain was very large. Their considerations were therefore not limited to the micro region but included a certain part of the macroscopic meniscus. Moreover, the influence of two-dimensional conduction was not quantified by a comparison to a full lubrication model. The influence of two-dimensional effects and the convective terms in the momentum equation has so far not been investigated at all.

A second unknown parameter is the surface topography. Existing models assume a molecular smooth surface while any technical surface will show a significant roughness compared to the dimensions of the liquid film. Ojha et al. [67] found the macroscopic contact angle to decrease with increasing roughness. They used a variable slip length and a modified Hamaker constant to fit their experimental data but up to now there has been no attempt to directly take the surface topography into account.

Finally, all models assume the validity of continuum mechanics within the liquid film. This assumption, however, is questionable due to the very small thickness of the liquid film near the adsorbed layer and the resulting large Knudsen number. Van den Akker et al. [2] performed a molecular dynamic simulation of the micro region. They classified the flow within the micro region as a transition flow based on an analysis of the local Knudsen temperature number. Hence it is at the boundary of continuum mechanics and might rather be described with the aid of statistical methods based on the Boltzmann equation [42]. However, such methods are computationally very expensive and large Knudsen numbers are only observed in a very small region near the adsorbed layer. Moreover, the continuum model predictions by Stephan and Busse [100] were in a good agreement to the molecular dynamic simulations performed by van den Akker et al. Therefore, the validity of continuum mechanics is postulated in all following considerations.

In this work, the model of Stephan and Busse [100] will be extended by the effect of contact line motion. From this model global results will be extracted which will be required in the simulation of the macroscopic drop impingement presented in the next chapter. To be able to quantify the error introduced by the usage of the lubrication approximation, a direct numerical simulation of the micro region heat and fluid flow will be presented. The simulation allows a detailed investigation of the two- or three-dimensional heat transfer within the micro region as well as of the microscopic wall topography onto the micro region heat transfer.

2.1 Thermodynamics of the near wall liquid-vapor interface

Before the actual model of the micro region is presented, the underlying thermodynamic principles will be introduced. For a proper modeling of the micro region one has to take into account certain additional physical phenomena which are normally negligible on the macroscopic scale but become important if the characteristic length and time scales get small.

2.1.1 Adhesion and the disjoining pressure

In thin films long range interaction forces¹ between the molecules of the liquid film and the solid wall can be important. These dispersion forces follow from van der Waals interaction forces and can be either attractive or repulsive depending on the particular material combination. In a continuum description the dispersion forces can be considered as a volumetric force. Due to the action of this force, the fluid pressure increases or decreases close to the wall if the force is attractive or repulsive, respectively. This pressure change is commonly referred to as the "disjoining pressure".

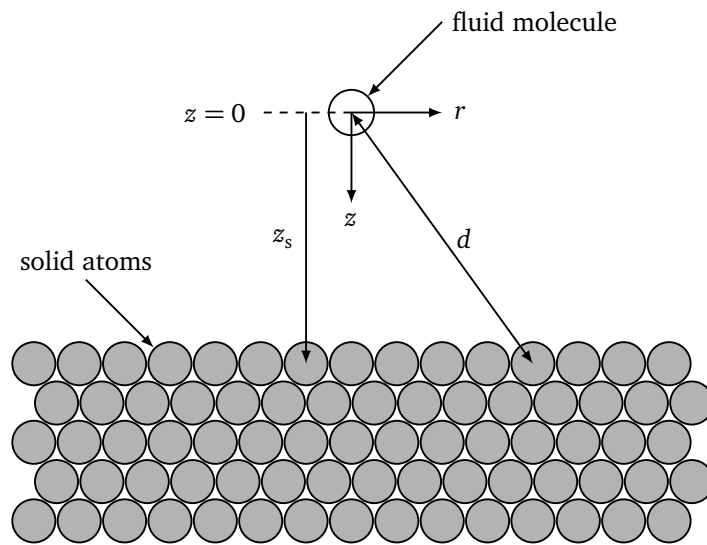


Figure 2.2.: Schematic of a fluid molecule near the wall.

As outlined by Carey [12, pp. 371–374] based on the original approach of Hamaker [31], the origin of this disjoining pressure can be illustrated considering the interaction of a single fluid molecule with the molecules of a solid wall as sketched in Fig. 2.2. For simplicity, the interaction potential between the fluid molecule and one single solid molecule is described as a function of the distance d between the molecules using the Lennard-Jones interaction potential

$$\phi_{fs}(d) = -\frac{C_{\phi,fs}}{d^6} \left[1 - \frac{D_m^6}{d^6} \right]. \quad (2.1)$$

For $C_{\phi,fs} > 0$ the potential has a global minimum at the separation distance $d = 2^{1/6}D_m$ and the parameter D_m can be interpreted to be the closest approach distance of the fluid molecule to the solid molecule [12, p. 373]. Accordingly this shape of the potential results in an attractive force for a large separation

¹ These long range interaction forces typically act over a distance of several nanometers. Even though this appears to be a rather short distance from a macroscopic point of view, it is large compared to the range of other intermolecular forces.

distance $d > 2^{1/6}D_m$ and a repulsive interaction otherwise. To get the interaction potential of the fluid molecule with all solid molecules in the wall, one has to integrate all the interaction potentials

$$\Phi_{\text{fmf}} = \int_{z=z_s}^{\infty} \int_{r=0}^{\infty} \int_{\varphi=0}^{2\pi} N_A \bar{\rho}_s \phi_{\text{fs}} r d\varphi dr dz \quad (2.2)$$

employing the cylindrical coordinate system introduced in Fig. 2.2 where $\bar{\rho}_s$ is the molar density of the solid and N_A is the Avogadro number. The distance between the molecules can be expressed by

$$d^2 = r^2 + z^2 \quad (2.3)$$

ending up with an expression for the overall potential,

$$\Phi_{\text{fmf}} = -\pi N_A \bar{\rho}_s C_{\phi, \text{fs}} \left[\frac{1}{6z_s^3} - \frac{D_m^6}{45z_s^9} \right]. \quad (2.4)$$

The force acting on a single fluid molecule due to the interaction is then given by the gradient of the potential,

$$\mathbf{F}_{\text{fs}} = -\nabla \Phi_{\text{fmf}} = \frac{\pi N_A \bar{\rho}_s C_{\phi, \text{fs}}}{2D_m^4} \left[\left(\frac{D_m}{z_s} \right)^4 - \frac{2}{5} \left(\frac{D_m}{z_s} \right)^{10} \right] \mathbf{e}_z. \quad (2.5)$$

As the distance between the fluid molecule and the wall is larger than D_m ,

$$z_s > D_m, \quad (2.6)$$

the $(D_m/z_s)^{10}$ term can be neglected. The resulting force per unit volume within a fluid with the molar density $\bar{\rho}_f$ is given by

$$\mathbf{f}_{\text{adh}} = \frac{\pi N_A^2 \bar{\rho}_f \bar{\rho}_s C_{\phi, \text{fs}}}{2z_s^4} \mathbf{e}_z. \quad (2.7)$$

Since the adhesion force is proportional to the density of the fluid, it is typically negligible in the gaseous phase compared to the forces acting on the liquid phase. The pressure resulting from the action of

adhesion within a quiescent liquid film with constant density $\bar{\rho}_l$ and infinite thickness at a distance y from a flat wall can be calculated via

$$p_{\text{disp}} = - \int_{z_s \rightarrow -\infty}^y \mathbf{f}_{\text{adh}} \cdot \mathbf{e}_z dz \quad (2.8)$$

$$= \frac{A_{ls}}{y^3},$$

where A_{ls} denotes the dispersion constant

$$A_{ls} = \frac{\pi N_A^2 \bar{\rho}_l \bar{\rho}_s C_{\phi,fs}}{6} \quad (2.9)$$

for the material combination of liquid l and solid s , which is linked to the Hamaker constant \tilde{A}_{ls} introduced by Hamaker [31] via

$$A_{ls} = \frac{\tilde{A}_{ls}}{6\pi}. \quad (2.10)$$

Even though the definition of the dispersion constant in Eq. (2.9) looks quite simple, the interaction parameter $C_{\phi,fs}$ is generally not known for arbitrary combinations of solid and fluid materials. Moreover, for real systems the actual molecular interaction potential might deviate from the simple Lennard-Jones potential. However, a possibility to predict the dispersion constant based on macroscopic material properties is given by the Lifshitz theory which is recapped by Israelachvili [39, pp. 176–212]. According to this theory the Hamaker constant for two different media interacting with each other can be obtained by the combination rule

$$\tilde{A}_{ls} \approx \sqrt{\tilde{A}_{ll} \tilde{A}_{ss}} \quad (2.11)$$

from the Hamaker constants of the liquid (\tilde{A}_{ll}) and the solid (\tilde{A}_{ss}) interacting with themselves when no other medium is involved. For electrically conductive metals such as chromium² the value of the Hamaker constant can be approximated as

$$\tilde{A}_{ss} \approx 4 \times 10^{-19} \text{ J}. \quad (2.12)$$

² The top layer of the wall in the experiments used for validation of the numerical model in this thesis is made of chromium.

For non-polar liquids in which the effect of H-bonds is negligible, the Hamaker constant can be correlated to the surface energy σ_1 of the liquid via

$$\tilde{A}_{11} \approx 24\pi\sigma_1 D_0^2, \quad (2.13)$$

where D_0 denotes a cutoff distance which can be estimated as $D_0 = 0.165$ nm. The usage of this universal empirical value for D_0 has been confirmed by van Voss et al. for a large number of different liquids [70]. For FC-72³ this estimation results in a Hamaker constant of $\tilde{A}_{11} \approx 1.7 \times 10^{-20}$ J. Finally the dispersion constant for the combination of FC-72 and chromium can be estimated to $A_{1s} = 4.37 \times 10^{-21}$ J.

It should be noted, that even though this rough estimation of the dispersion constant involves several uncertainties, the sensitivity of the micro region model to the exact value of A_{1s} is comparably low as will be shown in Section 2.3.4. In addition, in the literature several expressions for p_{disp} can be found which incorporate additional terms in order to account for other intermolecular interactions, e.g. due to the action of electrostatic forces. These approaches allow the prediction of a non-zero static contact angle in the isothermal case as shown by Ajaev et al. [1] but also include additional parameters which are in general unknown. Therefore, and since the fluid used in this work is almost perfectly wetting under isothermal conditions, Eq. (2.8) will be used in this work to describe the disjoining pressure.

2.1.2 Thermodynamic equilibrium at the liquid-vapor interface

Every two-phase thermodynamic system is in equilibrium if the two phases are in

- thermal equilibrium,
- mechanical equilibrium and
- chemical equilibrium.

Within this thesis a local equilibrium is postulated at the interface, while the bulk phases might be in a non-equilibrium state. Especially the existence of meta-stable superheated liquid is explicitly allowed.

The *thermal equilibrium* is fulfilled if the temperature on both sides of the interface is equal:

$$T_{v,\text{int}} = T_{l,\text{int}}. \quad (2.14)$$

The condition for the *mechanical equilibrium* in case of a curved interface in the absence of phase change reads

$$p_{v,\text{int}} - p_{l,\text{int}} = \sigma K, \quad (2.15)$$

³ FC-72 (perfluorohexane) has been used as working fluid in the experiments used for validation of the numerical model in this thesis.

which is typically referred to as the Young-Laplace equation. Herein, σ is the surface tension of the liquid-vapor interface and K is the interfacial mean curvature which is given by

$$K = \frac{1}{R_1} + \frac{1}{R_2} \quad (2.16)$$

with R_1 and R_2 being the principal radii of curvature.

In case of an interface with evaporative mass transfer occurring, the momentum balance in normal direction of the interface reads

$$p_{v,int} + \rho_v u_{v,int} (u_{v,int} - u_{int}) = \sigma K + p_{l,int} + \rho_l u_{l,int} (u_{l,int} - u_{int}), \quad (2.17)$$

where u_{int} is the normal velocity of the interface itself. Assuming a stationary interface⁴ ($u_{int} = 0$) and introducing the mass flux across the interface

$$m_{int} = \rho_v u_{v,int} = \rho_l u_{l,int} \quad (2.18)$$

the momentum balance can be simplified to

$$p_{v,int} - p_{l,int} = \sigma K - m_{int}^2 \left(\frac{1}{\rho_v} - \frac{1}{\rho_l} \right). \quad (2.19)$$

The last term on the right hand side of Eq. 2.19 is commonly referred to as the recoil pressure.

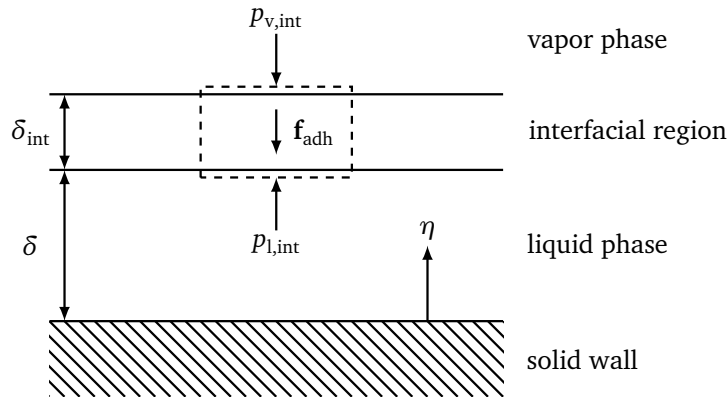


Figure 2.3.: On the action of adhesion forces in the interfacial region

It should be noted that opposed to the derivation given by Kern [44, pp. 14–16] there is no pressure jump across a flat interface due to adhesion forces. In Figure 2.3 a sketch of a flat thin liquid film of thickness δ close to a solid wall is shown. If evaporative mass transfer across the interface is neglected,

⁴ This is also valid for a moving interface if the velocities are defined in a moving reference frame in which the interface is stationary.

the adhesion forces acting on the interfacial region are balanced by the pressure difference between the liquid and vapor phase

$$\Delta p_{\text{int}} = p_{1,\text{int}} - p_{v,\text{int}} = \int_{\eta=\delta}^{\delta+\delta_{\text{int}}} f_{\text{adh}} d\eta. \quad (2.20)$$

For simplicity, we here assume a linear density variation across the interfacial region

$$\bar{\rho}_{f,\text{int}} = \bar{\rho}_1 + \frac{\bar{\rho}_v - \bar{\rho}_1}{\delta_{\text{int}}} (\eta - \delta). \quad (2.21)$$

With aid of the volumetric adhesion force given by Eq. (2.7) and using the above given expression for the molar density of the fluid, the pressure difference can be expressed by

$$\Delta p_{\text{int}} = \frac{\pi \bar{\rho}_s C_{\phi,fs}}{6} \left[\frac{\bar{\rho}_1}{\delta^3} - \frac{\bar{\rho}_1}{(\delta + \delta_{\text{int}})^3} - \frac{\bar{\rho}_1 - \bar{\rho}_v}{2(\delta + \delta_{\text{int}})^3} \left(\left(\frac{\delta_{\text{int}}}{\delta} \right)^2 + \frac{3\delta_{\text{int}}}{\delta} \right) \right]. \quad (2.22)$$

It follows, that for a Gibbs interface ($\delta_{\text{int}} \rightarrow 0$) the pressure difference vanishes

$$\lim_{\delta_{\text{int}} \rightarrow 0} \Delta p_{\text{int}} = 0 \quad (2.23)$$

in accordance to the findings of Stephan [97]. In addition, it can be shown that the pressure difference is limited by the two cases in which the interfacial region would consist only of vapor or liquid molecules, respectively,

$$\left[\frac{A_{vs}}{\delta^3} - \frac{A_{vs}}{(\delta + \delta_{\text{int}})^3} \right] \leq \Delta p_{\text{int}} \leq \left[\frac{A_{ls}}{\delta^3} - \frac{A_{ls}}{(\delta + \delta_{\text{int}})^3} \right] \quad (2.24)$$

which again both tend to zero for a Gibbs surface. It should be noted that these limits are obtained not only for the linear density profile introduced in Eq. (2.21), but for any monotonic density variation across the interfacial region.

Finally, to fulfill the *chemical equilibrium* the chemical potential at both sides of the interface has to be equal

$$\mu_{v,\text{int}} = \mu_{l,\text{int}}. \quad (2.25)$$

According to Stephan [97] the chemical potential of both phases can be expressed by integration of the Gibbs-Duhem equation

$$d\mu = -\bar{S}dT + \bar{V}dp - \bar{V}f_{adh} \cdot d\mathbf{r} \quad (2.26)$$

which has been augmented by the effect of adhesion forces since the internal energy and therefore also the chemical potential are depending on the spatial position in presence of adhesion forces.

A reference state is defined given by the interfacial temperature T_{int} , the corresponding saturation pressure

$$p_{sat} = p_{sat}(T = T_{int}), \quad (2.27)$$

and an infinite distance to the wall. The Gibbs-Duhem equation is integrated along an isothermal path from this reference state to the actual state of the interface

$$\mu_{v,int} = \mu_v(T_{int}, p_{sat}, y \rightarrow \infty) + \int_{sat}^{int} \bar{V}_v dp \quad (2.28)$$

$$\mu_{l,int} = \mu_l(T_{int}, p_{sat}, y \rightarrow \infty) + \int_{sat}^{int} \bar{V}_l dp - \int_{\eta \rightarrow \infty}^{\delta} \bar{V}_l (-f_{adh}) d\eta. \quad (2.29)$$

Herein, the contribution of the dispersion forces to the chemical potential of the vapor has been neglected as done by Carey [12, pp. 375–376] and the molar volumes of both phases have been assumed to be constant. For a flat interface in infinite distance from the wall, the integrals in Eqs. (2.28) and (2.29) vanish and one obtains

$$\mu_v(T_{int}, p_{sat}, \eta \rightarrow \infty) = \mu_l(T_{int}, p_{sat}, \eta \rightarrow \infty). \quad (2.30)$$

Combining the Eqs. (2.25) and (2.28–2.30) neglecting the pressure dependency of the phase densities results in

$$\bar{V}_v(p_{v,int} - p_{sat}) = \bar{V}_l(p_{l,int} - p_{sat}) - \bar{V}_l p_{disp} \quad (2.31)$$

which can be rearranged to an augmented form of the Thomson equation

$$p_{v,int} = p_{sat} - \frac{\rho_v}{\rho_l - \rho_v} (p_{v,int} - p_{l,int} + p_{disp}). \quad (2.32)$$

When substituting the pressure difference between both phases according to the mechanical equilibrium condition given by Eq. (2.19), one ends up with

$$p_{v,\text{int}} = p_{\text{sat}} - \frac{\rho_v}{\rho_l - \rho_v} \left[\sigma K - m_{\text{int}}^2 \left(\frac{1}{\rho_v} - \frac{1}{\rho_l} \right) + \frac{A}{\delta^3} \right]. \quad (2.33)$$

Neglecting the influence of dispersion forces and the recoil pressure in Eq. (2.33), one obtains the well known Thomson equation. For the sake of a clearer arrangement the term inside the brackets will be summarized as an augmented capillary pressure in the following

$$p_c = \sigma K - m_{\text{int}}^2 \left(\frac{1}{\rho_v} - \frac{1}{\rho_l} \right) + \frac{A}{\delta^3}. \quad (2.34)$$

2.1.3 Evaporation at the liquid-vapor interface

In many cases the phases are assumed to be in equilibrium directly at the interface even if evaporation occurs. However, in case of a strong evaporation rate as it is expected within the contact line region, the local state of the vapor at the interface might deviate from the state of the bulk vapor. Based on considerations of the kinetic theory of gases, Schrage [89, pp. 32–38] derived a relationship for the evaporative mass flux m_{evap} at the liquid-vapor interface

$$m_{\text{evap}} = f \frac{p_{v,\text{int}}}{\sqrt{2\pi\mathcal{R}T_{\text{int}}}} \left[1 - \frac{\rho_v}{\rho_{v,\text{int}}} \left(\frac{T_v}{T_{\text{int}}} \right)^{0.5} \Gamma \right]. \quad (2.35)$$

Herein, \mathcal{R} is the individual gas constant and f is the condensation coefficient. It reflects the ratio of molecules actually condensing at the interface to all gas molecules hitting the interface. The optimal theoretical value of f is unity. However, any impurities or surfactants which might accumulate at the interface in a real system will lower the value of the condensation coefficient. A detailed discussion on the influence of various influencing factors on f and a comparison of measured values from the literature is given by Marek and Straub [60]. Even though a distinction of the evaporation and condensation coefficient is suggested by Marek and Straub, both coefficients are assumed to be equal here. The exact choice of a value for this coefficient will be discussed in Section 2.3.4.

Inserting the ideal gas law into Eq. (2.35) to eliminate the vapor densities results in

$$m_{\text{evap}} = f \frac{1}{\sqrt{2\pi\mathcal{R}}} \left(\frac{p_{v,\text{int}}}{\sqrt{T_{\text{int}}}} - \frac{p_v}{\sqrt{T_v}} \Gamma \right). \quad (2.36)$$

The correction term Γ originates from the change in the velocity distribution of the gas molecules due to the net flow induced by evaporation. The correction term again depends on the evaporative mass flux via

$$\Gamma = e^{-\psi^2} - \psi \sqrt{\pi} [1 - \text{erf}(\psi)], \quad (2.37)$$

where the quantify ψ is given by

$$\psi = \frac{u_0}{\sqrt{2\mathcal{R}T_v}} = \frac{m_{\text{evap}}}{\rho_v \sqrt{2\mathcal{R}T_v}}. \quad (2.38)$$

However, for small values of ψ the correction function can be linearized, yielding

$$\Gamma \approx 1 - \psi \sqrt{\pi}. \quad (2.39)$$

For the maximal value of $\psi = 0.1$ reached within this work⁵ the linearization results in an error of only 1.2%. When substituting the linear approximation into Eq. (2.36), after some rearrangement an explicit expression for m_{evap} is obtained

$$m_{\text{evap}} = \frac{2f}{2-f} \frac{1}{\sqrt{2\pi\mathcal{R}}} \left(\frac{p_{v,\text{int}}}{\sqrt{T_{\text{int}}}} - \frac{p_v}{\sqrt{T_v}} \right). \quad (2.40)$$

The temperature of the vapor phase adjacent to the interface can be evaluated as $T_v = T_{\text{sat}} = T_{\text{sat}}(p_v)$. Assuming a comparably small deviation of the temperature from the equilibrium conditions, i.e. $(T_{\text{int}} - T_{\text{sat}})/T_{\text{sat}} \ll 1$, one obtains

$$m_{\text{evap}} = \frac{2f}{2-f} \frac{1}{\sqrt{2\pi\mathcal{R}T_{\text{sat}}}} (p_{v,\text{int}} - p_v). \quad (2.41)$$

The variation of the vapor pressure with temperature is given by the Clausius-Clapeyron equation

$$\frac{dp}{dT} = \frac{\rho_l \rho_v h_{lv}}{(\rho_l - \rho_v) T} \quad (2.42)$$

⁵ This number is obtained from the overall model for an evaporating contact line at a wall superheat of 20 K for the fluid FC-72.

which can be approximately integrated from the state of the vapor at the interface to the one of the bulk vapor

$$\frac{p_{\text{sat}} - p_v}{T_{\text{int}} - T_{\text{sat}}} \approx \frac{\rho_l \rho_v h_{\text{lv}}}{(\rho_l - \rho_v) T_{\text{sat}}} \quad (2.43)$$

Inserting this approximation into Eq. (2.41) and using the augmented Thomson equation (2.33) to eliminate the vapor sided interfacial pressure one finally ends up with

$$m_{\text{evap}} = \frac{2f}{2-f} \frac{\rho_l \rho_v h_{\text{lv}}}{(\rho_l - \rho_v) T_{\text{sat}} \sqrt{2\pi \mathcal{R} T_{\text{sat}}}} \left[T_{\text{int}} - T_{\text{sat}} \left(1 + \frac{p_c}{h_{\text{lv}} \rho_l} \right) \right] \quad (2.44)$$

which can be further simplified to

$$m_{\text{evap}} = \frac{2f}{2-f} \frac{\rho_v h_{\text{lv}}}{T_{\text{sat}} \sqrt{2\pi \mathcal{R} T_{\text{sat}}}} \left[T_{\text{int}} - T_{\text{sat}} \left(1 + \frac{p_c}{h_{\text{lv}} \rho_l} \right) \right] \quad (2.45)$$

provided that $\rho_v \ll \rho_l$. The evaporative mass flux is related to the heat flux at the interface through the energy balance at the interface. It can be simplified to

$$m_{\text{evap}} h_{\text{lv}} = q_{\text{evap}} \quad (2.46)$$

if the heat conduction in the vapor phase and the change of kinetic energy due to phase change are neglected. In terms of the evaporative heat flux Eq. (2.45) then reads

$$q_{\text{evap}} = \frac{2f}{2-f} \frac{\rho_v h_{\text{lv}}^2}{T_{\text{sat}} \sqrt{2\pi \mathcal{R} T_{\text{sat}}}} \left[T_{\text{int}} - T_{\text{sat}} \left(1 + \frac{p_c}{h_{\text{lv}} \rho_l} \right) \right] \quad (2.47)$$

which can be rewritten as

$$q_{\text{evap}} = \frac{T_{\text{int}} - T_{\text{int,min}}}{R_{\text{int}}} \quad (2.48)$$

where

$$R_{\text{int}} = \frac{2-f}{2f} \frac{T_{\text{sat}} \sqrt{2\pi \mathcal{R} T_{\text{sat}}}}{\rho_v h_{\text{lv}}^2} \quad (2.49)$$

denotes the interfacial heat resistance and

$$T_{\text{int,min}} = T_{\text{sat}} \left(1 + \frac{p_c}{h_{\text{lv}}\rho_l} \right) \quad (2.50)$$

is the minimal temperature of the interface at which evaporation will occur. It should be noted, that strictly speaking Eq. (2.45) is still an implicit expression for m_{evap} due to the influence of the recoil pressure, which is part of p_c , on the mass flux. However, this non-linearity is very weak and therefore not further considered.

2.2 Modeling of the evaporating micro region

A sketch of the micro region is presented in Fig. 2.4. Within this section the local coordinate system as indicated in the figure will be used. The direction of the coordinate ξ is within the wall plane and perpendicular to the apparent contact line while the coordinate η is normal to the wall. The origin of the system is at the transition from the adsorbed film to the micro region. The contact line movement will be modeled utilizing the presented coordinate system as a moving reference frame. The contact line speed u_{cl} is defined positive for an advancing or wetting meniscus while a receding motion of the meniscus corresponds to a negative contact line speed.

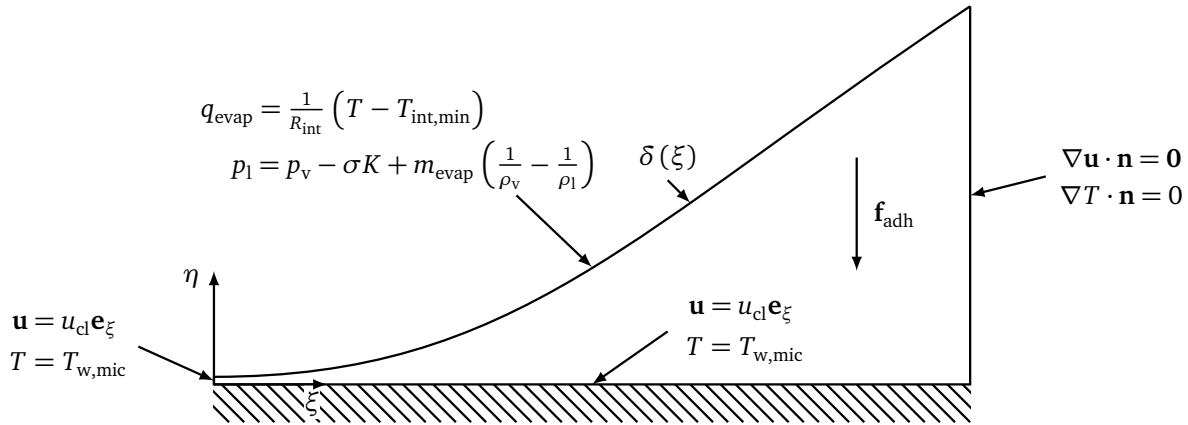


Figure 2.4.: Boundary conditions of the micro region.

In order to develop the model for heat and fluid flow within the micro region the following assumptions are made:

- The liquid flow within the micro region can be described using a continuum mechanics approach and the liquid shows a Newtonian behavior.
- The vapor is saturated and its pressure is constant.
- The wall temperature is constant in the micro region.
- The boundary conditions and the flow field are time-independent. In particular, the contact line velocity is constant.
- The fluid properties are constant and temperature independent.

Due to the assumption of validity of continuum mechanics the flow can be modeled by the steady-state, incompressible Navier-Stokes equations and the energy balance

$$\nabla \cdot \mathbf{u} = 0 \quad (2.51)$$

$$\rho_1(\mathbf{u} \cdot \nabla) \mathbf{u} = -\nabla p_1 + \mu_1 \Delta \mathbf{u} + \mathbf{f}_{\text{adh}} \quad (2.52)$$

$$\rho_1 c_1 \mathbf{u} \cdot \nabla T = k_1 \Delta T. \quad (2.53)$$

The momentum balance has been augmented by the effect of adhesion forces according to Eq. (2.7). Gravity can be completely neglected against that term as shown by Stephan [97]. The boundary conditions for the fluid flow within the micro region are given in Fig. 2.4. The boundary conditions at the interface have been deduced within the previous section. In addition, shear stresses at the interface are assumed to be zero due to the comparably low dynamic viscosity of the vapor. At the wall a no-slip condition is applied and the wall temperature is prescribed. An eventually existing Kapitza resistance at the wall-liquid interface, which would result in a small temperature jump across the boundary, is neglected.

The end of the micro region at its transition towards the macroscopic meniscus is not clearly defined. However, at the end of the modeling domain the liquid film thickness has to be large compared to the thickness of the adsorbed film. In particular, the effect of the adhesion forces onto the thermal equilibrium and the fluid flow as well as the thermal resistance of the interface should be negligible at this position. Throughout this work the end of the micro region is considered to be at $\xi_{\text{end}} = 0.5 \mu\text{m}$.

As already mentioned above, in the following two different modeling approaches will be presented. First, a simplified model based on the lubrication approximation will be shown. It allows relatively fast computations of the heat transfer in the micro region and provides therefore the possibility to conduct extensive parameter studies. However, due to the usage of the lubrication theory it is restricted to small values of the apparent contact angle. As will be shown later, this assumption is not always valid if the wall is significantly superheated against the saturation temperature or if the contact line velocity is high. Therefore, a large modeling error might be expected in these cases. In order to quantify the error introduced by the lubrication approximation, a direct numerical simulation of the fluid flow within the micro region is conducted. This simulation approach can be used to validate the simplified model but it is not feasible for parameter variations due to its computational costs.

2.2.1 One-dimensional lubrication model

The following additional assumptions have to be made for deriving the simplified lubrication model:

- The characteristic length scale L_ξ along the wall is much larger than the length scale L_η perpendicular to the wall, $(L_\eta/L_\xi)^2 \ll 1$. This goes along with a small apparent contact angle ($\theta_{\text{mic}} \ll \pi/2$).
- The flow is creeping, i.e. the scaled Reynolds number is small, $\text{Re}(L_\eta/L_\xi) \ll 1$.

An order analysis of the governing equations leads to the following simplified set of the conservation equations in two dimensions:

$$\frac{\partial u_\xi}{\partial \xi} + \frac{\partial u_\eta}{\partial \eta} = 0 \quad (2.54)$$

$$\frac{\partial p_l}{\partial \xi} = \mu_l \frac{\partial^2 u_\xi}{\partial \eta^2} \quad (2.55)$$

$$\frac{\partial p_l}{\partial \eta} = -\frac{3A}{\eta^4} \quad (2.56)$$

$$\frac{\partial^2 T}{\partial \eta^2} = 0 \quad (2.57)$$

This way of simplification of the balance equations is commonly referred to as the lubrication approximation in literature. It is widely used to describe thin film flows. A detailed overview of various applications of this approach also known as long wave theory is given by Oron et al. [68]. A detailed derivation of these simplified equations in the context of the micro region is given by Kern [44, pp. 23–29].

Energy balance

Integration of Eq. (2.57) results in a linear temperature profile within the liquid film. Supposing Dirichlet boundary conditions at the wall and the interface, the heat flux through the liquid film can be calculated to

$$q_w = \frac{k_l}{\delta} (T_{w,\text{mic}} - T_{\text{int}}), \quad (2.58)$$

where $T_{w,\text{mic}}$ denotes the wall temperature and T_{int} is the local temperature at the liquid-vapor interface. The heat flux at the liquid-vapor interface is driving the evaporation and is given by Eq. (2.47),

$$q_{\text{evap}} = \frac{1}{R_{\text{int}}} \left(T_{\text{int}} - T_{\text{sat}} \left(1 + \frac{p_c}{h_{lv}\rho_l} \right) \right). \quad (2.59)$$

Since the heat fluxes at the wall and at the interface are related to different surface areas if the interface has a non-zero slope, a correction is necessary in order to conserve the total heat flow,

$$q_w = q_{\text{evap}} \sqrt{1 + \delta'^2}. \quad (2.60)$$

The usage of this correction is strictly speaking not necessary in the framework of a lubrication approximation, but it has been found to significantly improve the global results. Combining the above equations and eliminating the interfacial temperature results in the following expression for the wall heat flux

$$q_w = \frac{T_{w,\text{mic}} - T_{\text{sat}} \left(1 + \frac{p_c}{h_{lv}\rho_1} \right)}{\frac{\delta}{k_1} + \frac{R_{\text{int}}}{\sqrt{1+\delta'^2}}}. \quad (2.61)$$

Momentum balance

Integration of the momentum balance in η -direction, Eq. (2.56), from the interface to an arbitrary position within the film

$$\int_{\tilde{\eta}=\delta}^{\eta} \frac{\partial p_1}{\partial \tilde{\eta}} d\tilde{\eta} = - \int_{\tilde{\eta}=\delta}^{\eta} \frac{3A}{\tilde{\eta}^4} d\tilde{\eta} \quad (2.62)$$

results in an expression for the pressure field within the liquid film

$$p_1(\xi, \eta) - p_{1,\text{int}}(\xi) = \frac{A}{\eta^3} - \frac{A}{\delta^3}. \quad (2.63)$$

Substitution of the mechanical equilibrium condition, Eq. (2.19), leads to

$$p_1(\xi, \eta) = p_v - \sigma K + m_{\text{evap}}^2 \left(\frac{1}{\rho_v} - \frac{1}{\rho_1} \right) + \frac{A}{\eta^3} - \frac{A}{\delta^3}. \quad (2.64)$$

Provided that the pressure in the vapor phase is constant, the gradient of the liquid pressure parallel to the wall can be calculated to

$$\frac{\partial p_1}{\partial \xi} = - \frac{\partial}{\partial \xi} \left[\sigma K - m_{\text{evap}}^2 \left(\frac{1}{\rho_v} - \frac{1}{\rho_1} \right) + \frac{A}{\delta^3} \right] \quad (2.65)$$

which is equivalent to

$$\frac{\partial p_1}{\partial \xi} = - \frac{\partial p_c}{\partial \xi} \quad (2.66)$$

according to the definition of p_c in Eq. (2.34). The velocity profile within the liquid film can be calculated from the momentum balance in ξ -direction, Eq. (2.55), by integrating twice with respect to η to

$$u_\xi(\xi, \eta) = \frac{1}{\mu_l} \frac{dp_l}{d\xi} \frac{\eta^2}{2} + C_1(\xi)\eta + C_2(\xi). \quad (2.67)$$

Together with the boundary conditions for the velocity

$$u_\xi(\xi, \eta = 0) = u_{cl} \quad (2.68)$$

$$\left. \frac{\partial u_\xi}{\partial \eta} \right|_{\xi, \eta = \delta} = 0 \quad (2.69)$$

the integration constants C_i can be determined. The velocity profile then reads

$$u_\xi(\xi, \eta) = \frac{1}{\mu_l} \frac{dp_l}{d\xi} \left(\frac{\eta^2}{2} - \delta\eta \right) + u_{cl} \quad (2.70)$$

or when substituting Eq. (2.66)

$$u_\xi(\xi, \eta) = -\frac{1}{\mu_l} \frac{dp_c}{d\xi} \left(\frac{\eta^2}{2} - \delta\eta \right) + u_{cl}. \quad (2.71)$$

Mass balance

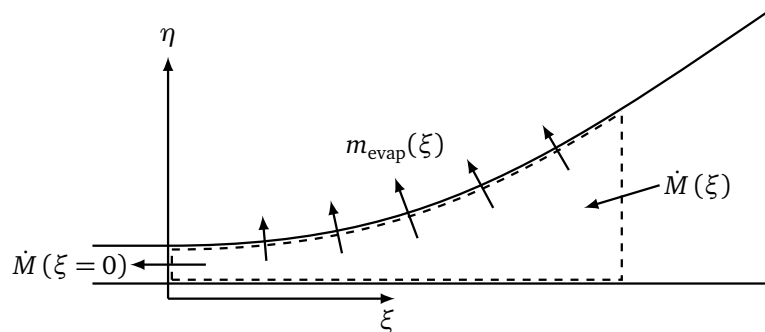


Figure 2.5.: Mass balance within the micro region.

A link between the fluid flow within the liquid film and the heat flux at the interface is given by the liquid mass balance. As depicted in Fig. 2.5 the total mass flow per unit contact line length \dot{M} towards

the adsorbed film at a given position ξ is given by the sum of the mass flow at $\xi = 0$ and the evaporating mass between the two positions

$$\dot{M}(\xi) = \int_0^{\xi} m_{\text{evap}} d\tilde{\xi} + \dot{M}(\xi = 0). \quad (2.72)$$

The mass flow at any position can be obtained by integration of the liquid mass flux over the film thickness

$$\dot{M}(\xi) = - \int_0^{\delta} \rho_1 u_{\xi} d\eta. \quad (2.73)$$

Substituting Eq. (2.71), introducing the integrated heat flux

$$\dot{Q} = \int_0^{\xi} q_w d\tilde{\xi} \quad (2.74)$$

and taking into account that the gradient of the augmented capillary pressure is zero within the adsorbed film yields

$$\frac{dp_c}{d\xi} = - \frac{3\nu_1}{\delta^3 h_{lv}} \left[\dot{Q} + \rho_1 h_{lv} u_{cl} (\delta - \delta_{ad}) \right]. \quad (2.75)$$

Interface curvature

The definition of the augmented capillary pressure p_c in Eq. (2.34) is used to derive another differential equation for the film thickness. The curvature of a two-dimensional interface is given by

$$K = \frac{\delta''}{(1 + \delta'^2)^{1.5}}, \quad (2.76)$$

where the prime denotes the derivative with respect to ξ . Inserting this relation into Eq. (2.34) and substituting the interfacial mass flux by the result obtained from the energy balance, one obtains

$$\delta'' = \frac{(1 + \delta'^2)^{1.5}}{\sigma} \left(p_c - \frac{A}{\delta^3} + \frac{1}{h_{lv}^2} \left[\frac{T_{w,\text{mic}} - T_{\text{sat}} \left(1 + \frac{p_c}{h_{lv}\rho_1} \right)}{\frac{\delta\sqrt{1+\delta'^2}}{k_l} + R_{\text{int}}} \right]^2 \left(\frac{1}{\rho_v} - \frac{1}{\rho_1} \right) \right). \quad (2.77)$$

System of differential equations

The above derived equations (2.61), (2.74), (2.75) and (2.77) can be represented as a system of four coupled first order ordinary, non-linear differential equations. The resulting system of equations is very similar to the one given by Stephan and Busse [100] but is now augmented by the effects of contact line motion and the recoil pressure and also includes the correction term introduced in Eq. (2.60).

$$\begin{aligned}
 \frac{d\delta}{d\xi} &= \delta' \\
 \frac{d\delta'}{d\xi} &= \frac{(1 + \delta'^2)^{1.5}}{\sigma} \left(p_c - \frac{A}{\delta^3} + \frac{1}{h_{lv}^2} \left[\frac{T_{w,mic} - T_{sat} \left(1 + \frac{p_c}{h_{lv}\rho_l} \right)}{\frac{\delta\sqrt{1+\delta'^2}}{k_l} + R_{int}} \right]^2 \left(\frac{1}{\rho_v} - \frac{1}{\rho_l} \right) \right) \\
 \frac{dp_c}{d\xi} &= -\frac{3\nu_l}{\delta^3 h_{lv}} \left[\dot{Q} + \rho_l h_{lv} u_{cl} (\delta - \delta_{ad}) \right] \\
 \frac{d\dot{Q}}{d\xi} &= \frac{T_{w,mic} - T_{sat} \left(1 + \frac{p_c}{h_{lv}\rho_l} \right)}{\frac{\delta}{k_l} + \frac{R_{int}}{\sqrt{1+\delta'^2}}}
 \end{aligned} \tag{2.78}$$

Alternatively, this system could be rewritten to a single fourth order ODE for the film thickness. It has, however, no analytical solution and the representation as a system of equations is more convenient for a numerical solution.

In order to solve the system (2.78), four initial conditions are required. Since the evaporative heat flux within the adsorbed layer should vanish, it follows directly from Eq. (2.74) that

$$\dot{Q}_{ad} = \dot{Q}(\xi = 0) = 0. \tag{2.79}$$

For the same reason the interfacial temperature has to be equal to the wall temperature. Hence, the augmented capillary pressure in the adsorbed layer region can be calculated from Eq. (2.61) to

$$p_{c,ad} = p_c(\xi = 0) = \left(\frac{T_{w,mic}}{T_{sat}} - 1 \right) h_{lv}\rho_l. \tag{2.80}$$

Moreover, the adsorbed film is flat

$$\delta'_{ad} = \delta'(\xi = 0) = 0 \tag{2.81}$$

and its curvature is zero. Accordingly, the film thickness of the adsorbed layer can be determined from Eq. (2.34) as

$$\delta_{\text{ad}} = \delta(\xi = 0) = \left(\frac{A}{P_{\text{c,ad}}} \right)^{1/3}. \quad (2.82)$$

Dimensionless formulation

The individual terms in system (2.78) are strongly varying in their order of magnitude. To make the numerical solution more efficient, a non-dimensional version of the system is formulated. The variables to be solved for can be non-dimensionalized with their value within the adsorbed film except for the integrated heat flow. Using the definitions

$$\begin{aligned} \xi^* &= \frac{\xi}{\delta_{\text{ad}}} \\ \delta^* &= \frac{\delta}{\delta_{\text{ad}}} \\ \delta'^* &= \delta' \\ p_{\text{c}}^* &= \frac{p_{\text{c}}}{p_{\text{c,ad}}} \\ \dot{Q}^* &= \frac{\dot{Q}}{k_1 (T_{\text{w,mic}} - T_{\text{sat}})} \end{aligned} \quad (2.83)$$

a non-dimensional version of the differential equations can be derived

$$\begin{aligned} \frac{d\delta^*}{d\xi^*} &= \delta'^* \\ \frac{d\delta'^*}{d\xi^*} &= D_1 (1 + \delta'^{*2})^{1.5} \left[p_{\text{c}}^* - \frac{1}{\delta^{*3}} + D_5 \left(\frac{1 - p_{\text{c}}^*}{\delta^* \sqrt{1 + \delta'^{*2}} + D_3} \right)^2 \right] \\ \frac{dp_{\text{c}}^*}{d\xi^*} &= - \frac{D_2 \dot{Q}^* + D_4 (\delta^* - 1)}{\delta^{*3}} \\ \frac{d\dot{Q}^*}{d\xi^*} &= \frac{1 - p_{\text{c}}^*}{\delta^* + D_3 \frac{1}{\sqrt{1 + \delta'^{*2}}}} \end{aligned} \quad (2.84)$$

with the dimensionless constants

$$\begin{aligned}
D_1 &= \frac{\delta_{\text{ad}} p_{\text{c,ad}}}{\sigma} \\
D_2 &= \frac{3v_1 k_1 (T_{\text{w,mic}} - T_{\text{sat}})}{h_{\text{lv}} \delta_{\text{ad}}^2 p_{\text{c,ad}}} \\
D_3 &= R_{\text{int}} \frac{k_1}{\delta_{\text{ad}}} \\
D_4 &= \frac{3\mu_1 u_{\text{cl}}}{\delta_{\text{ad}} p_{\text{c,ad}}} \\
D_5 &= \frac{k_1^2 (T_{\text{w,mic}} - T_{\text{sat}})^2}{p_{\text{c,ad}} \delta_{\text{ad}}^2 h_{\text{lv}}^2} \left(\frac{1}{\rho_v} - \frac{1}{\rho_l} \right).
\end{aligned} \tag{2.85}$$

The transformed initial conditions read

$$\begin{aligned}
\delta^* (\xi^* = 0) &= 1 \\
\delta'^* (\xi^* = 0) &= 0 \\
p_c^* (\xi^* = 0) &= 1 \\
\dot{Q}^* (\xi^* = 0) &= 0.
\end{aligned} \tag{2.86}$$

Solution algorithm

It should be noticed that the initial conditions already fulfill the system of differential equations since the adsorbed film is the trivial solution of (2.78). Hence, one has to slightly perturb the initial conditions to obtain the non-trivial solution of a curved meniscus. As proposed by Stephan [98] it is advisable to disturb the initial film thickness by a small constant

$$\delta^* (\xi^* = 0) = 1 + \varepsilon_1 \tag{2.87}$$

where $0 < \varepsilon_1 \ll 1$. This can also be imagined as starting the integration within the very beginning of the transition between the adsorbed film and the macroscopic meniscus. At the same time the initial value of the integrated heat flow has to be slightly modified accordingly to ensure that $p_c^* < 1$, i.e. that the pressure is decreasing in ξ direction. Hence, the initial integrated heat flow is set to

$$\dot{Q}^* (\xi^* = 0) = \varepsilon_2 \tag{2.88}$$

where $|\varepsilon_2| \ll 1$. The sign of ε_2 is depending on the ratio of D_2 and D_4 . It has been shown that the solution for the film profile reacts extremely sensitive on the perturbation ε_2 . For large values of ε_2 the film will show a negative slope and it might occur that the film thickness gets negative. If on the other hand ε_2 is too small, the interface might show an almost infinite slope. In between these two cases there is the desired shape of the meniscus corresponding to an optimal value of ε_2 which depends also on the value of ε_1 .

In the actual solution algorithm the value of the perturbation in film thickness ε_1 is prescribed. In principal its value can be chosen arbitrarily. However, its choice has an influence on the position of the transition region. As shown by Kunkelmann [47, pp. 29–30], the obtained meniscus shape is mainly shifted to larger values of ξ if ε_1 is reduced while the profile shape is basically not affected. For all calculations done in the frame of this thesis it is set to $\varepsilon_1 = 0.002$. The value of ε_2 is then determined iteratively. Its optimal value can be found utilizing a bisection algorithm until a physical solution is found for the interface profile, i.e. a profile which has neither a negative thickness nor a nearly infinite slope.

It might occur however that the film profile has not been converged while the difference between the determined maximal and minimal value of ε_2 is already smaller than the computational accuracy⁶. Kunkelmann [47, p. 29] has shown for non-moving contact lines that this limit is not reached if ε_1 is chosen sufficiently large but this conclusion cannot be drawn for moving contact lines unless a very large perturbation of the initial film thickness is chosen.

Instead, the initial perturbation is kept small and the solution method of splitting the meniscus into part menisci originally proposed by Stephan [98, pp. 41–44] is used. The overall algorithm is depicted in Fig. 2.6. The integration is first limited to the interval $[0 \ \xi_1^*]$ with $0 < \xi_1^* < \xi_{\text{end}}^*$. The perturbation factor ε_2 is approximated until a physically meaningful solution is obtained in which the non-dimensional film thickness is greater than unity everywhere and the maximal slope of the film is less than 10. If such a solution is found, the integration interval is enlarged and the approximation of ε_2 is carried on. If the correction of ε_2 reaches the numerical accuracy, the integration is stopped and the solution for the first percent of the solution interval is stored. Afterwards, the integration is restarted at the end of the stored meniscus and an additional perturbation is given to the non-dimensional integrated heat flow at this position. A new perturbation of the film thickness is not necessary at this position since the film thickness is already greater than unity. This calculation of meniscus parts proceeds until the end of the desired integration interval is reached. Then ε_2 is further converged until the curvature of the interface comes close to the given macroscopic curvature K_{mac} . Since the macroscopic curvature will not be exactly matched, the solution is treated as converged as soon as the actual curvature at the end of the micro region differs from the desired curvature by less than 5%. As stated by Stephan [98, p. 44] and quantified by Kunkelmann [47, p. 32] the actual value of the macroscopic curvature has only very little effect on the results as long as it is small compared to the maximal curvature within the micro region.

The final solution is continuous in terms of film thickness, slope and augmented capillary pressure but the integrated heat flow has small jumps at the boundaries of the part intervals. These jumps however are negligibly small. In the example presented in Fig. 2.7 the discontinuity of the heat flow at the border

⁶ If double precision is used, two floating point numbers cannot be distinguished from each other if their relative difference is smaller than $2^{-52} \approx 2.22 \times 10^{-16}$. That means that in the computation $1 + 10^{-16} = 1$ is true.

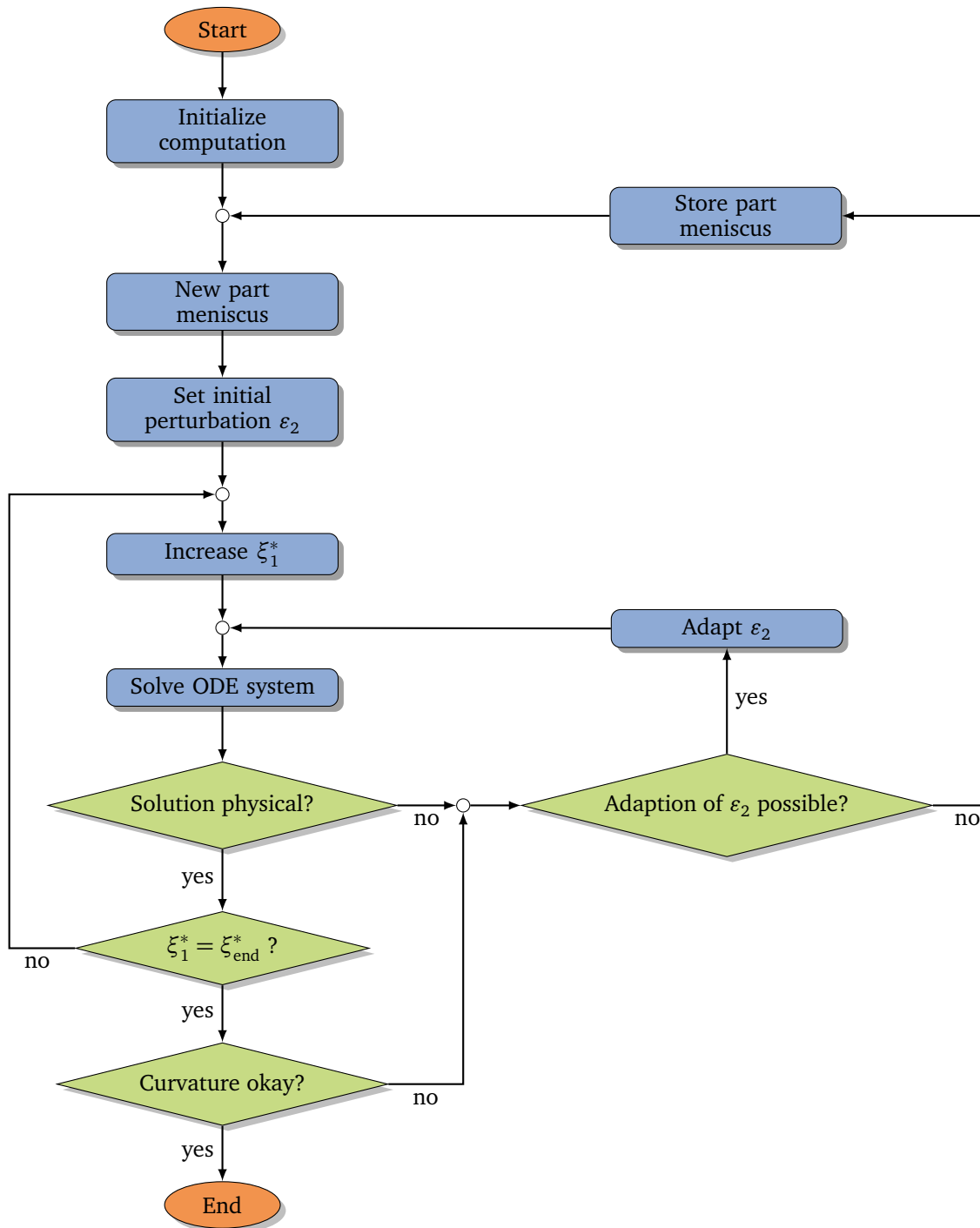


Figure 2.6.: Solution algorithm for the lubrication model.

of the two part menisci is about 2.7×10^{-11} W/m compared to the value of the integrated heat flow of 0.0022 W/m at the position of the jump and particularly to the value of 0.962 W/m at ξ_{end} .

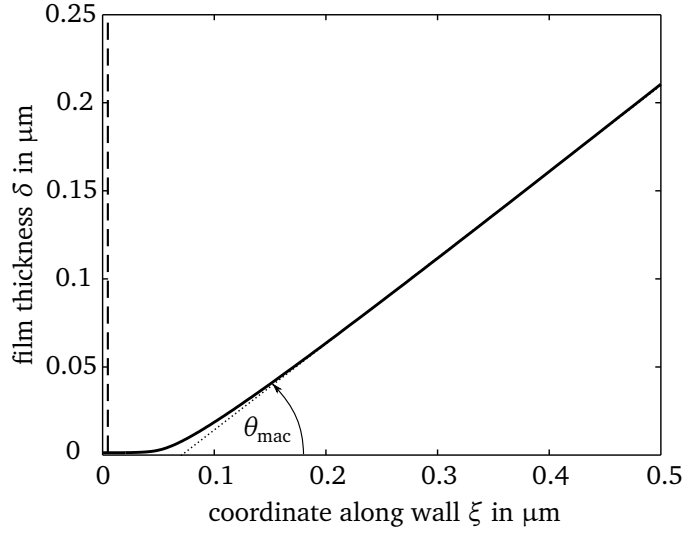


Figure 2.7.: Film profile calculated for FC-72 at a wall superheat of $\Delta T = 5$ K and $u_{\text{cl}} = 0$. The solution was obtained by integration of two part menisci. The border between the parts is indicated by the dashed line. The axes are not shown to scale

2.2.2 Direct numerical simulation

In the following the direct numerical simulation technique for solving the micro region problem will be presented. This approach published in [5] will be described in more detail here.

For the direct numerical simulation no additional simplifications of Eqns. (2.51)–(2.53) have to be made. In particular the apparent contact angle does not need to be small. Strictly speaking, the methodology introduced in this section is restricted to contact angles below 90 degrees. Since it is restricted to fluids which are perfectly wetting under isothermal conditions anyway, this limit will however never be reached for reasonable boundary conditions.

Even though the basic intention of the simulation technique presented here is to provide a validation basis for the lubrication model, the implementation is done in such a way that also three-dimensional calculations are possible.

In case of the direct numerical simulation the presence of the force term \mathbf{f}_{adh} within the momentum equation (2.52) causes some computational problems. Since the force is proportional to the inverse wall distance to the power of four, it diverges at the wall. Moreover, even if the force would be limited by some finite value, the large pressure gradients resulting from the force field close to the wall would require an extremely fine grid resolution near the wall.

To overcome these problems, a transformed pressure field \tilde{p} is defined as

$$\tilde{p} := p_l - p_v - p_{\text{disp}} \quad (2.89)$$

where p_{disp} is the dispersion pressure from Eq. (2.8). Using the relationship

$$\mathbf{f}_{\text{adh}} = \nabla p_{\text{disp}}, \quad (2.90)$$

which follows directly from the definition of the dispersion pressure in Eq. (2.8), the momentum equation can be rewritten as

$$\rho \nabla(\mathbf{u}\mathbf{u}) = -\nabla \tilde{p} + \mu \Delta \mathbf{u} \quad (2.91)$$

which now has the same structure as the standard steady-state Navier-Stokes equation and can hence be solved using standard solution methods like SIMPLE. Finally, the pressure boundary condition at the interface, Eq. (2.19), has to be transformed accordingly. It reads

$$\tilde{p}_{\text{int}} = -\sigma K + m_{\text{int}}^2 \left(\frac{1}{\rho_v} - \frac{1}{\rho_l} \right) - \frac{A}{\delta^3} = -p_c. \quad (2.92)$$

The remaining boundary conditions are set as depicted in Fig. 2.4.

Curvature calculation

For setting the boundary condition for the transformed pressure field at the grid boundary representing the interface, an accurate calculation of the curvature is required. A method for the calculation of the mean curvature at each individual boundary face is given by Tuković and Jasak [107, 108]. It is applicable to unstructured, three-dimensional grids and reasonably simple to implement.

The idea of their method is to evaluate the curvature of face f by a summation over all edges e bordering the face utilizing Gauss's theorem

$$K_f = \frac{1}{S_f} \sum_e \mathbf{m}_e \cdot \mathbf{n}_f L_e \quad (2.93)$$

where S_f is the area and \mathbf{n}_f is the outwards pointing unit normal vector of face f . L_e denotes the length of edge e and \mathbf{m}_e is the bi-normal vector of the edge defined as

$$\mathbf{m}_e = \mathbf{e} \times \frac{\mathbf{n}_i + \mathbf{n}_j}{2}. \quad (2.94)$$

Herein, the edge vector \mathbf{e} is pointing from point i to j defining the edge. The unit normal vectors of the boundary point \mathbf{n}_i is calculated as the normalized, inverse distance weighted average of the normals of all neighboring faces k sharing this point

$$\mathbf{n}_i = \frac{\sum_k \frac{(\mathbf{p}_i - \mathbf{p}_k) \times (\mathbf{p}_i - \mathbf{p}_{k+1})}{|\mathbf{p}_i - \mathbf{p}_k|^2 \times |\mathbf{p}_i - \mathbf{p}_{k+1}|^2}}{\left| \sum_k \frac{(\mathbf{p}_i - \mathbf{p}_k) \times (\mathbf{p}_i - \mathbf{p}_{k+1})}{|\mathbf{p}_i - \mathbf{p}_k|^2 \times |\mathbf{p}_i - \mathbf{p}_{k+1}|^2} \right|}. \quad (2.95)$$

Mesh adaption

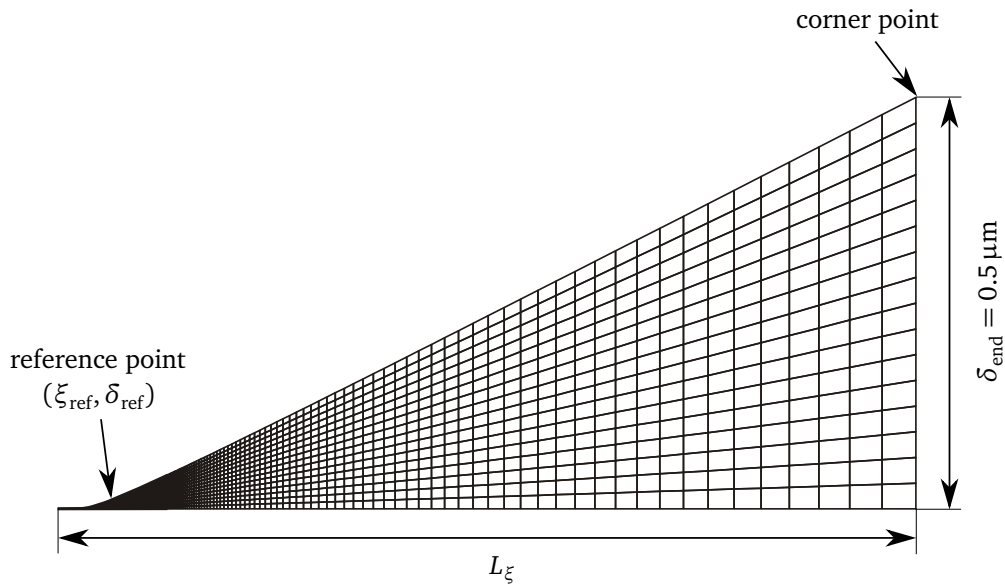


Figure 2.8.: Exemplary initial mesh.

The shape of the liquid-vapor interface is part of the solution and not known a priori. Hence, the mesh shape has to be initialized properly and then adapted iteratively to obtain the film profile. For initialization the profile calculated with the lubrication model is used. An exemplary initial mesh is shown in Fig. 2.8. A mesh motion algorithm is derived from the mass balance at the interface. In equilibrium, the amount of liquid evaporating at the interface has to be exactly balanced by liquid flowing towards the interface. The velocity of the liquid corresponding to the evaporating mass flux can be calculated as

$$u_{n,\text{evap}} = \frac{q_{\text{evap}}}{\rho_l h_{lv}} \quad (2.96)$$

while the velocity of the liquid flowing towards the interface $u_{n,\text{liq}}$ is known from the solution of the Navier Stokes equation. At steady state both velocities have to be equal. In turn, if they deviate from

each other, this would physically result in a motion of the interface. Within an unsteady simulation the displacement of the interface could be expressed by

$$\Delta\delta = \Delta\tilde{t} (u_{n,\text{liq}} - u_{n,\text{evap}}) \quad (2.97)$$

where $\Delta\tilde{t}$ is the simulation time step. Since here a steady-state solution technique is employed, $\Delta\tilde{t}$ is just a pseudo time step which can be set to an arbitrary value. Numerical experiments showed that its value influences the stability of the calculation significantly. If $\Delta\tilde{t}$ is chosen too large, the calculation becomes unstable and a large distortion of the interface can be observed. In contrary, too small values of the pseudo time step resulted in a very slow convergence behavior. The optimal value is thereby depending on the mesh resolution. In case of a fine mesh the system tends to become unstable at smaller values of $\Delta\tilde{t}$. In addition, it was found that a small value is in particular required where the film is comparably thin while it can be chosen larger in regions of a large film thickness. This is due to the non-linear dependency of the disjoining pressure on the film thickness. Hence, it is advisable to scale the pseudo time step with the local film thickness,

$$\Delta\tilde{t} = \frac{\delta}{\delta_{\text{ad}}} \Delta\tilde{t}_0. \quad (2.98)$$

The optimal value of $\Delta\tilde{t}_0$, which guarantees for stability and leads at the same time to a fast convergence behavior, is found in between 2.5×10^{-12} s and 10^{-11} s depending on the spatial resolution of the mesh.

Similar to the lubrication model, the simulation also tends to run into the trivial solution represented by the adsorbed film. This is prevented by fixing the film thickness at a specific reference point ξ_{ref} to a thickness of $\delta_{\text{ref}} = 3\delta_{\text{ad}}$ as indicated in Fig. 2.8. The choice of the reference point is arbitrary. Its position will change the position of the maximum curvature along the wall. Hence, if ξ_{ref} is too small, the condition of zero curvature cannot be fulfilled within the adsorbed film. If it is, however, too large, too many numerical cells will be located within the adsorbed film which is not efficient. Throughout this work, a value of $\xi_{\text{ref}} = 5$ nm has been used as a good compromise.

In addition, at the transition to the macroscopic meniscus, i.e. at the right boundary in Fig. 2.8, the flow profile is not known and hence a proper inflow condition is missing. However, the velocity at the interface at the first boundary face representing the liquid-vapor interface adjacent to the inflow boundary is strongly influenced by that boundary condition. Therefore, no reliable flow velocity can be obtained at this boundary face and the above introduced mesh motion algorithm cannot be applied there. Instead the film thickness at the corner point between interface and transition to the macroscopic meniscus is fixed. Of course fixing the film thickness at two positions, the reference and the corner point, would be contradictory. To resolve this issue, the length of the domain L_ξ is adapted iteratively. If the local film thickness at the reference point gets larger than the desired value, the complete mesh is stretched with a constant factor in ξ direction and vice versa. This is necessary to allow the contact angle to adjust itself during the simulation.

The overall algorithm is strongly non linear and has to be solved iteratively. The simulation is considered as converged if the maximal mesh motion has decreased to less than 10^{-16} m per iteration and the equation residuals are smaller than 10^{-9} . Depending on the boundary conditions and the mesh resolution these criteria are fulfilled after 25,000 to 250,000 iterations.

2.3 Results

In this section first the results of the lubrication model will be presented and the effect of the contact line motion on the local and global characteristics of the micro region will be discussed. Subsequently, the results obtained with the lubrication model will be compared to the direct numerical simulation in order to validate the simplifications going along with the lubrication approximation. Moreover, some crucial assumptions made in both approaches will be checked. In addition, the sensitivity of the global results on the dispersion constant and the condensation coefficient is quantified, since these two quantities are in general not exactly known and therefore introduce some uncertainty into the model. All results presented in this section are obtained using the fluid properties of FC-72 at a saturation pressure of 1 bar given in the appendix, Table A.1.

2.3.1 Influence of contact line motion on the microscopic heat and mass transfer

A comparison of the local profiles within the micro region for a varying contact line speed computed with the lubrication model is presented in Fig. 2.9. As already mentioned earlier, the liquid-vapor interface approaches the wall with an almost constant slope resulting in the impression of an finite apparent contact angle. When the interface comes very close to the wall it gets strongly curved and turns into the adsorbed layer towards $\xi = 0$.

It can be observed that the dynamic apparent contact angle increases with contact line speed. This finding is in line with the results of Mathieu et al. [62] and general observations for non-evaporating contact lines as well and can be attributed to purely hydrodynamic effects. In order to fulfill the mass balance within the micro region, the amount of liquid being evaporated has to be supplied by the liquid flow towards the micro region. The driving force for the liquid flow is the gradient of the augmented capillary pressure. The absolute pressure difference, i.e. $p_{c,ad}$, is however a function of the wall superheat alone. However, in case of an advancing contact line the moving wall present in the moving reference frame transports liquid out of the micro region towards the bulk meniscus. Hence, to fulfill the mass balance, the liquid film has to become thicker than in the non-moving case. This results on the one hand in a reduced evaporation rate since the thermal resistance of the liquid film increases and accordingly the liquid mass flux that needs to be supplied becomes smaller. On the other hand, for the same pressure gradient the liquid mass flow within the liquid film increases since the cross section of the flow is enlarged.

Accordingly, for a receding contact line a rather flat film is obtained, since the virtually moving wall tends to transport liquid towards the micro region and the thinner film results in a higher flow resistance. As can be observed in Fig. 2.9(b), the slope of the interface exceeds a local maximum near $\xi = 0.13 \mu\text{m}$ which corresponds to a negative interfacial curvature at this position. That means that also the gradient of the liquid pressure is reversed there and rather tends to transport liquid out of the micro region.

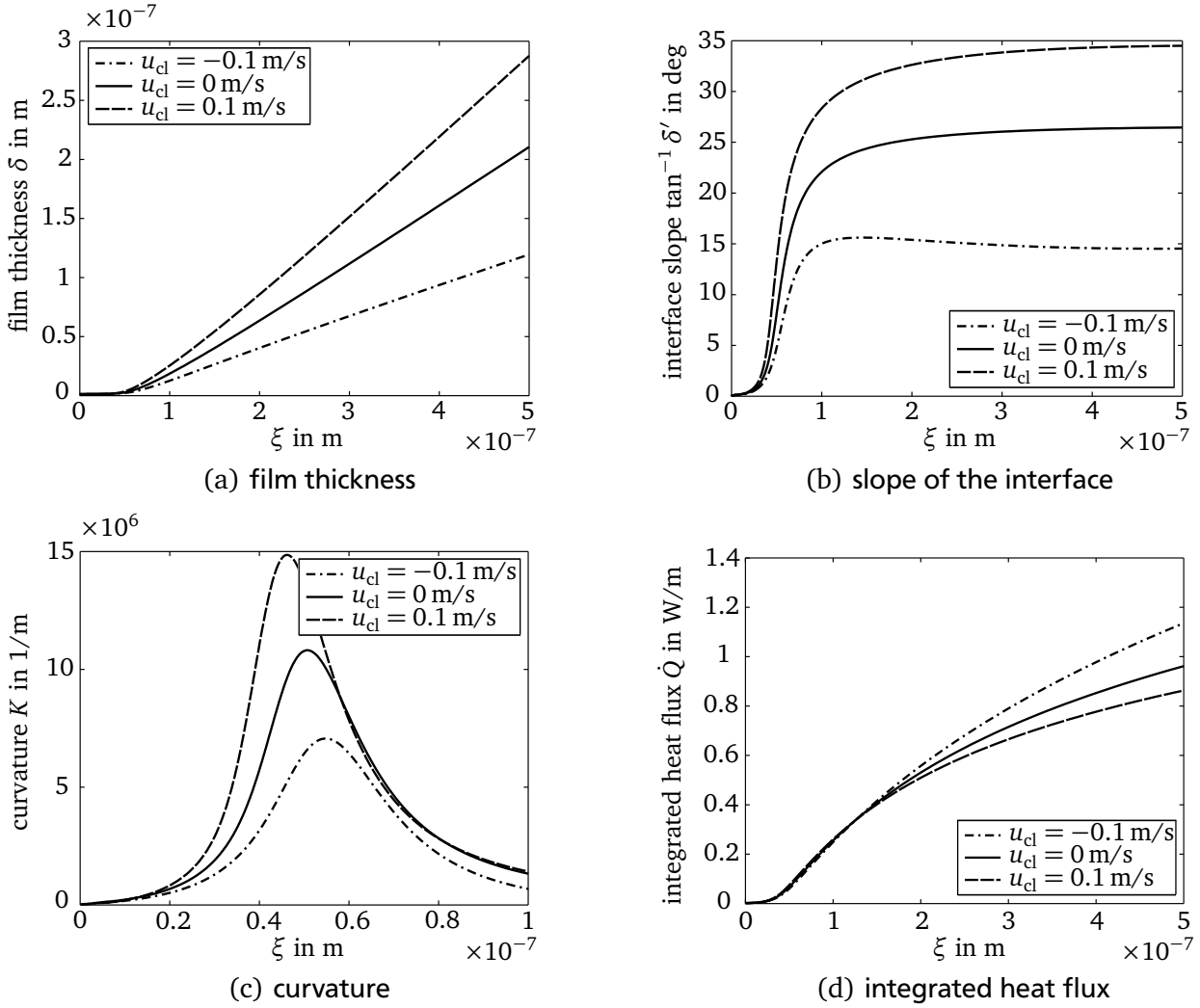


Figure 2.9.: Local profiles within the micro region for a wall superheat of $\Delta T = 5$ K. A positive value of the contact line speed u_{cl} indicates an advancing contact line.

This behavior can be observed for comparably large receding, i.e. negative contact line velocities only. In general, the heat transfer rate decreases with increasing speed of an advancing contact line since the evaporation at the liquid-vapor interface is reduced due to the increasing thermal resistance of the liquid film. The same observation is made for a decreasing absolute value of the contact line speed for a receding contact line.

The effect of a varying wall superheat on the micro region film profile is not displayed here since it has been thoroughly discussed by Stephan [98] and others. Intuitively an increasing wall superheat results in an increasing overall heat flow as can be recognized from Fig. 2.10. According to the increased evaporation rate, the liquid mass flux through the liquid film is rising, too. The pressure difference between adsorbed film and macroscopic meniscus is also slightly increasing but this increase is not sufficient to drive the additional liquid flow. Hence, similar to the situation in moving contact lines, the apparent contact angle increases resulting in a thicker liquid film.

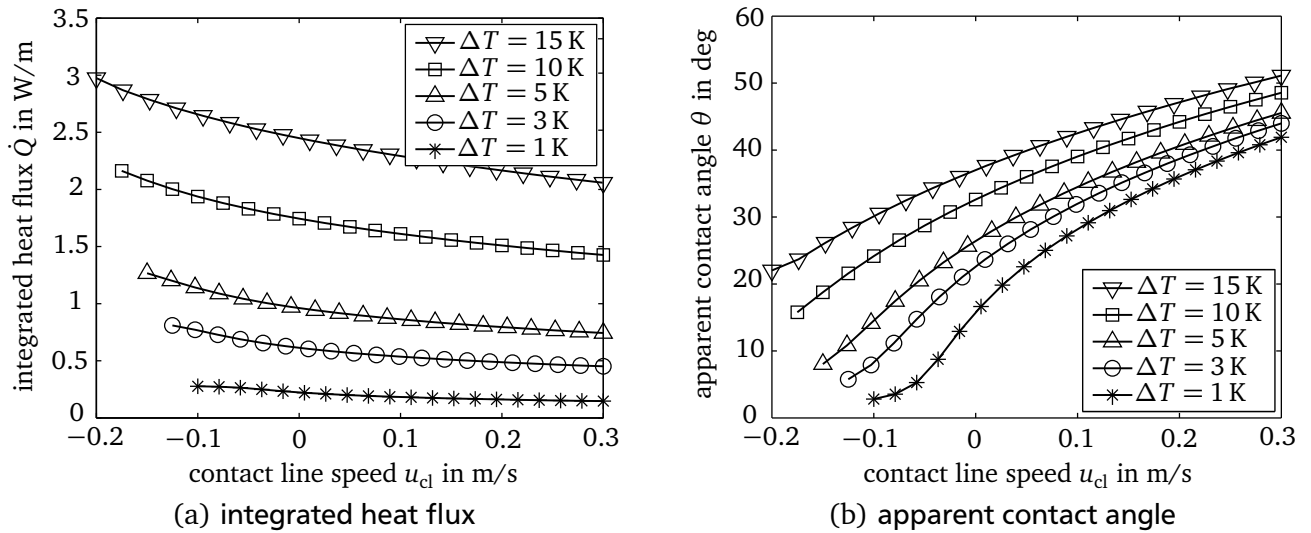


Figure 2.10.: Influence of the wall superheat and contact line speed on the global results of the micro region model.

2.3.2 Validation of the one-dimensional lubrication model

To validate the usage of the lubrication approximation within the one-dimensional model, the obtained results are compared to the results of the direct numerical simulation. An exemplary result of the simulation is shown in Fig. 2.11. Similar to the above presented profiles, the liquid-vapor interface shows a strong curvature at the transition from the adsorbed film region towards the macroscopic meniscus. The velocity profile seems to be nearly parabolic while the temperature changes almost linear in η -direction.

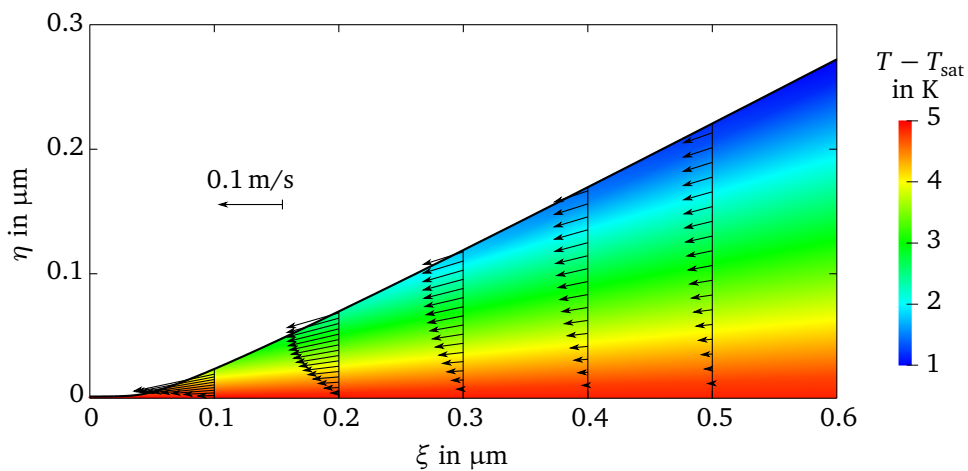


Figure 2.11.: Temperature field and velocity vectors within the micro region for a non-moving contact line at 5 K wall superheat.

However, before a quantitative comparison of the two solution approaches is performed, the simulation is checked for convergence. Therefore, a non-moving contact line at a medium wall superheat of $\Delta T = 5$ K is simulated on three different meshes. The properties of the meshes are listed in Table 2.1. All grids are structured as shown in Fig. 2.8 which depicts the medium mesh. The cell aspect ratio is maintained close

to unity within the entire domain and hence most of the cells are concentrated close to the adsorbed film and the transition region where also the largest gradients are supposed to appear.

mesh	resolution $\delta/\Delta x$	number of cells	computational time ⁷
coarse	8	2,880	0.43 h
medium	16	11,520	2.8 h
fine	32	46,080	26.2 h

Table 2.1.: Meshes used in the grid study and computational time required to reach convergence.

The overall calculation time strongly depends on the mesh used. In addition to the additional computational effort going along with the solution of the linear system for an increasing cell number, the relaxation constant introduced in the mesh motion algorithm $\Delta\tilde{t}_0$ has to be reduced if the mesh resolution is increased. Accordingly, more iterations are necessary to reach convergence in case of a finer mesh. Therefore, the overall calculation time increases roughly by a factor of 8 for each step in mesh resolution, i.e. from 26 minutes for the coarse mesh up to 26 hours for the fine mesh⁷.

The grid dependency of the integrated heat flux and the apparent contact angle, respectively, at the position $\xi = 0.5 \mu\text{m}$ are summarized in Table 2.2. The results obtained for the individual meshes can be extrapolated towards a grid independent solution utilizing a Richardson extrapolation (see e.g. [86, pp. 199–202]). The convergence of both quantities is slightly better than first order. Even on the coarse mesh the error in the heat flow compared to the extrapolated value is less than 2%. Hence, all further calculations will be performed on the medium mesh, which is considered to offer the best compromise between computational effort and accuracy of the results.

mesh	coarse	medium	fine	extrapolated
\dot{Q} in W/m	1.0153	1.0058	1.0014	0.9977
θ in deg	27.053	27.198	27.250	27.278
E_Q	1.77 %	0.82 %	0.38 %	-
E_θ	-0.83 %	-0.29 %	-0.10 %	-

Table 2.2.: Results of the grid study.

A comparison of the results obtained with the lubrication model to the simulation for a non-moving contact line at varying wall superheat is given in Fig. 2.12. The apparent contact angle is predicted very accurately by the lubrication model over the full range of wall superheat investigated even though the contact angle is comparably large. On the contrary, the heat transfer is underestimated by the lubrication model in case of a large wall superheat and hence of a large apparent contact angle. Numerical experiments have shown that the origin of the difference in heat flow is not due to the influence of convective heat transfer but rather due to the two-dimensional nature of heat conduction within the liquid film. Nevertheless, the maximal relative error is 6.5 % at a wall superheat of 20 K which is small compared to the overall uncertainty of the model as will be discussed below.

⁷ The computations were performed on a single core of an Intel Xeon E5-2680 CPU with 2.7 GHz.

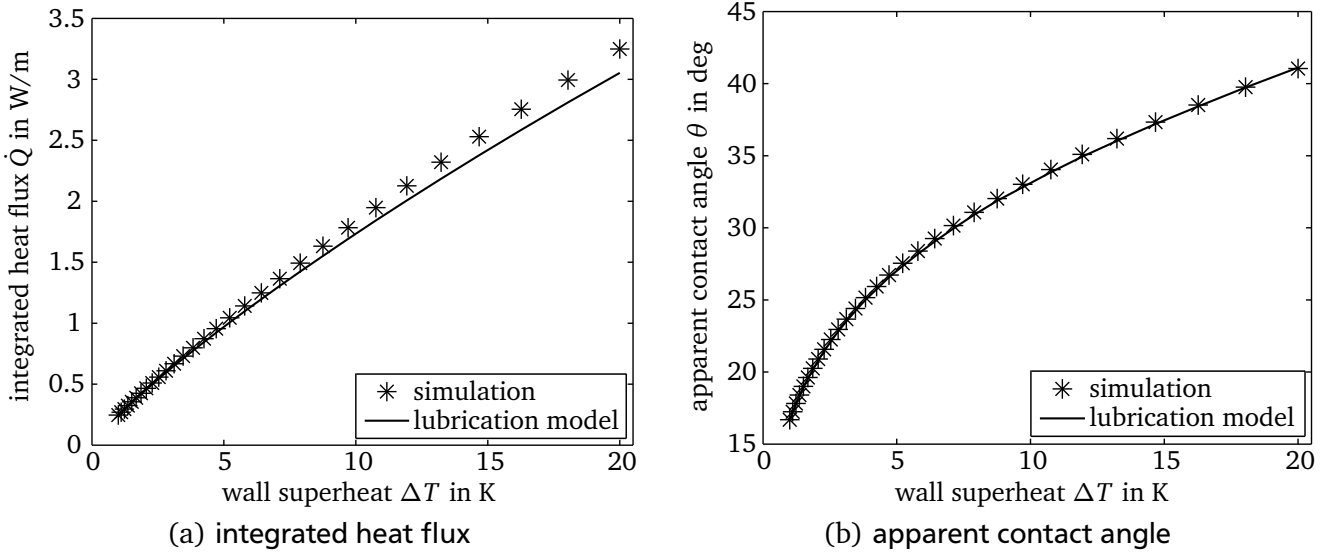


Figure 2.12.: Comparison of the lubrication model to the simulation for a non-moving contact line at varying wall superheat.

For a moving contact line very similar conclusions can be drawn. As illustrated in Fig. 2.13, the contact angle predicted by the approximation again only slightly deviates from the simulation results, except for fast receding contact lines. Accordingly, the error in the prediction of heat transfer is almost independent of the contact line speed. A more detailed analysis of the results obtained by the numerical simulation is given in [5].

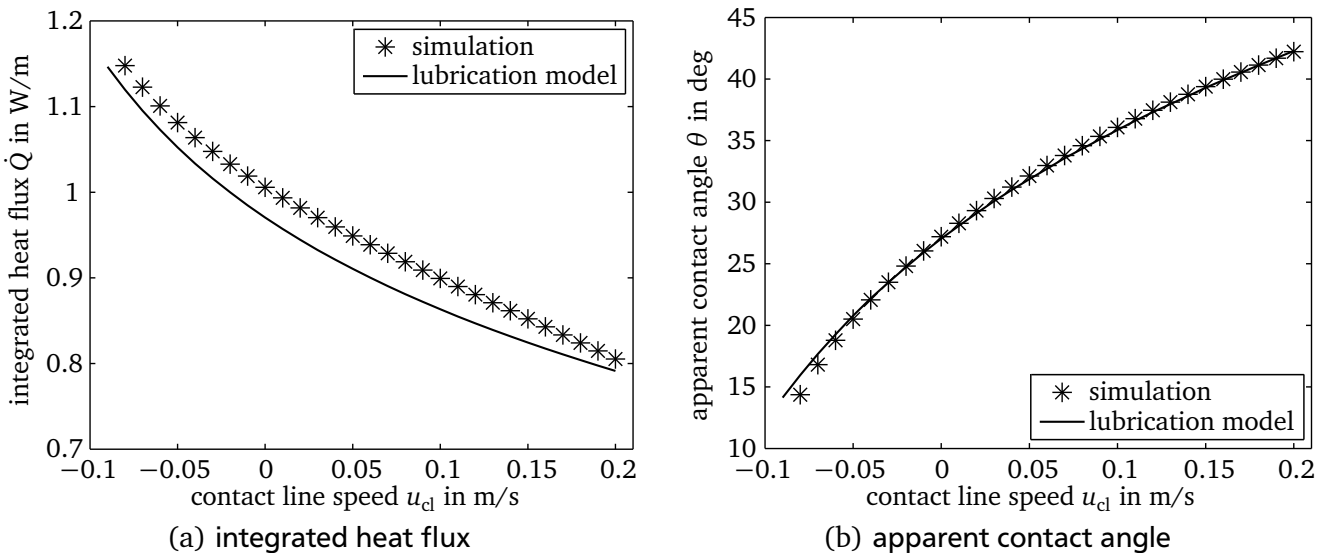


Figure 2.13.: Comparison of the lubrication model to the simulation for a moving contact lines at a wall superheat of 5 K.

It can be summarized that the usage of the lubrication theory in order to simplify the momentum equations is appropriate within the parameter range investigated in this work. On the contrary, the assumption that heat is transferred exclusively by one-dimensional heat conduction within the liquid film is not fully valid. However, the computational effort involved in conducting the direct simulation is more than

two orders of magnitude larger than the one for the solution of the lubrication model. For that reason and since the errors introduced by the approximation are in an acceptable range, the lubrication model is used to conduct large parameter variations. These variational calculations will be necessary to develop a correlation which can be coupled to the macroscopic numerical model as will be shown below.

The results further indicate that the hybrid model proposed by Mathieu et al. [62] seems to be the most appropriate approach to accurately model contact line heat transfer including the effect of two-dimensional heat conduction. They basically used the lubrication theory to model the fluid flow within the micro region while the heat transfer was predicted by a Finite-Elements simulation of the liquid film. However, the implementation of such a model and the comparison of its results to the full simulation has to be discussed elsewhere.

2.3.3 Validation of further modeling assumptions

In addition to the usage of the lubrication theory, some more simplifications have been introduced during the derivation of both, the lubrication model and the direct numerical simulation. Both approaches assume steady-state conditions within the micro region even though the contact line might be accelerating or the wall temperature might be dynamically changing. Moreover, the contact line has been assumed to be straight here, even though it will be curved in nearly every situation during drop impingement. In addition, the flow within the micro region has been assumed to be creeping. In the derivation of the interfacial heat resistance several simplification were made which might not be appropriate for a large wall superheat. Finally, the wall is always considered to be smooth on a molecular level, even though every technical surface shows a specific roughness which is much larger than the adsorbed film thickness. In the following, the effect of these simplifications will be evaluated.

Steady-state

Within the micro region model the time-independent form of the conservation equations has been solved. This assumption holds as long as the processes in the micro region are much faster than the processes on the macroscopic scale. A characteristic time scale \hat{t}_{mic} in the micro region can be defined by comparison of the latent heat stored within the liquid film and the supplied heat flow

$$\hat{t}_{\text{mic}} = \frac{M_1 h_{\text{lv}}}{\dot{Q}} \quad (2.99)$$

where the fluid mass is given by

$$M_1 = \rho_1 \int_{\xi=0}^{\xi_{\text{mic}}} \delta d\xi. \quad (2.100)$$

In case of a non-moving contact line at a wall superheat of 10 K the timescale can be estimated to $\hat{t}_{\text{mic}} \approx 2.5 \mu\text{s}$. For an advancing contact line more mass is stored in the micro region due to the larger contact angle. Nevertheless, for $\Delta T_w = 10 \text{ K}$ and $u_{\text{cl}} = 1 \text{ m/s}$ the time scale is still smaller than $35 \mu\text{s}$.

The hydrodynamic time scale commonly used for a drop impinging on a surface is given by the ratio of the initial droplet diameter and its initial velocity

$$\hat{t}_{\text{hyd}} = \frac{D_0}{u_0} \quad (2.101)$$

which will be in the order of $\hat{t}_{\text{hyd}} \approx 1 \text{ ms}$ throughout this study. Hence, the processes within the contact line region can be considered time-independent since $\hat{t}_{\text{mic}} \ll \hat{t}_{\text{hyd}}$.

Two-dimensional flow

In the above considerations the flow within the micro region was considered in two-dimensional planar coordinates. However, as illustrated in Fig. 2.14, in case of a droplet in contact to the wall it is more appropriate to describe the flow problem in cylindrical coordinates as done by for example by Lay and Dhir [52], Mann [58], and Kern [44] who considered the contact line heat transfer at the curved bubble foot in case of nucleate boiling.

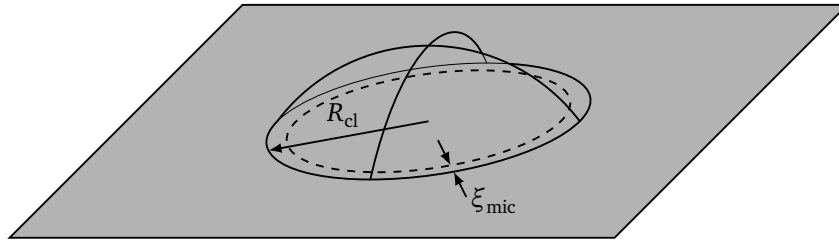


Figure 2.14.: Curvature of the contact line in case of a sessile droplet.

Nevertheless, provided that the radius of the contact line R_{cl} is large compared to the characteristic length of the micro region ξ_{mic} , the effect of curvature is negligible. To quantify the curvature effect, the heat transfer of a non-moving contact line is solved for a varying radius. In accordance to classical definitions the contact line radius R_{cl} is defined positive for a bubble type situation and negative for a droplet type situation as presented in Fig. 2.14. The solution is generated utilizing the direct numerical simulation since there only the geometry of the calculation domain has to be adapted while to incorporate the curvature effect into the lubrication model, some adaptations of the equations would have to be made (see e.g. [44]).

In Fig. 2.15 the dependency of the integrated heat flux on the contact line radius is presented relative to the situation of $R_{\text{cl}} \rightarrow \infty$, which corresponds to the formulation of the problem in a two-dimensional planar coordinate system. The absolute value of the radius is varied between $10 \mu\text{m}$ and 10 mm implying a ratio of $\xi_{\text{mic}}/R_{\text{cl}}$ between 0.05 and 5×10^{-5} . It can be recognized that the effect of the curvature is very small, even at comparably small contact line radii. In general, the change in heat

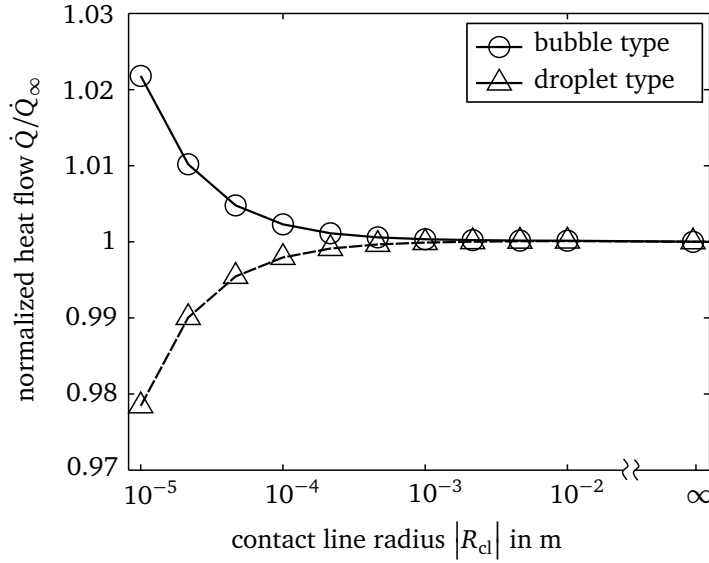


Figure 2.15.: Influence of the contact line radius on micro region heat transfer for a non-moving contact line and a wall superheat of 5 K. A droplet type situation corresponds to a negative radius.

flux is almost of the same magnitude for a bubble and for a droplet of the same radius but with opposite signs. The heat flow in case of a bubble is always larger than in the two-dimensional situation. The observed changes can mainly be attributed to the change in the interfacial area, which can be calculated to $S/S_\infty = 1 + 0.5\xi_{mic}/R_{cl}$.

The changes in contact angle are not displayed here, but in general they are about one order of magnitude smaller than the changes in heat flux. This also implies that the flow profile is not significantly influenced within the range of radii investigated. It can be expected that the effect is much stronger if the contact line radius becomes very small, but such tiny droplets will not be considered within this study.

Due to its very small effect and in order to keep the number of independent parameters small, the effect of the contact line radius will be ignored throughout this work.

Creeping flow

The inertial terms in the momentum equation have not been taken into account for the lubrication model. The validity of neglecting these terms can be judged by means of the Reynolds number. One possible definition of the Reynolds number of the liquid flow through the micro region is

$$\text{Re} = \frac{\rho_l \bar{u} \delta}{\mu_l}, \quad (2.102)$$

where \bar{u} denotes the average velocity within the film which can be linked to the mass flow rate through the micro region via

$$\rho_l \bar{u} \delta = \dot{M} = \frac{\dot{Q}}{h_{lv}} + \rho_l u_{cl} \delta_{ad} \quad (2.103)$$

and hence the Reynolds number can be reformulated to

$$\text{Re} = \frac{|\dot{Q} + \rho_l u_{cl} h_{lv} \delta_{ad}|}{h_{lv} \mu_l}. \quad (2.104)$$

It is obvious that the Reynolds number has its maximum value at the transition to the macroscopic meniscus since \dot{Q} is a monotonic function of ξ . The global maximum value of the Reynolds number within this work is found for a receding contact line with $u_{cl} = -0.2 \text{ m/s}$ and a wall superheat of $\Delta T_w = 20 \text{ K}$ and is about $\text{Re}_{\max} = 0.1$. At the same time the contact angle is comparably small in that situation. Hence it can be followed that $\text{Re} (L_\eta / L_\xi) \ll 1$ and accordingly the inertial terms in the momentum equation can indeed be neglected.

Simplifications concerning the interfacial heat resistance

In Section 2.1.3, multiple assumptions have been made in order to simplify the original equation of Schrage and to be able to express it as a Robin type boundary condition to the interface temperature. However, as proposed by Wang et al. [114], it is also possible to directly calculate the interfacial mass flux from Eq. (2.36)

$$m_{\text{evap}} = f \frac{1}{\sqrt{2\pi\mathcal{R}}} \left(\frac{p_{v,\text{int}}}{\sqrt{T_{\text{int}}}} - \frac{p_v}{\sqrt{T_v}} \Gamma \right). \quad (2.36)$$

Instead of taking the vapor density as constant during the integration of Eq. (2.28), one can approximate the density change using the ideal gas law. Then the augmented Thomson equation (2.33) is replaced by the following form of the Kelvin equation

$$p_{v,\text{int}} = p_{\text{sat}} \exp \left[\frac{1}{\mathcal{R} T_{\text{int}} \rho_l} (p_{v,\text{int}} - p_{\text{sat}} - p_c) \right]. \quad (2.105)$$

The vapor sided interfacial pressure is given by the root of the above function. The saturation pressure can be obtained also from a more accurate integration of the Clausius-Clapyeron equation (2.42), yielding

$$p_{\text{sat}} (T_{\text{int}}) = p_v \exp \left[\frac{h_{lv}}{\mathcal{R}} \left(\frac{1}{T_{\text{sat}}} - \frac{1}{T_{\text{int}}} \right) \right]. \quad (2.106)$$

To close the model for usage in the lubrication model, the energy balance for the liquid film reads

$$q_{\text{evap}} = \frac{k_l (T_{w,\text{mic}} - T_{\text{int}})}{\delta \sqrt{1 + \delta'^2}}. \quad (2.107)$$

Finally, the equations (2.36), (2.37), (2.38), (2.105), (2.106) and (2.107) can be combined to a coupled, non-linear system of equations from which the interfacial heat flux q_{evap} can be calculated numerically utilizing Newton's method. This calculation of the heat flux is then incorporated into the lubrication model.

The initial conditions of the integration do also slightly change when using the above approach. The disjoining pressure at the adsorbed film can be determined from Eq. (2.36) for $m_{\text{evap}} = 0$ in combination with Eq. (2.105), where the interfacial temperature is set equal to the wall temperature, to

$$p_{c,\text{ad}} = p_v \sqrt{\frac{T_{w,\text{mic}}}{T_{\text{sat}}}} - p_{\text{sat}}(T_{w,\text{mic}}) - \frac{1}{\mathcal{R} T_w \rho_l} \ln \left(\frac{p_v}{p_{\text{sat}}(T_{w,\text{mic}})} \sqrt{\frac{T_{w,\text{mic}}}{T_{\text{sat}}}} \right) \quad (2.108)$$

and the corresponding film thickness is given by Eq. (2.82) as

$$\delta_{\text{ad}} = \left(\frac{A}{p_{c,\text{ad}}} \right)^{1/3}. \quad (2.82)$$

A comparison of the global results obtained with this non-linearly coupled approach and the linear approximation presented in Section 2.1.3 is given in Table 2.3. Surprisingly, the error introduced by the linearization of the equations for the interfacial heat resistance decreases with increasing wall superheat, although one would expect that the linearization is more adequate for a small wall superheat. However, it should be noticed that the overall effect of the interfacial heat resistance is reduced if the wall superheat is large. This is mainly due to the increase of contact angle and thereby of the liquid film thickness with the wall superheat. Hence, the overall thermal resistance is dominated by the resistance of the liquid film in case of a large wall superheat ΔT_w , while the interfacial heat resistance is more important for a small superheat.

ΔT_w in K	non-linear solution		linear approximation		error of approximation	
	\dot{Q} in W/m	θ in deg	\dot{Q} in W/m	θ in deg	E_Q	E_θ
5	0.909	25.784	0.962	26.452	5.8 %	2.6 %
10	1.683	32.068	1.744	32.619	3.6 %	1.7 %
15	2.398	36.532	2.449	36.988	2.1 %	1.2 %
20	3.068	40.271	3.098	40.662	0.98 %	0.97 %

Table 2.3.: Effect of the linearizations needed in the derivation of the interfacial heat resistance on the global results for a non-moving contact line.

Overall the global error introduced by the linearization is acceptable since it is still small against the uncertainty in the condensation coefficient as will be discussed below. Moreover, the necessity to solve the non-linear system of equations presented above during the integration of the system of ordinary differential equations produces a significant additional computational effort, making it almost impossible to carry out a large parameter variation⁸.

Wall topology

All results shown above were obtained assuming the wall to be smooth down to the molecular length scale. However, any technical surface shows a certain roughness with a characteristic length scale significantly larger than the liquid film thickness within the micro region. Even though a direct simulation of the contact line region on a statistically rough surface is not feasible, at least the influence of a nano-structuring of the wall can be investigated with the simulation model. Moreover, while the effects of a random roughness on the flow might on average partially cancel, a regular structure is expected to show a stronger effect. Since the simulation model has been formulated in three dimensions, the topology of the wall can be accounted for directly via the topology of the mesh boundary. Parts of the results presented here are published in [5].

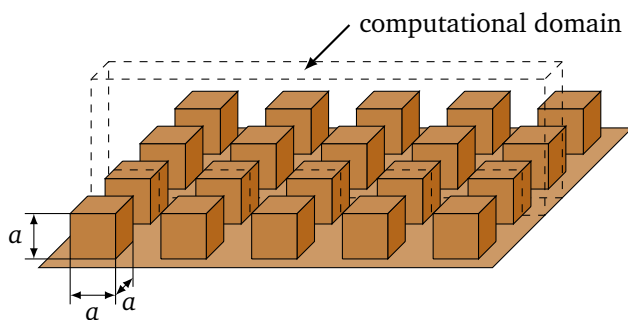


Figure 2.16.: Sketch of the investigated surface structure. The base length as well as the spacing of the cubes is 5 nm.

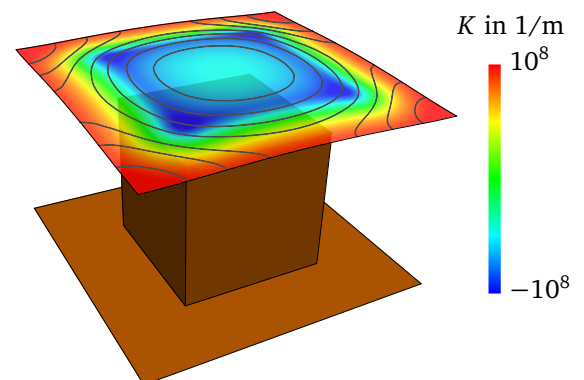


Figure 2.17.: Shape of the interface in the adsorbed film colored by curvature with lines of constant height, spaced by 0.5 nm. The wall superheat is 5 K.

As one example for the variety of possible structures, a wall structured with nano cubes is investigated as shown in Fig. 2.16. If the contact line is assumed to be aligned with one preferential direction of the structure, only half a row of cubes needs to be calculated taking advantage of the symmetry. If the characteristic length of the structure was chosen much smaller than the thickness of the adsorbed layer, no effect could be expected. On the contrary, if the structures are much larger than the adsorbed film thickness, the micro region would see more or less a smooth wall at the position of maximum heat transfer. Therefore, the base length of the cubes is chosen to $a = 5$ nm which is approximately five times

⁸ The computational time required for the solution of one parameter combination increased from a few seconds to several hours by taking into account the non-linear coupling. It should, however, be noted that the computational overhead would be significantly smaller in case of the direct numerical simulation since there an iteration process is required anyway.

larger than δ_{ad} . Moreover, a larger structure would involve large deformations of the interface requiring a partial re-meshing of the computational domain during the simulation to maintain a sufficient grid quality. Therefore, the presented solution algorithm is considered not feasible to simulate the effect of large structures. Unfortunately, only non-moving contact lines can be simulated. The fluid flow within the micro region near a moving apparent contact line on such kind of structure would be highly unsteady and can therefore not be modeled within a steady moving reference frame as it has been possible in case of a smooth wall. An investigation of the effect of a wall structure onto the evaporation near moving contact lines would require the formulation of an unsteady solution algorithm which is beyond the scope of this thesis.

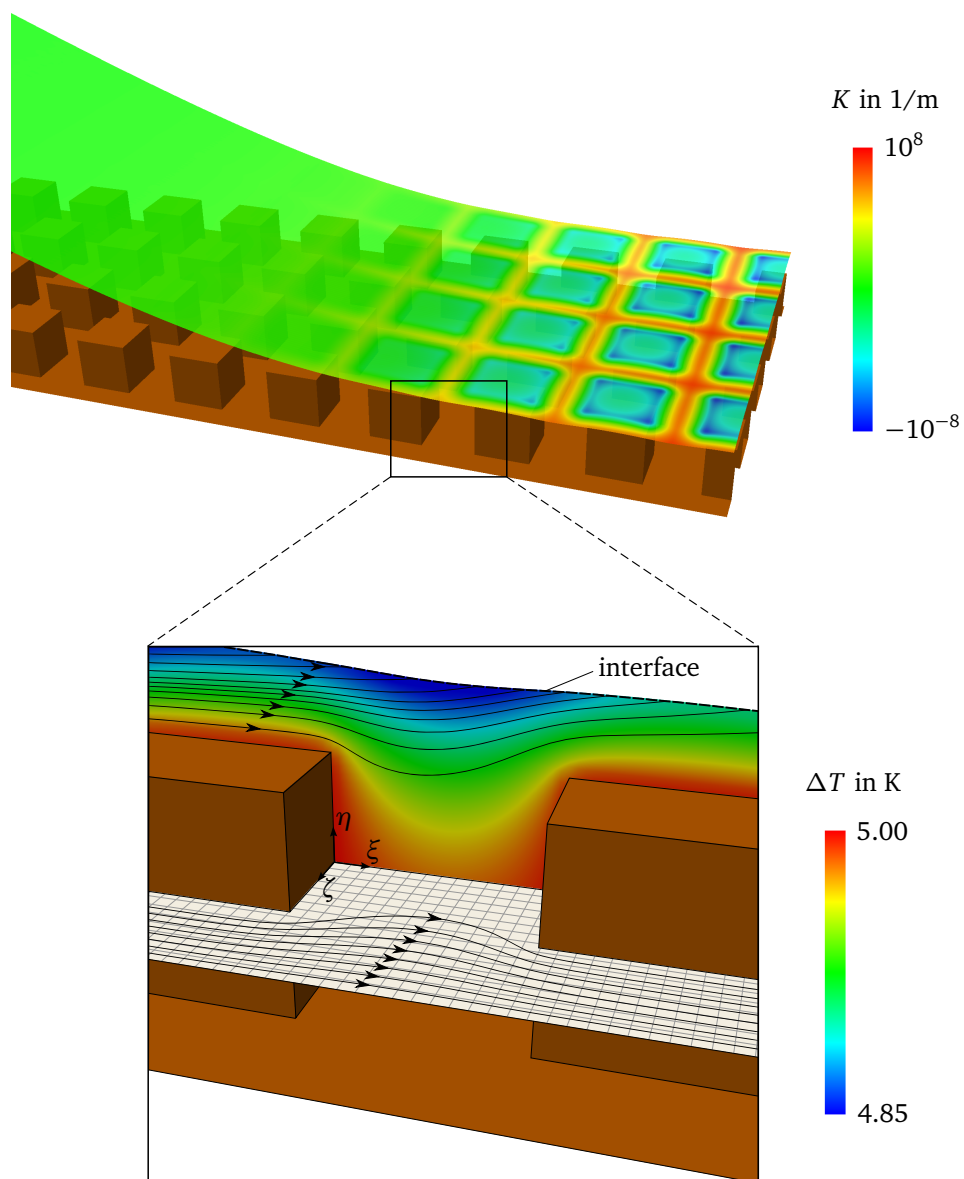


Figure 2.18.: Top: Shape of the interface in the micro region on a nano-structured wall colored by curvature.
 Bottom: Streamlines in the ξ, η - and ξ, ζ -plane and temperature field in the ξ, η -plane near the adsorbed film.

Due to the non-uniformity of the wall, the adsorbed film is not flat. Nevertheless, a stable, non-evaporating film can form above the structured wall. Since no evaporation should occur there, the augmented capillary pressure p_c has to fulfill Eq. (2.80) at the entire liquid-vapor interface. As can be seen in Fig. 2.17 this is obtained by an equilibrium between the disjoining and the capillary pressure. In regions where the distance from the interface to the wall is smaller than the thickness of the adsorbed film on a smooth wall in absence of any curvature would be, i.e. near the top edges of the cube, a negative curvature is observed. In turn, above the gap between the cubes the interface shows a strong positive curvature to balance the reduced contribution of the disjoining pressure to p_c at this position.

In spite of the significant local changes, no striking effect of the wall structure can be observed from a global point of view. While the apparent contact angle is slightly smaller in case of the structured wall by about 3 %, the global heat flow remains nearly unaffected. The small change in the contact angle can be attributed to a reduced flow resistance from the bulk meniscus towards the region of strong evaporation. As can be seen in Fig. 2.18 the liquid is able to flow also between the posts while the interface cannot penetrate these gaps due to their small spacing. Thereby the cross section of the flow is enlarged and accordingly the frictional pressure loss is reduced. Hence, including the effects of surface topology in the approximate solution via introducing a effective slip length as proposed by Ojha et al. [67] seems to be reasonable although they employed slip length values far larger than the physical roughness measured in their experiment to fit their computational results.

It can be summarized that the microscopic structure of the wall can be neglected, at least if the contact line is not moving and the characteristic length scale of the structure is in the order of magnitude of the adsorbed layer. A detailed parametric study of the influence of characteristic length or the shape of the structure is avoided due to the enormous computational effort involved. The simulation of the presented case has been performed on a mesh with about 500,000 cells and more than 500,000 iterations were required to reach convergence. The computation took about six days on eight CPUs.

2.3.4 Sensitivity analysis

In addition to the uncertainties arising from modeling assumptions the results depend on the choice of the physical quantities. Most of the material properties are at least in general available with a comparably small error. In contrary, especially the two quantities used to describe microscopic phenomena on a macroscopic scale, namely the dispersion constant and the condensation coefficient, are hard to access experimentally. Hence, one is forced to make an educated guess for these parameters keeping in mind that an additional uncertainty might arise from this choice. Therefore, in the following the sensitivity of the global results on both parameters is quantified.

Dispersion constant

In Section 2.1.1 a comparably rough estimation of the dispersion constant has been introduced. This is necessary since for most real material combinations no experimentally obtained values are available in literature. However, almost all measurements of the dispersion constant of non-polar fluids yielded quite similar values being at least in the same order of magnitude.

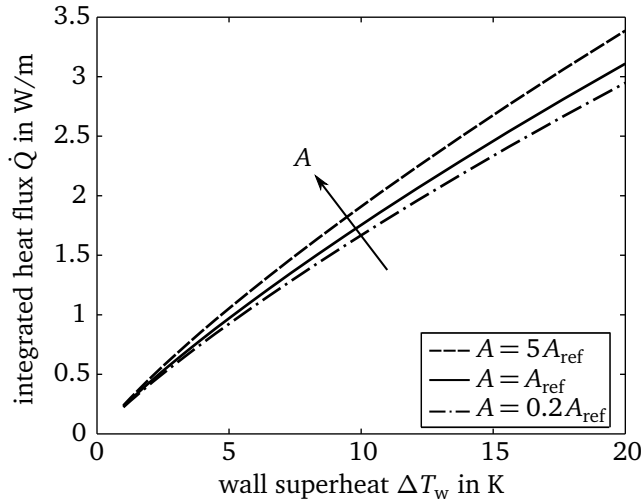


Figure 2.19.: Influence of the dispersion constant on heat transfer in the micro region.

The effect of the dispersion constant on the heat transfer within the micro region is presented in Fig. 2.19. Even though the value of the dispersion constant is varied by a factor of five against the reference value of $A_{\text{ref}} = 4.37 \times 10^{-21}$ J, the global heat flow changes by less than 9%. The changes in the apparent contact angle are similar but become even smaller for a large wall superheat. Hence, the exact choice of the dispersion constant is not of high importance as long as it is within the appropriate order of magnitude.

Condensation coefficient

The second quantity which is almost completely unknown is the condensation coefficient. As can be recognized from Fig. 2.20, it has a tremendous influence on the global outcome of the calculations. For a small wall superheat the relative deviation in the heat flux when assuming f to be 0.5 or unity, respectively, is more than 60%. As already stated above, the overall influence of the interfacial heat resistance decreases with increasing superheat but nevertheless the heat flow still changes by 20% for a wall superheat of 20 K. The situation becomes even worse bearing in mind that theoretically predicted and measured values of f vary over an even larger range from 0.001 to 1 [60].

Due to this strong uncertainty there are two conclusions to be drawn. Firstly, the modeling errors and uncertainties discussed above are negligible against the influence of the condensation coefficient. Secondly, a proper choice of f is crucial in order to accurately simulate the drop impingement process. It is obvious that the overall model will not even be able to predict the hydrodynamic behavior of the impinging droplet properly if the modeled equilibrium contact angle deviates strongly from the value determined from the experiment.

Hence, the condensation coefficient is adjusted according to the experiment on single drop impingement which will be presented in Section 4.1.1. Even though the contact angle could not directly be measured accurately in the experimental setup, the equilibrium angle can be determined indirectly at the end of the impact. Since the contact line radius is measured during the entire impact process, the radius at the end of the impact when the droplet is at rest is known. Following the approach of Myers and Charpin [64] the equilibrium droplet shape can be obtained by the solution of an ordinary differential

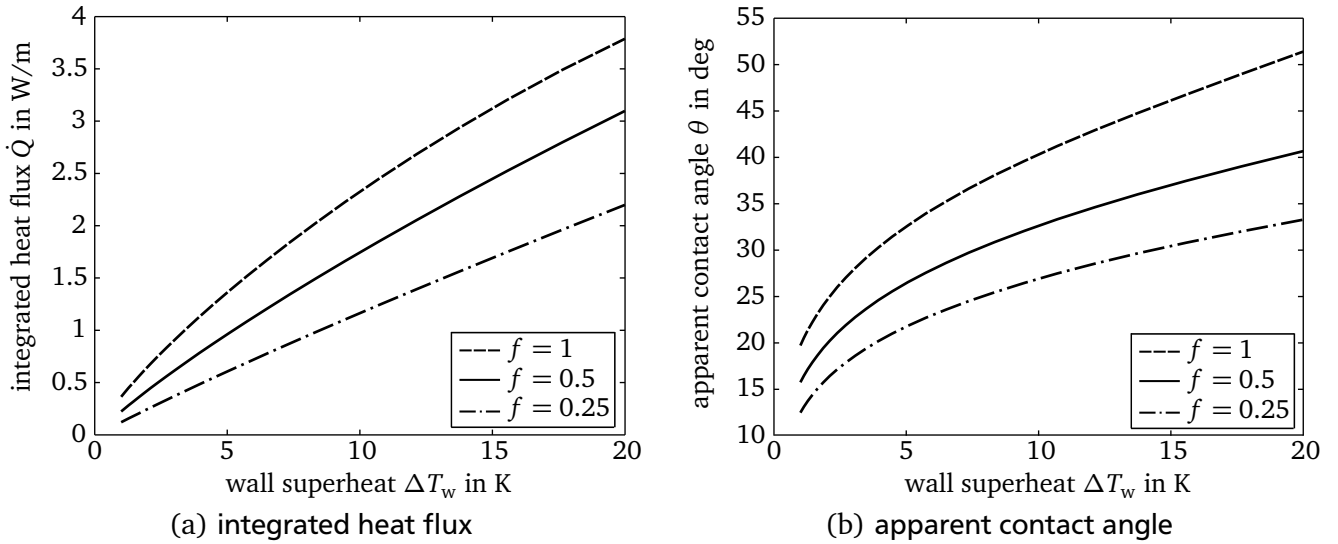


Figure 2.20.: Influence of the condensation coefficient.

equation derived from the Young-Laplace equation. The contact angle and the height of the droplet at the symmetry axis are gradually varied, until the calculated shape meets the measured contact line radius and the given initial droplet volume. For a local wall superheat of $\Delta T = 12.4$ K an equilibrium contact angle of $\theta_{\text{mac}} \approx 36$ degrees is found from the measured data. This contact angle is well predicted by the contact line model for $f = 0.5$, while choosing $f = 1$ results in an angle of 44 degrees. Again, the simulated hydrodynamics of an impinging droplet and thereby its heat transfer performance will be strongly erroneous if the equilibrium contact angle deviates by almost 25% from the value determined from the experiment. Therefore, the value of 0.5 will be used for the condensation coefficient throughout this thesis. It should be noted that van den Akker et al. [2] proposed the usage of a value for the condensation coefficient in the same order of magnitude to match the results of the lubrication model to the results of their molecular dynamic simulations.

2.3.5 Parameterization of the results

The global results of the micro region model have to be provided as an input to the macroscopic simulation. In turn, to solve the micro region problem, the local wall superheat and contact line velocity are required. Hence, due to the non-linear coupling between the two model parts, an iterative process will be necessary. In principal, the ODE-system could be solved during the global simulation using the local temperature and contact line speed information from the macroscopic model. This solution algorithm is however too expensive in terms of computational time. Especially in three-dimensional simulations the computational effort to solve the ODEs in every iteration and for every segment of the contact line would exceed the overall computational time required by the macroscopic model.

Instead, the global results of the micro region model, i.e. the integrated heat flux, the apparent contact angle, and the film thickness at the end of the micro region, are parameterized and a regression of the data with respect to the wall superheat and the contact line speed is provided to the CFD simulation.

Kunkelmann showed that the temperature dependency of all relevant output data Φ for a non-moving contact line can be well correlated to the wall superheat using a root series [47],

$$\Phi_0(\Delta T_w, u_{cl} = 0) = \sum_{i=1}^N a_{\Phi, T, i} \Delta T_w^{1/i}. \quad (2.109)$$

From the dimensionless parameters defined for the lubrication solution (2.85) only the parameter D_4 depends on the contact line velocity. Apart from the dependency of this parameter on the material properties it can be concluded that $D_4 \propto u_{cl}/\Delta T_w^{2/3}$, which indicates that the influence of speed and temperature cannot be correlated independently.

In order to keep the definition of the regression function simple, a product approach is chosen

$$\Phi(\Delta T_w, u_{cl}) = \Phi_0(\Delta T_w) \cdot \Phi_u(\tilde{u}_{cl}), \quad (2.110)$$

where Φ_u reflects the velocity influence and is given as a polynomial of M-th order

$$\Phi_u(\tilde{u}_{cl}) = \sum_{j=0}^M a_{\Phi, u, j} \tilde{u}_{cl}^j. \quad (2.111)$$

The argument of that function is a scaled contact line velocity given by

$$\tilde{u}_{cl} = u_{cl} \Delta T_w^{b_\Phi}. \quad (2.112)$$

Numerical experiments have shown that the optimal value of b_Φ , for which the best regression is obtained, might deviate from the theoretical value of $-2/3$ and it is therefore advisable to include it as an additional parameter into the fitting procedure.

To calculate the regression for the simulations to be performed within this thesis, the ODE-system is solved for a wide parameter range $(\Delta T_w, u_{cl}) \in [5\text{K}, 20\text{K}] \times [-0.1\text{m/s}, 2\text{m/s}]$ at 650 individual data points. The best fit to the data is obtained for $N = 6$ and $M = 8$. The regression reproduces the original input data with a very good quality as can be seen in Fig. 2.21 for the integrated heat flux at the end of the micro region. The extracted coefficients of the regressions are given in the appendix.

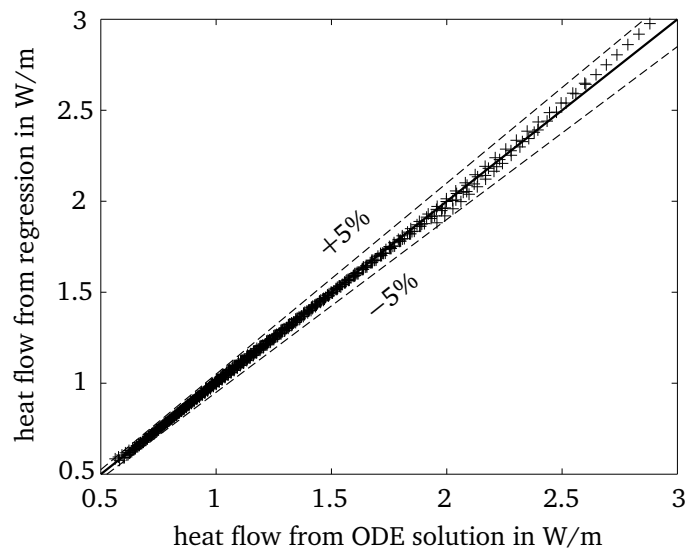


Figure 2.21.: Quality of the correlation for the heat flow per unit contact line length. The maximal relative error is less than 4 %.



Macro scale heat and fluid flow

After the model for contact line heat transfer has been presented, the macroscopic model used for the simulation of drop impingement will be introduced in this chapter. Besides the general need to capture the complex two-phase flow, special attention is paid to the modeling of heat transfer and evaporative phase change.

The macroscopic model is implemented into the open source CFD software OpenFOAM. For discretization of the conservation equations the Finite Volume Method on arbitrary unstructured meshes is utilized. A general introduction to the Finite Volume Method including considerations for unstructured grids is given by Schäfer [86, pp. 77–106], while the numerical details regarding the actually implemented algorithms in OpenFOAM can be found in [41] and [119]. Since the implementation of OpenFOAM relies on the usage of unstructured meshes, in the following special attention is paid to the applicability to general topologies during the development of numerical algorithms.

3.1 Governing equations

The macroscopic fluid flow can be modeled through the conservation laws of mass, momentum, and energy. Throughout this work the flow in each individual phase is assumed to be incompressible. A one-field approach is utilized which means that only one velocity, pressure, and temperature field is defined for both phases. The jump conditions at the interface have therefore to be converted to source terms in the governing equations. An additional transport equation has then to be solved to track the position of the interface. Here, the Volume of Fluid (VOF) method is used which will be briefly described in the next section.

Even though the flow in each individual phase is incompressible, the phase-averaged flow velocity is not always divergence free. Instead, the continuity equation reads

$$\nabla \cdot \mathbf{u} = \Sigma_V, \quad (3.1)$$

where the source term Σ_V reflects the volume change in case of phase change due to the density difference between the two phases. The evaporation rate and the resulting divergence of the velocity field have to be calculated by an evaporation model and will be specified below. The momentum conservation is given by Cauchy's equation of motion

$$\rho \left(\frac{\partial \mathbf{u}}{\partial t} + (\mathbf{u} \cdot \nabla) \mathbf{u} \right) = \nabla \cdot \mathbf{T} + \rho \mathbf{g} + \mathbf{f}_\sigma \quad (3.2)$$

with the stress tensor \mathbf{T} . The source terms on the right hand side account for gravity and surface tension effects, respectively. The liquid and vapor phase are both considered as Newtonian and accordingly the stress tensor can be expressed as

$$\mathbf{T} = - \left[p + \frac{2}{3} \mu (\nabla \cdot \mathbf{u}) \right] \mathbf{I} + \mu \left[\nabla \mathbf{u} + (\nabla \mathbf{u})^T \right] \quad (3.3)$$

where the Stokes' hypothesis has been used to eliminate the second coefficient of viscosity, commonly referred to as λ^* . The continuity and Navier-Stokes equation are solved by means of the PISO algorithm [40]. The energy conservation is reformulated in temperature form using Fourier's law

$$\frac{\partial (\rho c T)}{\partial t} + \nabla \cdot (\rho c \mathbf{u} T) = \nabla \cdot (k \nabla T) + \Sigma_e \quad (3.4)$$

but neglecting the pressure work and dissipation effects. The additional source term Σ_e is introduced to account for the latent heat of vaporization. Within the solid phase, the energy equation reduces to

$$\frac{\partial (\rho c T)}{\partial t} = \nabla \cdot (k \nabla T) \quad (3.5)$$

due to the absence of convective transport and phase change.

3.2 Interface tracking

Several approaches have been developed in the past to track the position of each individual phase on a fixed Eulerian grid. Harlow and Welch [33] proposed the Marker and Cell (MAC) method. Weightless particles are used as markers for the distribution of one of the phases. These markers are transported by convection through the domain and thereby follow the position of the interface. Later on this method has been further developed towards the Front Tracking utilized e.g. by Tryggvason et al. [106], using particles as markers for the interface between the phases. Another frequently used approach is the Level-Set method which uses a signed distance function from the interface to distinguish the phases [69, 103]. A transport equation is formulated to update the position of the interface, i.e. the zero level set, in each time step.

The method which is employed within this work is the Volume of Fluid method proposed by Hirt and Nichols [36]. To distinguish between the phases a new variable F is defined, reflecting the ratio of volume occupied by the liquid phase in each individual cell,

$$F = \frac{V_l}{V_c}. \quad (3.6)$$

Consequently, the volume fraction F is unity or zero in cells completely filled with liquid or vapor, respectively. The interface is located where the volume fraction takes intermediate values. To follow the evolution of the phase distribution with the flow, a purely convective transport equation is formulated,

$$\frac{\partial F}{\partial t} + \nabla \cdot (\mathbf{u}F) = 0. \quad (3.7)$$

All material properties γ required in the conservation equations¹ are defined as the volume weighted average of the properties of the pure phases,

$$\gamma = F\gamma_l + (1 - F)\gamma_v. \quad (3.8)$$

Through the formulation of a conservation equation for the volume fraction field, the mass of each phase is conserved by default. In the other interface tracking approaches listed above the mass conservation is not automatically fulfilled. However, the VOF method suffers from the effect of numerical diffusion of the interface. Solving Equation (3.7) with standard numerical schemes would result in a strong smearing of the interfacial region. Therefore, a special treatment of the convective transport is required. A very common and sophisticated approach to preserve a sharp interface is the piecewise-linear interface calculation (PLIC) [81]. In this technique, the interface is reconstructed as a linear segment within each cell in a way, that the volume of the liquid is conserved and the orientation of the normal is given by the gradient of F . Given this reconstructed interface, the volumetric fluxes of the volume fraction can be calculated. This geometrical advection preserves the interfacial region sharp. However, this technique has so far been applied in many multiphase codes using a cartesian grid while transferring it to general, three-dimensional grids is still work in progress [61].

Instead, an algebraic transport scheme is used within this work. As originally proposed by Weller [118] and used by default in OpenFOAM's two-phase solver `interFoam`, an additional compressive term is

¹ These are in particular the density ρ , the volumetric heat capacity (ρc), the dynamic viscosity μ , and the thermal conductivity k . Regarding the latter two properties, the linear interpolation between the properties of the pure phases might not always be adequate. Depending on the direction of the temperature or velocity gradient relative to the interface orientation, a harmonic interpolation might be more appropriate. However, the linear interpolation is applied throughout this thesis independent of the interface orientation which is also well established in the literature.

added to the transport equation which counteracts the numerical diffusion in the direct vicinity of the interfacial region,

$$\frac{\partial F}{\partial t} + \nabla \cdot (\mathbf{u}F) + \nabla \cdot (c_F |\mathbf{u}| \mathbf{n}_{\text{int}} (1 - F) F) = \Sigma_V F. \quad (3.9)$$

Again, the source term on the right hand side accounts for phase change. \mathbf{n}_{int} denotes the unit normal vector of the interface and will be defined below. c_F is a numerical factor which influences the strength of the compression but is always set to unity in this work. A detailed overview on this interface compression approach and the exact implementation of the basic incompressible two-phase solver without phase change `interFoam` is given by Deshpande et al. [18] including some classical validation cases.

It should be noted that the application of the phase change model presented below is not restricted to this treatment of the VOF transport. In the frame of this thesis, the overall model has also been tested utilizing the CICSAM scheme proposed by Ubbink and Issa [109], which is a more advanced algebraic transport scheme derived from the normalized variable diagram (NVD), to discretize the convective term in Eq. (3.7). It has been found to work perfectly together with the rest of the code² but there are still some open issues concerning numerical diffusion directly at the wall in this method.

To properly simulate two-phase flows the effect of surface tension has to be accounted for. The theoretical pressure jump across a curved interface cannot be directly incorporated using a VOF approach, since there is no direct information about the interface. Instead, the Continous Surface Force model (CSF) proposed by Brackbill et al. [9] is utilized. Therein, the surface force due to surface tension is converted into a volumetric force by scaling with the local gradient of the volume fraction field

$$\mathbf{f}_\sigma = \sigma K \nabla F \quad (3.10)$$

making use of the fact that the global volume integral over the gradient is exactly equal to the interfacial area. As suggested by Francois et al. [26], the applied discretization scheme to calculate the gradient of the volume fraction required here is exactly the same as for the pressure gradient within the pressure correction. This is necessary to provide a "balanced-force algorithm" [26], which means that the physical pressure jump was obtained if the curvature was known exactly. However, an accurate calculation of the interfacial curvature is not straight forward and subject to ongoing research, especially for unstructured grids. Errors in calculating the local curvature result in so-called spurious currents which are velocities solely generated by errors in the representation of surface tension forces. A classical way to define the curvature has been given by Brackbill et al. [9]

$$K = \nabla \cdot \frac{\nabla F}{|\nabla F|} \quad (3.11)$$

² The implementation of CICSAM for usage in OpenFOAM has been done by Daniel Deising from the group "Mathematical Modeling and Analysis" of the Center of Smart Interfaces at TU Darmstadt.

which gives a quite rough approximation of the curvature and hence produces comparably large spurious currents. However, especially in non-isothermal two-phase simulations these currents have to be much smaller than the physical velocity. Otherwise they might result in an artificial convective heat transfer towards the interface which can be much larger than the physical one. Therefore, a different approach is used to calculate the curvature here which will be presented in the next section.

3.3 Reconstruction of the interface

Another drawback of using the VOF representation of the two phases is that the exact position of the interface is not known but only a region containing the interface is defined. However, the knowledge of its position is crucial for calculating the temperature gradient required for the phase change model below. Therefore, a proper reconstruction of the interface from the volume fraction field is necessary.

In principle, there are two choices how to reconstruct the interface. First, again the surface reconstructed by the PLIC method could be employed. However, this surface is in general not continuous which results in a not straight forward calculation of the interfacial temperature gradient. Moreover, the utilized interface compression produces an interfacial region smeared out over a few numerical cells. This would result in the definition of the reconstructed interface in a band of cells within this smeared region if a PLIC reconstruction was performed as a post-processing step without utilizing it in the transport of the VOF field.

Instead, the iso-surface of $F = 0.5$ is considered as the interface. The choice of 0.5 is more or less arbitrary but suggests itself. The iso-surface is continuous and is not affected by the smearing of the interface. Moreover, it can be reconstructed independently from the advection scheme employed for the volume fraction field.

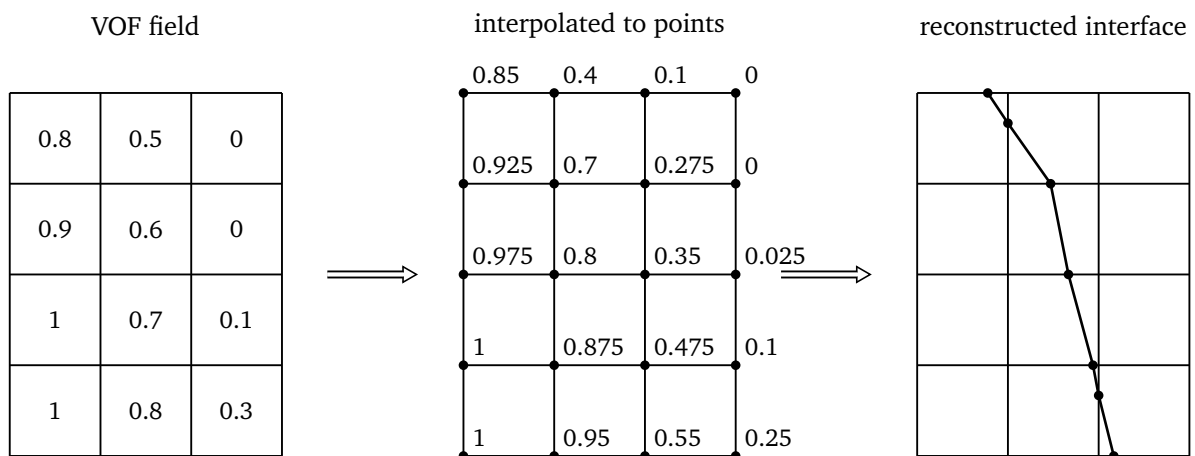


Figure 3.1.: Steps involved in the interface reconstruction algorithm.

The reconstruction is based on the algorithm proposed by Kunkelmann [48, 50] but several improvements have been included. The basic idea is outlined in Fig. 3.1. First of all, the volume fraction field is interpolated to the mesh points. If the sign of $(F - 0.5)$ is different at two points being connected by an edge, this edge is intersected by the iso-surface representing the interface. The exact location of the

intersection is calculated by a linear interpolation along the edge. Finally, all points of intersection are connected to a continuous surface. The individual steps involved in this process will be briefly outlined in the following. Beforehand, a closer look is taken at the wall boundaries.

3.3.1 Correction of boundary values

The volume fraction field lacks of a properly defined boundary condition at walls since the typical definition of the volume fraction only holds for cells and not for faces. This is no problem in terms of the advection of the volume fraction field because the volumetric flux across walls is zero and there is no diffusive term within the transport equation (3.9). However, for defining the position of the contact line one needs to define a suitable ghost value of F at the wall which can be used for the interpolation step.

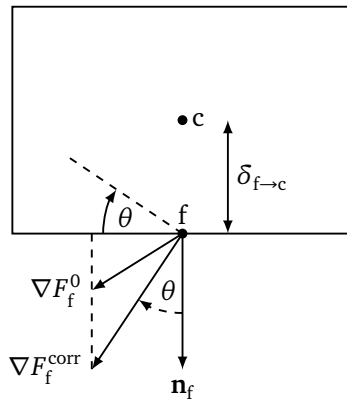


Figure 3.2.: Correction of the interface normal vector at walls.

The gradient of any scalar field in a specific point is orthogonal to its isosurface through this point [10, p. 669]. Therefore, the gradient vector of the volume fraction field at the wall should be oriented relative to the wall with regard to the prescribed contact angle θ . It should be stressed that this demand is not equivalent to setting the slope of the reconstructed interface according to the contact angle in the first cell layer since only the orientation of the gradient directly at the wall is known. To fulfill the requirement, a corrected gradient ∇F_f^{corr} of the volume fraction field is defined as depicted in Fig. 3.2. Its component normal to the wall is depending on the contact angle via

$$\nabla F_f^{\text{corr}} \cdot \mathbf{n}_f = \|\nabla F_f^{\text{corr}}\| \cos \theta, \quad (3.12)$$

where \mathbf{n}_f denotes the unit normal vector of the wall face f . However, the components of the gradient within the wall plane must not be affected by the applied correction since they define the orientation of the contact line. Therefore, a preliminary gradient at the face center ∇F_f^0 is defined to be equal to the cell-centered gradient of the volume fraction field assuming a homogeneous Neumann boundary condition at the wall. To preserve the wall tangential components of the preliminary gradient, the corrected gradient has to satisfy the condition

$$\nabla F_f^{\text{corr}} \times \mathbf{n}_f = \nabla F_f^0 \times \mathbf{n}_f. \quad (3.13)$$

Combining these equations the normal part of the corrected gradient can be determined

$$\nabla F_f^{\text{corr}} \cdot \mathbf{n}_f = \frac{\|\nabla F_f^0 \times \mathbf{n}_f\| \cos \theta}{\sin \theta} \quad (3.14)$$

supposed that $0 < \theta < \pi$. From the known surface normal gradient the value of the volume fraction at the wall can be extrapolated from the given cell value F_c ,

$$F_f = F_c + (\nabla F_f^{\text{corr}} \cdot \mathbf{n}_f) \delta_{f \rightarrow c}. \quad (3.15)$$

It should be noted that this extrapolated value is not bounded to the interval between 0 and 1, especially for small contact angles. However, since the volumetric flux across the wall faces is zero, this value has no effect on the transport of the volume fraction field. Accordingly, the unboundedness of F_f does not cause any problems in terms of mass conservation or the boundedness of the volume fraction field in the numerical cells. In principal the extrapolated value could be bounded, but that would change the position of the reconstructed contact line position. Instead F_f will only be bounded for the calculation of the material properties, Eq. (3.8).

Since these corrected boundary values will be used in the subsequent interpolation of the volume fraction field to the mesh points, the position of the reconstructed contact line depends on the applied correction. Accordingly, also the contact line speed u_{cl} is effected, given by the temporal derivative of the contact line position projected onto the wall tangential component of the interface normal \mathbf{n}_{int}

$$u_{cl} = -\frac{1}{\Delta t} (\mathbf{x}_{cl}^{(i)} - \mathbf{x}_{cl}^{(i-1)}) \cdot \left(\frac{\mathbf{n}_{\text{int}} - (\mathbf{n}_{\text{int}} \cdot \mathbf{n}_f) \mathbf{n}_f}{|\mathbf{n}_{\text{int}} - (\mathbf{n}_{\text{int}} \cdot \mathbf{n}_f) \mathbf{n}_f|} \right) \quad (3.16)$$

where $\mathbf{x}_{cl}^{(i)}$ and $\mathbf{x}_{cl}^{(i-1)}$ are the position vectors of the reconstructed contact line segments at the current and the last time step, respectively. Thereby also the dynamic contact angle is influenced by the applied correction. Because the correction itself is in turn depending on the contact angle via Eq. (3.14), an iteration process is required to solve the non-linear problem. To ensure convergence of the contact line position, the value of the contact angle is under-relaxed during the iterative procedure. The iteration process is stopped as soon as the contact angle changes by less than 0.01 degrees. This criterion is typically fulfilled after 10-30 iterations depending on the grid resolution and the actual contact line speed. Since the iterative correction needs only to be applied at walls, the additional computational effort is acceptable.

3.3.2 Interpolation

As outlined above, an interpolation algorithm from the cell centers to the mesh points is required for the volume fraction. The simplest interpolation method also employed by Kunkelmann [48] is to calculate

the interpolated volume fraction F_p at point p as the weighted average of the volume fractions of all adjacent cells c

$$F_p = \frac{\sum_c w_{p,c} F_c}{\sum_c w_{p,c}} \quad (3.17)$$

where the weights are given by the inverse cell-point distance

$$w_{p,c} = \frac{1}{|\mathbf{x}_c - \mathbf{x}_p|}. \quad (3.18)$$

For the points attached to a wall the face values obtained from the boundary correction discussed above are used rather than the adjacent cell values.

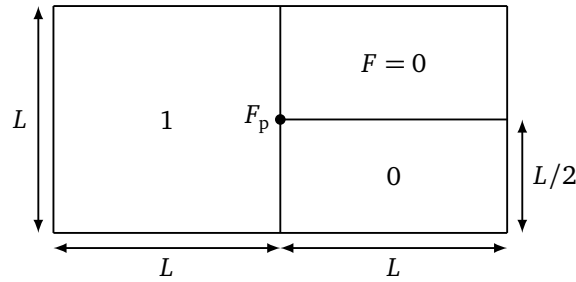


Figure 3.3.: Interpolation of the volume fraction field for an unstructured grid topology.

While the inverse distance weighted interpolation algorithm is very fast and accurate for structured grids, it is not directly applicable to unstructured meshes. Since all adjacent cells are equally weighted, the result of the interpolation might be biased if the number of cells adjacent to a given point is different in two opposite directions. This problem is illustrated for a generic situation in Fig. 3.3. The intuitive solution for the interpolated value at the point p is $F_p = 0.5$ since it is placed right in the middle between the liquid and the vapor phase. The above introduced interpolation method however predicts $F_p = 0.359$ since the information carried by the cells on the right hand side is used twice in the interpolation.

To overcome this problem, an alternative interpolation method is developed utilizing a local tri-linear function fitting procedure. The primitive function

$$F_{\text{fit}}(x, y, z) = a(x - x_p) + b(y - y_p) + c(z - z_p) + d \quad (3.19)$$

is defined locally for each individual mesh point. To determine the coefficients a to d , the volume fractions and cell center locations of all adjacent cells are used. The value of each cell is thereby weighted with the squared inverse distance between the respective cell and the current mesh point. Since the

coordinate system used in the primitive equation is centered at the mesh point, the interpolated volume fraction at point p is given by the offset value

$$F_p = F_{\text{fit}}(x_p, y_p, z_p) = d. \quad (3.20)$$

If the cell positions do not represent a full three-dimensional basis because they are either linear dependent or the stencil size is too small, a local coordinate system is utilized and the dimension of the fitting function is reduced. This situation occurs of course always in a two-dimensional grid, but also at the boundaries of a three-dimensional mesh. In some situations, e.g. at the boundary of a two-dimensional mesh, F_{fit} even reduces to a straight line.

Applying this interpolation method to the situation depicted in Fig. 3.3 results in the expected value of $F_p = 0.5$. The need to calculate the fit at any mesh point at each time step results in a slight computational overhead compared to the inverse distance weighting. Therefore, it is only used if the employed mesh is actually unstructured.

3.3.3 Reconstruction

Given the interpolated values at all mesh points, the actual reconstruction step is following. The reconstruction algorithm is exactly as proposed by Kunkelmann [48, pp. 24–28] based on the geometrical considerations by López and Hernández [55]. The resulting shape of the reconstructed interface segment is presented in Fig. 3.4 for an arbitrary cell shape. Because the resulting polygon is not necessarily completely plane, its center point \mathbf{x}_{int} has to be calculated via a triangulation of the polygon.

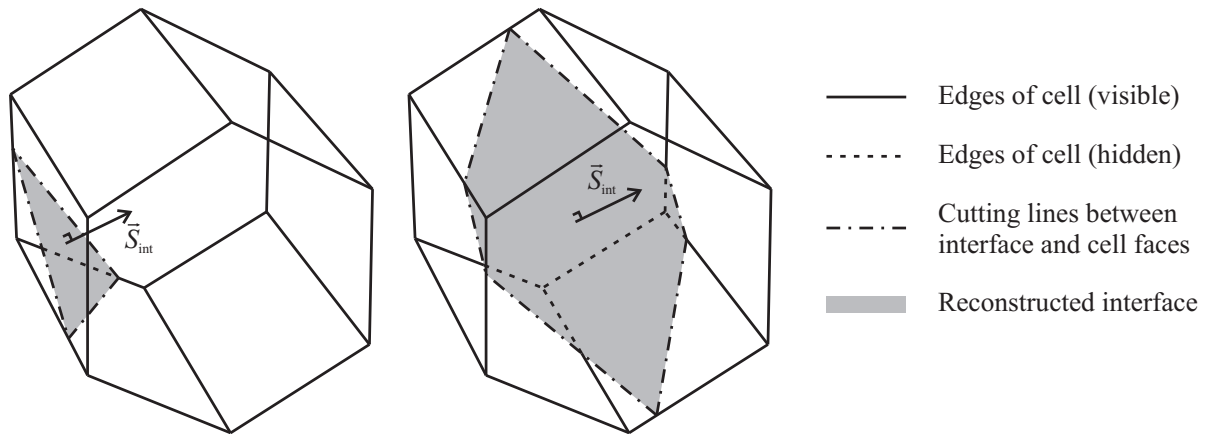


Figure 3.4.: Illustration of the general polygon created by the reconstruction algorithm within a general polyhedral cell [48].

The surface normal vector of the reconstructed interface segment is given by

$$\mathbf{s}_{\text{int}} = \sum_{i=1}^{N_p} \frac{1}{2} (\mathbf{x}_{p,i} \times \mathbf{x}_{p,i+1}) \quad (3.21)$$

where the corner points of the polygon $\mathbf{x}_{p,i}$ have to be ordered clockwise. The surface vector and accordingly also the unit normal vector

$$\mathbf{n}_{\text{int}} = \frac{\mathbf{S}_{\text{int}}}{|\mathbf{S}_{\text{int}}|} \quad (3.22)$$

are pointing from the vapor towards the liquid phase within this work. The surface area of the reconstructed interface is given by

$$S_{\text{int}} = |\mathbf{S}_{\text{int}}|. \quad (3.23)$$

Another important quantity that can be extracted from the reconstruction is the distance from the cell center \mathbf{x}_c to the interface, given by

$$d_{\text{int}} = (\mathbf{x}_c - \mathbf{x}_{\text{int}}) \cdot \mathbf{n}_{\text{int}}, \quad (3.24)$$

being positive on the liquid side of the interface and negative on the vapor side, respectively.

3.3.4 Distance field and curvature calculation

After the reconstruction step the normal vector and interface distance are known in cells intersected by the interface only. However, as will be shown later, these quantities are also required within a narrow band around the actual interface cells. Hence, a distribution algorithm is employed in order to make the geometrical information available in cells next to the interface.

Therefore, the mesh cells are divided into two groups: The donor cells, which already carry the geometrical information required, and the acceptor cells. The normal vector is consecutively passed from the donor cells to all neighboring cells sharing a face with the donor cell. If an acceptor cell receives the normal vector from more than one donor cell, a simple arithmetic averaging is performed. The new normal vector in the acceptor cell is normalized and further distributed to the cell neighbors in the next iteration. Similarly, the distance to the interface is extrapolated towards the acceptor cells. For that purpose, the distance is first calculated at all faces of the donor cell applying Eq. (3.24), substituting the cell center by the position of the face centroid. Within the acceptor cell, the distance between the cell centroid and the face shared with the donor cell projected to the given interface normal direction is then added to the distance value at the face to obtain the interface distance at the cell center. If the distance is defined on more than one face of the donor cell, the minimal absolute interface distance obtained is stored in the acceptor cell.

Finally, as proposed by Kunkelmann [48, pp. 28–30], the distributed normal vectors are used to calculate the interfacial curvature required for the calculation of the surface tension forces \mathbf{f}_σ via

$$K = -\nabla \cdot \mathbf{n}_{\text{int}}. \quad (3.25)$$

The prescribed contact angle at the wall boundary is accounted for by adjusting the boundary values of the interface normal vector at the wall according to the given contact angle as suggested by Brackbill et al. [9]. The resulting curvature is stored in cells inhabiting the interface, only. In order to reduce the spurious currents a median filtering is applied to the curvature field. Finally, the smoothed curvature field is distributed to non-interface cells within a narrow band around the interface and linearly interpolated to the mesh faces to enable its usage in the surface tension force calculation procedure according to Eq. (3.10).

3.4 Modeling of phase change

Within the macro region the influence of dispersion forces on the thermodynamic equilibrium at the interface can be neglected. Moreover, the curvature of the interface on a macroscopic scale is expected to be comparably small. Hence the interface can be assumed to be homogeneously at the saturation temperature corresponding to the system bulk pressure

$$T_{\text{int}} = T_{\text{sat}}(p_0). \quad (3.26)$$

An energy balance at the interface results in

$$m_{\text{evap}} h_{\text{lv}} = q_{\text{l} \rightarrow \text{int}} + q_{\text{v} \rightarrow \text{int}}, \quad (3.27)$$

where $q_{\text{l} \rightarrow \text{int}}$ and $q_{\text{v} \rightarrow \text{int}}$ are the heat fluxes transferred towards the interface from the liquid and vapor phase, respectively, and m_{evap} denotes the evaporating mass flux. If condensation occurs at the interface instead of evaporation, the mass flux becomes negative. Applying Fourier's law, the heat fluxes can be expressed according to the respective temperature gradient at the interface

$$q_{\text{l} \rightarrow \text{int}} = k_{\text{l}} \nabla_{\text{int}, \text{l}} T \quad (3.28)$$

$$q_{\text{v} \rightarrow \text{int}} = k_{\text{v}} \nabla_{\text{int}, \text{v}} T \quad (3.29)$$

which is the full temperature gradient projected onto the direction normal to the interface. The evaporating mass flow within a single grid cell is obtained by multiplying the mass flux with the area of the interface inhabited by the cell

$$\dot{M}_{\text{evap}} = m_{\text{evap}} S_{\text{int}} \quad (3.30)$$

which is known from the iso-surface reconstruction.

Instead of calculating the temperature gradient at the liquid-vapor interface, there are alternative ways given in the literature to determine the evaporation rate within an interface tracking framework. In the group of Dhir the level-set method was employed to simulate the evolution of the free surface. The evaporation was accounted for by setting the temperature in a band of cells with a small absolute value of the level-set function equal to the saturation temperature [95, 96]. However, this procedure appears to be not very accurate and quite grid dependent, but no detailed information on the grid convergence of this method for classical test cases is given in their references. Francois and Shyy [25] employed the immersed boundary method. Therein source terms within the energy equation are defined in such a way that the interfacial temperature corresponds to the given saturation temperature. In this method accounting for complex grid topologies is not straight forward. A very elegant way to determine the evaporation rate is presented by Nikolopoulos et al. [66] and Hardt and Wondra [32]. A relaxation model is employed which relaxes the temperature in the interfacial region towards the saturation temperature. This method is capable of using general grids without the need of modifications but it requires a very fine spatial discretization in the thermal boundary layer around the interface.

The determination of the evaporation rate by evaluating the gradient of the temperature (or of the vapor concentration in case of evaporation into air) is also widely used, e.g. by Strotos et al. [101, 102], Schlottke and Weigand [88], or Kunkelmann and Stephan [50, 51]. While these methods are found to be quite accurate even on a comparably coarse mesh, the implementation of the gradient calculation is rather complex, especially with three-dimensional and unstructured mesh topologies taken into account.

3.4.1 Calculation of the temperature gradient

Even though the definition of the temperature gradient at the interface looks rather simple, its actual calculation is not trivial since it is not possible to use standard differencing schemes to evaluate this gradient. Instead, the gradient on the liquid side of the interface can be approximated via

$$\nabla_{\text{int},l} T = \frac{T_l - T_{\text{sat}}}{d_{l \rightarrow \text{int}}} \quad (3.31)$$

where the assumption of the interface being at saturation temperature has already been used. All considerations in this chapter will be focusing on the calculation of the liquid sided gradient but the calculation for the vapor sided gradient follows analogously.

In order to calculate the temperature gradient as precise as possible, the point at which the liquid temperature T_l is evaluated should of course be located as close as possible to the interface. However, the temperature of the two-phase cell itself cannot be used for this purpose since due to the usage of a one-field approach only the averaged mixture temperature of the two phases is known and no distinct liquid and vapor temperature can be defined. Even if they could be distinguished, e.g. through the usage of a two-field approach as done by Ma [56] for instance, one would have to know the individual centroids of the liquid or the vapor within the cell in order to calculate the distance in the denominator of Eq. (3.31).

This information, however, is completely unavailable in the utilized code as no PLIC reconstruction is performed.

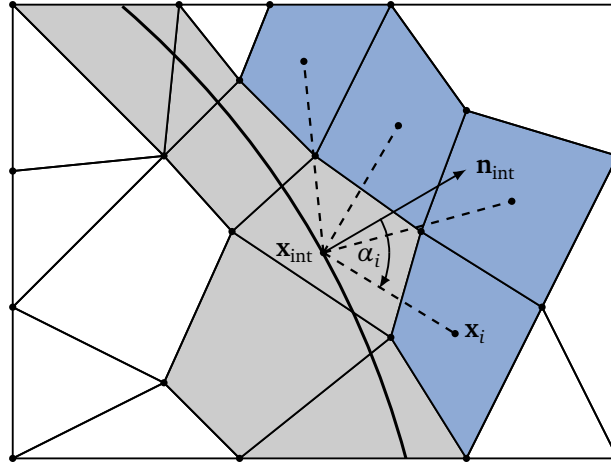


Figure 3.5.: Calculation of the interface normal temperature gradient on an arbitrary mesh.

Instead, the temperature in cells located next to the interface will be used to evaluate the gradient. For the sake of simplicity the basic situation is depicted for an arbitrary two-dimensional mesh in Fig. 3.5 but the methodology presented in this chapter is directly applicable to a three-dimensional configuration. The cells shaded in light grey are the cells inhabiting the reconstructed interface, while the ones shaded in blue are candidates for the definition of T_1 . As candidate cells all cells sharing a mesh point with the current two-phase cell that are not inhabiting a piece of interface itself and being mostly filled with liquid are taken into account. If no such cell exists, which might happen if the interface is strongly curved, the second generation of neighbor cells is used.

Of course, in general there is no candidate cell for which the centroid is exactly lying on the straight line defined by the center of the interface segment and its normal vector. Hence, to evaluate the gradient there are two possibilities. The simplest approach would be to calculate the gradient based on the temperature and distance of the cell, which shows the smallest angle α between the line connecting the cell centroid to the center of the interface segment and the interface normal. A more accurate way of evaluating the gradient is to include the information carried by all candidate cells i ,

$$\nabla_{\text{int},l} T = \sum_i w_i \frac{T_i - T_{\text{sat}}}{d_i} \quad (3.32)$$

but weighting the information from candidate cells lying in the direction of the interface normal more strongly than from cells farer off the normal direction according to

$$w_i = \frac{\cos \alpha_i}{\sum_j \cos \alpha_j} \quad (3.33)$$

where the respective angle is given by

$$\cos \alpha_i = \frac{(\mathbf{x}_i - \mathbf{x}_{\text{int}}) \cdot \mathbf{n}_{\text{int}}}{|\mathbf{x}_i - \mathbf{x}_{\text{int}}|}. \quad (3.34)$$

In general, it would also be possible to fit the temperatures of all candidate cells to a given function of the interface distance, e.g. to a straight line or an error function as proposed by Ma [56, pp. 60–63], and to evaluate the gradient at the interface based on that fit. However, this technique has not been worked out in this thesis since the presented algorithm offers a satisfying accuracy as will be shown below.

3.4.2 Implicit formulation of the gradient

The above presented definition of the temperature gradient, Eq. (3.32), assumes that the temperature T_i of the neighboring cells is known and given. But of course, the temperature in cells close to the interface depends on the actual energy source terms reflecting the evaporative mass transfer. Hence, an iteration process will in general be required to calculate the interfacial gradient if simply the given temperature field from the last solution of the energy equation is used.

A more elegant and at the same time more stable way is to formulate the gradient and thereby the source term implicitly, i.e. based on the unknown temperature field given by the solution of the energy equation. Reminding that after the spatial and temporal discretization utilizing the Finite Volume method the temperature in all cells of the mesh is given by the vector \mathbf{x} given by the solution of the linear system

$$\mathbf{A} \cdot \mathbf{x} = \mathbf{b}, \quad (3.35)$$

an implicit formulation of the source terms can be achieved by a modification of the matrix \mathbf{A} instead of the right-hand side \mathbf{b} . This is possible in this case since the source term is linearly depending on the unknown cell temperature according to Eq. (3.32). According to Fig. 3.5 the source terms in an interface cell depend on the temperature of the neighboring cells. That means that in order to formulate the source term implicitly a manipulation of the off-diagonal elements of \mathbf{A} is necessary linking the information of individual cells to each other. However, as commonly done in Finite Volume codes, in OpenFOAM a sparse matrix structure is implemented in order to limit the memory requirements to store the matrix. Unfortunately in this structure memory is reserved only for off-diagonal elements if the corresponding cells linked by that element are sharing a face. But as can be seen in Fig. 3.5, the temperature gradient is strongly influenced by neighboring cells not sharing a face but only a point with the current interface cell. Therefore, it is not directly possible to formulate Equation (3.32) implicitly in OpenFOAM.

Moreover, there is another problem arising from the fact that the source term in an interface cell is determined based on the temperature of cells not sharing a face with the actual cell. Due to this local decoupling the feed-back of the source term onto the temperature gradient is comparably weak. In other words, a large superheat of the cell next to the interface results in a larger temperature gradient. Accordingly, the temperature in the interfacial cell might fall well below the saturation temperature due

to the strong cooling. However, since there is no direct conductive heat transfer between the two cells if they are not sharing a face, this sub-cooling of the interface does not directly influence the temperature in the liquid cell and hence the cooling rate.

To overcome these two problems originating from the usage of cells only sharing a point with the interface cell to calculate the gradient, the following workaround is employed. Instead of defining the source terms for the energy equation in the interface cells, they are shifted towards the liquid cells. In a Finite Volume discretization it makes actually no difference for the liquid cell whether the energy is transferred towards its neighbor cell by conduction or the same amount energy is directly taken from that cell by a negative source term. Hence, the contributions of the liquid cell i to the temperature gradient of all interface cells j is summed up. The resulting heat flow is then set as the energy source in cell i ,

$$\Sigma_e = -\frac{\dot{Q}_{\text{evap},i}}{V_i} = -\frac{1}{V_i} \sum_j w_{i,j} S_{\text{int},j} \frac{k_l}{d_i} (T_i - T_{\text{sat}}). \quad (3.36)$$

The source term is now depending only on the temperature of the cell i itself and can hence be formulated implicitly by simply adjusting the diagonal terms of \mathbf{A} , while the off-diagonal terms remain unaffected. Due to the shifting of the source term towards the liquid cells, the diffusive heat flux from the liquid cells towards the interface cells has then to be suppressed artificially in order to preserve the energy conservation. The suppression of the diffusive heat flux is equivalent to setting the thermal conductivity of faces adjacent to interface cells to zero. It should be noted that the temperature of the interface cells is changing due to that shifting of the source terms but it is not used to determine the evaporation anyway.

Even though the employed implicit formulation is not completely straight forward, its usage reduces the overall computational effort significantly since no iterative solution algorithm is required. At the same time the stability of the calculation is increased. As will be shown for the validation case employed below, the accuracy is not influenced by the reformulation. In general, the definition of the source term outside the interfacial region would be a problem since the considerations made for the local energy balance do not hold for the local mass balances. Of course it is not advisable to define the volumetric source term reflecting the vapor generation inside the liquid cells since this would cause an additional smearing of the interfacial region. However, within this thesis the volumetric source terms are defined in a slightly different way as will be outlined below.

3.4.3 Distribution of the mass sources

After the source term within the energy equation has been defined, the volumetric source terms within the continuity equation has to be defined accordingly. It might appear that the volume change due to phase change could be expressed by

$$\Sigma_V = \frac{m_{\text{evap}} S_{\text{int}}}{V_c} \left(\frac{1}{\rho_v} - \frac{1}{\rho_l} \right)$$

which has actually been done by many authors in literature.

However, the usage of the presented algebraic VOF method in which the interface is not completely sharp but diffused over several cells prohibits to set the mass sources only in the cells intersected by the reconstructed interface. If the interface is moving due to evaporative phase change, the iso-surface, i.e. the reconstructed interface, will leave a two-phase cell before it is completely filled with liquid or vapor, respectively. Accordingly, as soon as the interface leaves the respective cell, the remaining volume fraction of liquid cannot be further evaporated if no source terms are defined in that cell. This in turn results in an additional smearing of the interfacial region. This problem is even more pronounced if the above introduced implicit formulation is utilized. In addition, the definition of a sink for the liquid volume fraction within a cell almost completely filled with vapor can result in the occurrence of volume fractions smaller than zero.

To overcome these limitations the re-distribution of the mass source terms proposed by Hardt and Wondra [32] is utilized. The basic idea of their method is to separate the extinction of one phase and the re-appearance of the other phase from each other and define the sources outside the interfacial region itself. That means that in case of evaporation liquid mass vanishes close to the interface but within the liquid bulk, while the produced vapor is introduced in the bulk vapor region. The initial distribution of the mass source term is given according to the energy source term

$$\psi_0 = \frac{m_{\text{evap}} S_{\text{int}}}{V_{\text{cell}}}. \quad (3.37)$$

This sharp distribution is smoothed out to a smooth distribution ψ being given by the solution of an inhomogeneous Helmholtz equation

$$\tilde{D} \Delta \psi = \psi - \psi_0 \quad (3.38)$$

which is very similar to a simple diffusion equation. The constant \tilde{D} determines the width of the region over which the source term is smeared out. Numerical experiments yielded that the source terms are distributed over a band of approximately three to four cells, if $\tilde{D} = (4\Delta x)^2$ is chosen. The mass source term is given by

$$\dot{\rho} = [N_v(1 - F)H(F_0 - F) - N_l F H(F_0 - 1 + F)] \psi \quad (3.39)$$

where $H(x)$ denotes the Heaviside function and F_0 is a cutoff value, both defined to ensure that the two regions, where mass sources for the liquid and the vapor phase are defined, do not overlap. The normalization coefficients are chosen to conserve the global mass as

$$\iiint_V \psi_0 dV = N_v \iiint_V (1 - F) H(F_0 - F) \psi dV \quad (3.40)$$

$$= N_l \iiint_V F H(F_0 - 1 + F) \psi dV. \quad (3.41)$$

The resulting volumetric source term within the continuity equation reads then

$$\Sigma_V = \dot{\rho} \left(H(F_0 - F) \frac{1}{\rho_v} - H(F_0 - 1 + F) \frac{1}{\rho_l} \right). \quad (3.42)$$

Moreover, an additional source term in the energy equation is required to compensate for the loss or production of sensible heat according to the removal or generation of mass in the evaporation region

$$\Sigma_{e,sens} = [N_v (1 - F) H(F_0 - F) c_v - N_l F H(F_0 - 1 + F) c_l] \psi T. \quad (3.43)$$

It should be noted that due to the distribution of the mass sources and sinks and due to their separation from each other, the need for a separation of the different velocities within the interfacial region as proposed by Schlotke [87, pp. 21–23] and also employed by Ma [56, pp. 42–47] and Ma and Bothe [57] is avoided in this work.

3.5 Coupling of micro and macro region heat transfer

In contrast to the evaporative heat transfer at the free liquid-vapor interface, the evaporation within the contact line region must not be completely modeled by the above introduced evaporation model but is already known from the micro region model. This known evaporation rate and the resulting wall heat flux have now to be included into the macroscopic model in an appropriate way. The general situation is illustrated in Fig. 3.6. The interface is approaching the wall and hits the wall at a certain position corresponding to the contact line. The actual position of the contact line is known from the interface reconstruction algorithm. A certain portion of the wall face inhabiting the contact line is covered with the liquid film. The correlation for the heat transfer in the micro region developed in Section 2.3.5 only describes the heat transfer for an arbitrary but fixed length ξ_{mic} , while the length of the liquid film b_{cl} is varying during the simulation. However, the total heat flux at the wall face is required as an input to the macroscopic energy equation. Hence, the heat transfer in that transition region between the micro region and the macroscopic meniscus has to be determined.

In Section 2.3.2 the heat conduction within the micro region was found to be two-dimensional if the contact angle is comparably large. Accordingly, also in the transition region the heat conduction might

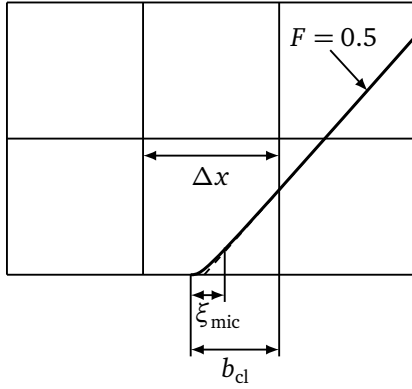


Figure 3.6.: On the origin of the transition region

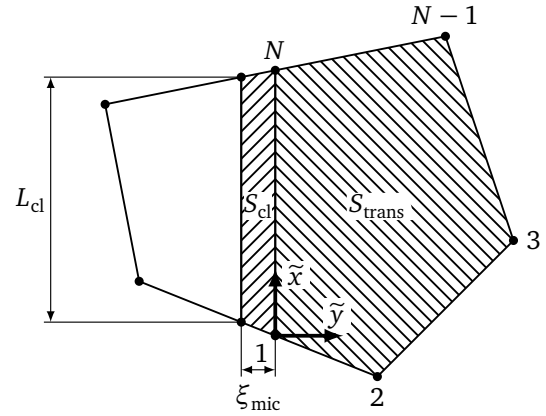


Figure 3.7.: The transition region in an arbitrary mesh

be two-dimensional. However, for the sake of simplicity the heat transfer in the transition region is considered to be governed by one-dimensional heat conduction within this work. The governing equations from the micro region lubrication model are therefore still valid, but can be simplified significantly within the transition region. The effect of dispersion forces and curvature on the thermal equilibrium can be neglected. The wall heat flux is then given by Eq. (2.61) with $p_c/(h_{lv}\rho_l) \ll 1$ as

$$q_w = \frac{T_{w,mic} - T_{sat}}{\frac{\delta}{k_l} + \frac{R_{int}}{\sqrt{1+\delta^2}}}. \quad (3.44)$$

Moreover, since the curvature of the interface is small, the shape of the interface can be assumed to be a plane. The contact line is approximated by linear segments. Therefore the film thickness does not depend on \tilde{x} in the local coordinate system introduced in Fig. 3.7. The slope of the plane corresponds to the macroscopic contact angle θ_{mac} and the offset of the plane is known from the film thickness δ_{mic} at the end of the micro region at $\tilde{y} = 0$. The film thickness within the transition region is hence given by

$$\delta(\tilde{y}) = \delta_{mic} + \tilde{y} \tan \theta_{mac}. \quad (3.45)$$

Substituting Eq. (3.45) into Eq. (3.44) leads to

$$q_w(\tilde{y}) = \frac{a}{\tilde{y} + b} \quad (3.46)$$

where the constants a and b are given by

$$a = \frac{k(T_{w,mic} - T_{sat})}{\tan \theta_{mac}} \quad (3.47)$$

and

$$b = \frac{1}{\tan \theta_{\text{mac}}} \left(\frac{kR_{\text{int}}}{\sqrt{1 + \tan^2 \theta_{\text{mac}}}} + \delta_{\text{mic}} \right). \quad (3.48)$$

The overall heat flow \dot{Q}_{trans} transferred within the transition region can be calculated by integrating the wall heat flux q_w over the entire transition region S_{trans}

$$\dot{Q}_{\text{trans}} = \iint_{S_{\text{trans}}} q_w dS \quad (3.49)$$

which can be rewritten as

$$\dot{Q}_{\text{trans}} = \iint_{S_{\text{trans}}} q_w(\tilde{y}) d\tilde{y}d\tilde{x}. \quad (3.50)$$

As can be seen from Fig. 3.7 the area of the transition region S_{trans} is bounded by piecewise linear segments. Therefore the outer integration over \tilde{x} is split into parts in which the boundary $\tilde{y}(\tilde{x})$ can be expressed as a linear function. This is achieved by splitting the integral at the points p_i of S_{trans}

$$\dot{Q}_{\text{trans}} = \sum_{i=1}^N \int_{\tilde{x}=\tilde{x}_i}^{\tilde{x}_{i+1}} \int_{\tilde{y}=0}^{\tilde{y}^{(i)}(\tilde{x})} q_w(\tilde{y}) d\tilde{y}d\tilde{x}. \quad (3.51)$$

The edge i of the surface connecting the points p_i and p_{i+1} is given by

$$\tilde{y}^{(i)}(\tilde{x}) = c_1^{(i)}\tilde{x} + c_2^{(i)} \quad (3.52)$$

with the two constants

$$c_1^{(i)} = \frac{\tilde{y}_{i+1} - \tilde{y}_i}{\tilde{x}_{i+1} - \tilde{x}_i} \quad (3.53)$$

and

$$c_2^{(i)} = \tilde{y}_i - \frac{\tilde{y}_{i+1} - \tilde{y}_i}{\tilde{x}_{i+1} - \tilde{x}_i} \tilde{x}_i. \quad (3.54)$$

Combining Equations (3.51) and (3.52) one obtains

$$\dot{Q}_{\text{trans}} = \sum_{i=1}^N \int_{\tilde{x}=\tilde{x}_i}^{\tilde{x}_{i+1}} \int_{\tilde{y}=0}^{c_1^{(i)}\tilde{x}+c_2^{(i)}} q_w(\tilde{y}) d\tilde{y}d\tilde{x}. \quad (3.55)$$

The integration along \tilde{y} results in

$$\dot{Q}_{\text{trans}} = \sum_{i=1}^N \int_{\tilde{x}=\tilde{x}_i}^{\tilde{x}_{i+1}} a \left[\ln(\tilde{y} + b) \right]_{\tilde{y}=0}^{c_1^{(i)}\tilde{x}+c_2^{(i)}} d\tilde{x} \quad (3.56)$$

$$= \sum_{i=1}^N \int_{\tilde{x}=\tilde{x}_i}^{\tilde{x}_{i+1}} a \ln \left(\frac{c_1^{(i)}\tilde{x} + c_2^{(i)} + b}{b} \right) d\tilde{x} \quad (3.57)$$

and after the second integration one finally ends up with

$$\begin{aligned} \dot{Q}_{\text{trans}} = \sum_{i=1}^N a \left[\tilde{x}_{i+1} \ln \left(1 + \frac{c_1^{(i)}\tilde{x}_{i+1} + c_2^{(i)}}{b} \right) - \tilde{x}_i \ln \left(1 + \frac{c_1^{(i)}\tilde{x}_i + c_2^{(i)}}{b} \right) \right. \\ \left. + \frac{b + c_2^{(i)}}{c_1^{(i)}} \ln \left(\frac{c_1^{(i)}\tilde{x}_{i+1} + c_2^{(i)} + b}{c_1^{(i)}\tilde{x}_i + c_2^{(i)} + b} \right) - (\tilde{x}_{i+1} - \tilde{x}_i) \right]. \end{aligned} \quad (3.58)$$

This expression cannot be directly evaluated numerically if $c_1^{(i)} = 0$, i.e. if the surface area has a rectangular shape, since the division by zero would result in a floating point exception. In that case the limit of $\dot{Q}_{\text{trans}}^{(i)}$ reads

$$\lim_{c_1^{(i)} \rightarrow 0} \dot{Q}_{\text{trans}}^{(i)} = a (\tilde{x}_{i+1} - \tilde{x}_i) \ln \left(1 + \frac{\tilde{y}_i}{b} \right), \quad (3.59)$$

which is the same expression obtained by Kunkelmann [48] for the consideration of a two-dimensional grid. Within the CFD calculation this expression is used as soon as $|c_1^{(i)}| < 10^{-5}$ due to the limited computational accuracy. This slope corresponds to an inclination of less than 0.0006 degrees.

The wall heat flux at the boundary face inhabiting the contact line is then finally given by

$$q_{w,\text{cl}} = \frac{\dot{Q}_{\text{cl}}L_{\text{cl}} + \dot{Q}_{\text{trans}}}{S_f} \quad (3.60)$$

where the integrated heat flux \dot{Q}_{cl} from the micro region model has to be multiplied with the contact line length L_{cl} to get the total heat flow. The heat transferred to the vapor at the non-wetted fraction of the boundary face is neglected.

3.6 Conjugate heat transfer between fluid and solid

The energy equations in the solid and fluid region are solved independently from each other on individual meshes. Hence, they have to be appropriately coupled through the boundary conditions. The transition condition at the solid-fluid interface is the continuity of heat flux and temperature field. To couple the temperature fields to each other an explicit Dirichlet-Neumann algorithm is employed. On one side of the coupled boundary the temperature is prescribed as a Dirichlet condition. Then the energy equation is solved for this side and the heat flux at the boundary can be calculated. This heat flux is then prescribed as a Neumann boundary condition on the other side of the boundary. After the solution of the energy equation, a new boundary temperature field is given and the boundary condition on the Dirichlet side can be updated. This alternating solution is performed until the temperature change between subsequent iterations is smaller than a certain limit³. It can be shown that this algorithm is more stable if the Neumann boundary condition is prescribed in the domain of higher thermal conductivity [116]. Therefore, the heat flux will be specified at the boundary of the solid domain while the temperature is prescribed on the fluid side. By ensuring that the energy equation on the solid side is solved at the end of the iteration procedure, the global energy conservation can be guaranteed.

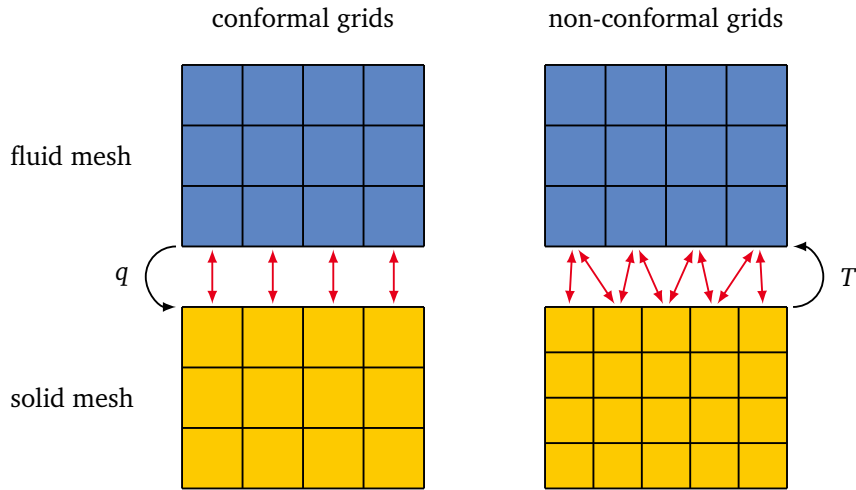


Figure 3.8.: Mapping procedure involved in the fluid-solid coupling.

In addition, the heat flux transferred at the contact line has to be accounted for within this procedure. The heat flux at the fluid boundary is given by

$$q_{w,f} = \begin{cases} q_{w,cl} & \text{at the contact line} \\ k_{f,w} (\nabla T_f \cdot \mathbf{n}_w) & \text{elsewhere} \end{cases} \quad (3.61)$$

³ In this work a threshold value of 10^{-4} K is used.

with \mathbf{n}_w being the outwards pointing unit normal vector of the wall boundary face and $k_{f,w}$ is the thermal conductivity of the fluid at the wall. It is assumed that the heat flow in the contact line region is completely consumed by evaporation. Hence, the thermal conductivity of the fluid at the wall is set to zero at the contact line to prevent the transfer of sensible heat. Instead, the evaporation rate corresponding to the contact line heat flow is directly added to the mass source ψ_0 defined in Eq. (3.37).

The exchange of boundary conditions between the two domains incorporates a mapping procedure. As can be seen in Fig. 3.8, the complexity of the mapping depends on the conformity of the mesh. If the discretization of the boundary is identical on both sides of the boundary the information can be directly mapped between the domains. On the contrary, if the discretization is unequal, an interpolation of the quantities is required. To maintain the global and local energy conservation in this case, a conservative mapping procedure based on a local Galerkin projection [21] is employed. An implementation of this arbitrary mesh interpolation technique (AMI) has already been available in OpenFOAM. Nevertheless, whenever possible a conformal discretization of the boundary meshes is aimed for within this work.

3.7 Acceleration techniques

In order to perform the rather complex simulation of a drop impingement, several acceleration techniques can be employed either reducing the overall computational effort or reducing the calculation time via parallelization of the simulation.

3.7.1 Adaptive time step

For an instationary simulation, a temporal discretization has to be performed. Throughout this thesis a one-step method is employed for the time integration. While for the momentum and energy equation the implicit Euler scheme is used, the volume fraction equation is solved explicitly. It is obvious that the overall computational time decreases if the time step of the simulation is increased. However, to ensure stability of the explicit solution method for the volume fraction, the Courant number⁴

$$Co = \frac{|\mathbf{u}| \Delta t}{\Delta x} \quad (3.62)$$

based on the local values of velocity and grid size has to be smaller than unity within the entire domain at any time instant. This convective time step limit is required since the volume fraction cannot be transported through the mesh further than one cell within a single time step when an explicit integration scheme is utilized. Throughout this thesis, the time step is adjusted such that $Co \leq 0.1$ holds for all simulations. In addition, if surface tension effects are important, the capillary limit introduced by Brackbill et al. [9]

$$\frac{2 \sqrt{\frac{\sigma \pi}{\rho_l + \rho_v}} \Delta t}{\Delta x^{1.5}} \leq 1 \quad (3.63)$$

⁴ also known as the Courant-Friedrichs-Lewy (CFL) number

has to be accounted for in order to be able to capture the development and propagation of capillary waves. If the fluid properties are constant, the maximal time step satisfying this constraint is a function of the minimal mesh resolution only. For FC-72 the maximal acceptable time step is 10^{-6} s (3.5×10^{-7} s) for a grid resolution of $4 \mu\text{m}$ ($2 \mu\text{m}$). On the contrary, the diffusion number

$$D = \frac{2\alpha\Delta t}{\Delta x^2} \quad (3.64)$$

where α denotes the diffusion coefficient of any convection-diffusion equation, has not to be maintained smaller than unity since the volume fraction equation has no diffusive term and the implicit Euler scheme is employed for time integration of the other balance equations, which is not suffering from large time steps in terms of stability. Nevertheless, D is always smaller than unity since the above shown capillary time step limit is much more restrictive for the fluid and all meshes used in this work.

While the capillary time step limit is fixed for a given fluid and mesh resolution, the convective time step limit is depending on the solution. Hence, an adaption of the time step can be performed during the simulation based on the current flow field. The final time step is given by the largest possible step size ensuring stability as

$$\Delta t = \min \left(\frac{0.1}{u} \Delta x, \frac{1}{2} \sqrt{\frac{\rho_l + \rho_v}{\pi\sigma}} \Delta x^{1.5} \right). \quad (3.65)$$

3.7.2 Dynamic mesh refinement

The accuracy of the flow solver and in particular of the evaporation model is strongly depending on a sufficient spatial resolution of the field gradients. Therefore a fine resolution is required near the liquid-vapor interface as well as at the solid-liquid boundary where the temperature and velocity gradients are expected to be very steep. In the bulk vapor domain far away from the droplet the mesh can be kept much coarser without any loss of accuracy. However, since the droplet and thereby the interfaces are moving through the domain during the computational run, it is not possible to adequately define the region of interest where a fine mesh is needed a priori at the instant of mesh generation. On the other hand, using a high mesh resolution in the complete region where the interface might eventually pass through during the computation or even in the entire domain will result in a massive computational overhead, especially in case of a three-dimensional simulation.

Instead, an adaptive mesh refinement procedure (AMR) readily provided by OpenFOAM is employed to maintain the overall number of computational cells as small as possible, while ensuring a sufficient spatial resolution where actually required. For that purpose a coarse base mesh is created. Based on an indicator function the cells that need to be refined are selected. Within this work, the distance to the interface is used as the indicator function which is already known from the iso-surface reconstruction introduced above. If a cell is closer to the interface than a certain threshold value, it is selected to be refined. During the refinement process, any cell is split into eight daughter cells as illustrated in

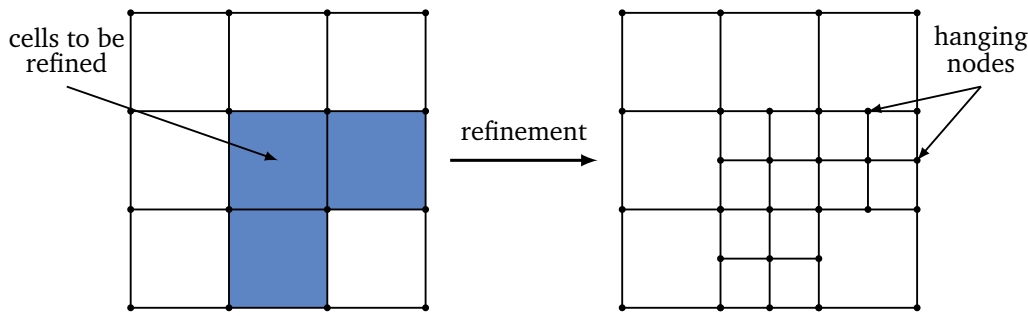


Figure 3.9.: Illustration of the adaptive mesh refinement procedure. For the sake of better visibility the refinement of a two-dimensional grid is shown although the employed algorithm is applied to three-dimensional grids only.

Fig. 3.9. This splitting algorithm is exclusively applicable to three-dimensional hexahedral cells but these hexahedra are allowed to be non-orthogonal as well. The information about the connectivity of cells originating from the same parent is stored enabling a coarsening of the mesh at a later time instant to recover the original coarse base mesh when the region of interest has moved. As can be noticed from Fig. 3.9 the non-conformal splitting of cells produces so-called hanging nodes at the transition from the refined to the original mesh. Consequently, the mesh quality is comparably poor in terms of orthogonality and skewness at this transition. Therefore, one has to take care that this transition is placed far enough from the location of the steep gradients at the interface, i.e. the threshold value must be chosen sufficiently large. In the solid domain the grid adaption is simply following the refinement of the fluid domain since there the distance function is not defined. Thereby a conformal meshing of the coupled boundary patches is preserved. It is also possible to consecutively perform multiple levels of refinement thus increasing the adaptivity of the mesh. Subsequently to the modification of the mesh, the field data have to be mapped to the new mesh. For cell values this is done in a conservative way. However, the volumetric flux field stored on the cell faces cannot be directly mapped and hence it is mandatory to perform another pressure correction step before resuming the solution algorithm.

The additional computational effort introduced by the need for a partial re-calculation of the mesh is far outweighed by the speed-up in the solution of the linear equation sets gained through the reduction of degrees of freedom.

3.7.3 Parallelization and load balancing

The ongoing trend of parallelization in computer industry and the development of multi-core processors makes it essential that numerical calculations can be carried out in parallel in order to efficiently make use of the computational resources. The strategy of parallelization most frequently used for flow simulations is the grid partitioning technique. The idea behind this strategy is to split the overall computational domain into smaller parts and simultaneously conduct the algebraic operations for these subdomains on different processors or cores. Of course the individual subdomains have to be coupled to each other. For that purpose a communication between the processes is necessary. In OpenFOAM this communication is based on sending and receiving of messages between the individual processors (Message Passing Interface, MPI). The advantage of this way of communication is its flexibility. Utilizing MPI it is also

possible to use processors on different machines as necessary for running calculations on the Lichtenberg high performance cluster without any modifications. General information about parallelization and considerations on the efficiency are given e.g. by Schäfer [86, pp. 295–306].

The aim of parallelization is to speed-up the overall computation. Therefore, the additional computational costs arising from the need of communication have to be outweighed by the reduction of floating point operations per processor. Since the processes are not independent from each other, the overall speed of the computation will be limited by the slowest processor. The major part of calculations is linked to the solution of the linear systems produced by the discretization procedure. The computational time required for solution of the system mainly depends on the number of unknowns. Hence, to equally load the individual processors, the number of cells per subdomain should be approximately the same. This is of course not a new finding and attention is payed to an equal distribution of cells to processors in any CFD software including OpenFOAM. However, this becomes in particular important when combining parallelization and adaptive meshes.

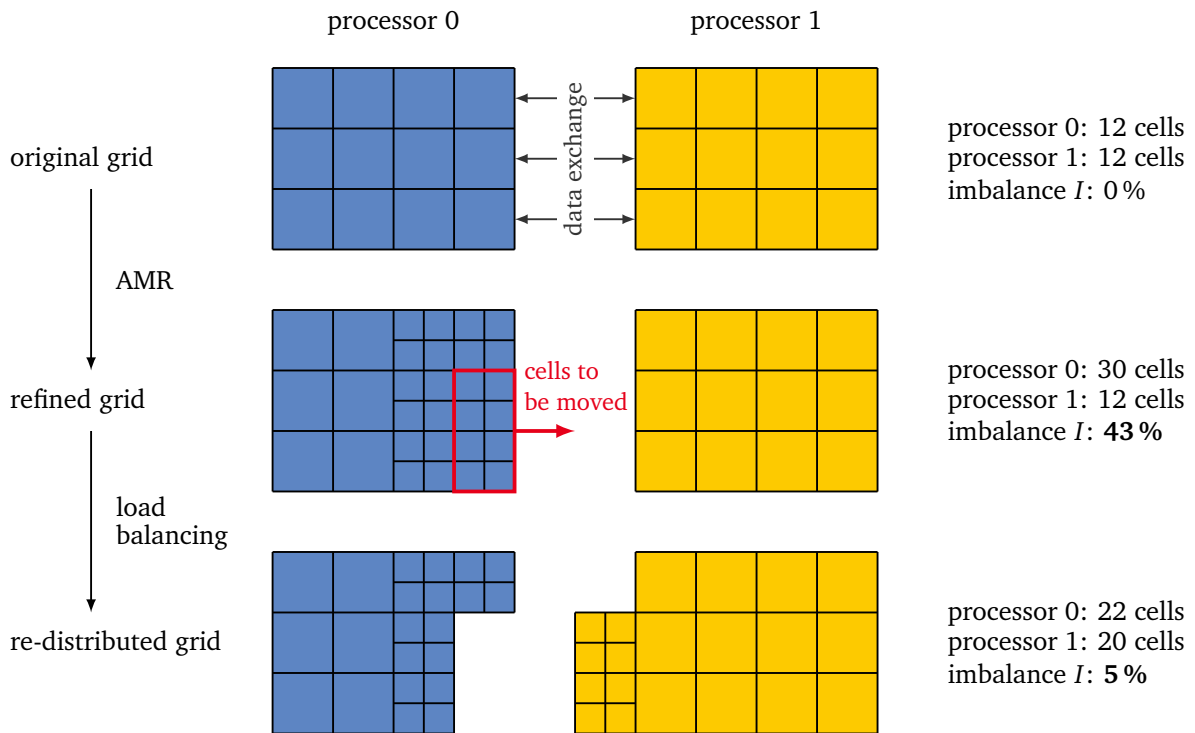


Figure 3.10.: Illustration of the load balancing procedure in a parallel computation with AMR.

As illustrated in Fig. 3.10, the number of cells per subdomain changes during the run time due to the adaptive mesh refinement and thereby the relative load of the processors gets worse. To preserve an acceptable performance, a load balancing algorithm is necessary. In the frame of this work, an "on the fly" redistribution of the mesh has been implemented. The idea is to pause the simulation as soon as the imbalance between the processors

$$I = \max \left(\frac{|N_{c,i} - N_{c,avg}|}{N_{c,avg}} \right), \quad (3.66)$$

where $N_{c,i}$ is the number of cells on processor i and $N_{c,avg}$ is the average cell number per processor, exceeds a certain limit, which is set to 10 % within this thesis. Then a new distribution of the cells to subdomains is calculated. Thereby one has to make sure that cells originating from the same parent in the coarse base grid do not get distributed to different processors to enable a coarsening of these cells at a later time step. For this purpose a new decomposition method has been implemented into OpenFOAM. Cells having the same parent are combined to clusters which are then distributed as a whole. If now a cell is assigned to a different processor than it is currently assigned to, this cell is moved to the neighboring processor and integrated into the existing mesh there as illustrated in the bottom part of Fig. 3.10. Finally, the field data stored in the cells that have been moved must be mapped to the new target processor as well. The algorithm for the shift of cells between subdomains has already been provided by OpenFOAM, while a customization has been necessary to properly transfer the information required by the AMR engine⁵.

The fact that this on-the-fly distribution works in parallel is crucial to the usage of an adaptive mesh in large parallel calculations like the ones on droplet coalescence that will be presented at the end of the next chapter. Beforehand an offline redistribution algorithm was employed consisting of stopping the simulation, rebuilding a single mesh out of the subdomains, calculating a new distribution, distributing the mesh, and restarting the simulation. This procedure included several hard disk operations to read and write the mesh or field data and therefore became very slow when the total cell number was getting large. In contrast, the new procedure basically scales with the number of cells per processor instead of scaling with the total cell number. To give an example, the offline redistribution of a grid consisting of 6.7 million cells decomposed to 16 processors takes approximately 16 minutes while the new algorithm does the same job in parallel in less than 12 seconds.

3.8 Model overview

An overview over the entire solution algorithm as implemented into OpenFOAM is presented in Fig. 3.11. Even though the reconstruction of the interface and the evaporation model are taking the major part of the illustration, the fraction of computational time consumed by these parts is comparably small. In fact, more than 50 % of the overall computational time for one time step are required to solve the pressure correction. Hence, this step is the bottleneck for the overall computations.

The actual implementation is making use of the object oriented programming representing the basic idea behind OpenFOAM. As such, the overall interface reconstruction for example is put into a separate library. This results on the one hand in a very clear arrangement of the source code since the entire reconstruction procedure is condensed to one single line in the source code of the top-level solver. On the other hand this enables the exchange of separate model parts with other projects in the framework of cooperations.

Besides the results presented in the frame of this thesis, the developed numerical model has also been used and validated in additional studies on drop impingement in the Leidenfrost regime [17] and flow boiling in micro channels [73].

⁵ Here, I would like to thank Daniel Deising from the group "Mathematical Modeling and Analysis" of the Center of Smart Interfaces at TU Darmstadt for the fruitful discussions.

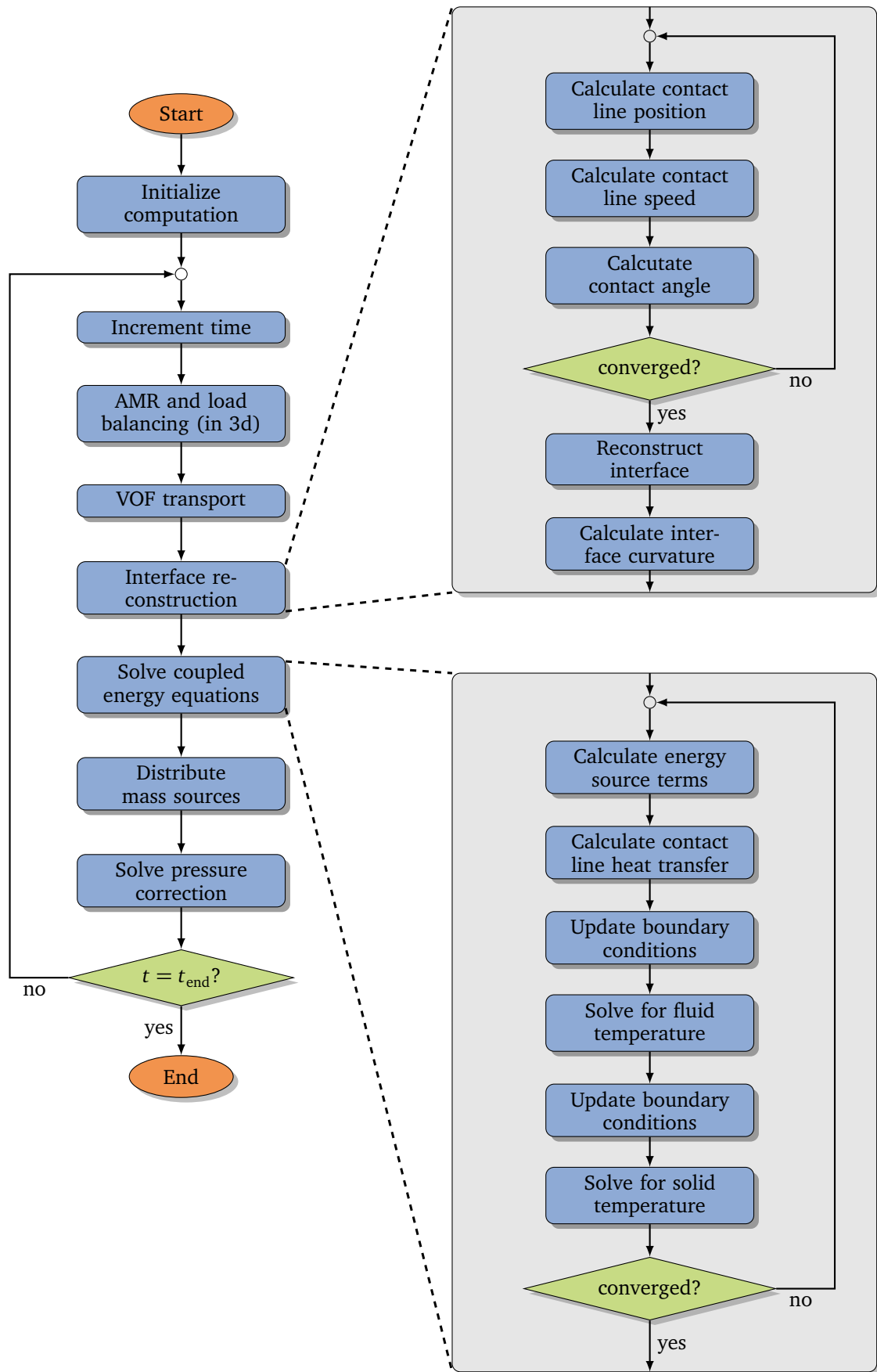


Figure 3.11.: Solution algorithm for the overall macroscopic model.

3.9 Validation studies

Before the overall model is applied to the final simulation of drop impingement the most relevant model parts, namely the evaporation model and the treatment of the contact line, need to be validated separately. The validation of the full model will be performed based on the computation of single drop impingement and comparison to experimental data in Section 4.1.3.

3.9.1 Evaporation model

For validation of the evaporation model, the growth of a small vapor bubble within an infinitely extended superheated liquid pool is employed. For the heat transfer controlled stage of the growth process, Scriven [91] has worked out an analytical solution. In principle, the growth of the bubble is influenced by inertial and surface tension forces during the very initial stage of the growth [75] because these forces influence the thermodynamic equilibrium at the liquid-vapor interface according to Eq. (2.33). When the vapor bubble grows, the effect of inertial and surface tension forces on the thermal equilibrium decreases and the growth rate is controlled by heat diffusion from the bulk towards the interface only. However, since the effect of inertial and capillary forces on the equilibrium is ignored in both, the simulation and the analytical solution, they can be directly compared to each other over the full range of bubble radius.

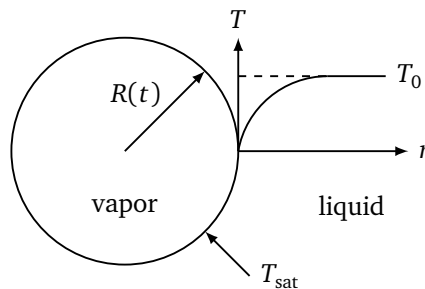


Figure 3.12.: Sketch of the validation case for the evaporation model

The analytical solution starts with $R = 0$ and a homogeneously superheated liquid phase at the initial time instant $t = 0$. This temperature step results in an infinite growth rate of the infinitesimal small bubble at the start time which cannot be reflected by the numerical model. Instead, the simulation is started at $t_0 > 0$ with $R_0 > 0$. To ensure that the simulation and the reference solution are comparable, the temperature profile around the bubble is initialized according to the analytical solution. The initial temperature profile around a bubble within a pool of liquid FC-72 with a superheat of 10 K at the time instant $t_0 = 0.1$ ms after its nucleation is shown in Fig. 3.13.

Since the validation problem configuration is spherically symmetric it can be solved in one, two, or three dimensions enabling to judge the ability of the model to predict multidimensional evaporation processes.

First, the grid dependency of the model is checked in the one-dimensional configuration. As usually done in OpenFOAM, the model is not formulated separately in spherical coordinates but the discretization is always based on three-dimensional cartesian coordinates. Instead, the calculation domain is chosen as a

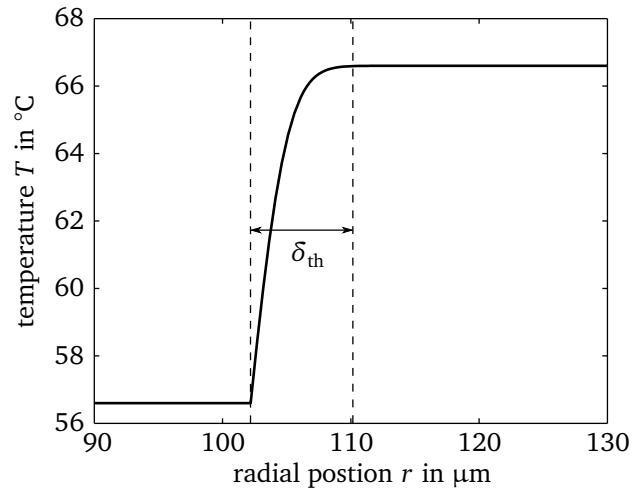


Figure 3.13.: Initial temperature profile for the test case at $t_0 = 0.1$ ms. The initial thermal boundary layer thickness is $\delta_{th} \approx 8 \mu\text{m}$.

single cell row according to one piece of the actual geometry employing symmetry conditions. To reflect a part of a sphere, the shape of the overall mesh has the shape of a pyramid with a square base where the apex corresponds to the origin of the coordinate system at $r = 0$.

In Fig. 3.14 the temporal evolution of the bubble radius is presented for three different meshes with a spatial resolution of $1 \mu\text{m}$, $2 \mu\text{m}$, and $4 \mu\text{m}$. While on the fine and the medium mesh the bubble growth is in a good agreement to the analytical solution, the deviation is comparably large for the coarse mesh. However, as shown in Fig. 3.13 the thermal boundary layer is initially only about $8 \mu\text{m}$ wide, which corresponds to the width of only two numerical cells. Due to the missing ability to capture the initial temperature field properly, it is clear that the numerically predicted growth rate cannot follow the analytical solution accurately. The results shown in the figure have been obtained utilizing the implicit formulation of the evaporation rate. However, no difference can be detected between the usage of the implicit or explicit formulation in terms of the growth rate. In contrast the numerical effort is of course larger if the explicit model is used. A difference between the model formulations can be detected in the temperature of the cells intersected by the interface. However, this temperature is not of further interest in the simulation.

In order to evaluate the actual performance of the presented model, it is compared to the predictions obtained utilizing the evaporation model proposed by Hardt and Wondra [32]. This model is a very elegant relaxation model which is quite easy to implement for arbitrary mesh shapes in three dimensions. The growth rate predicted by that model is also given in Fig. 3.14. Even though the finest mesh was used, the growth rate is far overestimated. Accordingly, a much finer spatial discretization would be required to accurately capture the bubble growth with Hardt's model at the given liquid superheat whereas the resolution of the medium mesh turns out to be sufficient to predict the growth rate with the model developed in this thesis.

In addition to the one-dimensional tests, the validation problem is solved on an axisymmetric domain. Besides a structured mesh with a spatial resolution of $2 \mu\text{m}$, an unstructured mesh is utilized allowing the quantification of the impact of the grid quality. The unstructured mesh consists of quads only and

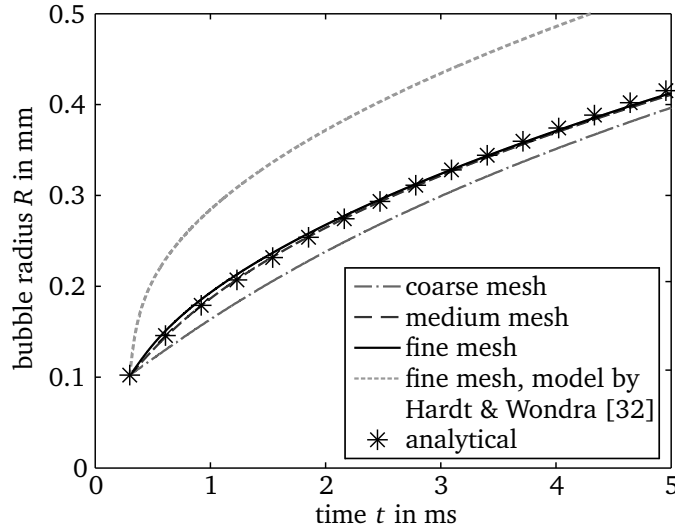


Figure 3.14.: Growth of a vapor bubble in the spherically symmetric case.

has been created utilizing the commercial grid generation tool ICEM CFD from ANSYS. The average grid size approximately matches to the one of the structured mesh but is slightly varying in space as can be recognized from Fig. 3.15.

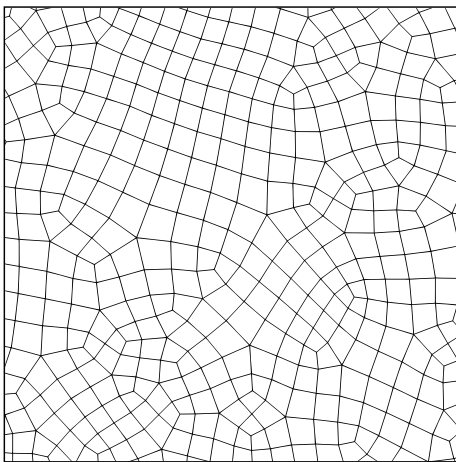


Figure 3.15.: Detail of the unstructured mesh. The section shown here measures $40 \times 40 (\mu\text{m})^2$.

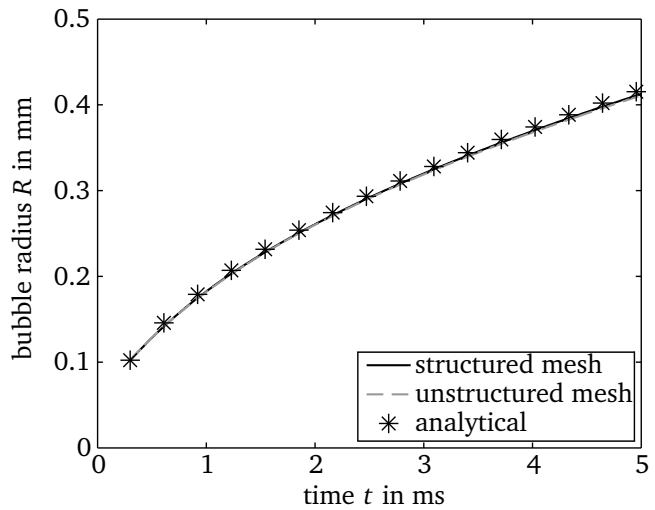


Figure 3.16.: Bubble growth in the axisymmetric case. The grid size is approximately $2 \mu\text{m}$ for both meshes.

As can be seen in Fig. 3.16, almost no difference can be detected between the bubble growth on the two grids. This indicates that the gradient calculation procedure presented in Section 3.4.1 is able to accurately evaluate the interfacial temperature gradient even on non-orthogonal meshes.

Moreover, the isotropy of the evaporation model, i.e. the affinity of the bubble to grow along a certain direction (e.g. along the coordinate axis), is very small. The maximal error in the sphericity

$$\Psi = \max \left(\frac{|R - R_{\text{mean}}|}{R_{\text{mean}}} \right) \quad (3.67)$$

is about 0.68 % for both meshes at the end of the simulation, which is approximately corresponding to the grid resolution. It should be stressed that in this test the surface tension forces were neglected and hence there is no force present that drives the bubble towards a spherical shape during its growth. Instead, the initial spherical shape is preserved only if the calculation of the volumetric source term is homogeneous.

Finally, the three-dimensional simulation of bubble growth is carried out. To keep the computational effort small, only one eighth of the bubble is simulated making use of the symmetry planes. In Fig. 3.17 a comparison between the evolution of the bubble radius in one, two and three dimensions is given. Only minor differences can be detected. The smaller growth rate in the three-dimensional case might be attributed to a smaller effective grid resolution. The direction of the temperature gradient is diagonal to the mesh for cells lying off the axes of the coordinate system. Accordingly the thermal boundary layer is on average captured by less numerical cells in the three-dimensional case resulting in a smaller growth rate.

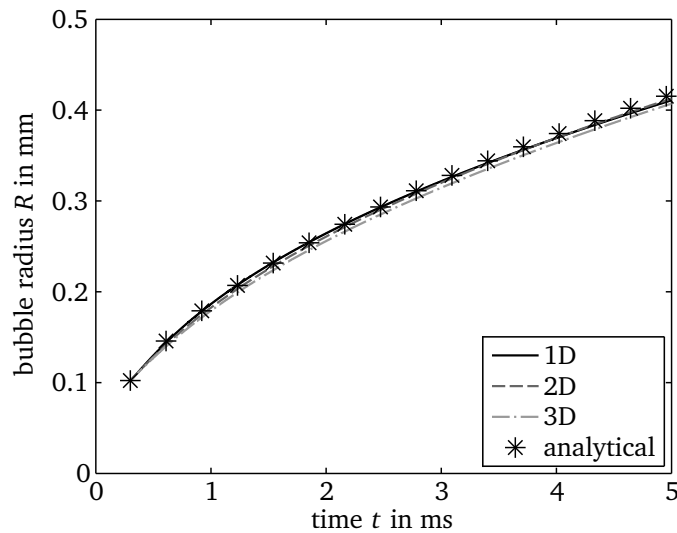


Figure 3.17.: Comparison of the bubble growth in multiple dimensions. The grid size is $2 \mu\text{m}$ in all cases.

In addition the growth of the three-dimensional bubble is calculated on a coarse mesh with a basic resolution of $8 \mu\text{m}$ utilizing two levels of grid refinement in a band of $50 \mu\text{m}$ around the liquid-vapor interface. While the overall number of cells is reduced by more than one order of magnitude through the usage of the AMR, no significant differences are present in the growth rate.

3.9.2 Contact line evaporation

As discussed above, the overall evaporation model including contact line evaporation cannot be directly validated due to the lack of accurate experimental data on the scale of the micro region. However, the coupling procedure between the microscopic and macroscopic heat transfer can be checked by a comparison to the calculations of a single evaporator groove done by Stephan and Busse [100]. They used the same type of micro region modeling but used a highly resolved, boundary fitted Finite Elements simulation for the macroscopic heat transfer. Hence, these simulations can be used as a benchmark for

the presented coupling model. The comparison of the results rather gives a verification of the model than a real validation.

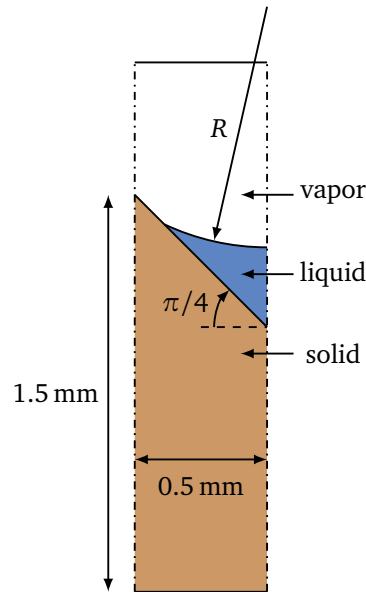


Figure 3.18.: Sketch of the validation case for contact line evaporation.

The problem configuration is sketched in Fig. 3.18. A two dimensional groove of aluminum is partially filled with liquid ammonia. The interface separating the liquid from the pure vapor atmosphere has a curvature of $K = 1100 \text{ 1/m}$. The thermal properties of ammonia and aluminum are given in the appendix. The bottom wall is $\Delta T = 1.31 \text{ K}$ superheated against the liquid saturation temperature and the macroscopic contact angle is fixed to $\theta_{\text{mac}} = 19.7$ degrees.

Since the internal flow within the liquid phase was not accounted for by Stephan and Busse, only the coupled steady-state energy equations are solved for by the presented model to obtain comparable results. The shape of the liquid-vapor interface has been initialized as a circular arc, taking into account the geometrical constraints. The utilized physical properties of aluminum and ammonia are given in the appendix in Table A.3 and Table A.4, respectively.

A comparison of the obtained heat flux at the bottom wall with the results by Stephan and Busse is given in Table 3.1. The deviations between the predictions and the reference solution are extremely small, especially when compared to the remaining uncertainty in the reference solution which is characterized by an error in the global energy balance of about 3% [98, pp. 72, 120–122]. The simulation results do not show a clear convergence when the mesh is refined. However, the overall small deviations suggest that the results are already converged for the fine meshes. Moreover, a mesh independent solution cannot be found, since the usage of a multiscale approach limits the minimal cell size to the size of the micro region.

In addition, the influence of the boundary correction introduced in Section 3.3.1 for the determination of the contact line position is quantified in Table 3.1. If the correction is neglected, the size of the transition region is underestimated and accordingly the global heat flux is smaller. Even though there is

Δx in μm	with correction		without correction	
	q_w in W/m^2	$(q_w - q_{\text{ref}})/q_{\text{ref}}$	q_w in W/m^2	$(q_w - q_{\text{ref}})/q_{\text{ref}}$
10	30.3847	1.28 %	29.7576	-0.81 %
5	30.2541	0.85 %	29.5532	-1.49 %
2.5	30.0592	0.20 %	28.8936	-3.69 %
1.25	30.2055	0.69 %	29.5254	-1.58 %
Reference [100]	30.0	-	30.0	-

Table 3.1.: Results of the validation case

no tremendous change in the heat flux, an avoidable error is introduced when neglecting the boundary correction.



Results and discussion

In this chapter the results of the simulations on drop impingement will be presented. First, the basic hydrodynamic behavior of an impinging drop and the dominating heat transfer phenomena are analyzed. For the purpose of validation of the overall model, the simulation results are compared to experimental data. Afterwards the most important impact parameters are identified and their influence on the heat transfer is quantified. Finally, the simultaneous impingement of two droplets is calculated and their interaction is studied.

Unless noted otherwise, all results are obtained utilizing the fluid properties of FC-72 at a saturation pressure of 1 bar as given in the appendix, Table A.1.

4.1 Single drop impingement

Before the actual simulation results will be discussed, the experimental setup providing data for the validation of the numerical model is described briefly. Subsequently, the numerical setup is presented. The hydrodynamic behavior of the droplet and the global heat transfer performance from the numerics are compared to the experimental data and the sensitivity of the outcome on individual parts of the model will be investigated.

4.1.1 Reference experiment

The setup of the reference experiment is depicted in Fig. 4.1. It has been briefly described earlier in [23] and [34] and further information on the underlying measurement principle can be found in the thesis of Sebastian Fischer [22] who conducted the experiments at the Institute of Technical Thermodynamics at TU Darmstadt.

The test cell consists of a closed chamber which is completely filled with vapor of FC-72. Residual air has been removed from the chamber prior to the experimental run. A small, slightly subcooled needle is placed inside the test cell. Due to the subcooling, liquid condenses there and forms a small pending droplet. As soon as it exceeds a certain volume, it falls off the needle due to gravity. The droplet then

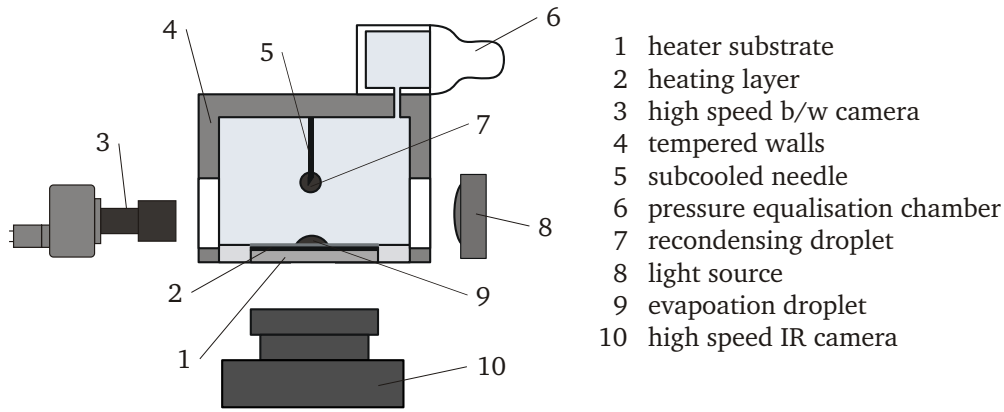


Figure 4.1.: Sketch of the experimental setup [34].

falls through the vapor and impinges on the heater. While the droplet size is more or less fixed for a given fluid and needle geometry, its velocity can be tuned by changing the vertical position of the needle tip. A black and white camera is used to observe the falling droplet from the side, enabling the determination of its size and velocity directly before it impacts the surface.

The utilized heater consists of a 2 mm thick infrared transparent calcium fluoride glass (CaF_2) with lateral dimensions of 20×22 mm. This calcium fluoride block is coated with two thin layers. The first layer consists of chromium nitride to provide a sufficient emissivity for measuring the temperature of this layer with an infrared camera arranged underneath the glass substrate. The second layer, which is the surface actually in contact to the fluid, is made of pure chromium. This layer is exposed to an electric current and acts a Joule heater, thus providing a heat source at the top of the heater. Both layers are manufactured via a sputtering process and their thickness measures about 400 nm, each. According to the very small thickness and the small resulting thermal inertia and resistance, the measured temperature is assumed to be very close to the actual temperature of the solid-fluid boundary. From the measured temperature field the boundary heat flux can be calculated. Therefore, the transient three-dimensional heat conduction within the glass substrate is numerically simulated in OpenFOAM. The computational domain corresponds to the relevant interrogation window of the heater where the droplet is expected to hit the wall. The measured temperature field is used as a transient boundary condition at the coated boundary of the glass. Assuming the other boundaries of the heater to be adiabatic, a transient, two-dimensional heat flux field at the boundary between the glass and the chromium nitride layer is obtained from the simulation. Neglecting heat conduction within the two individual layers, the heat flux at the solid-fluid interface can be obtained by superposing the calculated heat flux and the input heat flux from the chromium layer. Further details on the heater design and the postprocessing procedure are given in [22] and [24].

Unfortunately, the input heat flux is not known exactly. Small variations in the sputtering process result in a varying layer thickness and morphology of the chromium layer influencing its electrical resistance. Moreover, the assumption of adiabatic boundaries in the heat flux calculation procedure is questionable. However, the effect of the thermal losses and the input heat flux on the calculated heat flux at the solid-fluid boundary is not distinguishable. Hence, both effects can be combined to an effective input heat flux. This effective heat flux can be determined from a consideration of the total heat flow at the boundary. In

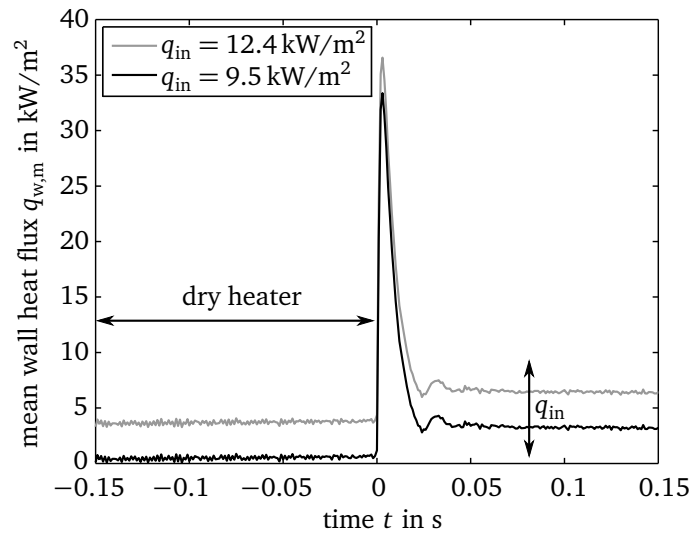


Figure 4.2.: Determination of the effective input heat flux for scenario B (see Table 4.1).

Fig. 4.2 the mean heat flux at the heater surface is shown for two different values of the effective input heat flux q_{in} . The droplet impinges the surface at $t = 0$. At this time the heat flux suddenly increases due to the interaction of the droplet with the wall. After reaching a maximum the heat flux decreases because of the diminishing dynamics of the impingement. For $t > 50$ ms a sessile droplet is sitting on the surface corresponding to a rather constant heat flux which is slightly larger than the one observed prior to the impact. This characteristic evolution of the heat flux will be investigated in more detail below.

It should be noted that before the droplet hits the surface, i.e. at $t < 0$, the entire heater is in contact with the vapor phase. Since heat transfer is solely driven by natural convection in the vapor phase, in this situation a small heat transfer rate can be expected at the solid-vapor interface while the major fraction of the input heat flux results in a transient heat-up of the heater substrate. If however the input heat flux is taken as 12.7 kW/m^2 as it has been estimated from the measured electrical current through the heating layer and its estimated electrical resistance, a nonphysically strong heat transfer from the solid to the vapor is observed. Therefore, the effective input heat flux is chosen such that the heat flow to the vapor at the time of a dry heater surface is close to zero. It should be stressed that the choice of the input heat flux only shifts the profile to larger or smaller values while its shape is not influenced.

Besides the heat transfer rate the hydrodynamic behavior of the droplet is of interest. In particular the transient contact line radius is a relevant quantity frequently used to characterize the impingement process. In principle, the black and white camera could be used to evaluate the position of the contact line. However, it has been shown that a more precise determination of the contact line radius can be achieved with the aid of the calculated heat flux profile. Since the contact line is assumed to be at the location of the maximal heat transfer rate, its position can be determined from the given heat flux field. The utilized algorithm is described by Fischer [22].

From the available experimental data two scenarios are selected to serve as validation cases for the numerical model. The relevant boundary conditions of these scenarios are listed in Table 4.1. Due to the drop generation procedure, the droplet size is similar in both cases while the impact velocity as well as the initial wall superheat are quite different.

property	symbol	scenario A	scenario B
droplet size	D_0	1.02 mm	0.977 mm
impact velocity	u_0	0.262 m/s	0.584 m/s
impact Reynolds number	Re	955	2040
impact Weber number	We	13.7	65.3
Bond number	Bo	0.5	0.46
initial wall superheat	ΔT_w	12.7 K	17.4 K
input heat flux	q_{in}	4000 W/m ²	9500 W/m ²

Table 4.1.: Validation cases.

4.1.2 Numerical setup

In the experiments no three-dimensional effects breaking the symmetry during the impingement process have been observed. Consequently, the numerical simulations can be carried out making use of the axial symmetry of the problem.

Mesh and boundary conditions

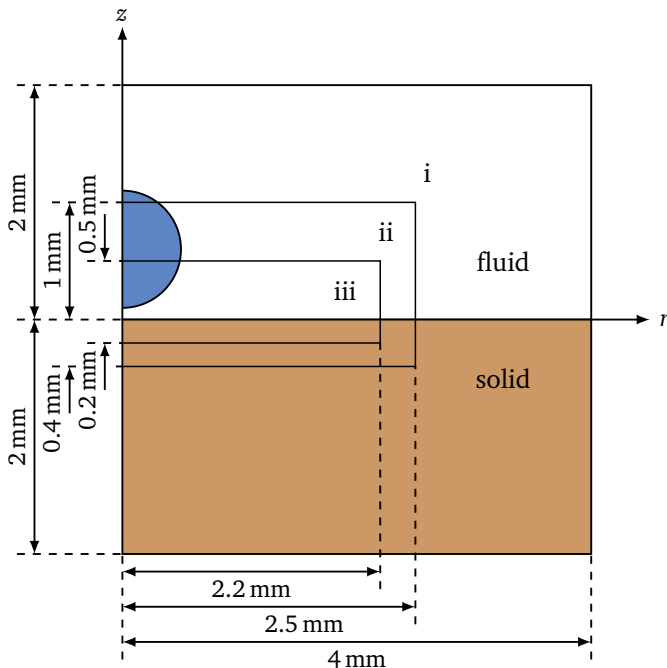


Figure 4.3.: Structure of the mesh used for the validation scenarios.

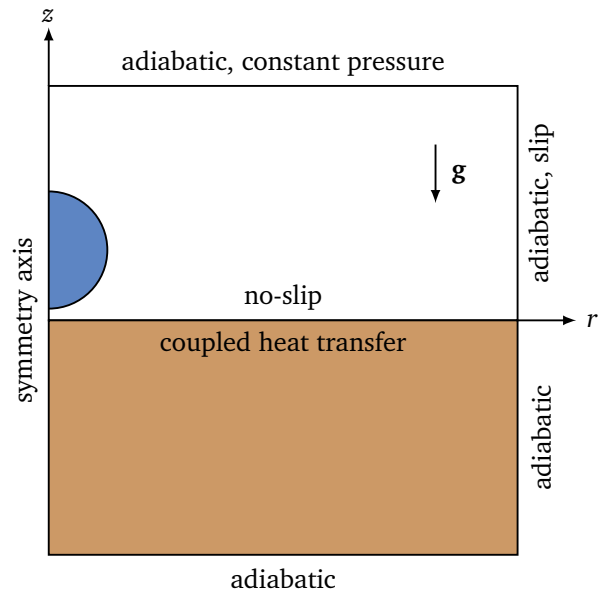


Figure 4.4.: Boundary conditions for the solid and fluid region.

A sketch of the computational domain is given in Fig. 4.3. A size of the bounding box of the fluid domain of about $4D_0 \times 2D_0$ has been found sufficiently large to eliminate boundary effects. The solid and fluid domain are meshed individually but always such that the discretization of the coupled boundary is conformal (c.f. section 3.6). For the base mesh a Cartesian discretization is chosen. To be able to quantify

the grid dependency of the obtained results, meshes with a different spatial resolution are required. This higher resolution is however only necessary in that region in which the major part of heat transfer is expected to take place, i.e. where the droplet will be present. To preserve a reasonable total number of cells the resolution is exclusively increased in regions (ii) and (iii) as indicated in Fig. 4.3 by splitting the cells of the base grid in both, the r - and the z -direction. Thereby hanging nodes are produced at the borders of the respective regions identical to the situation emerging from the usage of the adaptive mesh refinement algorithm. The local grid size of the meshes used for the simulation of the validation scenarios is given in Table 4.2 where the coarse mesh corresponds to the Cartesian base grid.

According to the vanishing thickness of the coatings on the solid heater substrate used in the experiments, the heat storage in as well as the thermal conduction through these layers are completely ignored in the simulation. Instead, the heat generation in the upmost layer is accounted for as a constant offset in the heat flux at the boundary of the solid and fluid domain, respectively. The other boundary conditions applied to the computational domain are presented in Fig. 4.4.

	region	coarse mesh	medium mesh	fine mesh
grid size Δx	i	8 μm	8 μm	8 μm
	ii	8 μm	4 μm	4 μm
	iii	8 μm	4 μm	2 μm
cell number N_c	fluid	125,000	242,375	448,625
	solid	125,000	171,950	254,450

Table 4.2.: Properties of the meshes used for the validation cases.

Initial conditions

Above the heater surface a thermal boundary layer is present. The actual temperature profile is not known from the experiment and has to be estimated. Before the droplet impacts the surface, it is completely dry. The dominant mechanism of heat transfer is assumed to be natural convection in the vapor phase. The Nusselt number for laminar natural convection over a horizontal plate can be calculated via [111, pp. 668–669]

$$\text{Nu} = 0.766 \left(\text{Ra} \left[1 + \left(\frac{0.322}{\text{Pr}_v} \right)^{11/20} \right]^{-20/11} \right)^{1/5} \quad (4.1)$$

where the Rayleigh number is given by

$$\text{Ra} = \frac{(T_w - T_\infty) g L_0^3}{T_\infty \nu_v^2} \text{Pr}_v. \quad (4.2)$$

The characteristic length scale is given by the ratio of the area of the heated surface to its circumference to $L_0 = 5.238$ mm. The corresponding heat transfer coefficient h can be calculated from the definition of the Nusselt number

$$\text{Nu} = \frac{hL_0}{k_v}. \quad (4.3)$$

The thickness of the thermal boundary layer can finally be estimated via

$$\delta_{\text{th}} \approx \frac{k_v}{h} \quad (4.4)$$

to approximately $\delta_{\text{th,A}} = 0.7934$ mm and $\delta_{\text{th,B}} = 0.745$ mm for scenario A and B, respectively. The initial temperature profile in the vapor phase is approximated through an exponential function as

$$T(z) = T_{\text{sat}} + \Delta T_w \exp\left(-\frac{y}{\delta_{\text{th}}}\right). \quad (4.5)$$

This thermal boundary layer will however be considerably deformed when the droplet falls through it. In order to account for this deformation as well as the deformation of the droplet itself and the wake it produces, a pre-simulation is conducted. In this simulation the droplet is initialized spherically at a position of 3.6 mm above the heated surface. Its temperature is assumed to be homogeneous and equal to the saturation temperature. The initial thermal boundary layer in the vapor phase is prescribed according to the estimation made above and the wall temperature is kept constant. The initial velocity of the droplet is chosen such that the droplet approximately accelerates due to gravity to the given droplet velocity in the respective scenario. The vapor is quiescent in the beginning. While the droplet falls towards the solid surface, it slightly deforms and a weak internal flow is building up. Moreover, the thermal boundary layer is deformed and a wake is produced behind the falling droplet. To prevent a shrinking of the drop due to evaporation, no mass sources are calculated within the pre-simulation. In

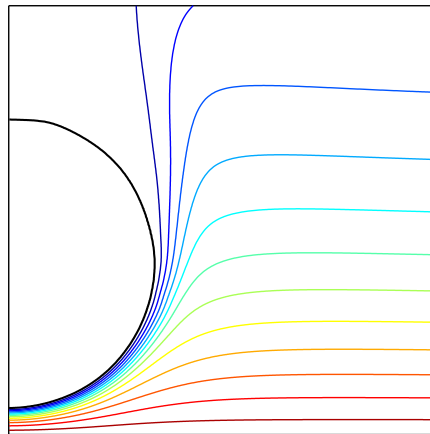


Figure 4.5.: Initial droplet shape and vapor isotherms for scenario A.
The spacing between the isotherms is $\Delta T = 1$ K.

contrast, the energy source term is accounted for to obtain a reasonable temperature field, i.e. to keep the liquid-vapor interface at saturation temperature. As soon as the droplet's center of gravity reaches the position of $z = 0.6$ mm above the wall the simulation is stopped and the result is mapped to the actual computational domain serving as initial condition for the full simulation. The obtained velocity field is scaled to obtain the given mean velocity of the droplet since it slightly deviates from the given value at the end of the pre-simulation. The droplet shape and the temperature field obtained from the pre-simulation for scenario A are depicted in Fig. 4.5.

4.1.3 Basic phenomena and validation

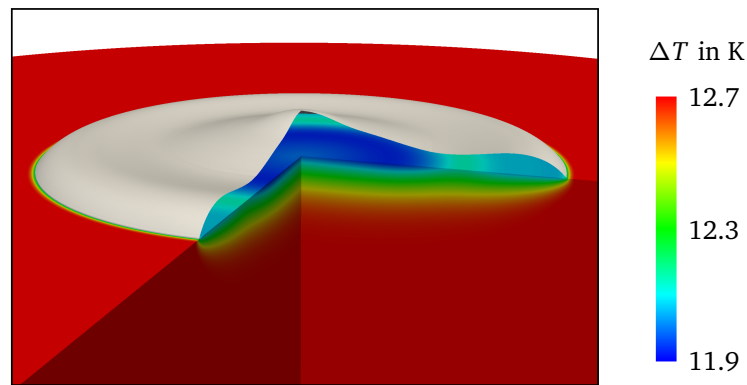


Figure 4.6.: Computed droplet shape and superheat inside the solid heater during the reference scenario A at $t = 4$ ms after the initial contact (three-dimensional representation of two-dimensional results).

For the description of the general phenomena occurring during drop impingement the two reference scenarios A and B are chosen. A snapshot of the simulation result for scenario A is shown in Fig. 4.6. A local cooling of the wall underneath the droplet can be observed. Before, however, the heat transfer is described in detail, first the hydrodynamic behavior of an impinging droplet is characterized. It is self-evident that the heat transfer cannot be predicted reliably unless the hydrodynamics of the drop is reflected properly. Parts of the principal findings presented here have been published earlier [34], but will be described in more details here.

Droplet hydrodynamics

As sketched in Fig. 4.7, the overall impingement process can be subdivided into three phases. When the droplet hits the solid wall, it carries a certain inertia. Accordingly the liquid flows radially outwards along the wall away from the stagnation point. Thereby the radius of the contact line R_{cl} , defining the outer limit of the wetted region, increases. During this stage, which is commonly referred to as the *spreading phase* (I), the kinetic energy of the liquid is gradually dissipated or converted to surface energy stored in the additional liquid-vapor interface being created. When the kinetic energy is completely consumed, the contact line radius reaches its maximum and afterwards the contact line contracts due to the action of surface tension forces. The droplet develops towards its equilibrium shape roughly represented by a

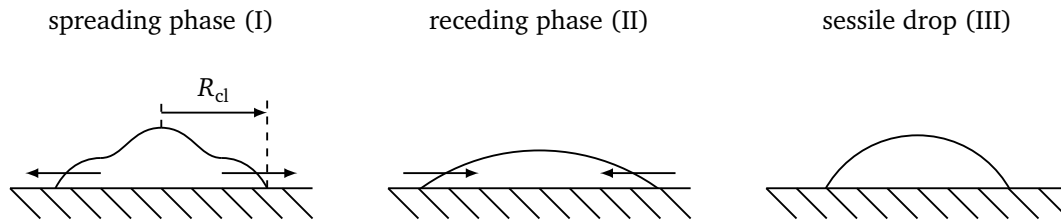


Figure 4.7.: Phases of the impingement process.

truncated sphere if the influence of gravity is small corresponding to a small Bond number. Since during this *receding phase* (II) again a considerable part of the surface energy is converted back to kinetic energy, the contact line contracts further than to its equilibrium shape and its radius reaches a local minimum. Finally, the droplet might show residual oscillations until the situation of an evaporating *sessile drop* is achieved (phase III).

The computed shape of the impinging droplet for scenario A is depicted in Fig. 4.8 at different time instants during the spreading and receding phase. The creation of a small rim at the outer boundary of the wetted region can be observed at the end of the spreading while a comparably thin liquid film is covering the wall near the center of the splat (curves no. 4 and 5), commonly referred to as lamella. When the droplet contracts during the receding phase, the liquid film near the center of the drop becomes very thin but no rupture of the film is observed.

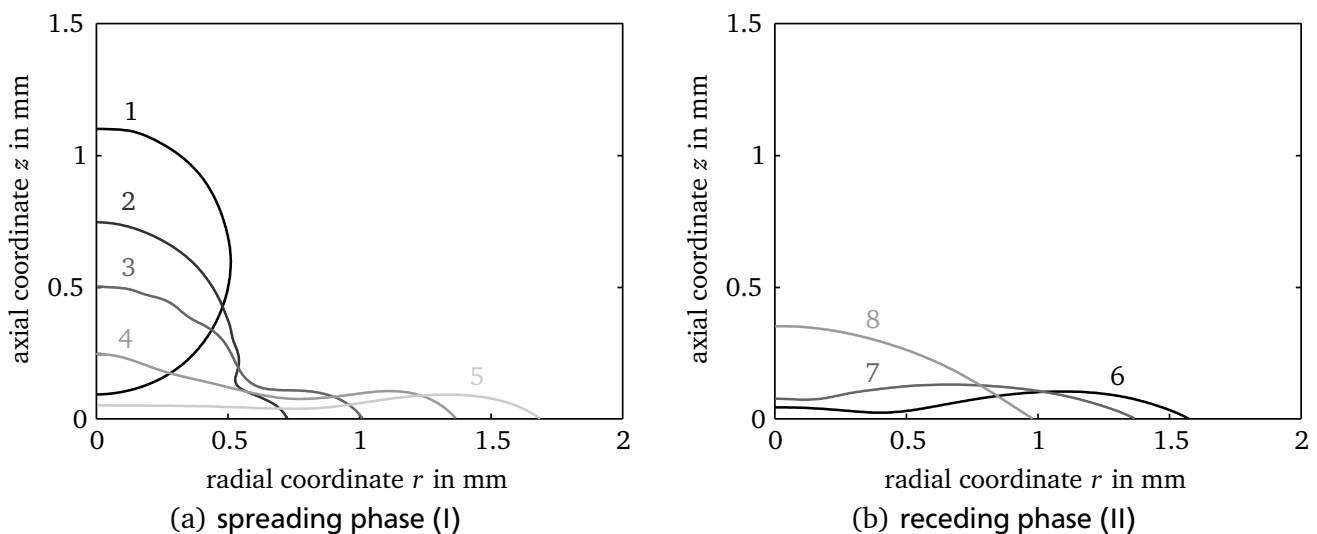


Figure 4.8.: Evolution of the droplet shape for scenario A; 1: initial shape, 2: $t = 1$ ms after impact, 3: $t = 2$ ms, 4: $t = 4$ ms, 5: $t = 8.6$ ms (instance of maximal spreading), 6: $t = 15$ ms, 7: $t = 20$ ms, 8: $t = 28.6$ ms (end of receding phase).

The computed shapes cannot be quantitatively compared to the pictures obtained during the experiments with the help of the black and white camera since only the projection of the full droplet shape to the r, z -plane is recorded. Nevertheless, a qualitative evaluation is of course possible. In Fig. 4.9 the image from the black and white camera is shown for scenario A about 2 ms after the initial contact of the droplet to the wall. In agreement to the computed shape (curve no. 3 in Fig. 4.8) capillary waves can be observed traveling along the droplet. Another indication of a reasonable description of the hydrodynamics is

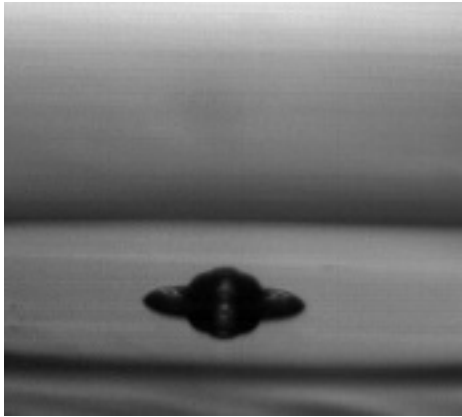


Figure 4.9.: Shadowgraphy image of the impinging droplet for scenario A at $t = 2$ ms after the impact.

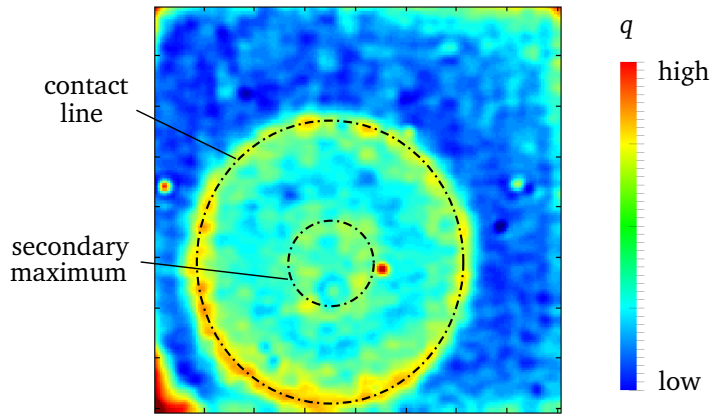


Figure 4.10.: Local wall heat flux for scenario A from the experiments at $t = 15$ ms. This time instant corresponds to curve no. 6 in Fig. 4.8.

found during the receding phase. In Fig. 4.10 the local heat flux at the solid-fluid interface obtained from the post-processing of the experimental data is shown. In addition to the ring shaped heat flux peak corresponding to the position of the contact line a smaller but visible secondary circular maximum is observed inside the impinging droplet. The origin of this maximum is not straightforward to explain directly from the measurements themselves. However, precisely at the same time instant the computed droplet shape (curve no. 6 in Fig. 4.8) shows a local minimum in film thickness at approximately the same radial position. The low thermal resistance of the thin liquid film between the superheated wall and the liquid-vapor interface at this position offers an explanation for the maximum in the measured heat flux.

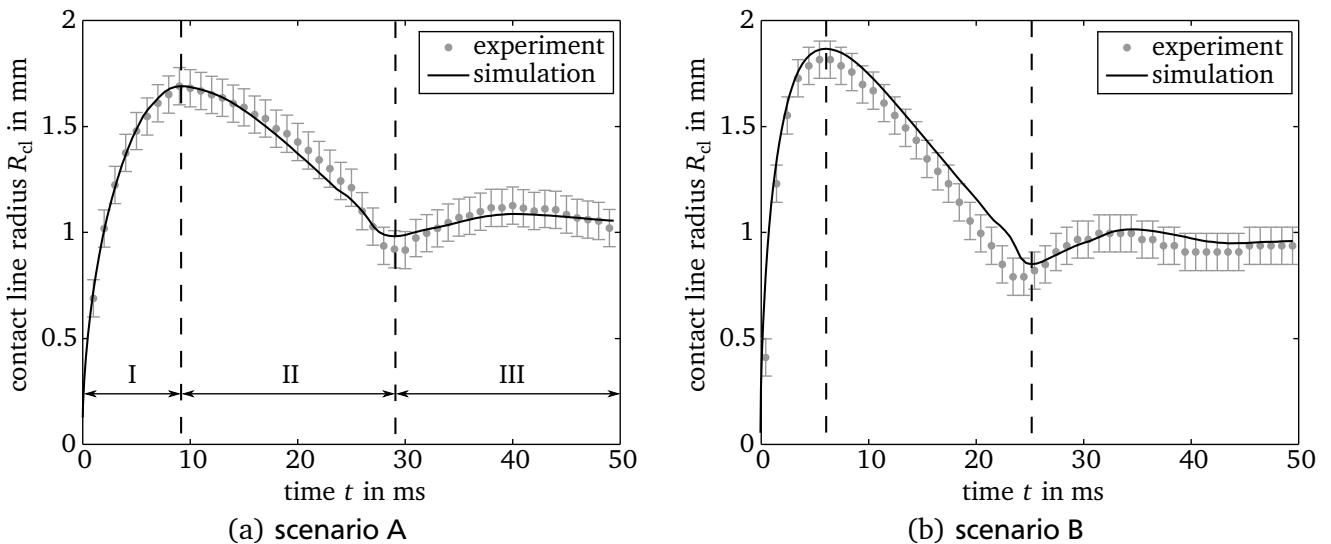


Figure 4.11.: Temporal evolution of the contact line radius.

In contrast to the recorded drop shapes, the transient contact line radius obtained from the measured heat flux profiles provides the opportunity to perform also a quantitative inspection of the numerical results. The evolution of the contact line radius for the scenarios A and B is presented in Fig. 4.11. For both scenarios a very good agreement between simulations and experiments is observed. In phase I the

contact line radius increases roughly with $t^{1/2}$ as proposed in the literature (see e.g. [121]). While the maximum spreading radius is in perfect agreement slight deviations are visible at the end of the receding phase (II). In the experiment the droplet rather tends to over-contract more strongly at this instant and accordingly the residual oscillations of the drop in phase III are more pronounced. The equilibrium shape of the droplet, which is mainly determined by the static contact angle, is again reproduced precisely. As will be shown later, the hydrodynamic characteristics in the receding phase are also dominated by the wetting characteristics. Keeping in mind that the prediction model of the static and dynamic contact angle includes only one adjustable parameter used to match the experimental conditions, i.e. the condensation coefficient f as stated in section 2.3.4 and set to $f = 0.5$ throughout this thesis, the hydrodynamic behavior of the droplet is predicted very accurately over a wide range of conditions.

All results shown in this section have been obtained with the medium mesh. Altogether, only insignificant differences can be observed between the calculations on the three presented meshes. Even though no clear convergence trend can be recognized, the maximal spreading radius differs by less than 1% between the coarse and the fine mesh. At the end of phase II a slightly larger difference of about 2% is present which is anyhow still very small. Hence the presented results can be considered as virtually grid independent.

It should be noted that except for the simulation of scenario A on the coarse mesh the simulation shows the formation of a small vapor rest underneath the impinging droplet. The entrapment of gas during the impingement process has also been observed experimentally e.g. by Chandra and Avedisian [13]. The general way of how this bubble gets entrapped is quite clear. When the droplet approaches the wall, the pressure in the gas phase near the stagnation point at the center of the droplet gets higher than in the surrounding atmosphere. Accordingly the droplet is deformed by this increased pressure and a small dimple is developing at the front of the moving drop. When the droplet then hits the wall, the contact line is formed at the edge of that dimple separating the gas phase outside and inside the wetted region; a small amount of gas is entrapped. However, the formation of a gas bubble is not always observed and the exact conditions to be fulfilled for gas entrapment are not yet understood. Nevertheless, in all data available from the reference experiment described above entrapment was never observed. Even though the optical resolution might be insufficient to resolve the initial bubble itself, it would have surely been visible in the heat flux fields due to the existence of an additional contact line inside the droplet.

A possible explanation of the absence of the vapor entrapment might be given considering the liquid-vapor thermodynamics. Liu et al. [54] have shown that the gas might be considerably compressed at the instant of entrapment. If the compression was so strong that the absolute pressure in the vapor exceeded the vapor pressure corresponding to the wall temperature, the vapor would condense and thereby disappear. However, the pressure increase estimated by Liu et al. seems to be not sufficient to cause this effect for the combination of wall superheat and impact speed in both reference scenarios.

Nevertheless, since the formation of a small vapor bubble in the impact region has not been observed in the reference experiment, its prediction by the model is considered as a numerical artifact. Therefore it is artificially removed during the simulation whenever it is created. Otherwise the additional contact line and interfacial area being created would substantially influence the global heat transfer impeding the comparability of the heat transfer from the simulation to the experiment.

Even though the experimental setup introduced above provides spatially resolved data on the heat transfer at the solid-fluid interface (compare Fig. 4.10), a comparison of the local heat flux to the numerical results is difficult. As will be shown below, a considerable part of the total heat transfer is taking place in the direct vicinity of the apparent three-phase contact line, i.e. in a region with a width of about one micron. In contrast, the optical resolution of the infrared camera providing the local temperature field is approximately 30 micron and hence the measurement is not at all able to resolve this small scale. Moreover, to attenuate the noise of the camera an additional spatial smoothing of the recorded temperature field is necessary prior to the heat flux evaluation procedure. Due to the applied spatial averaging of the local temperature field by both, the camera and the additional smoothing, the obtained heat flux is spatially smoothed out, too, as investigated in detail by Sielaff [92, pp. 52–57] for thin foil heaters. Accordingly, even if the numerical model would be perfectly able to predict the real temperature field at the wall, the resulting heat flux field would strongly differ from the measured one.

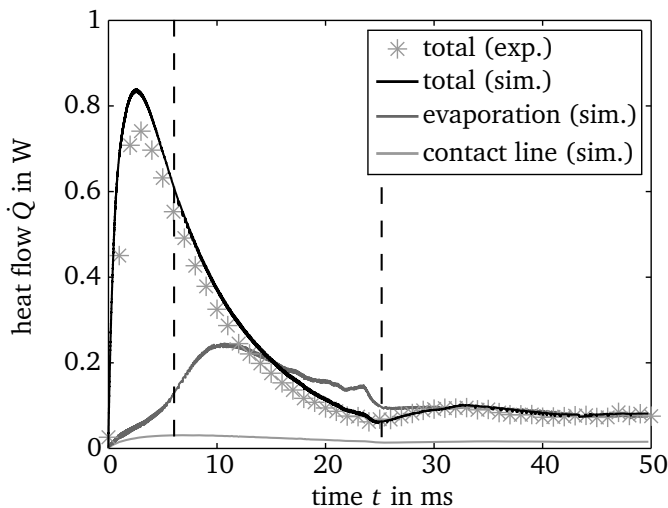


Figure 4.12.: Global heat flows versus time for scenario B.

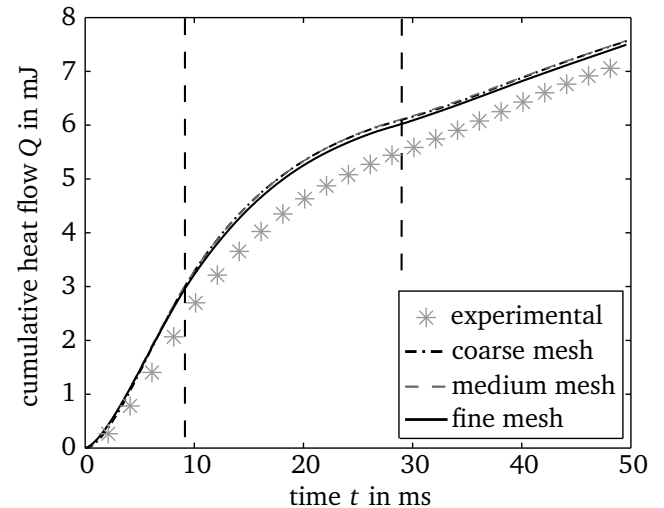


Figure 4.13.: Cumulative total heat flow for scenario A.

Nevertheless, a global comparison of the heat transfer is of course possible. In Fig. 4.12 the total heat flow from the wall to the droplet for scenario B is shown. The dashed lines reflect the borders between the individual stages of the impingement process. The strongest heat transfer is observed during the spreading of the droplet. During the receding phase the heat flow strongly decreases reaching a local minimum at the border between phases II and III. In phase III the heat consumed by the droplet is almost constant. It is noteworthy that the maximal heat flow is observed before the wetted region reaches its maximal extension in both, the experiment and the simulation. This behavior can be explained by the dominating heat transfer mode in this situation. As can be recognized from Fig. 4.12, the fraction of the total heat transferred directly at the contact line is almost negligible during the spreading. Hence, most of the heat is transferred by convection towards the liquid phase. Since the liquid decelerates during the spreading and at the same time the thermal boundary layer at the heated wall is developing, the heat transfer coefficient of convection is decreasing. In the initial phase this decrease is outweighed by the

increasing area of the wetted region until the observed maximum is reached. As soon as the motion of the liquid further decays, the fraction of heat transferred at the contact line, which is roughly proportional to the contact line length, becomes more and more important. At the end of the impingement process, i.e. in phase III, almost 20 % of the total heat is transferred in this extremely small region. Based on these results it should be emphasized that no reliable prediction of the evaporative heat transfer in the later stages of the impingement would be possible without a proper modeling of the near contact line heat transfer.

The numerical prediction reflects all the principal characteristics observed in the experiment. Even though the value of the maximal heat flow seems to get slightly overpredicted, the overall quantitative agreement is very good, too. Moreover, it seems to be impossible to specify the overall uncertainty of the experimental heat flow data due to the complex evaluation procedure involved and the influence of the unknown input heat flux from the heating layer. A basic consideration of possible sources of errors is given by Fischer [22].

The grid dependency of the numerical results is shown in Fig. 4.13 for the integral total heat flow in scenario A. Similar to the conclusions drawn for the hydrodynamic behavior of the droplet, no clear trend of convergence can be observed while the relative difference of heat flow is already very small between the three grids employed. In particular, for scenario A the total heat transferred during the spreading and receding phase differ by about 2 % and 0.7 %, respectively. Accordingly, the resolution of the coarse mesh can be considered sufficient to resolve the relevant processes in both scenarios.

In addition to the convective heat transfer the amount of liquid being evaporated during the impingement process is of interest. The total evaporation rate of the droplet is also presented in Fig. 4.12. The presence of certain oscillations can be recognized in the total evaporation rate. These fluctuations results from an fluctuating evaporative heat flow in the transition region near the contact line originating from the discontinuous size of the transition region due to the finite discretization as will be shown in more detail in the following section. Apart from this unphysical behavior it is noteworthy, that the evaporation at the free liquid-vapor interface, i.e. the overall evaporation reduced by the contact line heat transfer, is extremely small during the spreading phase while it becomes quite large during the receding motion of the droplet. Within that phase the droplet provides even more heat to the evaporation than it obtains from the wall. This is possible since the droplet is able to store sensible heat. Overall, during the phases I and II about 3 % (6 %) of the droplet is evaporated in case of scenario A (scenario B).

The strong increase of the evaporation rate at the beginning of the receding motion can be explained with aid of the local flow pattern within the liquid drop. In Fig. 4.14 the streamlines in a moving reference

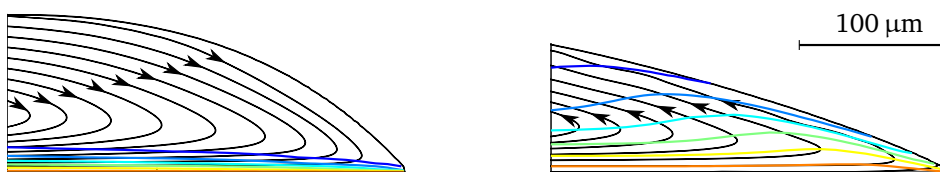


Figure 4.14.: Isotherms and streamlines near the contact line in the moving reference frame during the spreading (left, $t = 4$ ms) and receding (right, $t = 20$ ms) for scenario A. The spacing between the isotherms is $\Delta T = 2$ K.

frame moving with the contact line velocity are presented during the spreading and the receding phase. The contact line radius is approximately equal in both situations. During the spreading the no-slip boundary condition at the wall induces a rolling-like motion of the liquid. This vortex transports cooler liquid from the bulk towards the wall and thereby enhances the convective heat transfer there. If the motion direction reverses, the vortex changes its rotation accordingly. In that situation superheated liquid is transported from the superheated thermal boundary layer towards the liquid-vapor interface. The much wider spreading of the isotherms implies a less intense heat transfer at the wall while the transport of superheated liquid towards the interface supports evaporative phase change at the free interface. This effect has been found earlier to play an important role in pool boiling heat transfer and also at single moving menisci. Kunkelmann et al. [49] reported a strong dependency of the near contact line wall heat flux on the contact line speed in case of an advancing meniscus while a very weak dependency was observed for receding menisci. This observation can be made in a very similar way for the drop impingement (compare Fig. 16 in [34]). It should be noted that there seems to be a contradiction to the results obtained from the micro region model. As shown in Fig. 2.10 the heat transferred directly in the micro region tends to decrease with increasing speed. However, one has to keep in mind that both phenomena take place on a different length scale. The experimental investigations by Kunkelmann et al. were not able to resolve the contact line heat transfer itself but only the large scale convection effect was observed.

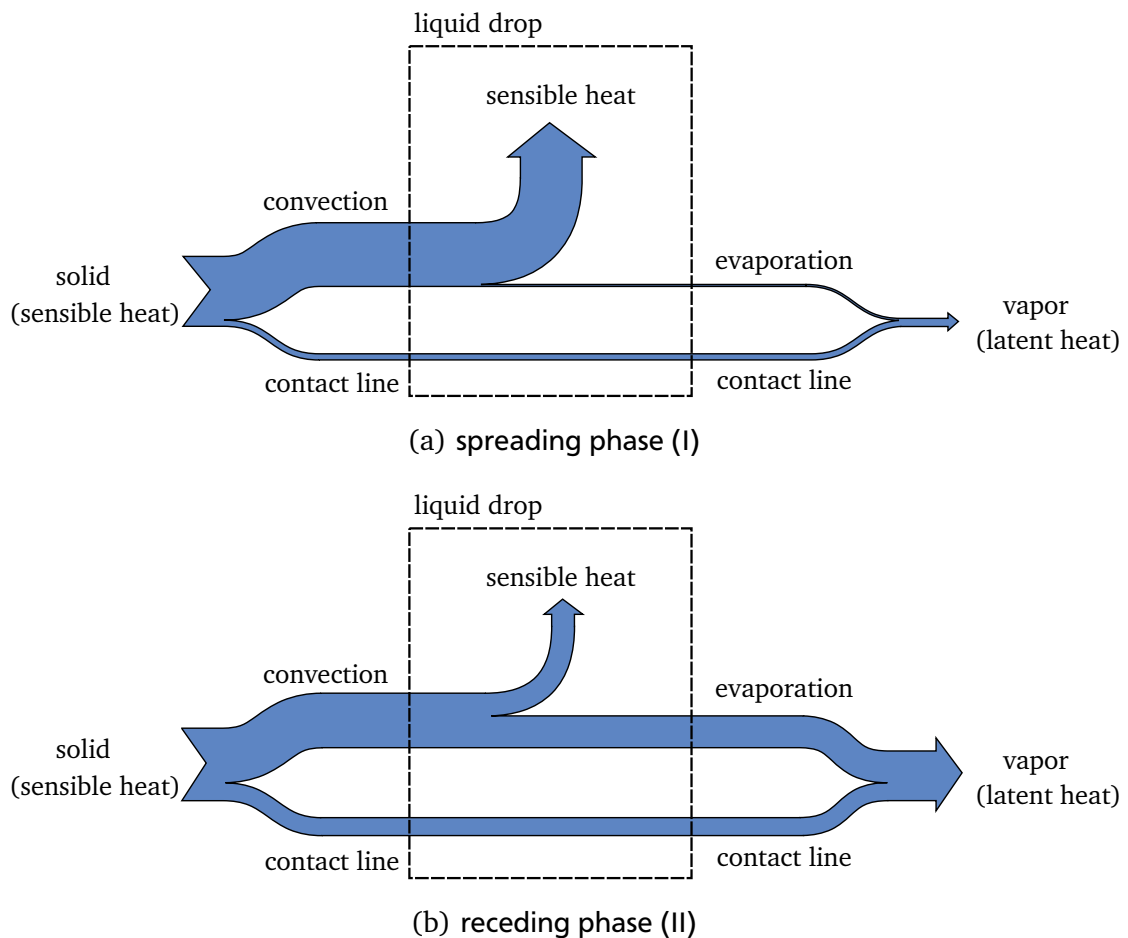


Figure 4.15.: Chart of energy flows during the spreading and the receding phase. The thickness of the arrows is related to the absolute values of heat transferred in scenario A.

A summary of the dominating heat transfer mechanisms in the individual phases of the impingement is given in form of an energy flow chart in Fig. 4.15. The major part of convective heat transfer is occurring during the spreading while the evaporation is the strongest during the receding phase. In the situation of the sessile droplet at larger times the heat transferred to the droplet by conduction is completely balanced by the heat consumed by evaporation at the interface.

4.1.4 Influence of modeling details

Apart from the measurement errors there are several uncertainties introduced by the modeling procedure. While the grid dependency has already been discussed, the influence of certain assumptions and details of the computational model will be addressed in the following.

Dynamic contact line model

A major part of this thesis has been dedicated to the influence of the contact line motion on the heat transfer and fluid flow within the micro region. Therefore, the necessity of using a dynamic contact line model will be discussed here. The dynamics of the contact line is accounted for in the macroscopic model via two quantities: the dynamic contact angle and the velocity dependency of the contact line heat flow. The effects of these both input quantities are investigated individually in the following.

First, the influence of the dynamic contact angle is investigated. Therefore, the dependency of the angle on the contact line speed is ignored while it is still taken as a function of the local wall temperature. A comparison of the spreading radius obtained for scenario A with and without the usage of the dynamic contact angle is given in Fig. 4.16. The maximal spreading radius is clearly overpredicted. The subsequent contraction of the contact line is much faster. Since the static contact angle is larger than the dynamic one during the receding phase, it exerts less resistance on the contraction. Therefore, also the minimal radius at the end of phase II is smaller and is in addition reached earlier. According to the additional dynamics of the process, the oscillation of the droplet in phase III is much more pronounced. The differences in fluid dynamics of course affect the heat transfer. Because of the larger maximal spreading radius the maximal heat flux is predicted 10 % higher while the minimal heat flux is 13 % smaller at the end of phase III. Hence, the usage of a dynamic contact angle model is advisable for an accurate prediction of the hydrodynamic behavior of an impinging drop as also claimed in the literature (see [6, 25, 93] for instance) which is crucial for a proper description of heat transfer.

Regarding the contact line heat transfer, the impact of considering the velocity dependency is not that obvious. Neglecting the influence of the contact line speed on the contact line heat transfer Q_{cl} and the thickness of the liquid film at the end of the micro region¹ while accounting for the dynamic contact angle, the hydrodynamics of the droplet are not affected at all. Accordingly, the convective heat transfer within the liquid phase is not altered, too. Solely in the evaporation rate there is certain influence. In Fig. 4.17 the cumulative heat transferred at the contact line is compared when accounting for the

¹ This value has been used in the modeling of heat transfer in the transition region (see section 3.5) and therefore influences the overall heat transfer as well.

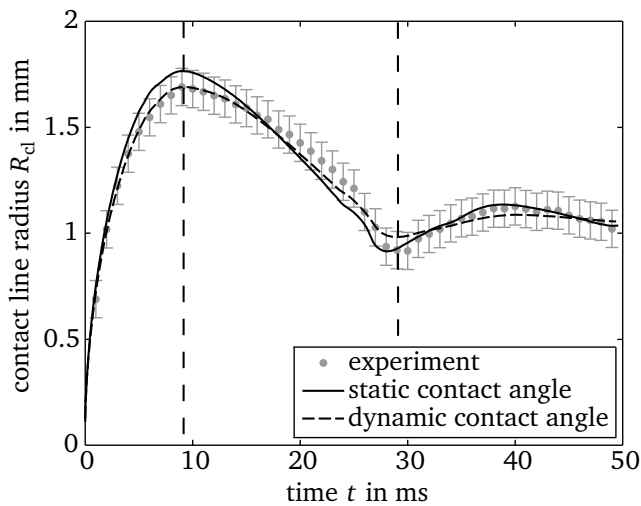


Figure 4.16.: Evolution of the contact line radius in scenario A when a static contact angle is employed.

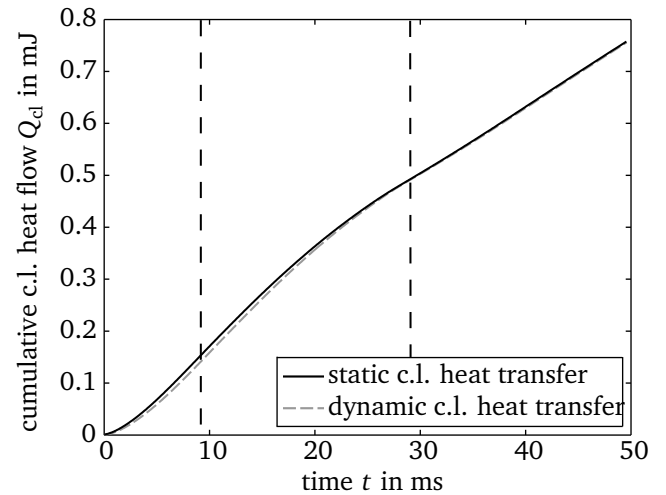


Figure 4.17.: Impact of the dynamic contact line model on heat transferred at the contact line in scenario A.

velocity dependency or not. During the spreading the heat transferred at the contact line is 8.5 % larger in the static case. Due to the minor contribution of the contact line to the overall heat transfer, the total heat transferred and the overall evaporation rate in phase I are increased by only 0.4 % and 5.5 %, respectively. In addition, during the receding the evaporation rate is higher in the dynamic case and at the end of the receding phase both effects nearly cancel out. In spite of the very little influence, the dynamic contact line heat transfer is accounted for within this work. On the one hand the overall model is considered more consistent if the same prediction method is used for the heat transfer and the contact angle obtained from the micro region model. On the other hand accounting for the velocity dependency of the contact line heat transfer introduces no additional computational effort.

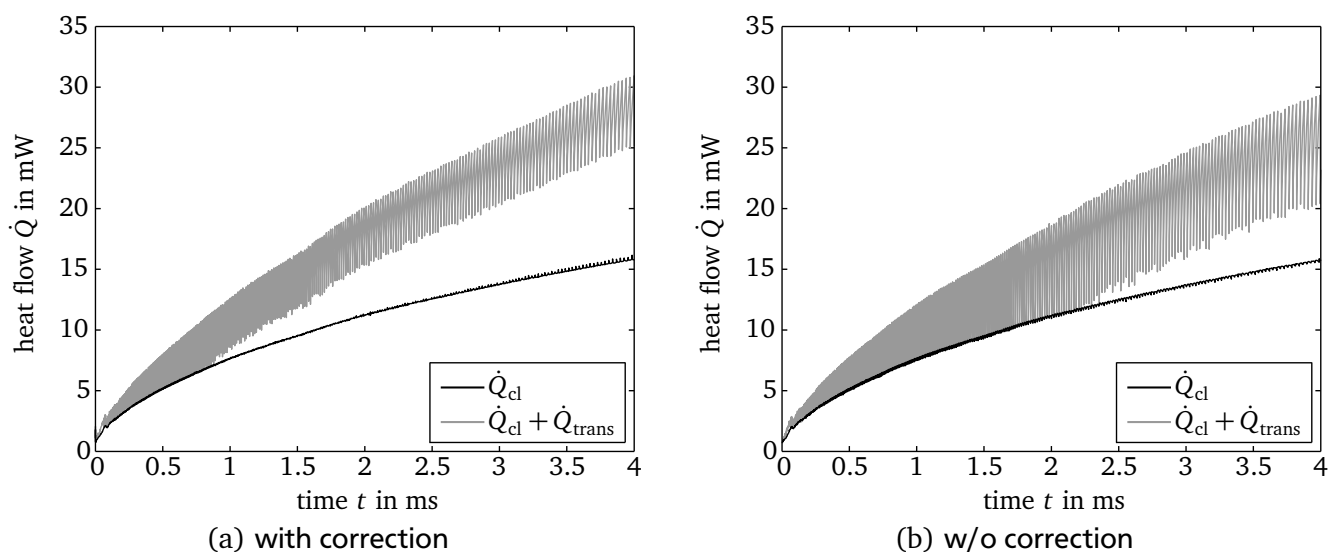


Figure 4.18.: Influence of the boundary correction applied to the VOF field on the contact line heat transfer.

The heat transfer in the transition region is significantly influenced by the area of this region and thereby by the exact position of the contact line (compare Section 3.5). Since the contact line is defined as the line of intersection of the reconstructed liquid-vapor interface and the solid wall, its position is altered by the boundary correction of the VOF field at the wall introduced in section 3.3.1. The influence of the employed correction on the heat transferred within the transition region during the spreading is presented in Fig. 4.18. For comparison the transferred heat is given neglecting the correction and applying homogeneous Neumann boundary conditions for the volume fraction field at the wall. The heat flow is strongly oscillating in both cases. Every single peak corresponds to the time instant at which a new boundary face is added to the transition region or a face formerly belonging to that region is no longer part of it. This oscillatory behavior cannot be fully avoided and has already been recognized in the global evaporation rate. Moreover, the oscillations do not vanish if the grid is refined. They are a manifestation of the fact that the sub-grid scale model will always predict the heat transfer near the contact line different from the macroscopic flow solver. Even though the oscillations do not fully vanish if the correction is applied, their amplitude is significantly reduced. Hence, the more accurate determination of the exact position of the contact line appears to partially bridge the gap between the microscopic and the macroscopic model. In addition to the modified amplitude, also the average heat transfer is larger when the correction is applied since otherwise the size of the transition region is systematically underestimated as has already been observed for the validation case in section 3.9.2. Hence, the correction which introduces a certain additional computational effort is considered necessary for a more accurate calculation.

Temperature dependent viscosity

Among others, Berberović et al. [6] reported a considerable influence of the temperature dependency of several thermophysical properties of the liquid on the hydrodynamic behavior of the liquid. In particular, the dependency of the viscosity on the liquid temperature has been found to influence the spreading ratio at the end of the spreading and during the entire receding phase. Therefore, the constant kinematic viscosity utilized in the formerly presented simulations is replaced by the simplest form of a temperature dependent viscosity given by the linear function

$$\nu_1(T) = \nu_{1,0} + \frac{d\nu_1}{dT} (T - T_{\text{sat}}) \quad (4.6)$$

where the linear coefficient has been estimated to $d\nu_1/dT = -2.159 \times 10^{-9} \text{ m}^2/(\text{s K})$. However, using this formulation only small deviations have been found compared to the reference solution. In case of reference scenario B the maximal spreading radius is increased by less than 1% and the contact line radius at the end of phase II is predicted to be 2.3% smaller. Accordingly, the maximal heat flow is also slightly increased by about 1.5% due to the increased size of the wetted area. Nevertheless, the influence of the temperature dependency of the viscosity is overall found to be negligible and will not be further considered in this thesis. The more obvious influence reported by Berberović et al. can be explained by the far larger temperature differences of up to 100 K involved in their simulations.

To estimate the influence of the transient heat conduction within the solid substrate on the drop impingement process, the simulation of reference case A is repeated assuming a constant wall temperature. The wall temperature is chosen constant and equal to the previously used initial wall superheat ΔT_w . As can be recognized from Fig. 4.19, the contact line radius is not changing significantly during the spreading phase if a constant wall temperature is employed. This is expected, since this phase of the impingement is dominated by the inertial and viscous forces. In contrast, the contraction of the contact line is finished earlier and the minimal radius is smaller, too. The reason for this behavior is a change in the contact angle. Due to the strong heat transfer at the contact line, the wall is subject to a strong local cooling near the contact line if heat conduction within the substrate is accounted for. While this local cooling is comparably weak during the spreading phase because of the high velocity of the droplet front (compare Fig. 4.6), the local cool-down is roughly 1.2K during the receding phase. Thereby the contact angle is reduced by about 10% compared to angle corresponding to the initial substrate temperature, thus providing a smaller driving force to the droplet to contract.

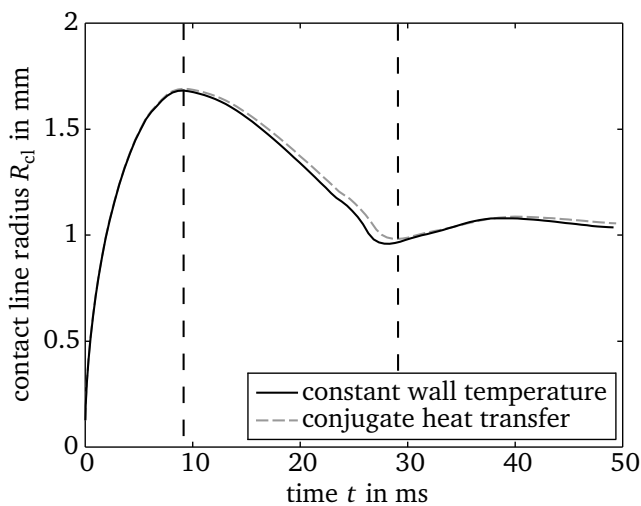


Figure 4.19.: Evolution of the contact line radius assuming a constant wall temperature in scenario A.

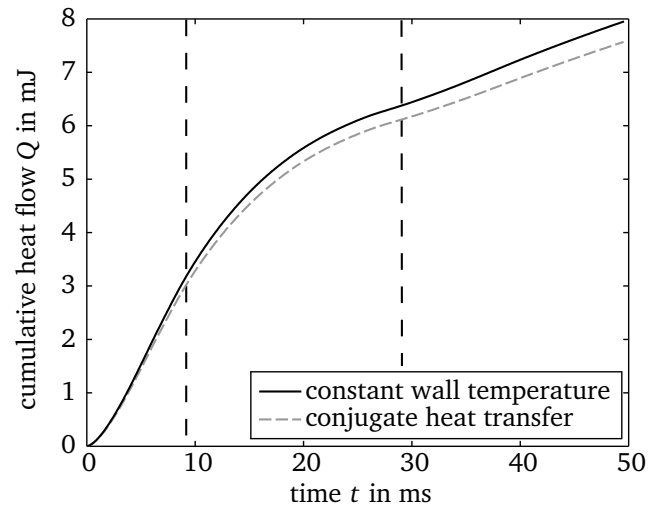


Figure 4.20.: Cumulative total heat flow assuming a constant wall temperature in scenario A.

Even though the wetted area is underestimated when assuming a constant wall temperature, the heat transfer is overpredicted as shown in Fig. 4.20. This is of course due to the fact that both, convection and contact line evaporation, are intensified if the driving temperature difference is increased. A more detailed investigation of the effect of wall properties on the heat transfer will be given below.

An additional uncertainty was introduced into the model by the lacking knowledge about the exact heat input in the heating layer during the experiment. However, by comparing the energy provided by the heating within the interaction zone during the impingement to the heat consumed by the droplet

$$\frac{Q_{\text{heater}}}{Q_{\text{drop}}} \approx \frac{q_{\text{in}} \pi D_0^2 t_{\text{impact}}}{Q_{\text{drop}}}, \quad (4.7)$$

it turns out that only 6 % for case A (8 % for case B) of the total heat consumed by the drop in phases I and II are provided by the heat input while the major fraction of energy is supplied by the sensible heat stored inside the solid substrate. Hence, the exact value of heat input has only a minor influence on the wall temperature and thereby on the heat transfer.

Initial conditions

In order to account for the initial deformation of the droplet, the wake flow within the vapor and the deformation of the thermal boundary layer, a pre-simulation has been conducted. However, the observed deformations of the liquid drop were very small and an insignificant internal circulation has developed during the free falling time. In contrast, the thermal boundary layer was clearly disturbed, but the influence of the temperature distribution within the vapor phase on the impingement process might be considered weak due to the small thermal capacity and conductivity of the vapor. Moreover, a quite rough estimate has been made for the initial temperature field in the gas phase since no information on the distribution have been gathered in the experiments.

To evaluate the overall influence of the choice of initial conditions, an additional simulation of scenario A is performed in which the simplest initial conditions are chosen. The droplet is initialized spherically at $z = 0.6$ mm above the heater surface. Its velocity is set homogeneously to the target velocity and the temperature within the entire fluid domain is set to the saturation temperature.

Utilizing these initial conditions, only insignificant changes of far less than 1 % are observed in both, the spreading radius and the total heat flow. Only the overall evaporation rate is slightly reduced by about 1.4 % since no heat is provided for the phase change by the superheated thermal boundary layer. Based on these findings, the initial conditions can be chosen as described here in the following parameter studies. Thereby not only the computational effort is reduced since the pre-simulation is unnecessary, but also the thermal boundary layer thickness is no longer an unknown parameter in the simulations.

4.2 Identification of the governing influencing parameters

Compared to experimental investigations, the numerical model provides the great advantage that every parameter can be varied individually. Therefore, the influence of the dominating parameters will be studied systemically in the following. Besides the various dimensionless groups that can be derived from the properties of the droplet also the thermal characteristics of the solid wall are expected to influence the overall heat transfer. In order to reduce the number of parameters, the studies on the droplet properties are carried out assuming an isothermal wall, while the wall properties will be investigated separately afterwards. For simplicity, all properties are considered temperature independent. Some conclusions drawn in this chapter have been published earlier [35] but will be discussed in more detail here.

4.2.1 Influence of droplet parameters

Some dimensionless numbers characterizing the hydrodynamics properties of the impinging droplet have already been introduced in section 1.2, namely the Reynolds number Re , the Weber number We and the Bond number Bo . Since here the heat transfer performance is of interest, also the thermal properties of the droplet have to be considered. The thermal properties of the liquid itself can be characterized utilizing the Prandtl number

$$Pr = \frac{\mu_l c_l}{k_l}. \quad (4.8)$$

A way of defining a non-dimensional wall superheat is the usage of the Jacobs number

$$Ja = \frac{c_l \Delta T_w}{h_{lv}}, \quad (4.9)$$

which is commonly employed for boiling systems. There is an alternative definition of the Jacobs number frequently used in literature on boiling heat transfer which additionally includes the density ratio between the liquid and the vapor phase. While this variant is appropriate for nucleate boiling to reflect the volume change due to evaporation of a bubble confined by a liquid pool, there is no reason why the vapor density should come into play here.

Following the Buckingham Π -theorem one additional independent non-dimensional quantity can be defined, provided that the ten dimensioned parameters D_0 , u_0 , ρ_l , μ_l , σ , c_l , k_l , g , h_{lv} and ΔT_w are dominating. This additional number can be given as

$$A^* = \frac{u_0^2}{h_{lv}},$$

thus reflecting the ratio of kinetic energy to the latent heat of the fluid. Since dissipation is however ignored within this study and in general $A^* \ll 1$, no attention is paid to any changes of this quantity.

In order to be able to compare the heat transfer to droplets of different size it is advisable to consider dimensionless quantities as well. The hydrodynamic behavior can be characterized by the non-dimensional spreading ratio

$$S = \frac{D_{cl}}{D_0}$$

as introduced in Eq. (1.5). The time is rescaled by the hydrodynamic time scale to obtain the dimensionless time τ as given by Eq. (1.4)

$$\tau = \frac{tu_0}{D_0}.$$

The heat transferred to the droplet can be related to the maximal heat transferable to the droplet, which is the amount of energy necessary to evaporate it completely,

$$E^* = \frac{6Q}{\pi\rho_1 D_0^3 h_{lv}}. \quad (4.10)$$

The definition of E^* might be adapted if an initial subcooling of the droplet would be accounted for. A dimensionless representation of the heat flow is given by the derivative of E^* with respect to the dimensionless time τ via

$$\dot{Q}^* = \frac{6\dot{Q}}{\pi\rho_1 D_0^2 u_0 h_{lv}}. \quad (4.11)$$

In a similar manner the non-dimensional evaporative heat transferred and the non-dimensional evaporation rate can be expressed in terms of the evaporated mass M_{evap} and the evaporation rate \dot{M}_{evap} via

$$M^* = \frac{6M_{\text{evap}}}{\pi\rho_1 D_0^3} \quad (4.12)$$

and

$$\dot{M}^* = \frac{6\dot{M}_{\text{evap}}}{\pi\rho_1 D_0^2 u_0}, \quad (4.13)$$

respectively. An alternative to the introduced quantities to describe the heat transfer would be the usage of a Nusselt number via

$$\text{Nu} = \frac{hL_0}{k_1} = \frac{4D_0\dot{Q}}{\pi D_{\text{max}}^2 k_1 \Delta T_w} \quad (4.14)$$

where the droplet diameter has been used as the characteristic length scale and the heat transfer area has been chosen as $\pi D_{\text{max}}^2/4$, which is a measure for the area of thermal interaction. Herein, D_{max} is the maximal diameter of the contact line during the impingement. Some authors also use the actual size of the wetted region as reference area (e.g. [25]). However, the usage of E^* appears to be more appropriate to characterize the heat transfer efficiency in the context of e.g. spray cooling, since it relates the heat

removed by the droplet to the amount of fluid mass utilized for the purpose of cooling. In case of the non-dimensional heat flow the denominator in its definition is proportional to the mass flow rate. Hence, an increase of \dot{Q}^* reflects an increased heat transfer at the very same flow rate. Moreover, a non-linear relation of the heat flow to the wall superheat is expected when evaporative heat transfer is involved, thus making the usage of a Nusselt number in general questionable. Nevertheless, the definitions are not fully independent since the Nusselt number can be rewritten as

$$\text{Nu} = \frac{2 \text{Re Pr } \dot{Q}^*}{3 \text{Ja } S^2}. \quad (4.15)$$

In the dimensional analysis above, the numbers characterizing the contact line heat transfer given by Eq. (2.85) have been ignored. However, besides the influence of these properties on the contact line heat transfer itself, they also dominate the predicted value of the apparent contact angle. The contact angle in turn might have a substantial influence on the hydrodynamic behavior of the droplet and thereby on the heat and mass transfer. Therefore, when varying the dimensionless groups, a manipulation of the fluid properties is avoided. The Reynolds and Weber number can be controlled by adjusting the ratio of droplet size and velocity. For changing the Bond number the gravitational acceleration is modified. To adjust the Prandtl number the specific heat capacity of the liquid is changed, which is no input quantity to the contact line model. However, at the same time the latent heat of evaporation must be changed in order to keep the Jacobs number constant. This modified value of h_{lv} is however not accounted for in the contact line model due to the above given reasons. Alternatively, Pr could also be adjusted by varying the liquid thermal conductivity. Then the contact line heat flow Q_{cl} has to be rescaled accordingly. Moreover, the interfacial heat resistant has to be scaled by $1/k_l$ to keep the ratio of heat transferred in the micro region and the transition region constant. Numerical tests showed no significant differences between the two ways of variation.

All variations presented in the following are related to a reference scenario where the quantities are set to $\text{Re} = 1000$, $\text{We} = 15$, $\text{Bo} = 0.5$, $\text{Pr} = 9.54$ and $\text{Ja} = 0.13$. The chosen Prandtl number corresponds to the original properties of FC-72 and the Jacobs number implies a wall superheat of $\Delta T_w = 10 \text{ K}$. The calculations are performed on a mesh similar to the coarse mesh used above. The grid size is chosen as $\Delta x = \min(D_0/125, 8 \mu\text{m})$ which is similar to the resolution of the coarse grid used for the calculation of the validation scenarios. The droplet parameters of the individual simulations is given in the appendix A.3.

Hydrodynamics

The influence of each dimensionless group on the temporal evolution of the dimensionless contact line radius S versus the dimensionless time τ is presented in Fig. 4.21. A comparison of the dimensioned quantities would be pointless since the individual droplets deviate in their size and initial velocity by almost one order of magnitude. The results of the parametric study basically confirm the formerly drawn conclusions for the hydrodynamic characteristics of drop impingement. The dominant influence of the Reynolds number on the maximal spreading ratio implies that the inertial and frictional forces

are the dominant forces in this phase. In contrast, since the receding motion of the droplet is driven by capillary forces, the influence of the Weber number and the wetting properties is maximal there. Even though the wetting properties were not changed directly, the contact angle predicted by the contact line model increases with wall superheat and hence with the Jacobs number. Therefore the Jacobs number has an indirect influence on the hydrodynamics. In case of a weak surface tension effect corresponding to a large Weber number or if the contact angle is small, the receding motion of the droplet is comparably slow and no undershoot of the contact line radius can be observed at the end of the receding phase. Accordingly, the distinct boundary between the phases II and III as introduced above vanishes.

Of course there is also some crossover characteristics to be observed. Due to the larger maximal spreading ratio in case of a large Reynolds number, the receding motion of the droplet is faster, too. Consequently, for the smallest Reynolds number the distinct limit between phases II and III is vanishing as well. At the same time, the surface tension forces represented by the Weber number and the wetting characteristics have a certain impact on the spreading phase, too. In particular, the duration of the spreading phase is increasing with the Weber number and also the maximal spreading ratio is slightly increased for larger Weber numbers. It might be surprising that the value of the Prandtl number influences the spreading ratio as well even though it only describes the thermal properties of the liquid. However, as will be shown below, the evaporation rate increases considerably for very small values of Pr. Accordingly, the droplet volume decreases during the impingement and thereby the contact line radius is reduced. In general, gravitational forces are completely ignored in studies on drop impingement. However, the Bond number is found to influence the hydrodynamics of the droplet throughout the entire impingement process. When comparing the initial kinetic energy of the droplet to the change of its potential energy, one finds the gravitational forces to be relevant if $4Bo/We$ is of the order of unity [35].

In order to condense to above described effects into a mathematical formulation, the scaling of the characteristic quantities of the impingement process with the dimensionless numbers is of interest. The duration of the spreading phase is found to scale as

$$\tau_{\max} \propto \left(\frac{We}{1 - \cos \theta_0} \right)^{1/4} (1 - M_s^*) \quad (4.16)$$

where M_s^* is the dimensionless mass being evaporated during the spreading phase. If the prefactor is chosen to 0.85, the simulation data are reproduced with a maximal error of less than 10%. The similar trend of the spreading time with respect to the Weber number has been found experimentally by Antonini et al. [4] for water droplets on a glass surface. It should be noted that this empirical correlation is quite different from the scaling of the overall contact time of bouncing droplets which has been found to scale as $\tau_{\text{contact}} \propto We^{0.5}$ by Richard et al. [80] on superhydrophobic surfaces.

A common way to obtain a correlation for the maximal spreading ratio is to set up an energy balance for the impingement process. This approach has been used for instance by Chandra and Avedisian [13] and has later been modified by Pasandideh-Fard et al. [72] and by Ukiwe and Kwok [110].

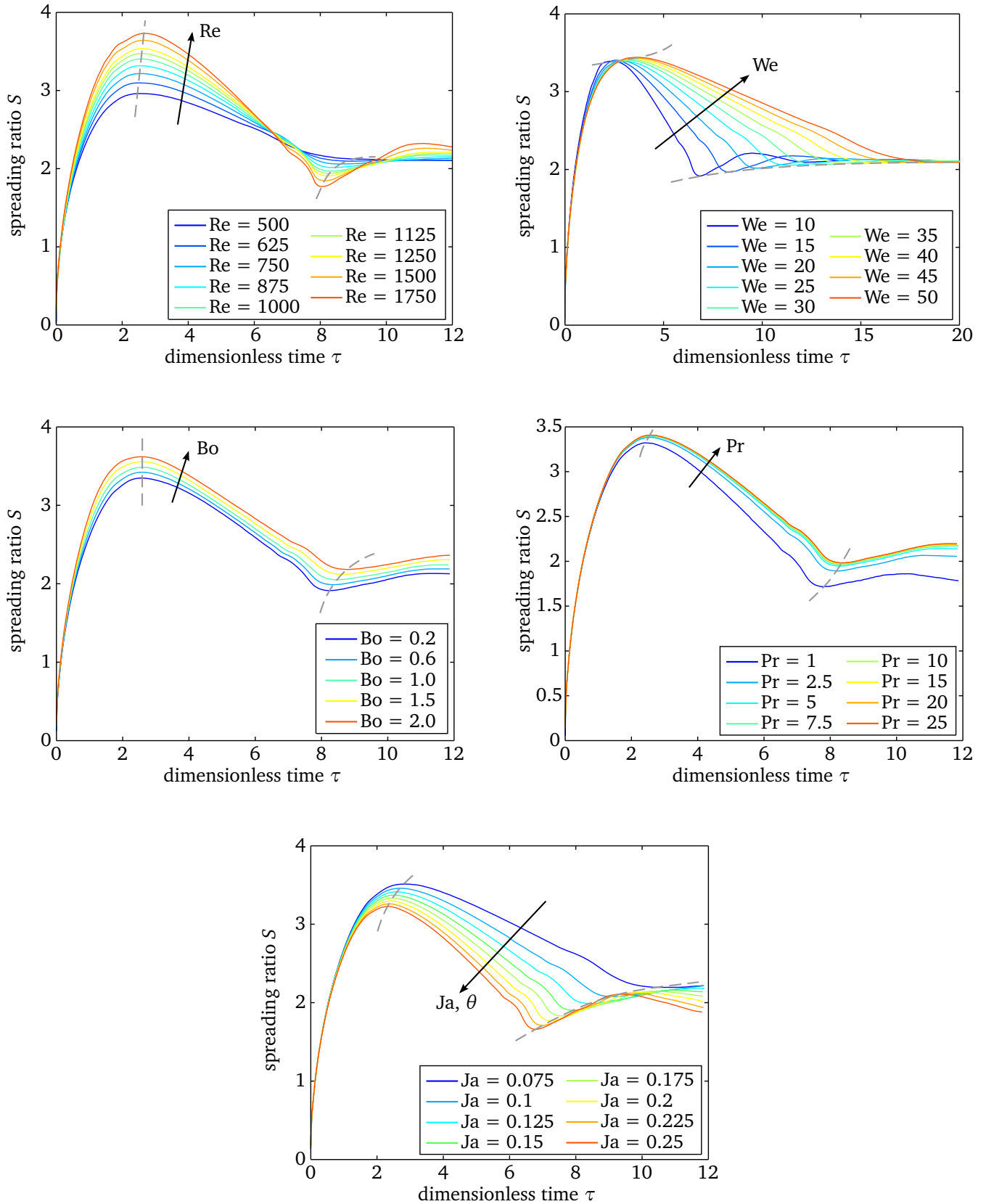


Figure 4.21.: Dependency of the spreading ratio on the drop characteristics. If not denoted otherwise, the impact parameters are $Re = 1000$, $We = 15$, $Bo = 0.5$, $Pr = 9.54$ and $Ja = 0.13$. The borders between the respective phases of the impingement are indicated by the dashed grey lines.

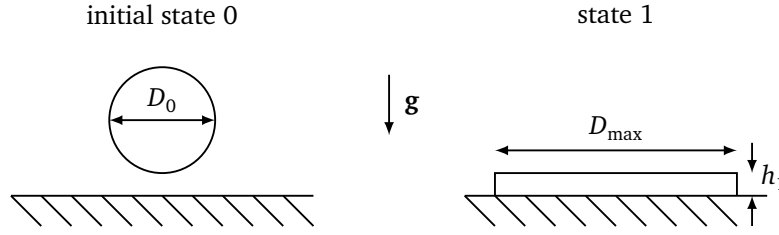


Figure 4.22.: Simplified geometry of the droplet at the initial state and at the end of the spreading.

Following the approach outlined by Ukiwe and Kwok, the energy balance is set up between the initial state 0 and the instant of maximal spreading 1 as presented in Fig. 4.22. The change of the droplet's kinetic, potential, and surface energy has to be balanced by the work of dissipation

$$E_{\text{kin},0} - E_{\text{kin},1} + E_{\text{pot},0} - E_{\text{pot},1} + E_{\text{surf},0} - E_{\text{surf},1} = W_{\text{diss}}. \quad (4.17)$$

The change of the potential energy has not been accounted for in the above given references. However, since gravity appears to have an influence on the spreading ratio in the range of impingement parameters studied here, it is reasonable to include it (c.f. the influence of the Bond number on the spreading ratio in Fig. 4.21). The droplet is assumed to be spherical in the initial state while the shape of the liquid is taken as a cylinder of diameter D_{max} and height h_1 at the instant of maximal spreading as shown in Fig. 4.22.

The kinetic energy in the initial state is given by the known mass and velocity of the droplet. In state 1 the kinetic energy is assumed to be zero. The change of the potential energy is proportional to the change of the droplet's center of gravity which is approximately given by $D_0/2$ provided that $h_1 \ll D_0$. Moreover, the change in the surface energy has to be determined. The energy of the liquid-vapor interface is given by the surface tension times the area of the interface. The size of the sides of the liquid cylinder in state 1 can be neglected. However, not only the liquid-vapor interface is changing its size and hence its energy during the impingement but also the solid surface is getting wetted. Thereby the size of the solid-vapor interface is reduced by $\pi D_{\text{max}}^2/4$ and the size of the solid-liquid interface is enlarged by the same amount. The surface energies of the solid-vapor and the solid-liquid interface σ_{sv} and σ_{sl} are related to the surface energy σ of the liquid-vapor interface via Young's equation

$$\sigma_{\text{sv}} - \sigma_{\text{sl}} = \sigma \cos \theta_0 \quad (4.18)$$

with the static contact angle θ_0 . Substituting the respective energy changes in Eq. (4.17) results in

$$\frac{\pi}{12} \rho D_0^3 u_0^2 + \frac{\pi}{12} \rho D_0^4 g + \pi \sigma D_0^2 - \frac{\pi}{4} \sigma D_{\text{max}}^2 (1 - \cos \theta_0) = W_{\text{diss}}. \quad (4.19)$$

Finally, the energy balance can be rewritten in dimensionless form as

$$\text{We} + 4\text{Bo} + 12 - 3(1 - \cos \theta_0) S_{\max}^2 = \frac{12 W_{\text{diss}}}{\pi \sigma D_0^2} \quad (4.20)$$

where $S_{\max} = D_{\max}/D_0$ is the maximal spreading ratio. While the determination of the energies is quite straight forward, an appropriate guess has to be made to evaluate the dissipation work. By an inspection of the dissipation function the work can be approximated as

$$W_{\text{diss}} \approx \mu \left(\frac{u_0}{\delta} \right)^2 V_{\text{drop}} t_c \quad (4.21)$$

as derived in detail by Chandra and Avedisian [13]. Herein, t_c is the time scale of the impingement process which is given by $t_c \approx (8/3)D_0/u_0$. The volume of the drop is given by $V_{\text{drop}} = (\pi/6)D_{\max}^2 h_1$ where the height of the liquid cylinder in state 1 is given by

$$h_1 = \frac{2 D_0^3 (1 - M_s^*)}{3 D_{\max}^2} \quad (4.22)$$

due to volume conservation but accounting for the mass being evaporated during the impingement. The characteristic length scale δ has been set equal to the height h_1 by Chandra and Avedisian. Alternatively, Pasandideh-Fard et al. [72] chose this length scale according to the thickness of the boundary layer as $\delta \propto \text{Re}^{-1/2}$. However, no significant qualitative changes are observed when following this approach.

At the end, the energy balance can be expressed as

$$\text{We} + 4\text{Bo} + 12 - 3(1 - \cos \theta_0) S_{\max}^2 = 12 \frac{\text{We}}{\text{Re} (1 - M_s^*)} S_{\max}^4. \quad (4.23)$$

From this equation, the maximal spreading ratio can be determined. A comparison of the spreading ratio observed in the simulation to the values predicted by Eq. (4.23) is presented in Fig. 4.23. While the correlation seems to reflect the effects of the Reynolds, Bond, Jacobs and Prandtl number² qualitatively correct, the effect of the Weber number not captured at all. In contrast to the simulations, which show an increase of the spreading ratio with Weber, the correlation predicts $dS/d\text{We} < 0$. This wrong trend is even more pronounced if the time scale of the impingement t_c used in the calculation of the dissipation work is replaced by the duration of the spreading phase given by Eq. (4.16).

As mentioned above the major uncertainty in the energy balance is introduced by the unknown dissipation work. It has been assumed that the major part of the dissipation is taking place within the spreading liquid film with a uniform thickness. This seems to be indeed a good approximation of the spreading droplet's shape in the range of very large Weber numbers, i.e. when the surface tension effects are com-

² Even though the Jacobs and Prandtl number are not explicitly included in Eq. (4.23), they have an indirect effect on S_{\max} due to their influence on the contact angle θ_0 and the evaporated mass M^* .

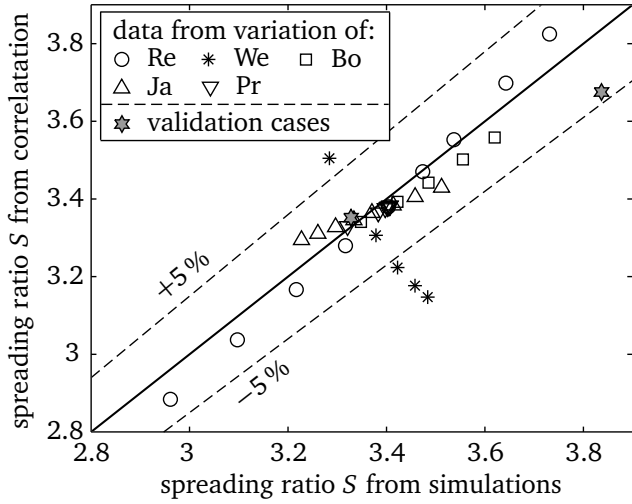


Figure 4.23.: Correlated versus simulated spreading ratio for Eq. (4.23) derived from an energy balance.

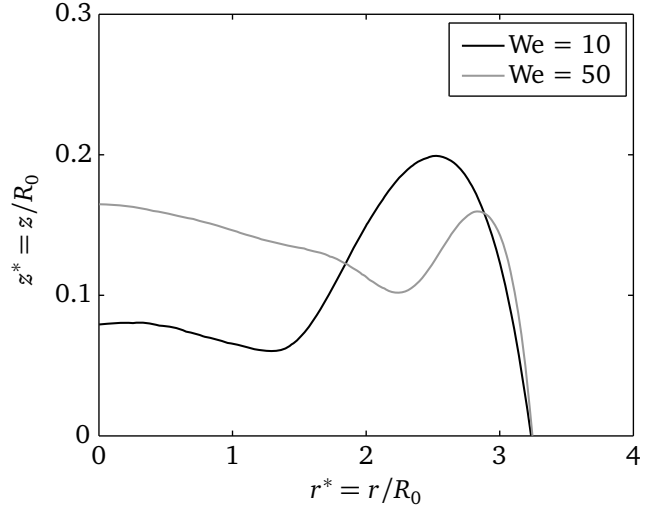


Figure 4.24.: Computed droplet shape at $\tau = 2$ for different impact Weber numbers. The axes are not shown to scale.

pletely negligible against the inertia of the fluid. In contrast, for a small Weber number the shape of the liquid-vapor interface is influenced by surface tension. In Fig. 4.24 the computed droplet shapes during the spreading phase are compared at the smallest and highest value of the Weber number investigated. While for $We = 50$ the film thickness is pretty much constant from the center to the contact line, a much stronger variation is observed for $We = 10$. In the latter case a broad rim is formed near the moving contact line. Due to the accumulation of mass within the rim, the liquid film near the center of the droplet is much thinner in this case. The characteristic length δ of the flow in z -direction required in the estimation of the dissipation work in Eq. (4.21) is however related to the local distance between the interface and the wall. Since this characteristic length is smaller in case of a smaller Weber number and enters into the dissipation as $W_{\text{diss}} \propto \delta^{-2}$, it is reasonable that the maximal spreading ratio is reduced by the increased dissipation at a small Weber number.

To compensate for the shortcomings in the definition of the dissipation work, it might be possible to use a tailored expression for the dissipation as done by Mao et al. [59]

$$\frac{12 W_{\text{diss}}}{\pi \sigma D_0^2} = a \frac{We^b}{Re^c} S_{\text{max}}^2$$

to fit the simulation data. This approach can be interpreted as a generalized form of the dissipation work introduced in [13] and [72]. However, since there is no clear physical motivation for this type of approach, such a fitting is avoided. Moreover, the number of simulations performed is considered too small to obtain a fit with general validity, especially because the cross-characteristics are not investigated in detail.

It should be stressed that an increase of S_{max} with We has also been observed experimentally by Antonini et al. [4] even though they found $S_{\text{max}} \propto We^{0.25}$ which appears to be much stronger than the dependency

found in this work being roughly $S_{\max} \propto We^{0.05}$. However, in their study the droplet diameter was kept constant corresponding to a constant Ohnesorge number while the results presented here were obtained at a constant Reynolds number³. Moreover, their power law was shown to depend also on the contact angle.

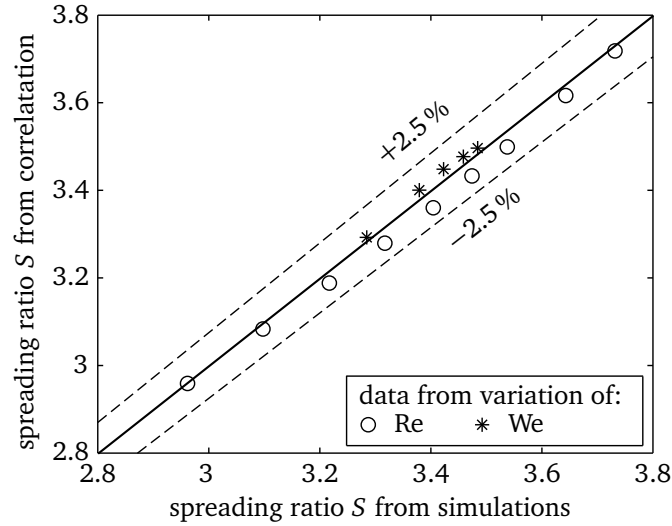


Figure 4.25.: Correlated versus simulated spreading ratio for the adapted correlation from Roisman, Eq. (4.24).

Roisman [84] proposes a completely different type of correlation given by

$$S_{\max} = aRe^{1/5} - bRe^{2/5}We^{-1/2} \quad (4.24)$$

where the first term on the right hand side reflects the tendency for $We \rightarrow \infty$ and the second term incorporates the fluid flow within the rim for a finite Weber number. As shown in Fig. 4.25 this correlation is able to capture the general tendencies of Re and We if the two constants are chosen according to $a = 0.92$ and $b = 0.08$. These fitted constants are fairly different from the original values given by Roisman to $a = 0.87$ and $b = 0.4$. However, also his correlation was originally derived for higher values of Re and We. Hence, the wetting characteristics were neglected while they were found to influence the spreading in this study. Unfortunately, Roisman's correlation is not able to describe the effects of gravity, evaporation and the contact angle.

It can be summarized that no correlation has been found in the literature which is able to describe the influence of all dimensionless numbers onto the maximal spreading ratio qualitatively correctly. Nevertheless, a proper prediction of this quantity is very important due to its influence on the heat transfer as will be shown below. Hence, more effort has to be put into a better understanding of the hydrodynamics during the impingement process of isothermal droplets, in particular at low values of the Reynolds and Weber number.

³ The simulation results show the rough dependency of $S_{\max} \propto Re^{0.2}We^{0.05}$ which is equivalent to $S_{\max} \propto Oh^{-0.2}We^{0.15}$ because of $Re = We^{0.5}Oh^{-1}$ (see the definition of Oh in section 1.2). Hence the difference in the exponents to the Weber number is smaller than it appears.

A comparison of the dimensionless total heat transferred during the impingement E^* versus the dimensionless time τ is given in Fig. 4.26. Even though the spreading ratio was found to increase with the Reynolds number and accordingly the area of heat transfer is enlarged, the value of E^* is decreasing during the entire impingement process. This result might first appear counter-intuitive. However, the dimensionless heat E^* is related to the droplet volume rather than to the area of heat transfer. Moreover, in the present study the Reynolds number has been increased at a constant Weber number and hence the droplets corresponding to the high Reynolds numbers have a comparably large diameter and a small velocity. In addition, if the Reynolds number would have been increased by lowering the viscosity, the thermal conductivity had to be lowered to the same extent in order to keep the Prandtl number constant. From this point of view the influence of the Reynolds number on the heat transfer is more obvious. In contrast, the increase of the heat transfer with the Bond number is solely caused by the enlargement of the area wetted by the droplet.

While it appears that the heat transferred up to a fixed instant in terms of the dimensionless time is decreasing with increasing Weber number during the spreading, the heat being transferred during the entire spreading phase is increasing. Due to the slower subsequent contraction of the droplet in case of a large Weber number, the heat transfer is also enhanced during the receding phase in case of a larger Weber number. The delay in heat transfer can be explained with help of the altering shape of the droplet during the spreading phase. As shown in Fig. 4.24, the liquid film thickness near the center of the splat is thinner if the Weber number is small. Thereby, the liquid-vapor interface penetrates the thermal boundary layer (see also Fig. 11 in [35]). This results not only in an increased evaporation rate but also in a steeper temperature gradient within the liquid film and hence to an enhancement of the wall heat transfer.

The influence of the Prandtl and the Jacobs number are quite intuitive. If the Prandtl number is increased the heat transfer is strongly decreasing. In the present variation the changes in the dimensionless heat are mainly caused by the larger latent heat of vaporization at a larger value of Pr but the same effect would be achieved by a lower thermal conductivity of the liquid. Finally, when increasing the Jacobs number and hence the wall superheat, the heat transfer is of course intensified. However, this increase is not linear. Even though the Jacobs number was varied in equidistant steps, the absolute change in the heat transfer becomes smaller for large values of Ja . This is mainly due to the decreasing trend of the spreading ratio with increasing Jacobs number caused by the increasing apparent contact angle.

Since the heat transfer within the spreading phase is dominated by convection, it can be described by a Nusselt correlation. The flow of the liquid during the spreading is very similar to the flow at a single impinging jet. The average Nusselt number for a single impinging jet is given by [111, p. 746]

$$\text{Nu}_{\text{m,jet}} = 2 \frac{1 - 1.1/r^*}{r^* + 0.1(h^* - 6)} \left[\text{Re} \left(1 + 0.005 \text{Re}^{0.55} \right) \right]^{0.5} \text{Pr}^{0.42} \quad (4.25)$$

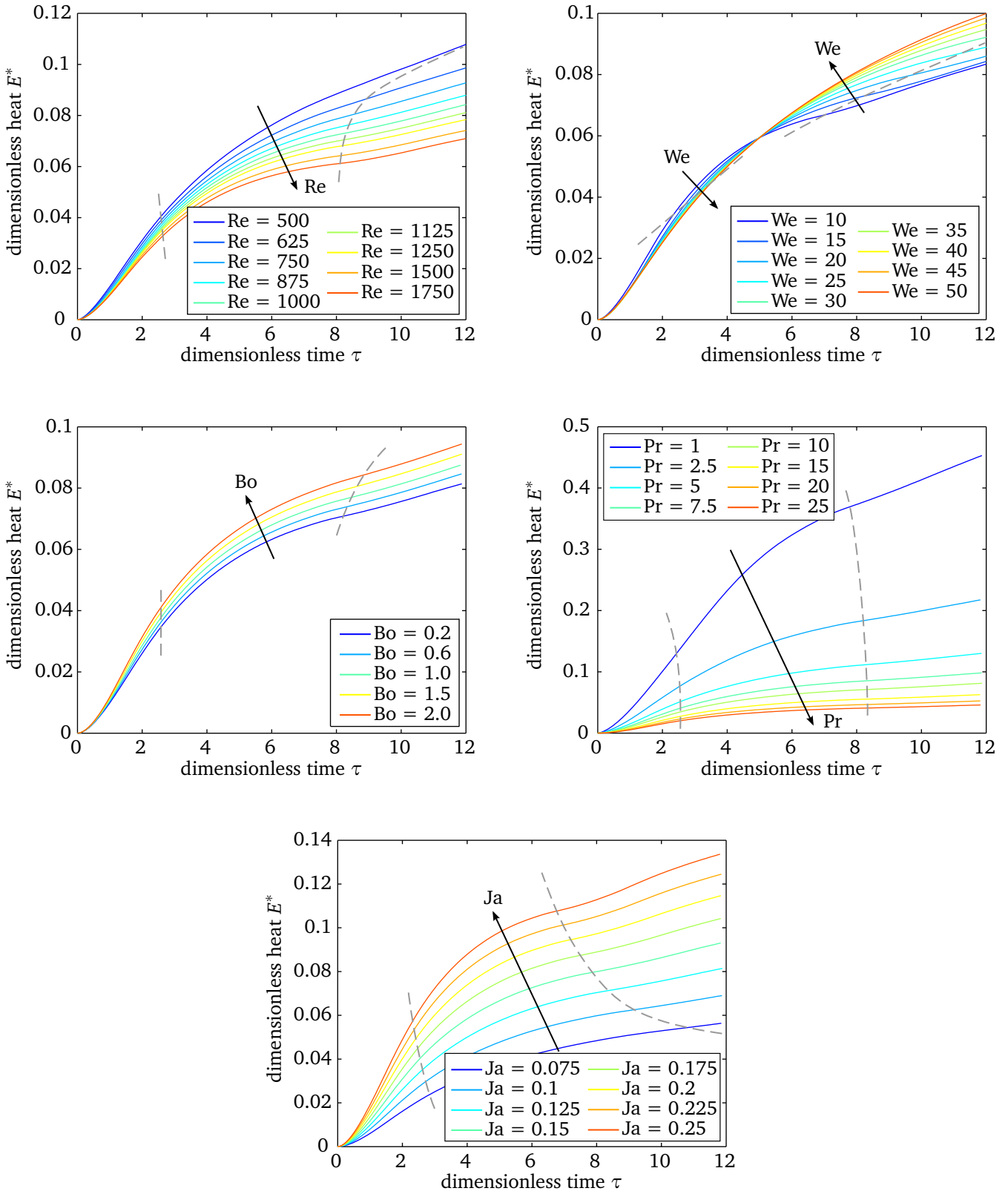


Figure 4.26.: Dependency of the total heat transfer on the dimensionless numbers. If not denoted otherwise, the impact parameters are $Re = 1000$, $We = 15$, $Bo = 0.5$, $Pr = 9.54$ and $Ja = 0.13$. The borders between the respective phases of the impingement are indicated by the dashed grey lines.

where r^* is the radius of the area of interest normalized by the half nozzle diameter. Hence, it is similar to the maximal spreading ratio S_{\max} . The parameter h^* denotes the dimensionless distance of the nozzle to the surface and is set to zero in this situation. Assuming that the overall heat transferred during the spreading phase is proportional to the convective heat transfer described by the above given Nusselt number, Eq. (4.15) can be rewritten as

$$E_s^* \propto \frac{3}{2} \frac{\text{Ja} S_{\max}^2}{\text{Re} \text{Pr}} \tau_{\max} \text{Nu}_{m,\text{jet}}. \quad (4.26)$$

Substituting Eq. (4.25) into Eq. (4.26) an expression for the dimensionless heat transferred during the spreading can be obtained

$$E_s^* = 3a \frac{S_{\max} (S_{\max} - 1.1)}{(S_{\max} - 0.6)} \frac{(1 + 0.005 \text{Re}^{0.55})^{0.5} \text{Ja}}{\text{Re}^{0.5} \text{Pr}^{0.58}} \tau_{\max} \quad (4.27)$$

with the proportionality constant a . A comparison of the heat transferred during the spreading phase obtained from the simulations to the above prediction is shown in Fig. 4.27. Herein, S_{\max} and τ_{\max} are taken from the individual simulations. The empirical constant has been fitted globally to $a = 4/3$ based on the simulation data.

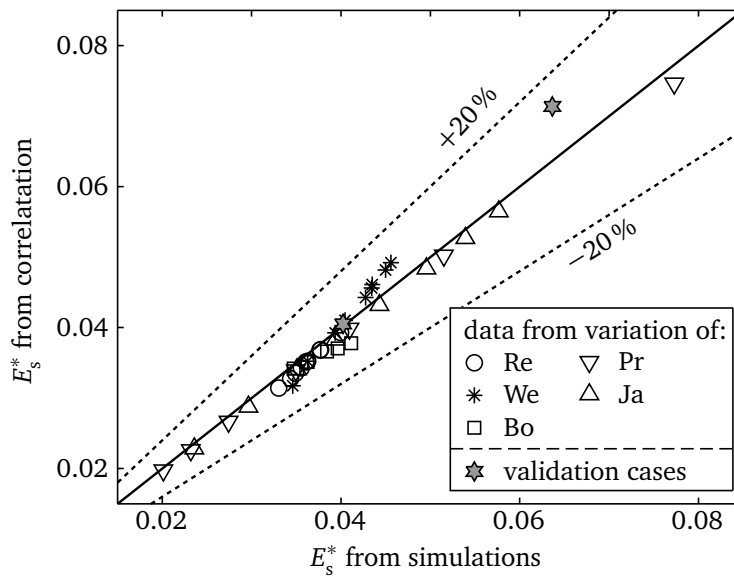


Figure 4.27.: Dimensionless heat transferred during the spreading phase compared to the prediction by Eq. (4.27).

The simple prediction is found to capture the main features of the heat transfer during the spreading phase. Only the effect of the Weber number seems to slightly deviate from the prediction. Moreover, the heat transferred during the validation scenario B is overestimated by 13.8%. However, this simulation result was not obtained at a constant wall superheat but including the transient heat transfer within the solid substrate and thereby the local cool-down of the wall. Thereby the heat transfer performance is

significantly reduced as will be shown below. The lower wall temperature underneath the droplet could also be interpreted in terms of a smaller effective Jacobs number.

Again the different conclusion that can be drawn from the Nusselt number and the dimensionless energy used within this thesis should be stressed. While Eq. (4.25) leads to the impression that an increasing Reynolds or Prandtl number would result in an improvement of the heat transfer performance, Eq. (4.27) implies the exact opposite. The evaluation of the two numbers can also be interpreted as seeing heat transfer from two different perspectives. While the Nusselt number relates the transferred heat to the area of the surface to be cooled, the dimensionless heat provides a comparison of the heat being transferred to a droplet to its capability of consuming heat.

The sensitivity of the dimensionless evaporated mass M^* to the impingement parameters is given in Fig. 4.28. The general trends are very similar to the observations made for the total heat transfer. However, since most of the evaporation is taking place during the receding phase, the delay of the heat transfer with increasing Weber number for instance is much more pronounced. Also the non-linearity of the evaporated mass versus the Jacobs number is even stronger. Besides the fact that the heat transfer area is smaller in case of large Ja, also the heat transfer coefficient of the contact line evaporation decreases with increasing wall superheat due to the non-linear behavior of the micro region (see for example Fig. 2.12(a)).

While the convective heat transfer is a phenomenon somehow related to the size of the wetted area, the evaporation is preferentially taking place near the contact line and is therefore rather related to the contact line length L_{cl} . The evaporation rate directly at the contact line \dot{M}_{cl} is known from the micro region modeling. Moreover, the evaporated mass should be proportional to the duration of the respective impingement phase t_{ph} . Overall the parameter

$$X = L_{cl,max} \dot{M}_{cl,0} t_{ph} = \frac{\pi D_0 S_{max} \dot{Q}_{cl,0} t_{ph}}{h_{lv}} \quad (4.28)$$

can be used as a measure for the overall evaporation rate. For simplicity, the heat flow per unit contact line length for a non-moving contact line $\dot{Q}_{cl,0}$ is utilized here. As can be seen in Fig. 4.29, a linear correlation is found between the quantity X and the cumulative evaporation rate for the spreading phase, except for a very small Prandtl number. In that case the evaporation at the free liquid-vapor interface is much more important which does not scale with D_0 but rather with the area of the interface and hence with D_0^2 .

The linear correlation between X and M_{evap} in the spreading phase could have been expected since during the discussion of the validation cases it already turned out that most of the evaporation during the spreading is taking place in the direct vicinity of the contact line. However, also during the receding phase the evaporated mass correlates clearly with X even though the contact line evaporation plays a minor role during the receding. Nevertheless, the evaporation during the receding phase was found to be driven by a vortex-like secondary flow near the moving contact line (compare Fig. 4.14). This phenomenon is however also related rather to the length of the contact line than to the wetted area. Nevertheless, the correlation between X and the evaporation rate during the receding phase in Fig. 4.30

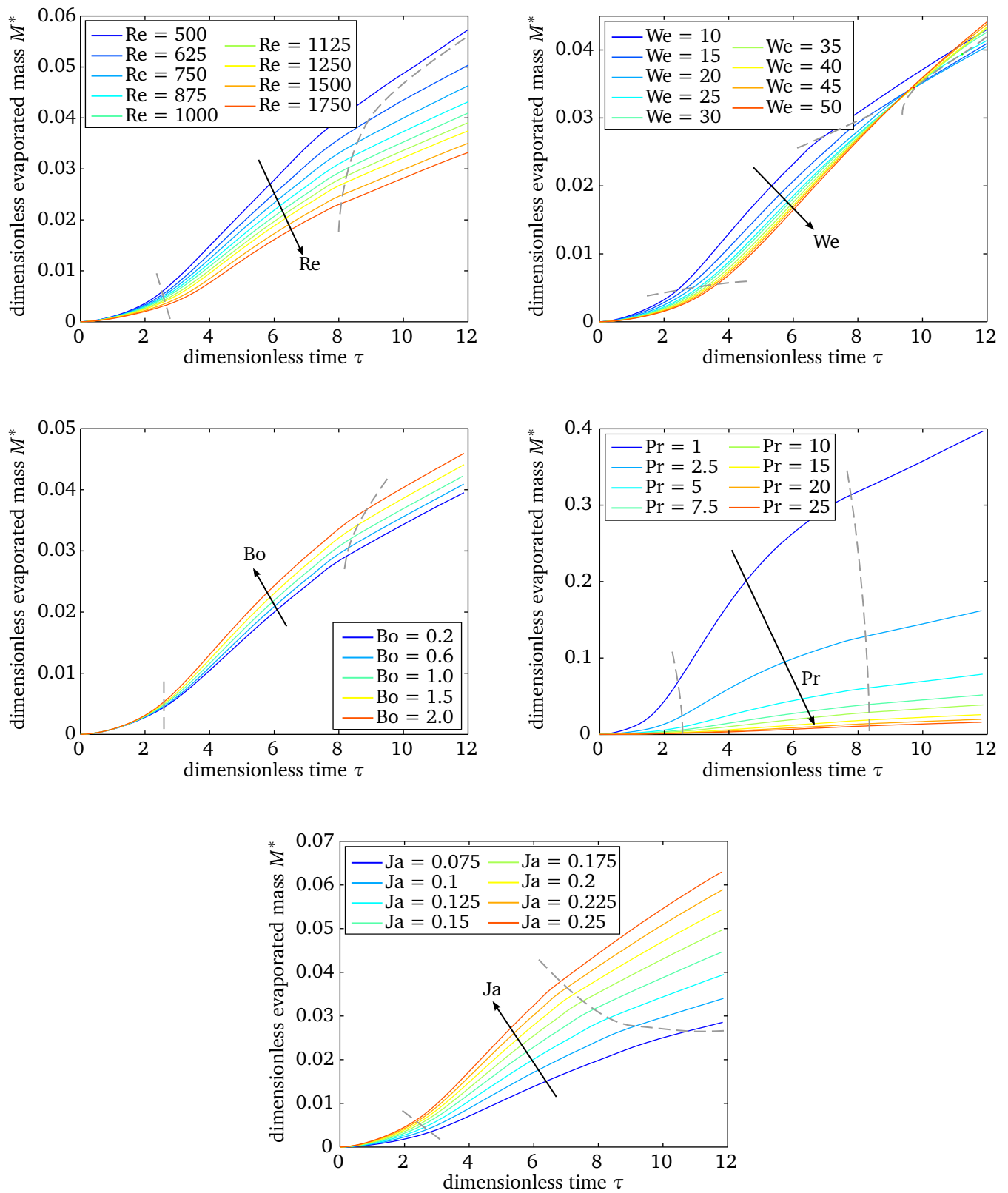


Figure 4.28.: Dependency of the mass transfer on the dimensionless numbers. If not denoted otherwise, the impact parameters are $Re = 1000$, $We = 15$, $Bo = 0.5$, $Pr = 9.54$ and $Ja = 0.13$. The borders between the respective phases of the impingement are indicated by the dashed grey lines.

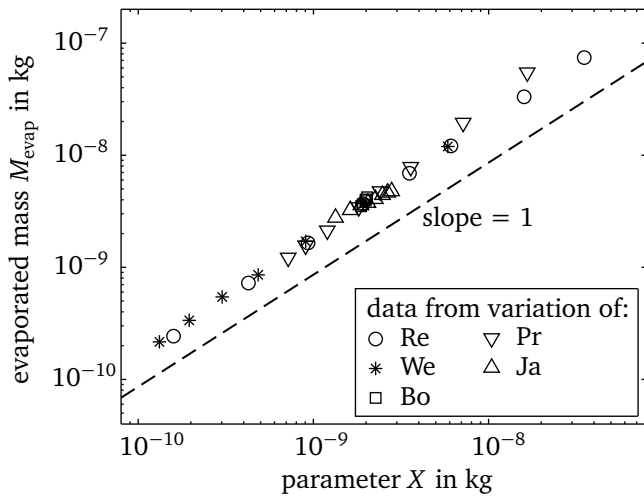


Figure 4.29.: Evaporated mass during the spreading phase versus the parameter X .

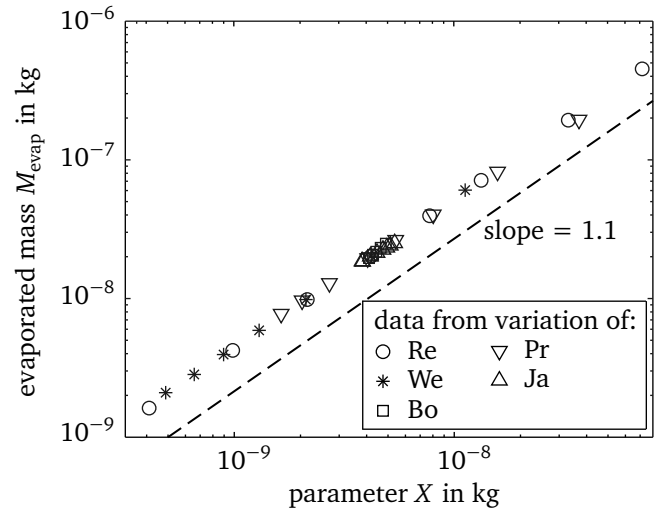


Figure 4.30.: Evaporated mass during the receding phase versus the parameter X .

is found not strictly linear but a little stronger. This slightly larger slope can be attributed to surface effects. Once more, the points corresponding to very small Prandtl numbers show a different tendency due to the much larger overall evaporation rate.

The dimensionless evaporative heat can be linked to the quantity X via

$$M^* \propto \frac{X}{\rho D_0^3} \quad (4.29)$$

but it is not possible to express directly as a combination of the dimensionless impingement parameters as it has been possible in case of the overall heat transfer.

4.2.2 Influence of wall properties

In Section 4.1.4 a certain influence of the transient heat conduction within the solid substrate on the drop heat transfer has been observed. In particular, the heat transferred to the droplet was found smaller in case of conjugate heat transfer than in case of an isothermal wall. In the following the influence of the wall thermal properties on the drop impingement process will be discussed in more details.

The two physical properties of the wall playing a role are the thermal conductivity k_s and the product of density and specific heat capacity $\rho_s c_s$. Moreover, the thickness of the solid substrate is believed to influence the heat transfer since it determines the amount of energy that can be provided by the substrate. The influence of the substrate thickness H can be characterized via the Fourier number

$$Fo = \frac{\alpha_s t_0}{H^2} \quad (4.30)$$

which can be interpreted as a dimensionless time based on a thermal time scale. The thermal diffusivity of the solid material is herein given by $\alpha_s = k_s / (\rho_s c_s)$. The Fourier number gives an indication whether

the thermal boundary layer developing inside the solid material reaches the other side of the substrate or not. If $Fo \ll 1$, the diffusion front of the temperature has not yet reached the lower boundary of the heater within the given time t_0 . In that case, the solid substrate can be considered as a semi-infinite body. On the contrary, if $Fo \gg 1$, the diffusion front has already reached the other boundary and the wall thickness is expected to have an influence onto the heat transfer at the solid-fluid boundary.

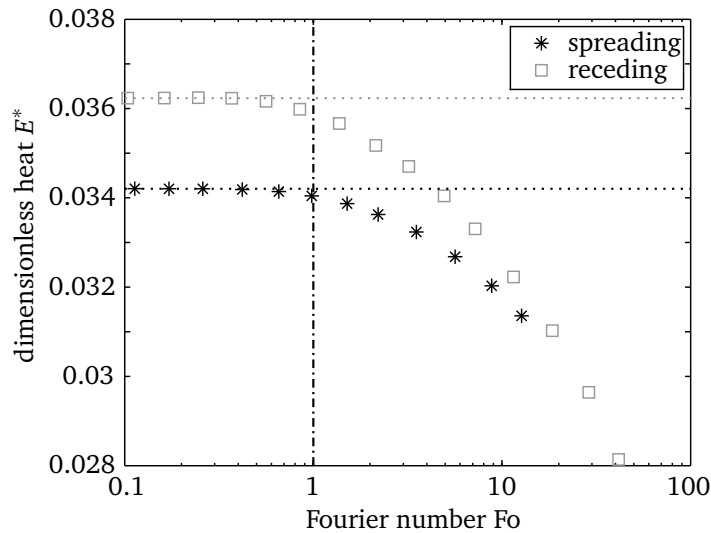


Figure 4.31.: Effect of the substrate thickness H on the total heat transferred during the spreading and the receding phase. (Note: The Fourier number is defined by the individual end time of the spreading and receding phase, respectively, and $Fo \propto H^{-2}$.)

In Fig. 4.31 the heat transferred during the spreading and receding phase, respectively, is presented for a varying substrate thickness. The droplet parameters are chosen according to the reference case introduced above. The Fourier number is calculated with the time at the end of the respective impingement phase. A clear transition can be observed near a Fourier number of unity. As expected, the heat transfer is not influenced by the wall thickness for small values of Fo , while it tends to decrease with increasing values of the Fourier number. Since a large Fourier number corresponds to a small substrate thickness, the sensible heat stored in the solid material is limited and hence less heat is provided to the impinging drop. The thickness resulting in a Fourier number of unity for CaF_2 is about 0.18 mm at the end of the spreading phase and 0.32 mm at the end of the receding phase. Hence, substrates thicker than these threshold values can be considered as semi-infinite bodies in terms of heat transfer. In this case it would be sufficient to take only the part of the substrate close to the wall into account without any loss of accuracy provided that the initial temperature is homogeneous.

In the variation of the droplet parameters in Section 4.2.1 the wall has been assumed to be isothermal. However, even if the substrate can be considered as semi-infinite, the heat that can be provided by the solid material to the solid-fluid interface during the spreading and receding of the droplet is finite. Hence, the wall will locally be cooled down during the impingement process (c.f. Fig. 4.6). The strength of the

local temperature change directly at the solid-fluid interface is related to the ratio of thermal effusivities $\epsilon = \sqrt{\rho ck}$ of the solid and the liquid material

$$R_{\epsilon,sl} = \frac{\epsilon_s}{\epsilon_l} = \sqrt{\frac{(\rho ck)_s}{(\rho ck)_l}}. \quad (4.31)$$

If two semi-infinite bodies 1 and 2 with different initial temperatures T_1 and T_2 are brought into sudden contact, the temperature at the boundary between the two bodies T_{int} is given by [111, p. 647]

$$T_{\text{int}} = \frac{R_{\epsilon,12}T_1 + T_2}{1 + R_{\epsilon,12}}.$$

Hence, the temperature at the boundary is closer to the initial temperature of the body with the higher thermal effusivity. Moreover, if the effusivity ratio tends to infinity, the body 1 can be considered as isothermal.

The above consideration is however limited to the case in which heat is transferred by conduction only. Even though during drop impingement convection and contact line evaporation come into play, the effusivity ratio is considered as an appropriate measure for characterizing the temperature change at the solid-fluid boundary.

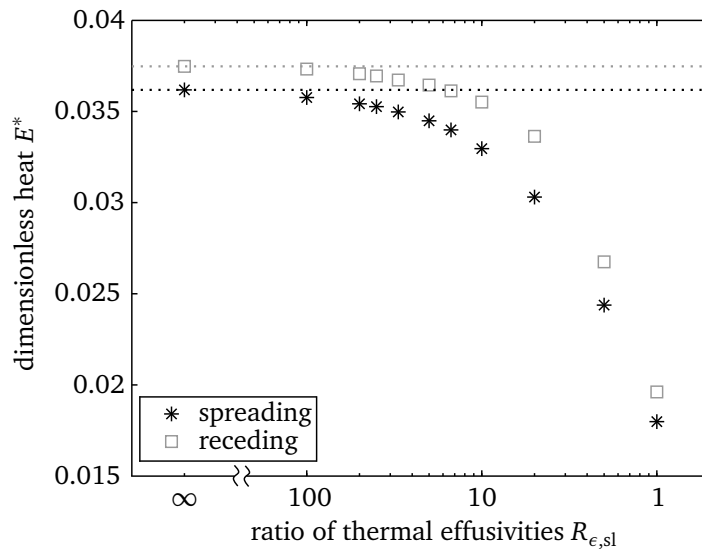


Figure 4.32.: Effect of the effusivity ratio on the total heat transferred during the spreading and the receding phase.

The heat transferred during the spreading and receding phase for the reference case is shown in Fig. 4.32 versus the effusivity ratio. Herein, the effusivity of the solid material has been varied by adjusting both, the thermal conductivity and the heat capacity, in order to keep the thermal diffusivity constant. The transferred heat is found to strongly decrease with decreasing effusivity ratio. The limit of $R_{\epsilon,sl} \rightarrow \infty$ is represented by the assumption of an isothermal wall. The combination of FC-72 and CaF_2 is characterized by $R_{\epsilon,sl} = 16.9$. Hence the wall cannot be considered as fully isothermal as has already been

concluded in section 4.1.4. If however the substrate material was replaced by copper, the resulting ratio of 121.7 implies that the assumption of an isothermal wall would be much more justifiable.

Another quantity often employed to characterize the transient thermal conduction within a solid body subject to convective cooling is the Biot number

$$\text{Bi} = \frac{hH}{k_s}.$$

While the Biot number provides information about the homogeneity of the temperature within the solid substrate, this temperature is not related to the initial temperature of the substrate. If the substrate thickness H is small, the Biot number gets very small as well. Hence, the temperature differences within the solid material are very small due to $\text{Bi} \rightarrow 0$ but the wall temperature will also drop very fast due to the small thermal capacity of the substrate. Accordingly, the Biot number is no appropriate quantity to decide whether the wall can be considered as isothermal.

4.3 Coalescence of two simultaneously impinging droplets

All consideration made in this thesis up to this point have been limited to one single droplet without any interaction with other droplets. However, during the impingement of a spray onto a solid wall, a huge number of droplets is impinging the surface and the individual droplets will certainly interact with each other. As a first step towards the understanding of the interaction of droplets during their impingement the simultaneous impingement of two droplets is investigated. The considerations are restricted to two droplets of equal size and equal initial velocity in order to simplify the problem. The initial configuration of the impingement is sketched in Fig. 4.33. The interaction between the droplets is characterized by an additional parameter, namely the spacing parameter

$$e = \frac{d}{D_0} \quad (4.32)$$

which is the ratio of the distance between the two droplets and their initial diameter. The droplets are expected to hydrodynamically interact with each other if the spacing is smaller than the maximal extend of the two droplets reached during the spreading phase, i.e. if $e < S_{\text{max}}$. Since only two identical droplets are considered, two planes of symmetry can be employed in the simulation and only one half droplet has to be calculated as indicated in the figure.

The droplet parameters are chosen according to the reference case introduced in the previous section. The transient heat conduction within the solid substrate is accounted for. As substrate material calcium fluoride is chosen and the substrate is thick, i.e. the Fourier number is smaller than unity. The impingement process is simulated for two different spacing parameters. For the smaller value of $e = 1.5$ the interaction is supposed to occur very early during the spreading phase. The larger spacing parameter of $e = 3$ is close to the maximal value for which an interaction is expected. Hence, the two droplets will touch at the end of the spreading phase.

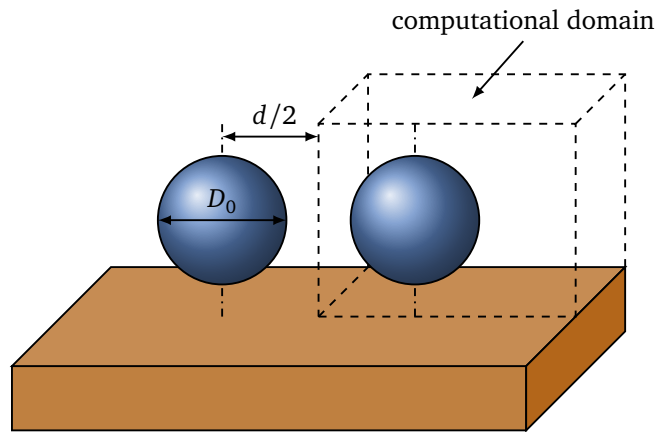


Figure 4.33.: Configuration of the drop coalescence case.

The simulations have to be carried out on a three-dimensional mesh. To provide a sufficient mesh resolution to capture the fluid dynamics during the hydrodynamic interaction of the two droplets, the grid size is chosen to $\Delta x = 4 \mu\text{m} \approx D_0/250$. The size of the fluid domain is $4 \times 2 \times 2.8 \text{ (mm)}^3$ which would result in a cell number of 350,000,000 if a Cartesian mesh would be utilized. However, creating a coarse base mesh and employing 2 subsequent levels of adaptive mesh refinement within the entire liquid phase and in a band of $70 \mu\text{m}$ around the liquid-vapor interface, the cell number can be reduced to about 10,000,000. With this reduced mesh size the simulation of the coalescence can be performed within one week on 96 CPUs on the Lichtenberg high performance cluster.

In Fig. 4.34 the shape of the liquid-vapor interface is presented at various time steps for the small spacing parameter of $e = 1.5$. During the initial phase of the impingement the droplets do not influence each other. At $t = 1.48 \text{ ms}$ the contact lines of both droplets touch each other and the droplets start to coalesce. The liquid within the spreading lamella has still a considerable kinetic energy at this early stage of the impingement. Due to the interaction of the droplets, a stagnation point is present at the position where the two contact lines touch each other. Accordingly, the liquid flow is redirected towards the sides and also upwards. This motion results in the formation of a bump between the droplets. In contrast, the spreading process in a certain distance from the actual interaction is not influenced by the presence of the second droplet. As the spreading proceeds the bump grows and at the same time small capillary waves are traveling from the interaction zone outwards towards the other side of the droplets. As soon as the liquid motion decays, the bump is not further fed with liquid from the spreading droplets. Instead, the liquid is flowing outwards and the bump starts to vanish. At $t = 9 \text{ ms}$ the maximal size of the wetted region is reached and the liquid starts to contract. Thereby a single droplet is formed. Due to the large mass of the coalesced droplet the receding is much slower than for a single droplet. At the end of the impingement process only one single sessile droplet is produced.

The formation of a bump within the hydrodynamic interaction zone has also been observed experimentally by Cossali et al. [16] during the simultaneous impingement of three droplets. In their study these bumps were very pronounced and produced secondary droplets. However, the Weber number was much larger in their experiments than in the situation presented here. A theoretical description of this phenomenon is given by Roisman et al. [85].

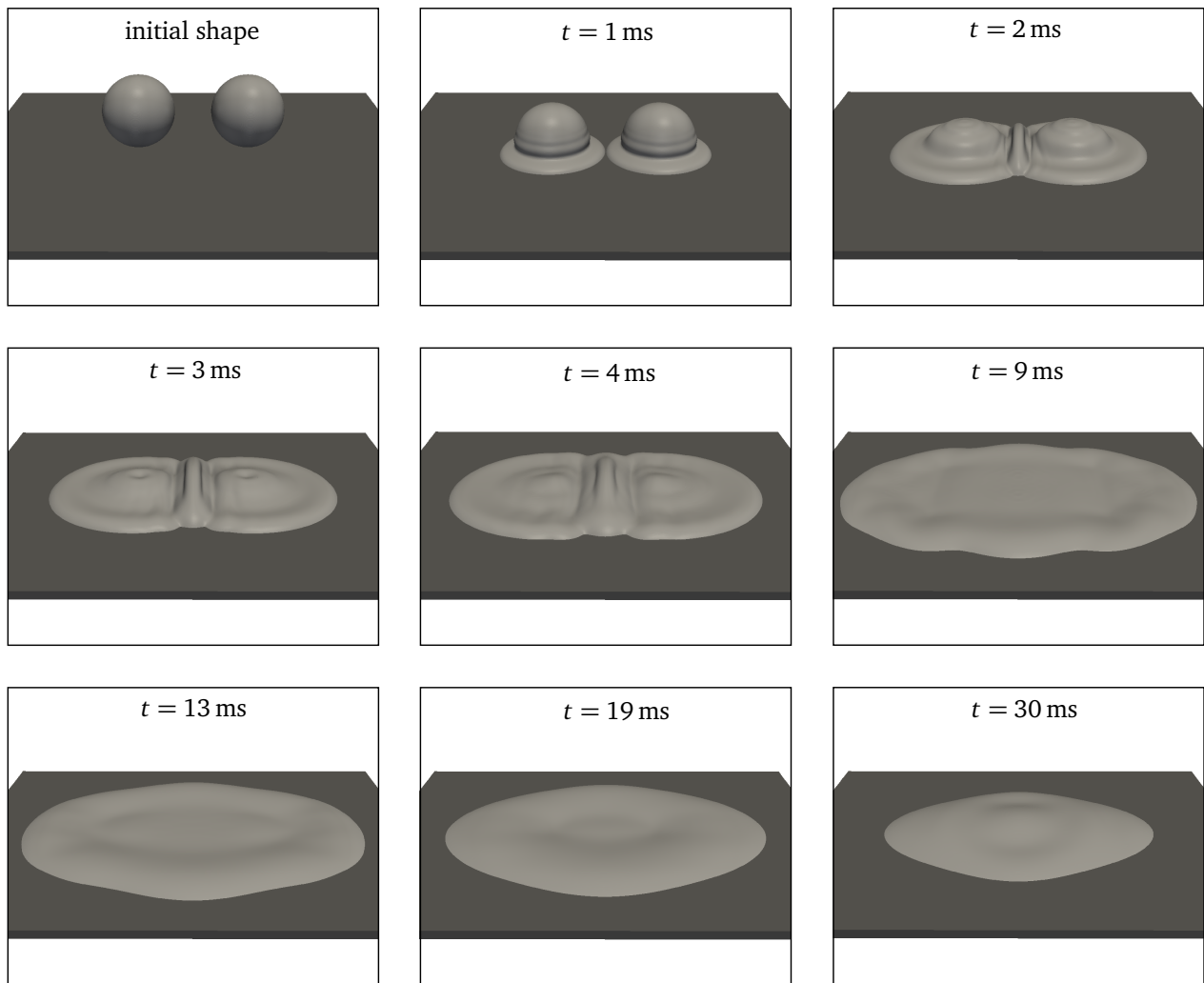


Figure 4.34.: Snapshots of the computed droplet shape for the simultaneous impingement of two droplets with a low separation of $e = 1.5$.

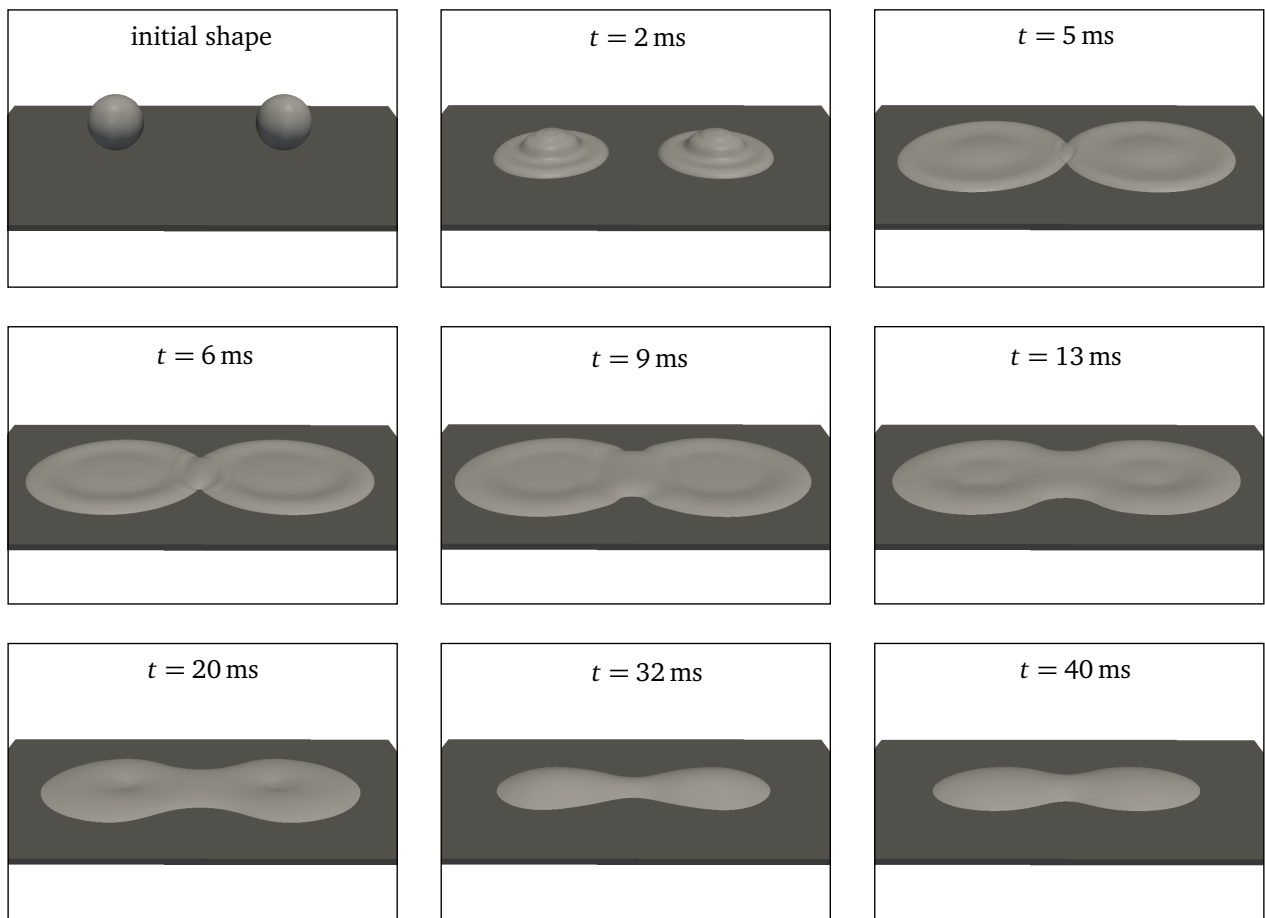


Figure 4.35.: Snapshots of the computed droplet shape for the simultaneous impingement of two droplets with a high separation of $e = 3$.

If the separation distance between the droplets is larger, the hydrodynamic interaction is occurring much later. Snapshots of the computed droplet shape for the higher spacing parameter $e = 3$ are presented in Fig. 4.35. The first contact between the two droplets is established at $t = 4.87$ ms. At this stage of the impingement the initial kinetic energy of the droplets has almost completely been dissipated. Hence, no pronounced bump is created in the hydrodynamic interaction zone. Nevertheless, the neck between the two droplets is slowly moving outwards until the maximal size of the wetted region is obtained at $t \approx 9$ ms. When the droplets start to recede, they are still clearly distinguishable from each other and the neck is becoming even smaller. Thereby the droplets seem to separate again during the receding motion but at $t = 32$ ms the neck reaches its minimum width and starts to grow again. The receding motion appears overall to be not strong enough to cause a separation of the droplets. Instead the capillary force drives them towards a complete coalescence. Finally, similar to the result obtained for the small spacing, a single sessile droplet will be produced. A separation of interacting impinging droplets during the receding phase has actually been observed experimentally by Ebner [19] for much higher values of the Reynolds and Weber number ($Re > 3000$ and $We > 100$). Even though he also performed measurements of the local heat transfer during the coalescence, the results are unfortunately not comparable to the present study. It turned out that a certain contamination of the working fluid accumulated at the solid surface during the experiments resulting in uncontrollable and unknown wetting characteristics.

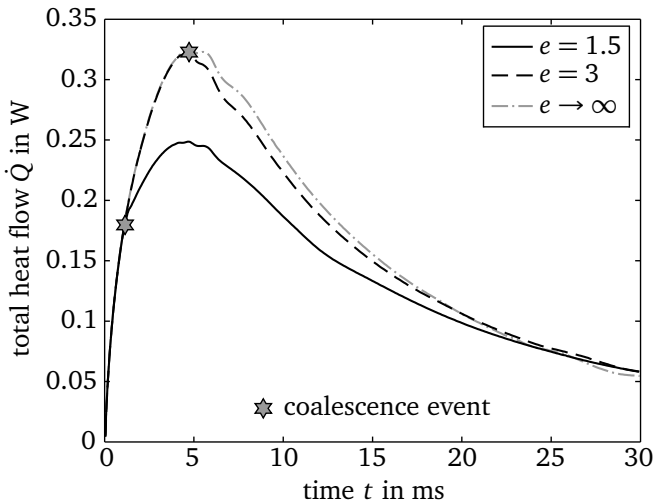


Figure 4.36.: Total wall heat flow for different spacing ratios.

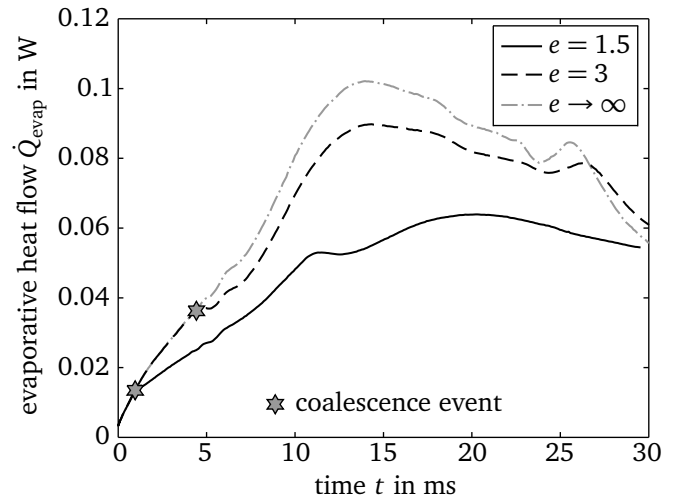


Figure 4.37.: Total evaporative heat flow for different spacing ratios.

The strong hydrodynamic interaction between the droplets of course impacts the heat transfer performance. In Fig. 4.36 the total heat flow removed from the wall is presented for the two different spacing ratios. For reference, the heat flow obtained for two non-interacting droplets, i.e. for $e \rightarrow \infty$, is additionally given in the figure. It can be observed that the heat flow is not influenced as long as the droplets do not touch each other. However, as soon as the two droplets touch each other, the overall heat transfer is strongly reduced compared to the reference case. This breakdown is in particular observed for the small separation distance. In this case, the hydrodynamic interaction takes place during the spreading phase, in which the heat transfer is dominated by the forced convection of the liquid. As soon as the droplets touch, the further enlargement of the wetted surface is suppressed resulting in a lower heat transfer. At the same time, the stagnation point formed between the droplets damps the motion of the liquid. Both

effects together lower the overall heat transfer. The damping of the convective heat transfer is much less pronounced if the two droplets start to interact near the end of the spreading as it is observed for the large separation distance since the kinetic energy is small anyway at this instant.

During the initial stage of the spreading phase, evaporation occurs mainly near the contact line. Accordingly the evaporation rate is roughly proportional to the contact line length. Due to the interaction of the droplets, the contact line is shortened compared to the reference case. Therefore, the evaporation rate is reduced as soon as the droplets touch as can be seen in Fig. 4.37. The evaporation rate during the receding phase has been found to be strongly influenced by the flow pattern within the droplet near the contact line for single droplets in section 4.1.3. The receding motion induced a secondary flow within the droplet transporting superheated liquid from the thermal boundary layer towards the liquid-vapor interface. Especially for the low separation ratio the receding motion was observed to be very slow. Hence, the secondary flow is much weaker as well and the evaporation rate is very small compared to the non-interacting droplets. Moreover, also in the receding phase the contact line length is reduced resulting in an additional reduction of the evaporation rate.

For the larger separation ratio the general effects are analogous to the one described above. However, since the droplets start to interact near the end of the spreading phase, the overall influence is much weaker. Nevertheless, the evaporation rate is again smaller than in the reference case since the receding motion is partially suppressed where the droplets have coalesced. Even though the contact line seems to be comparably long during the receding phase (see e.g. the droplet shape at $t = 32$ ms in Fig. 4.35), it is indeed shorter than for two separate droplet during the entire process.

It can be summarized that an interaction of impinging droplets in general appears to impair both, heat transfer as well as evaporation. However, it cannot be concluded that the overall heat transfer in a spray system would be improved by avoiding any interaction. Then the spray would have to be very dilute and the resulting small number of droplets would lead to a small heat transfer coefficient. In contrast, if the spray was extremely dense, it would form a continuous liquid film on the target surface again worsening the heat transfer performance. Hence, there should be an optimal state in between these two extrema. Moreover, in a real system the probability for two neighboring droplets to impinge exactly simultaneously will be very low. Hence they will not necessarily interact with each other even if $e < S_{\max}$ since they will not reach their maximal extend at the same time.



Summary and conclusions

The heat and mass transfer during the impingement of a single droplet onto a superheated wall is of high technical importance, in particular for an improved understanding of spray cooling. Numerical simulations provide a detailed insight into the local phenomena occurring inside the droplet and can therefore be employed to investigate the effect of individual heat transfer mechanisms onto the global cooling effectiveness of an impinging droplet.

Special attention has been paid to the local evaporation at the moving three-phase contact line. The physics of thin near-wall liquid films has been reviewed and the existing lubrication model for the steady **micro region** heat transfer by Stephan and Busse [100] has been augmented to account for the effects introduced by a motion of the contact line. This augmented lubrication model has been used to predict the local evaporation rate near the contact line as well as the apparent contact angle. In case of an advancing contact line the local evaporation rate has been found to decrease with increasing contact line speed while the apparent contact angle increases with the velocity of the contact line. In case of a receding contact line the effects are exactly opposite.

The derivation of the lubrication model incorporates several simplifying assumptions. In order to quantify the error introduced by neglecting two-dimensional phenomena within the micro region, a direct numerical simulation of the micro region has been performed. The fluid flow has been found to be captured satisfyingly by the lubrication approximation even for comparably large values of the apparent contact angle. On the contrary, the heat conduction within the micro region is strongly two-dimensional in case of a large contact angle and can hence not be predicted very accurately when assuming the heat to be transferred exclusively by one-dimensional heat conduction. The simulation has also been used to take into account a microscopic wall structure but no significant influence of the investigated micro structure was found for non-moving contact lines.

Despite the effort of accurately describing of the heat and fluid flow within the micro region, the model is found to suffer substantially from the uncertainty in the exact value of the condensation coefficient. In fact, the error introduced by this quantity exceeds all the other uncertainties. Due to its strong influence on the apparent contact angle, the condensation coefficient had to be fitted to the experimental conditions. Otherwise a proper prediction of the hydrodynamic behavior of an impinging droplet is not

possible. Nevertheless, the value obtained from the fitting based one single measurement sequence resulted also in a good agreement of simulation and experiment in case of a different wall superheat. The lubrication model has finally been employed to derive a regression of the contact line heat flow and the apparent contact angle as a function of local wall superheat and contact line speed which has then been used in the macroscopic simulation of drop impingement.

For capturing the heat and fluid flow of the impinging droplet a **macroscopic simulation model** has been developed. The VOF method is employed to track the position of the liquid-vapor interface. The interface reconstruction algorithm by Kunkelmann and Stephan [50] has been further developed towards a more accurate representation of the liquid-vapor interface. Based on this reconstruction a novel implicit evaporation model has been introduced which allows an accurate and stable calculation of evaporative phase change. The simulation model has been implemented in OpenFOAM and supports the usage of arbitrary three-dimensional mesh topologies and is running fully in parallel. A novel load balancing procedure enables the efficient usage of the dynamic mesh refinement algorithm in parallel computations which is crucial for an efficient simulation of three-dimensional processes.

The dominant heat transfer mechanisms during **single drop impingement** have been found to differ during the individual stages of the impingement process. During the spreading of the droplet single phase convection of the liquid represents the major contribution to overall heat transfer. The evaporation of the droplet is found to occur particularly during the subsequent receding phase of the impingement. Contact line evaporation contributes to the global phase change during the entire impingement but becomes particularly important as soon as the motion of the liquid within the droplet decays.

The influence of the respective non-dimensional numbers characterizing the properties of the droplet and the solid substrate has been quantified. In particular, the heat transferred to the droplet during the impingement is increasing with the Weber, Bond and Jacobs number while it tends to decrease with increasing Reynolds and Prandtl number.

The **interaction of droplets** has been studied through the simulation of the coalescence of two simultaneously impinging droplets. An interaction is found to generally impair the heat transfer performance, particularly if the hydrodynamic interaction occurs during the very initial stage of the impingement process. It can be concluded that the effect of interaction can only be understood if the dominant heat transfer mechanisms for the single drop impingement are known.

Outlook

Future studies will be performed to investigate the influence of the system pressure. If the pressure approaches the fluid's critical point, the compressibility of the fluid becomes important. At the same time the strength of surface tension effects decreases which might give rise to the formation of instabilities during the impingement process, even at a comparably low impact speed. The knowledge of the interplay of hydrodynamic instabilities and evaporation is highly relevant to cover a larger range of impingement parameters. Due to its three-dimensional formulation, the developed simulation model can be used in these studies. However, one has to assure that instabilities emerging from the simulation are physical and not only numerical artifacts.

In addition, when approaching the critical point, the thickness of the liquid-vapor interface increases considerably. Therefore, the assumption of a Gibbs interface is no longer valid within the micro region. Instead a diffuse interface approach has to be employed for an adequate description of the processes in the region near the apparent contact line. This work has already been started and will be accomplished within the further progress of part project C1 of the collaborative research center SFB-TRR 75.

Currently, the description of the gaseous phase is being augmented to account for the presence of non-condensable gases. This enables the simulation of processes in which the evaporation is no longer limited by the heat transfer towards the liquid-vapor interface but rather by the diffusion process of the vapor within the gas phase. In this situation the saturation temperature at the interface varies in space and accordingly Marangoni convection might have to be considered. On a long term this is a first step towards the development of a model for the evaporation of mixtures of two or more evaporating components.



Bibliography

- [1] V. S. Ajaev, T. Gambaryan-Roisman and P. Stephan. Static and dynamic contact angles of evaporating liquids on heated surfaces. *Journal of Colloid and Interface Science*, 342(2):550–558, 2010.
- [2] E. A. T. van den Akker, A. J. H. Frijns, C. Kunkelmann, P. A. J. Hilbers, P. Stephan and A. A. van Steenhoven. Molecular Dynamics simulation of the microregion. *International Journal of Thermal Sciences*, 59:21–28, 2012.
- [3] E. Aktinol and V. K. Dhir. Numerical Simulation of Nucleate Boiling Phenomenon Coupled with Thermal Response of the Solid. *Microgravity Science and Technology*, 24(4):255–265, 2012.
- [4] C. Antonini, A. Amirfazli and M. Marengo. Drop impact and wettability: From hydrophilic to superhydrophobic surfaces. *Physics of Fluids*, 24(10):102104, 2012.
- [5] S. Batzdorf, T. Gambaryan-Roisman and P. Stephan. Direct numerical simulation of the heat and mass transfer in the 3-phase contact line region. *International Journal of Heat and Mass Transfer*, 2015, submitted.
- [6] E. Berberović, I. V. Roisman, S. Jakirlić and C. Tropea. Inertia dominated flow and heat transfer in liquid drop spreading on a hot substrate. *International Journal of Heat and Fluid Flow*, 32(4):785–795, 2011.
- [7] R. Bhardwaj, J. P. Longtin and D. Attinger. Interfacial temperature measurements, high-speed visualization and finite-element simulations of droplet impact and evaporation on a solid surface. *International Journal of Heat and Mass Transfer*, 53(19-20):3733–3744, 2010.
- [8] A.-L. Bianco, C. Clanet and D. Quéré. Leidenfrost drops. *Physics of Fluids*, 15(6):1632–1637, 2003.
- [9] J. U. Brackbill, D. B. Kothe and C. Zemach. A continuum method for modeling surface tension. *Journal of Computational Physics*, 100(2):335–354, 1992.
- [10] I. N. Bronstein and K. A. Semendjajew. *Taschenbuch der Mathematik*. Deutsch, Thun and Frankfurt am Main, 5th edition, 2001. ISBN 3-8171-2005-2.
- [11] M. Bussmann, J. Mostaghimi and S. Chandra. On a three-dimensional volume tracking model of droplet impact. *Physics of Fluids*, 11(6):1406–1417, 1999.

-
- [12] V. P. Carey. *Liquid-vapor phase-change phenomena: An introduction to the thermophysics of vaporization and condensation processes in heat transfer equipment*. Taylor and Francis, New York, 2nd edition, 2008. ISBN 978-1-59169-035-1.
- [13] S. Chandra and C. T. Avedisian. On the Collision of a Droplet with a Solid Surface. *Proceedings of the Royal Society A: Mathematical, Physical and Engineering Sciences*, 432(1884):13–41, 1991.
- [14] D. Chatzikyriakou, S. P. Walker, C. P. Hale and G. F. Hewitt. The measurement of heat transfer from hot surfaces to non-wetting droplets. *International Journal of Heat and Mass Transfer*, 54(7-8):1432–1440, 2011.
- [15] G. E. Cossali, A. Coghe and M. Marengo. The impact of a single drop on a wetted solid surface. *Experiments in Fluids*, 22:463–472, 1997.
- [16] G. E. Cossali, M. Marengo and M. Santini. Multiple drop impact on heated surface. In *Proceedings of the 9th International Conference on Liquid Atomization and Spray Systems (ICLASS)*, 2003.
- [17] A. H. Dawi, S. Herbert, I. V. Roisman, T. Gambaryan-Roisman, P. Stephan and C. Tropea. Numerical Investigation of Drop Impact onto Hot Surfaces. In *Proceedings of the 25th European Conference on Liquid Atomization and Spray Systems (ILASS)*, 2013.
- [18] S. S. Deshpande, L. Anumolu and M. F. Trujillo. Evaluating the performance of the two-phase flow solver interFoam. *Computational Science & Discovery*, 5(1):014016, 2012.
- [19] S. Ebner. *Experimentelle Bestimmung des Wärmeübergangs von einzelnen und koaleszierenden Tropfen*. Master thesis, Technische Universität Darmstadt, 2014.
- [20] H. Y. Erbil. Evaporation of pure liquid sessile and spherical suspended drops: A review. *Advances in Colloid and Interface Science*, 170(1-2):67–86, 2012.
- [21] P. E. Farrell and J. R. Maddison. Conservative interpolation between volume meshes by local Galerkin projection. *Computer Methods in Applied Mechanics and Engineering*, 200(1-4):89–100, 2011.
- [22] S. Fischer. *Experimental Investigation of Heat Transfer during Evaporation in the Vicinity of Moving Three-Phase Contact Lines*. Ph.D. thesis, Technische Universität Darmstadt, Darmstadt, 2015.
- [23] S. Fischer, S. Herbert, T. Gambaryan-Roisman and P. Stephan. Local heat flux investigation during single drop impingement onto a heated wall. In *Proceedings of the 25th European Conference on Liquid Atomization and Spray Systems (ILASS)*, 2013.
- [24] S. Fischer, S. Herbert, A. Sielaff, E. M. Slomski, P. Stephan and M. Oechsner. Experimental Investigation of Nucleate Boiling on a Thermal Capacitive Heater Under Variable Gravity Conditions. *Microgravity Science and Technology*, 24(3):139–146, 2012.
- [25] M. Francois and W. Shyy. Computations of drop dynamics with the immersed boundary method, part 2: Drop impact and heat transfer. *Numerical Heat Transfer, Part B: Fundamentals*, 44(2):119–143, 2003.

-
- [26] M. M. Francois, S. J. Cummins, E. D. Dendy, D. B. Kothe, J. M. Sicilian and M. W. Williams. A balanced-force algorithm for continuous and sharp interfacial surface tension models within a volume tracking framework. *Journal of Computational Physics*, 213(1):141–173, 2006.
- [27] T. Fuchs, J. Kern and P. Stephan. A Transient Nucleate Boiling Model Including Microscale Effects and Wall Heat Transfer. *Journal of Heat Transfer*, 128(12):1257–1265, 2006.
- [28] E. Fuhrmann and M. E. Dreyer. Heat and mass transfer at a free surface with diabatic boundaries in a single-species system under microgravity conditions. *Experiments in Fluids*, 55(6), 2014.
- [29] J. Fukai, Z. Zhao, D. Poulikakos, C. M. Megaridis and O. Miyatake. Modeling of the deformation of a liquid droplet impinging upon a flat surface. *Physics of Fluids A*, 5(11):2588–2599, 1993.
- [30] T. Gambaryan-Roisman and P. Stephan. Analysis of Falling Film Evaporation on Grooved Surfaces. *Journal of Enhanced Heat Transfer*, 10(4):445–458, 2003.
- [31] H. C. Hamaker. The London-van der Waals attraction between spherical particles. *Physica*, 4(10):1058–1072, 1937.
- [32] S. Hardt and F. Wondra. Evaporation model for interfacial flows based on a continuum-field representation of the source terms. *Journal of Computational Physics*, 227(11):5871–5895, 2008.
- [33] F. H. Harlow and J. E. Welch. Numerical Calculation of Time-Dependent Viscous Incompressible Flow of Fluid with Free Surface. *Physics of Fluids*, 8(12):2182, 1965.
- [34] S. Herbert, S. Fischer, T. Gambaryan-Roisman and P. Stephan. Local heat transfer and phase change phenomena during single drop impingement on a hot surface. *International Journal of Heat and Mass Transfer*, 61:605–614, 2013.
- [35] S. Herbert, T. Gambaryan-Roisman and P. Stephan. Influence of the governing dimensionless parameters on heat transfer during single drop impingement onto a hot wall. *Colloids and Surfaces A: Physicochemical and Engineering Aspects*, 432:57–63, 2013.
- [36] C. W. Hirt and B. D. Nichols. Volume of fluid (VOF) method for the dynamics of free boundaries. *Journal of Computational Physics*, 39(1):201–225, 1981.
- [37] K. Ibrahim, M. Abd Rabbo, T. Gambaryan-Roisman and P. Stephan. Experimental investigation of evaporative heat transfer characteristics at the 3-phase contact line. *Experimental Thermal and Fluid Science*, 34(8):1036–1041, 2010.
- [38] K. Ibrahim, M. F. Abd Rabbo, T. Gambaryan-Roisman and P. Stephan. Experimental Investigation of Micro-Scale Heat Transfer at an Evaporating Moving 3-Phase Contact Line. In *Proceedings of the 14th International Heat Transfer Conference*, pages 783–790, 2010.
- [39] J. N. Israelachvili. *Intermolecular and surface forces*. Academic Press, London, 2nd edition, 6th printed edition edition, 1997. ISBN 0-12-375181-0.
- [40] R. I. Issa. Solution of the implicitly discretised fluid flow equations by operator-splitting. *Journal of Computational Physics*, 62(1):40–65, 1986.

-
- [41] H. Jasak. *Error Analysis and Estimation for the Finite Volume Method with Applications to Fluid Flows*. Ph.D. thesis, Imperial College of Science, Technology and Medicine, London, 1996.
- [42] S. G. Kandlikar and W. J. Grande. Evolution of Microchannel Flow Passages—Thermohydraulic Performance and Fabrication Technology. *Heat Transfer Engineering*, 24(1):3–17, 2003.
- [43] Y. Kantomani. Evaporator film coefficients of grooved heat pipes. In *Proceedings of the 3rd International Heat Pipe Conference*, 1978.
- [44] J. Kern. *Modellierung und numerische Berechnung des Wärmeübergangs beim Blasensieden binärer Gemische*. VDI-Verlag, Düsseldorf, 2002. ISBN 978-3-1837-2703-2.
- [45] J. Kern and P. Stephan. Theoretical Model for Nucleate Boiling Heat and Mass Transfer of Binary Mixtures. *Journal of Heat Transfer*, 125(6):1106, 2003.
- [46] J. Kim. Spray cooling heat transfer: The state of the art. *International Journal of Heat and Fluid Flow*, 28(4):753–767, 2007.
- [47] C. Kunkelmann. *Modellierung und numerische Berechnung des Wärmetransports bei der Verdampfung aus Kapillarstrukturen in Wärmerohren*. Diploma thesis, Technische Universität Darmstadt, 2007.
- [48] C. Kunkelmann. *Numerical Modeling and Investigation of Boiling Phenomena*. Ph.D. thesis, Technische Universität Darmstadt, Darmstadt, 2011.
- [49] C. Kunkelmann, K. Ibrahim, N. Schweizer, S. Herbert, P. Stephan and T. Gambaryan-Roisman. The effect of three-phase contact line speed on local evaporative heat transfer: Experimental and numerical investigations. *International Journal of Heat and Mass Transfer*, 55(7-8):1896–1904, 2012.
- [50] C. Kunkelmann and P. Stephan. Modification and extension of a standard Volume-of-Fluid solver for simulating boiling heat transfer. In *Proceedings of the 5th European Conference on Computational Fluid Dynamics*, 2010.
- [51] C. Kunkelmann and P. Stephan. Numerical simulation of the transient heat transfer during nucleate boiling of refrigerant HFE-7100. *International Journal of Refrigeration*, 33(7):1221–1228, 2010.
- [52] J. H. Lay and V. K. Dhir. Shape of a Vapor Stem During Nucleate Boiling of Saturated Liquids. *Journal of Heat Transfer*, 117(2):394–401, 1995.
- [53] J. Lee, J. Kim and K. Kiger. Time- and space-resolved heat transfer characteristics of single droplet cooling using microscale heater arrays. *International Journal of Heat and Fluid Flow*, 22:188–200, 2001.
- [54] Y. Liu, P. Tan and L. Xu. Compressible air entrapment in high-speed drop impacts on solid surfaces. *Journal of Fluid Mechanics*, 716, 2013.

-
- [55] J. López and J. Hernández. Analytical and geometrical tools for 3D volume of fluid methods in general grids. *Journal of Computational Physics*, 227(12):5939–5948, 2008.
- [56] C. Ma. *Mathematische Modellierung und Direkte Numerische Simulation oberflächenspannungsgetriebener Zweiphasenströmungen mit und ohne Verdunstung*. Shaker, Aachen, 2012. ISBN 978-3-8440-1639-0.
- [57] C. Ma and D. Bothe. Numerical modeling of thermocapillary two-phase flows with evaporation using a two-scalar approach for heat transfer. *Journal of Computational Physics*, 233:552–573, 2013.
- [58] M. Mann. *Ein Mikrozonenmodell zur Beschreibung der Blasenbildung und des Wärmeübergangs beim Sieden*. VDI-Verlag, Düsseldorf, 2001. ISBN 3-18-370803-5.
- [59] T. Mao, D. C. S. Kuhn and H. Tran. Spread and rebound of liquid droplets upon impact on flat surfaces. *AIChE Journal*, 43(9):2169–2179, 1997.
- [60] R. Marek and J. Straub. Analysis of the evaporation coefficient and the condensation coefficient of water. *International Journal of Heat and Mass Transfer*, 44(1):39–53, 2001.
- [61] T. Marić, H. Marschall and D. Bothe. voFoam - A geometrical Volume of Fluid algorithm on arbitrary unstructured meshes with local dynamic adaptive mesh refinement using OpenFOAM. *arXiv:1305.3417*, 2013.
- [62] B. Mathieu, O. Lebaigue and L. Tadriss. Numerical investigation of a dynamic contact line model for perfectly wetting liquids on a heated wall of finite conductivity. In *Proceedings of the 12th International Heat Transfer Conference*, pages 455–466, 2002.
- [63] C. Mundo, M. Sommerfeld and C. Tropea. Droplet-wall collisions: Experimental studies of the deformation and breakup process. *International Journal of Multiphase Flow*, 21(2):151–173, 1995.
- [64] T. G. Myers and J. P. F. Charpin. A mathematical model of the Leidenfrost effect on an axisymmetric droplet. *Physics of Fluids*, 21(6):063101, 2009.
- [65] V. S. Nikolayev. Dynamics of the triple contact line on a nonisothermal heater at partial wetting. *Physics of Fluids*, 22(8):082105, 2010.
- [66] N. Nikolopoulos, A. Theodorakakos and G. Bergeles. A numerical investigation of the evaporation process of a liquid droplet impinging onto a hot substrate. *International Journal of Heat and Mass Transfer*, 50(1–2):303–319, 2007.
- [67] M. Ojha, A. Chatterjee, G. Dalakos, P. C. Wayner and J. L. Plawsky. Role of solid surface structure on evaporative phase change from a completely wetting corner meniscus. *Physics of Fluids*, 22(5):052101, 2010.
- [68] A. Oron, S. H. Davis and S. G. Bankoff. Long-scale evolution of thin liquid films. *Reviews of Modern Physics*, 69(3):931–980, 1997.

-
- [69] S. Osher and J. A. Sethian. Fronts propagating with curvature-dependent speed: Algorithms based on Hamilton-Jacobi formulations. *Journal of Computational Physics*, 79(1):12–49, 1988.
- [70] C. J. van Oss, M. K. Chaudhury and R. J. Good. Interfacial Lifshitz-van der Waals and polar interactions in macroscopic systems. *Chemical Reviews*, 88(6):927–941, 1988.
- [71] M. Pasandideh-Fard, S. Chandra and J. Mostaghimi. A three-dimensional model of droplet impact and solidification. *International Journal of Heat and Mass Transfer*, 45(11):2229–2242, 2002.
- [72] M. Pasandideh-Fard, Y. M. Qiao, S. Chandra and J. Mostaghimi. Capillary effects during droplet impact on a solid surface. *Physics of Fluids*, 8(3):650, 1996.
- [73] A. Pattamatta, M. Freystein and P. Stephan. A parametric study on phase change heat transfer due to Taylor-Bubble coalescence in a square minichannel. *International Journal of Heat and Mass Transfer*, 76:16–32, 2014.
- [74] J. L. Plawsky, A. Chatterjee and P. C. Wayner. Modeling contact line dynamics in evaporating menisci. In *Proceedings of the 2009 Comsol User’s Conference*, 2009.
- [75] M. S. Plesset and S. A. Zwick. The Growth of Vapor Bubbles in Superheated Liquids. *Journal of Applied Physics*, 25(4):493–500, 1954.
- [76] M. Potash and P. C. Wayner. Evaporation from a two-dimensional extended meniscus. *International Journal of Heat and Mass Transfer*, 15(10):1851–1863, 1972.
- [77] D. Quéré. Leidenfrost Dynamics. *Annual Review of Fluid Mechanics*, 45(1):197–215, 2013.
- [78] R. Raj, C. Kunkelmann, P. Stephan, J. Plawsky and J. Kim. Contact line behavior for a highly wetting fluid under superheated conditions. *International Journal of Heat and Mass Transfer*, 55(9–10):2664–2675, 2012.
- [79] M. Rein. Phenomena of liquid drop impact on solid and liquid surfaces. *Fluid Dynamics Research*, 12(2):61–93, 1993.
- [80] D. Richard, C. Clanet and D. Quéré. Surface phenomena: Contact time of a bouncing drop. *Nature*, 417:811, 2002.
- [81] W. J. Rider and D. B. Kothe. Reconstructing Volume Tracking. *Journal of Computational Physics*, 141(2):112–152, 1998.
- [82] M. Rieber and A. Frohn. A numerical study on the mechanism of splashing. *International Journal of Heat and Fluid Flow*, 20(5):455–461, 1999.
- [83] R. Rioboo, C. Tropea and M. Marengo. Outcomes from a drop impact on solid surfaces. *Atomization and Sprays*, 11(2):155–165, 2001.
- [84] I. V. Roisman. Inertia dominated drop collisions. II. An analytical solution of the Navier–Stokes equations for a spreading viscous film. *Physics of Fluids*, 21(5):052104, 2009.

-
- [85] I. V. Roisman, B. Prunet-Foch, C. Tropea and M. Vignes-Adler. Multiple Drop Impact onto a Dry Solid Substrate. *Journal of Colloid and Interface Science*, 256(2):396–410, 2002.
- [86] M. Schäfer. *Computational engineering: Introduction to numerical methods*. Springer, Berlin and New York, 2006. ISBN 978-3-540-30685-6.
- [87] J. Schlottke. *Direkte numerische Simulation von Mehrphasenströmungen mit Phasenübergang*. Verlag Dr. Hut, München, 2010. ISBN 978-3-86853-372-9.
- [88] J. Schlottke and B. Weigand. Direct numerical simulation of evaporating droplets. *Journal of Computational Physics*, 227(10):5215–5237, 2008.
- [89] R. W. Schrage. *A theoretical study of interphase mass transfer*. Columbia University Press, New York, 1953.
- [90] N. Schweizer. *Multi-Scale Investigation of Nucleate Boiling Phenomena in Microgravity*. Ph.D. thesis, Technische Universität Darmstadt, Darmstadt, 2010.
- [91] L. E. Scriven. On the dynamics of phase growth. *Chemical Engineering Science*, 10(1-2):1–13, 1959.
- [92] A. Sielaff. *Experimental Investigation of Single Bubbles and Bubble Interactions in Nucleate Boiling*. Ph.D. thesis, Technische Universität Darmstadt, Darmstadt, 2014.
- [93] Š. Šikalo, H.-D. Wilhelm, I. V. Roisman, S. Jakirlić and C. Tropea. Dynamic contact angle of spreading droplets: Experiments and simulations. *Physics of Fluids*, 17(6):062103, 2005.
- [94] C. Sodtke, V. S. Ajaev and P. Stephan. Evaporation of thin liquid droplets on heated surfaces. *Heat and Mass Transfer*, 43(7):649–657, 2007.
- [95] G. Son and V. K. Dhir. Numerical Simulation of Film Boiling Near Critical Pressures With a Level Set Method. *Journal of Heat Transfer*, 120(1):183, 1998.
- [96] G. Son, V. K. Dhir and N. Ramanujapu. Dynamics and Heat Transfer Associated With a Single Bubble During Nucleate Boiling on a Horizontal Surface. *Journal of Heat Transfer*, 121(3):623–631, 1999.
- [97] K. Stephan. Influence of dispersion forces on phase equilibria between thin liquid films and their vapour. *International Journal of Heat and Mass Transfer*, 45(24):4715–4725, 2002.
- [98] P. Stephan. *Wärmedurchgang bei Verdampfung aus Kapillarrillen in Wärmerohren*. VDI-Verlag, Düsseldorf, 1992. ISBN 978-3-1814-5919-5.
- [99] P. Stephan and J. Hammer. A new model for nucleate boiling heat transfer. *Heat and Mass Transfer*, 30(2):119–125, 1994.
- [100] P. C. Stephan and C. A. Busse. Analysis of the heat transfer coefficient of grooved heat pipe evaporator walls. *International Journal of Heat and Mass Transfer*, 35(2):383–391, 1992.

-
- [101] G. Strotos, M. Gavaises, A. Theodorakakos and G. Bergeles. Numerical investigation of the cooling effectiveness of a droplet impinging on a heated surface. *International Journal of Heat and Mass Transfer*, 51(19-20):4728–4742, 2008.
- [102] G. Strotos, M. Gavaises, A. Theodorakakos and G. Bergeles. Numerical investigation on the evaporation of droplets depositing on heated surfaces at low Weber numbers. *International Journal of Heat and Mass Transfer*, 51(7–8):1516–1529, 2008.
- [103] M. Sussman. A second order coupled level set and volume-of-fluid method for computing growth and collapse of vapor bubbles. *Journal of Computational Physics*, 187(1):110–136, 2003.
- [104] T. Tran, H. J. J. Staat, A. Prosperetti, C. Sun and D. Lohse. Drop Impact on Superheated Surfaces. *Physical Review Letters*, 108(3), 2012.
- [105] T. Tran, H. J. J. Staat, A. Susarrey-Arce, T. C. Foertsch, A. van Houselt, H. J. G. E. Gardeniers, A. Prosperetti, D. Lohse and C. Sun. Droplet impact on superheated micro-structured surfaces. *Soft Matter*, 9(12):3272–3282, 2013.
- [106] G. Tryggvason, B. Bunner, A. Esmaeeli, D. Juric, N. Al-Rawahi, W. Tauber, J. Han, S. Nas and Y.-J. Jan. A Front-Tracking Method for the Computations of Multiphase Flow. *Journal of Computational Physics*, 169(2):708–759, 2001.
- [107] Ž. Tuković and H. Jasak. Simulation of free-rising bubble with soluble surfactant using moving mesh finite area/volume method. In *Proceedings of the 6th International Conference on CFD in Oil & Gas, Metallurgical and Process Industries, SINTEF/NTNU, Trondheim, Norway, 2008*.
- [108] Ž. Tuković and H. Jasak. A moving mesh finite volume interface tracking method for surface tension dominated interfacial fluid flow. *Computers & Fluids*, 55:70–84, 2012.
- [109] O. Ubbink and R. Issa. A Method for Capturing Sharp Fluid Interfaces on Arbitrary Meshes. *Journal of Computational Physics*, 153(1):26–50, 1999.
- [110] C. Ukiwe and D. Y. Kwok. On the Maximum Spreading Diameter of Impacting Droplets on Well-Prepared Solid Surfaces. *Langmuir*, 21(2):666–673, 2005.
- [111] VDI-Gesellschaft Verfahrenstechnik und Chemieingenieurwesen (GVC), editor. *VDI Heat Atlas*. Springer, Berlin and Heidelberg, 2nd edition, 2010. ISBN 978-3-540-77876-9.
- [112] E. Wagner, C. Sodtke, N. Schweizer and P. Stephan. Experimental study of nucleate boiling heat transfer under low gravity conditions using TLCs for high resolution temperature measurements. *Heat and Mass Transfer*, 42(10):875–883, 2006.
- [113] A.-B. Wang, C.-H. Lin and C.-C. Cheng. Pattern analysis of a single droplet impinging onto a heated plate. *Heat Transfer – Asian Research*, 34(8):579–594, 2005.
- [114] H. Wang, S. V. Garimella and J. Y. Murthy. Characteristics of an evaporating thin film in a microchannel. *International Journal of Heat and Mass Transfer*, 50(19–20):3933–3942, 2007.

-
- [115] P. C. Wayner, Y. K. Kao and L. V. LaCroix. The interline heat-transfer coefficient of an evaporating wetting film. *International Journal of Heat and Mass Transfer*, 19(5):487–492, 1976.
- [116] P. Weber, H. Marschall and D. Bothe. Species Transport and Stability Issues in ALE Frameworks. In *Proceedings of the 2nd International Conference on Numerical Methods in Multiphase Flows*, pages 119–120, 2014.
- [117] C. Weickgenannt, Y. Zhang, A. Lembach, I. Roisman, T. Gambaryan-Roisman, A. Yarin and C. Tropea. Nonisothermal drop impact and evaporation on polymer nanofiber mats. *Physical Review E*, 83(3):036305, 2011.
- [118] H. G. Weller. A new approach to VOF-based interface capturing methods for incompressible and compressible flow. *Technical Report TR/HGW/04, OpenCFD Ltd.*, 2008.
- [119] H. G. Weller, G. Tabor, H. Jasak and C. Fureby. A tensorial approach to computational continuum mechanics using object-oriented techniques. *Computers in Physics*, 12(6):620–631, 1998.
- [120] A. M. Worthington. *The splash of a drop*. The Society for Promoting Christian Knowledge, London, 1895.
- [121] A. L. Yarin. Drop Impact Dynamics: Splashing, Spreading, Receding, Bouncing. . . . *Annual Review of Fluid Mechanics*, 38(1):159–192, 2006.
- [122] Z. Zhao, D. Poulikakos and J. Fukai. Heat transfer and fluid dynamics during the collision of a liquid droplet on a substrate – I. Modeling. *International Journal of Heat and Mass Transfer*, 39(13):2771–2789, 1996.



A.1 Material properties

property	symbol	liquid	vapor
density	ρ	1619.82 kg/m ³	13.36 kg/m ³
dynamic viscosity	μ	4.5306×10^{-4} kg/(m s)	9.4602×10^{-6} kg/(m s)
specific heat capacity	c	1098.41 J/(kg K)	885.04 J/(kg K)
thermal conductivity	k	0.05216 W/(m K)	0.00864 W/(m K)
saturation temperature	T_{sat}	329.75 K	
latent heat of vaporization	h_{lv}	84515 J/kg	
surface tension	σ	0.008273 N/m	
individual gas constant	\mathcal{R}	24.45 J/(kg K)	
dispersion constant	A	4.37×10^{-21} J	
condensation coefficient	f	0.5	

Table A.1.: Properties of FC-72 at a saturation pressure of 1 bar.

property	symbol	value
density	ρ	3180 kg/m ³
specific heat capacity	c	854 J/(kg K)
thermal conductivity	k	9.71 W/(m K)

Table A.2.: Properties of CaF₂.

property	symbol	value
thermal conductivity	k	221 W/(m K)

Table A.3.: Properties of aluminum.

property	symbol	liquid	vapor
density	ρ	600 kg/m ³	9 kg/m ³
dynamic viscosity	μ	1.3×10^{-4} kg/(m s)	-
thermal conductivity	k	0.48 W/(m K)	0.02773 W/(m K)
saturation temperature	T_{sat}	300 K	
latent heat of vaporization	h_{lv}	1.18×10^6 J/kg	
surface tension	σ	0.02 N/m	
individual gas constant	\mathcal{R}	488 J/(kg K)	
dispersion constant	A	2×10^{-21} J	
condensation coefficient	f	1	

Table A.4.: Properties of ammonia at a saturation pressure of 10.64 bar.

A.2 Correlation coefficients for the contact line model

i	1	2	3	4	5	6	7	8
$a_{Q,T,i}$	-0.467552	104.787	-1420.92	5223.68	-6989.60	3082.80	-	-
$a_{Q,u,i}$	1.0	-2.11704	9.14288	-34.0527	74.9144	-91.4608	57.4550	-14.4560
b_Q	-0.343704							
$a_{\theta,T,i}$	-9.27067	2538.08	-37961.6	145453	-199078	89077	-	-
$a_{\theta,u,i}$	1.0	16.0275	-101.163	342.739	144.270	-4190.60	10161.1	-7733.42
b_θ	-0.879093							
$a_{\delta,T,i}/10^{-8}$	6.59440	-1015.69	13104.6	-46868.9	61763.3	-26980.0	-	-
$a_{\delta,u,i}$	1.0	3.84269	-2.60049	14.5642	-34.3249	42.8145	-24.5278	5.22288
b_δ	-0.183823							

Table A.5.: Correlation coefficients for FC-72 in the range $5 \text{ K} \leq \Delta T \leq 20 \text{ K}$ and $-0.1 \text{ m/s} \leq u_{\text{cl}} \leq 2 \text{ m/s}$.

i	1	2	3	4	5	6
$a_{Q,T,i}$	0.232721	55.1645	-318.744	799.659	-856.921	326.359
$a_{\theta,T,i}$	2.44615	-200.720	2069.64	-6629.94	8248.57	-3471.60
$a_{\delta,T,i}/10^{-8}$	-0.641294	56.1350	-449.896	1176.52	-1142.83	375.464

Table A.6.: Correlation coefficients for ammonia in the range $0.1 \text{ K} \leq \Delta T \leq 2 \text{ K}$ (velocity independent coefficients only).

A.3 Parametric study

Re	We	Bo	Pr	Ja	D_0 in mm	u_0 in m/s	g in m/s ²	ΔT_w in K	c_l in J/(kg K)	h_{lv} in kJ/kg
500	15	0.5	9.54	0.13	0.2553	0.5478	156.73	10	1098.41	84.515
625	15	0.5	9.54	0.13	0.3989	0.4382	64.197	10	1098.41	84.515
750	15	0.5	9.54	0.13	0.5744	0.3652	30.959	10	1098.41	84.515
875	15	0.5	9.54	0.13	0.7818	0.3130	16.711	10	1098.41	84.515
1000	15	0.5	9.54	0.13	1.021	0.2739	9.796	10	1098.41	84.515
1125	15	0.5	9.54	0.13	1.292	0.2435	6.115	10	1098.41	84.515
1250	15	0.5	9.54	0.13	1.596	0.2191	4.012	10	1098.41	84.515
1500	15	0.5	9.54	0.13	2.298	0.1826	1.935	10	1098.41	84.515
1750	15	0.5	9.54	0.13	3.127	0.1565	1.044	10	1098.41	84.515
1000	10	0.5	9.54	0.13	1.532	0.1826	4.354	10	1098.41	84.515
1000	15	0.5	9.54	0.13	1.021	0.2739	9.796	10	1098.41	84.515
1000	20	0.5	9.54	0.13	0.7659	0.3652	17.414	10	1098.41	84.515
1000	25	0.5	9.54	0.13	0.6127	0.4565	27.210	10	1098.41	84.515
1000	30	0.5	9.54	0.13	0.5106	0.5478	39.182	10	1098.41	84.515
1000	35	0.5	9.54	0.13	0.4376	0.6391	53.332	10	1098.41	84.515
1000	40	0.5	9.54	0.13	0.3829	0.7304	69.658	10	1098.41	84.515
1000	45	0.5	9.54	0.13	0.3404	0.8217	88.160	10	1098.41	84.515
1000	50	0.5	9.54	0.13	0.3064	0.9130	108.84	10	1098.41	84.515
1000	15	0.2	9.54	0.13	1.021	0.2739	3.918	10	1098.41	84.515
1000	15	0.6	9.54	0.13	1.021	0.2739	11.755	10	1098.41	84.515
1000	15	1.0	9.54	0.13	1.021	0.2739	19.591	10	1098.41	84.515
1000	15	1.5	9.54	0.13	1.021	0.2739	29.387	10	1098.41	84.515
1000	15	2.0	9.54	0.13	1.021	0.2739	39.182	10	1098.41	84.515
1000	15	0.5	1.0	0.13	1.021	0.2739	9.796	10	115.127	8.8560
1000	15	0.5	2.5	0.13	1.021	0.2739	9.796	10	287.818	22.140
1000	15	0.5	5.0	0.13	1.021	0.2739	9.796	10	575.637	44.280
1000	15	0.5	7.5	0.13	1.021	0.2739	9.796	10	863.455	66.420
1000	15	0.5	10	0.13	1.021	0.2739	9.796	10	1151.27	88.560
1000	15	0.5	15	0.13	1.021	0.2739	9.796	10	1726.91	132.84
1000	15	0.5	20	0.13	1.021	0.2739	9.796	10	2302.55	177.12
1000	15	0.5	25	0.13	1.021	0.2739	9.796	10	2878.18	221.40
1000	15	0.5	9.54	0.075	1.021	0.2739	9.796	5.77	1098.41	84.515
1000	15	0.5	9.54	0.100	1.021	0.2739	9.796	7.69	1098.41	84.515
1000	15	0.5	9.54	0.125	1.021	0.2739	9.796	9.62	1098.41	84.515
1000	15	0.5	9.54	0.150	1.021	0.2739	9.796	11.54	1098.41	84.515
1000	15	0.5	9.54	0.175	1.021	0.2739	9.796	13.47	1098.41	84.515
1000	15	0.5	9.54	0.200	1.021	0.2739	9.796	15.39	1098.41	84.515
1000	15	0.5	9.54	0.225	1.021	0.2739	9.796	17.31	1098.41	84.515
1000	15	0.5	9.54	0.250	1.021	0.2739	9.796	19.24	1098.41	84.515

Table A.7.: Case summary of the parametric study of droplet parameters.



Curriculum vitae

Personal information

Name	Stefan Batzdorf
Date of birth	June, 2 nd 1985
Place of birth	Fulda
Name of birth	Stefan Herbert
Family status	Married
Nationality	German

Education

08/1991 – 07/1995	Elementary school in Fulda-Johannesberg
08/1995 – 06/2004	Secondary school Marianum in Fulda

Studies of mechanical engineering

10/2005 – 03/2009	Bachelor studies Mechanical and Process Engineering at Technische Universität Darmstadt
04/2009 – 02/2011	Master studies Mechanical and Process Engineering at Technische Universität Darmstadt

Professional career

since 03/2011	Research assistant at the Institute of Technical Thermodynamics at Technische Universität Darmstadt Research project: Numerical modeling of drop impingement heat transfer
---------------	---



Publications

Peer reviewed journal papers

S. Fischer, **S. Herbert**, A. Sielaff, E. Slomski, P. Stephan and M. Oechsner. Experimental Investigation of Nucleate Boiling on a Thermal Capacitive Heater under Variable Gravity Conditions. *Microgravity Science and Technology*, 24:139–146, 2012.

C. Kunkelmann, K. Ibrahim, N. Schweizer, **S. Herbert**, P. Stephan and T. Gambaryan-Roisman. The effect of three-phase contact line speed on local evaporative heat transfer: Experimental and numerical investigations. *International Journal of Heat and Mass Transfer*, 55:1896–1904, 2012.

S. Hardt, **S. Herbert**, C. Kunkelmann, S. Mahjoob and P. Stephan. Unidirectional bubble growth in microchannels with asymmetric surface features. *International Journal of Heat and Mass Transfer*, 55:7056–7062, 2012.

T. Baier, G. Dupeux, **S. Herbert**, S. Hardt and D. Quéré. Propulsion Mechanisms for Leidenfrost Solids on Ratchet Surfaces. *Physical Review E*, 87:021001, 2013.

S. Herbert, S. Fischer, T. Gambaryan-Roisman and P. Stephan. Local heat transfer and phase change phenomena during single drop impingement on a hot surface. *International Journal of Heat and Mass Transfer*, 61:605–614, 2013.

S. Herbert, T. Gambaryan-Roisman and P. Stephan. The influence of the dominant parameters on heat transfer during single drop impingement onto a hot wall. *Colloids and Surfaces A: Physicochemical and Engineering Aspects*, 432:57–63, 2013.

A. Sielaff, J. Dietl, **S. Herbert** and P. Stephan. The influence of system pressure on bubble coalescence in nucleate boiling. *Heat Transfer Engineering*, 35(5):420–429, 2014.

S. Fischer, **S. Herbert**, E. M. Slomski, P. Stephan and M. Oechsner. Local heat flux investigation during pool boiling single bubble cycles under reduced gravity. *Heat Transfer Engineering*, 35(5):482–491, 2014.

S. Batzdorf, T. Gambaryan-Roisman and P. Stephan. Direct numerical solution of the heat and mass transfer from the 3-phase contact line region. *International Journal of Heat and Mass Transfer*, 2015, submitted.

- S. Fischer, **S. Herbert**, E. M. Slomski, P. Stephan and M. Oechsner. Local heat flux investigation during pool boiling single bubble cycles under reduced gravity. In *Proceedings of the 8th International Conference on Boiling and Condensation Heat Transfer*, Lausanne, Switzerland, 2012.
- A. Sielaff, J. Dietl, **S. Herbert** and P. Stephan. The influence of system pressure on bubble coalescence in nucleate boiling. In *Proceedings of the 8th International Conference on Boiling and Condensation Heat Transfer*, Lausanne, Switzerland, 2012.
- P. Stephan, A. Sielaff, S. Fischer, J. Dietl and **S. Herbert**. A contribution to the basic understanding of nucleate boiling phenomena: Generic experiments and numerical simulations. In *Proceedings of the 3rd International Forum on Heat Transfer*, Nagasaki, Japan, 2012.
- T. Baier, **S. Herbert** and S. Hardt. Leidenfrost Solids On Structured Surfaces. In *Proceedings of the 3rd European Conference on Microfluidics*, Heidelberg, Germany, 2012.
- A. H. Dawi, **S. Herbert**, I. V. Roisman, T. Gambaryan-Rosiman, P. Stephan and C. Tropea. Investigation of Drop Impact onto Heated Surfaces under High Ambient Pressure. In *Proceedings of the 25th European Conference on Liquid Atomization and Spray Systems (ILASS)*, Chania, Greece, 2013.
- S. Fischer, **S. Herbert**, T. Gambaryan-Roisman and P. Stephan. Local heat flux investigation during single drop impingement onto a heated wall. In *Proceedings of the 25th European Conference on Liquid Atomization and Spray Systems (ILASS)*, Chania, Greece, 2013.
- S. Fischer, **S. Batzdorf**, T. Gambaryan-Roisman and P. Stephan. High Resolution Heat Transfer Measurements at the Three Phase Contact Line of a Moving Single Meniscus. In *Proceedings of the 15th International Heat Transfer Conference*, Kyoto, Japan, 2014.

Further conference contributions (non reviewed or abstracts only)

- S. Fischer, **S. Herbert**, A. Sielaff, E. M. Slomski, P. Stephan and M. Oechsner. Experimental investigation of nucleate boiling on a thermal capacitive heater under variable gravity conditions. *Eurotherm Seminar No.92, Gravitational Effects on Liquid-Vapour Phase Change*, Prequière de Giens, France, 2011.
- A. Sielaff, S. Fischer, **S. Herbert**, M. Freystein, P. Stephan, N. Schweizer and O. Schoele-Schulz. Experimental Investigation of Pool Boiling Phenomena in Reduced and Micro Gravity. *4th International Symposium on Physical Sciences in Space (ISPS-4)*, Bonn, Germany, 2011.
- S. Herbert**, S. Fischer, P. Stephan and T. Gambaryan-Roisman. Untersuchung des Wärmeübergangs beim Einzeltropfenaufprall auf beheizte Wände – Simulation und Experiment. *Tagung des Fachgruppe Wärme- und Stoffübertragung, ProcessNet VDI/Dechema*, Weimar, Germany, 2012.
- S. Herbert**, S. Fischer, T. Gambaryan-Roisman and P. Stephan. Local heat transfer and phase change phenomena during single drop impingement on a hot surface. *Eurotherm*, Poitiers, France, 2012.

S. Herbert, S. Fischer, T. Gambaryan-Roisman and P. Stephan. Wärmeübergang beim Einzeltropfenaufrall auf beheizte Wände – Identifikation der dominanten Parameter. *Tagung der Fachgruppe Wärme- und Stoffübertragung, ProcessNet VDI/Dechema*, Baden-Baden, Germany, 2013.

S. Batzdorf, T. Gambaryan-Roisman and P. Stephan. Direkte numerische Simulation des Wärme- und Stoffübergangs im Bereich bewegter Dreiphasen-Kontaktlinien bei Verdampfungsvorgängen. *Tagung der Fachgruppe Wärme- und Stoffübertragung, ProcessNet VDI/Dechema*, Fulda, Germany, 2014.

S. Batzdorf, J. Dietl and P. Stephan. Accurate calculation of interfacial temperature gradients for simulation of evaporation and condensation in a VOF framework. *2nd International Conference on Numerical Methods in Multiphase Flows (ICNMMF II)*, Darmstadt, Germany, 2014.